Coordination compounds for molecular electronics:

Synthesis, characterization and electronic transport properties of copper rotaxanes and molecular complexes.

Instituto de Ciencia Molecular
Universitat de València

&

Memoria presentada por Julia Ponce González para aspirar al grado de Doctor en Nanociencia y Nanoteconología (programa ref. 3045)

&

Dirigida por el Dr. Eugenio Coronado Miralles y el Dr. Sergio Tatay Aguilar

D. Eugenio Coronado Miralles, Catedrático de Química Inorgánica de la Universidad de Valencia y D. Sergio Tatay Aguilar, doctor por la misma universidad y actualmente investigador Juan de la Cierva en la Universidad de Valencia

CERTIFICAN:

Que la memoria presentada por Dña. Julia Ponce González con título "Coordination compounds for molecular electronics: Synthesis, characterization and electronic transport properties of copper rotaxanes and molecular complexes" ha sido realizada bajo su dirección en el Instituto de Ciencia Molecular, autorizando mediante este escrito la presentación de la misma para optar al grado de Doctor en Nanociencia y Nanotecnología.

En Paterna, a 23 de Abril de 2014

D. Eugenio Coronado Miralles D. Sergio Tatay Aguilar

Julia Ponce González

Agradecimientos

Quisiera agradecer esta tesis:

A mis directores.

Eugenio y Sergio. A Eugenio, por sus ideas brillantes, algunas de las cuales he podido materializar y forman parte de esta tesis. También por el amplio margen de actuación con el que me ha dejado para trabajar, el cual me ha permitido equivocarme tanto y aprender mucho más. Y en segundo lugar, aunque no menos importante, a Sergio y su boli rojo por todo el empeño que han puesto para que esta tesis pudiera terminarse. Tú empezaste el camino que yo luego he habido de continuar, con mayor o menor acierto. Sin duda he aprendido muchísimo discutiendo contigo, y aunque una etapa acabe aquí, siempre puedes contar conmigo para darte la réplica. Y aunque formalmente no figure, también aquí quisiera agradecerle a Pablo Gaviña su participación en la dirección y su inalterable buen humor. Eres un artesano de la química orgánica y espero haber asimilado algo de ese "saber hacer" en el laboratorio que tú y Sergio compartís.

A la financiación.

Al ministerio de cambiante nombre que me concedió la beca predoctoral y también a los proyectos CONSOLIDER-INGENIO en Nanociencia Molecular, ELFOS y ERC-Advanced Grant SPINMOL que han financiado esta investigación.

A mis colaboradores.

En primer lugar a los más directos. A Jorge Gómez Magenti, que está continuando parte de este trabajo con mucha ilusión y muchas ganas y al que le auguro un futuro muy prometedor. Aunque sea incapaz de apuntar nada. También la gente de Delft; Herre, Ferry, Carlos y Riccardo; que son unos de nuestros principales colaboradores y con quienes tenemos un feedback muy intenso. A Eliseo Ruíz y Daniel Aravena, de la Universidad Autónoma de Barcelona, quienes han sido extremadamente diligentes con los cálculos teóricos de la parte de transporte. A Nacho Vayà, que realizó parte de las

medidas y a Juan Aragó y Enrique Ortí, que han hecho un gran trabajo en la interpretación de la fotofísica de los complejos de Iridio. También a la gente de los servicios centrales de investigación. A César e Isabel, del servicio de RMN, a Salomé de absorción atómica y a las muy eficaces chicas del MALDI. También a Marcelo y a la gente del servicio de microscopía. Y a los profesores de la Universidad de Valencia: Salvador Gil, quién nos ha ayudado en más de una ocasión con los RMNs, y Antonio Domenech, quien se prestó muy amablemente a resolver algunas de nuestras dudas de electroquímica. También a Alicia Forment, que fue la primera en enseñarme electroquímica y a Josep, con quien nos estamos iniciando en la plasmónica.

A mis inseparables.

Concha y Efrén. Sin vosotros esta tesis habría sido la mitad de bonita, el doble de corta y cien veces menos divertida. Considero que nuestra amistad de las mejores cosas que han salido de mi doctorado.

A la gente del ICMol

O mis colaboradores menos directos. A Angelito, que es un crack y lo arregla todo. A Chema y Gloria por las medidas, la paciencia y por su sentido del humor. A Eva por todos los análisis de masas. A Carlos Martí por sus consejos y a Francisco y Modesto por su ayuda en temas diversos. A Jose, María, Mauri, Nora, Yan, Sonsoles, Eva, Miguel, Alicia, Alejandra, Alex Gaita, Helena… y a toda la gente simpática y colaboradora con la que he trabajado he tenido el placer de trabajar o simplemente charlar. También muy importante, quiero mostrar mi gratitud a la gente de administración: Paco, Estela, Manuel, Marian, Mº Jesús y Amparo, porque hacen su trabajo con una amabilidad excepcional. A Amparo, que lo mantiene todo tan limpio como le dejamos. Y especialmente a los que han sido mis compis de despacho/pecera: Concha, Murad, Salva, Efrén, Michelino, Juampi, Sara, Walter, Pini y Cristina quienes te ayudan a sobrellevar los reveses, tirarte una pelotita y hacer que acabes riendote de todo ello. Como un junco. Muchos de vosotros habéis pasado de ser mis compañeros a mis amigos.

A mis seres más queridos.

A mis perras: Concha, Ana, Eva, Encarna, Alba, Isa, Inmi, Mari y Sandra. Por los viajes, las risas, las noches cortas y los días al sol. A Pablo. A la gente de Izana, que es mi particular oasis de tranqilidad en este mundo. A los amigos de la piedra. Y en general a todos mis buenos amigos.

Y a mi familia, a los valencianos y a los sorianos, porque a pesar de que muchas veces no lo han entendido siempre me han apoyado. Y por encima de todo a mis padres y mi hermana. Por la financiación, el apoyo, el cariño… y una lista interminable de cosas. Vosotros sois a los que más debo porque sois de quien más he aprendido.

Gracias a todos porque sin duda lo mejor de este viaje ha sido la compañía.

A mi familia

Table of contents

Abstract

Coordination compounds attract a particular interest in chemistry due to its unique optical, redox and magnetic properties. In this thesis we will take advantage of these properties for the development of functional molecular electronic devices based on tailor-made coordination compounds.

The first systems treated will be bistable copper rotaxanes. These interlocked molecules, developed for the first time in the nineties by Prof. Sauvage in Strasbourg, present an electrochemically-triggered switching behavior that is accompanied by relative molecular motions of large amplitude. The first chapter of this thesis comprises the design, synthesis and characterization of two new bistable rotaxanes performing reversible shuttling and pirouetting motions. Owing to the presence of several coordination units and the lability of copper complexes, the preparation of these threaded systems tends to be troublesome. On the other hand, the nature of the coordination units has demonstrated to have a profound effect on the characteristics of the switching process. Looking for the simplification of the synthetic procedures and for the enhancement of the thermodynamic and the kinetic properties, we have optimized the chemical structure of this two threaded molecules. This research came up with a pirouetting rotaxane presenting a wide redox hysteresis and the fastest switching rates reported to date in copper-complexed interlocked systems.

In the second chapter of this thesis, the polytopic ligands that arose from the preparation of shuttling rotaxanes were further employed in the development of discrete supramolecular coordination entities. Attending to the coordination requirements of ligands and metals, a good level of control over the final shape of the resulting assembly have been achieved in the combination of terpy/phen conjugates with different coordination indexes metal ions. Thereby, two quite uncommon architectures: a pentanuclear trigonal bypiramidal cage and a family of heterometallic square grids could be obtained in a toposelective self-assembly process.

Finally, the third chapter deals with the development of switching electronic unimolecular devices from the chemical structures developed in the first chapter. With the aim of implementing the pirouetting copper interlocked system studied previously into a single-molecule junction, we have substituted the stoppers of the rotaxane axle with different anchoring groups, which afforded a family of conjugated molecular wires comprising a metal coordination site. The electronic transport features of the family of monostable Cu(I) rotaxanes with these wires revealed a variable coordination effect on the molecular conductance of depending of the anchoring group. This effect had never been observed before. With the aid of DFT calculations this effect could be rationalized in terms of the alignment of the molecular levels with the Fermi level of the electrodes. Once the electrical characterization of the Cu(I) complexes was completed, we came up with the most suitable conducting platform for the evaluation of the conductance response to the redox switching in a equivalent bistable threaded system. For that purpouse we prepared a bistable rotaxane in its Cu(I) and Cu(II) forms in order to characterize separately both oxidation states in the molecular junction. Unfortunately, transport measurements are currently under investigation and no electron transport results could be included in this thesis. Finally, taking advantage of the coordination abilities of this family of molecular wires we tested their potential for the development of metal-based optoelectronic devices. For that purpose we prepared their corresponding Ir(III) cyclometallated complexes. The complete electrochemical and photophysical study of these complexes together with the comprehensive knowledge of the conducting abilities of these molecules revealed the promising features of these coordination compounds for the observation of relevant photoconducting phenomena.

Abbreviations

bipy	2,2′-Bipyridine
B3LYP	Becke, three-parameter, Lee-Yang-Parr
Boc	*tert*-Butyloxycarbonyl
BPE	Bipyridyl oligophenyleneethynylene
CBPQT	Cyclobis(paraquat-*p*-phenylene)
COSY	Correlation Spectroscopy
ct-PA	*cis-trans*-Polyacetylene
CuAAC	Copper-catalyzed Azide-Alkyne Cycloaddition
CV	Cyclic Voltammetry
DCC	Dynamic Covalent Chemistry
DFT	Density Functional Theory
DIEA	N,N-Diisopropylethylamine
DMA	N,N-Dimethylacetamide
DMF	N,N-Dimethylformamide
dmp	2,9-Dimethyl-phenanthroline
DMSO	Dimethyl sulfoxide
dpb	2,9-Diphenyl-2,2′-bipyridine
dpbiiq	8,8′-Diphenyl-3,3′-biisoquinoline
dpp	2,9-Diphenyl-phenanthroline
Ea	Activation Energy
EDAX	Energy-dispersive X-ray Spectroscopy
EPR	Electron Paramagnetic Resonance
ES	Electrospray
et al.	*et alii* (and others)
Fc/Fc^+	Ferrocene/Ferricinium couple

FET	Field-effect transistors
FWHM	Full Width at Half Maximum
ΔG	Thermodynamic Free Energy Difference
HR	High Resolution
HOMO	Highest Occupied Molecular Orbital
IR	Infra-red
JFP	Junction Formation Probability
LC	Ligand-centred
LLCT	Ligand-to-Ligand Charge Transfer
LUMO	Lowest Unoccupied Molecular Orbital
MALDI	Matrix-Assisted Laser Desorption/Ionization
MS	Mass Spectrometry
NBS	N-Bromosuccimide
MCBJ	Mechanically Controlled Break-Junction
MLCT	Metal-to-Ligand Charge Transfer
MOM	Methoxymethyl ether
NEGF+DFT	Non-equilibrium Green Functions together with DFT calculations
Neo_2B_2	Bis(neopentyl glycolato)diboron
NMR	Nuclear Magnetic Resonance
NOE	Nuclear Overhauser Effect
NOESY	Nuclear Overhauser Effect Spectroscopy
pin_2B_2	Bis(pinacolato)diboron
phen	1,10-Phenanthroline
$Pd(ddpf)Cl_2$	[1,1-Bis(diphenylphosphino)ferrocene]dichloropalladium(II)
SB	Self-breaking
SCE	Saturated Calomelane Electrode
STM	Scanning Tunneling Microscopy

ROESY	Rotating Frame Nuclear Overhauser Effect Spectroscopy
TBA(PF_6)	Tetrabutylammonium hexafluorophosphate
terpy	2,2′:6′,2′′-Terpyridine
MCBJ	Mechanically Controlled Break Junction
MLCT	Metal-to-Ligand Charge Transfer
Me_6Tren	Tris[2-(dimethylamino)ethyl]amine ligand
OLED	Organic Light-Emitting Diodes
OPE	Oligophenyleneethylene
OPV	Oligo phenylene vinylene
OT	Oligothiophenes
OY	Oligoynes
p-PP	Planar polyphenyl
PF	Polyfuran
SAc	Acetyl-thiol
SAMs	Self-Assembled Monolayers
STM	Scanning Transmission Microscopy
STM-BJs	Scanning Tunneling Microscopy Break Junctions
STS	Scanning Tunnel Spectroscopy
TBA(PF_6)	Tetrabuthylammonium hexafluorophosphate
3TD	Three terminal devices
TEA	Triethylamine
TFA	Trifluoroacetic acid
TMS	Trimethylsilyl
TMSPhen	Bis((trimethylsilyl)ethynyl)-1,10-phenanthroline
TMT	Trimethyltin
TTF	Tetrathiafulvalene
t-PA	All *trans*-polyacetylene

t-PP	Twisted polyphenyl
UV-Vis	Ultraviolet-Visible
XPS	X-ray Photoemission Spectroscopy

Products list

Chapter 1

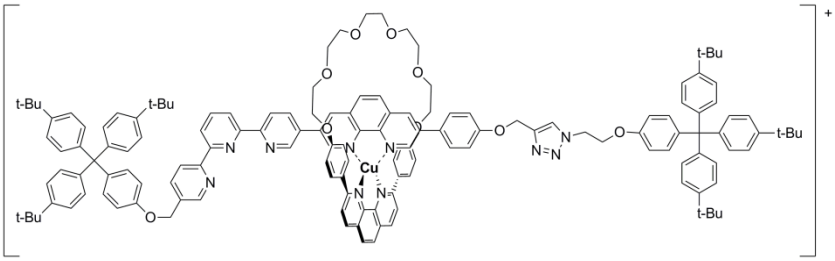

R1^{+}

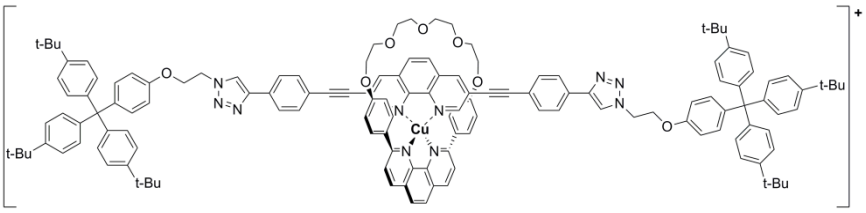

R2^{+}

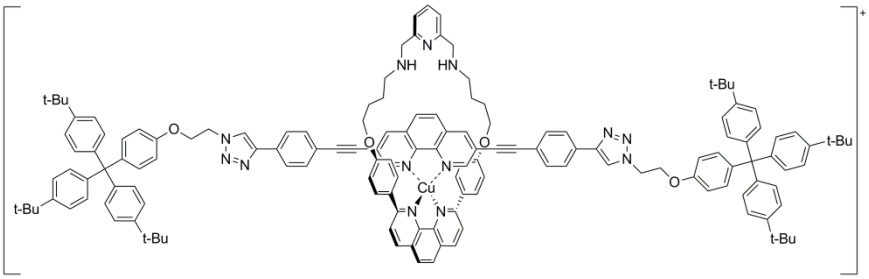

R3^{+}

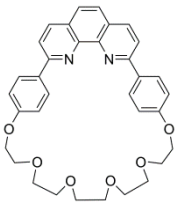

M1

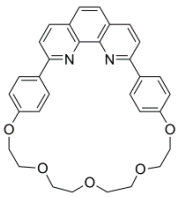

M2

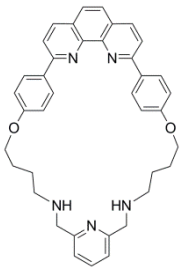

M3

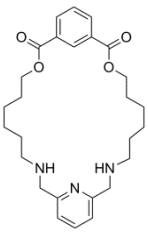

M4

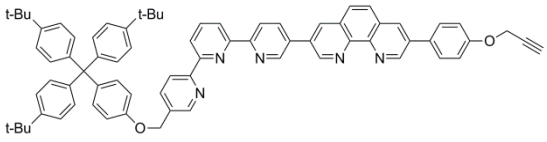

2

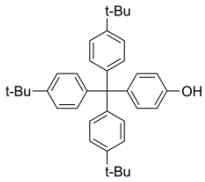

3

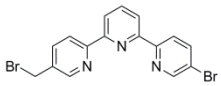

4

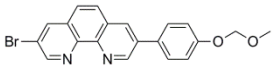

5

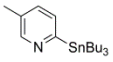

6

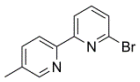

7

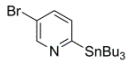

8

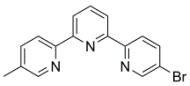

9

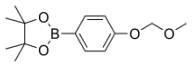

10

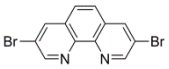

11

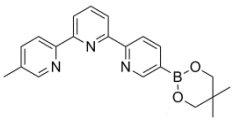

12

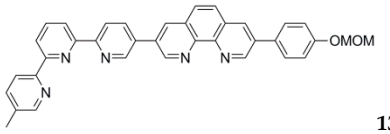

13

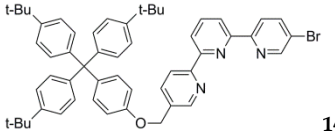

14

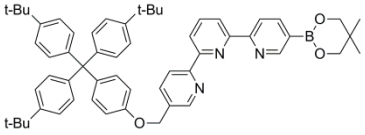

15

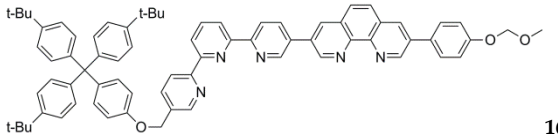

16

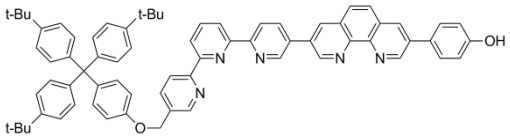

17

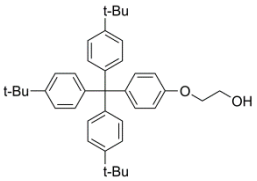

18

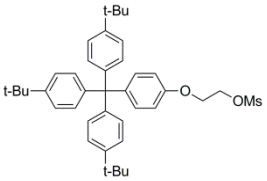

19

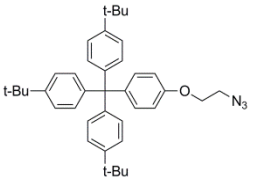

20

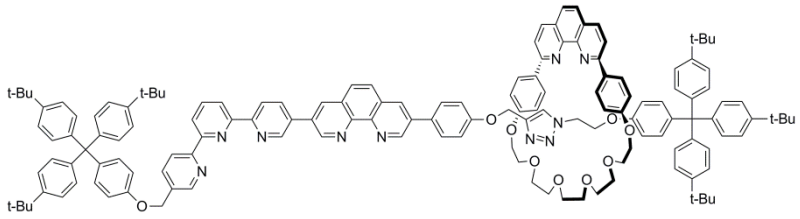

21

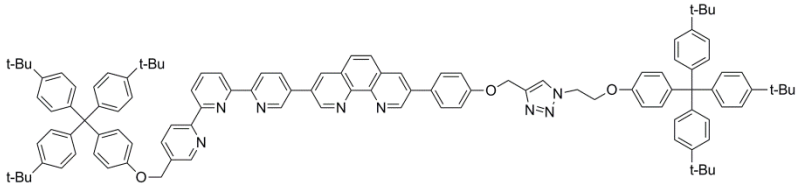

22

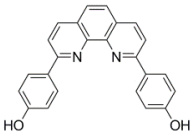

23

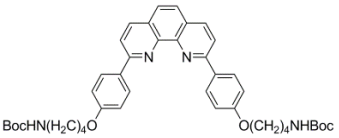

24

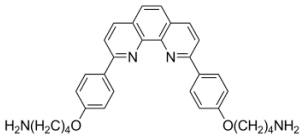

25

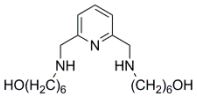

26

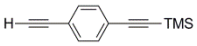

28

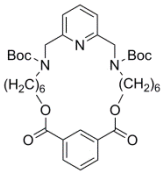

27

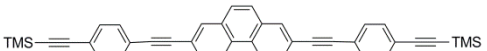

29

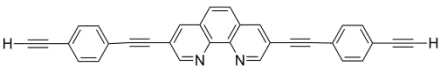

30

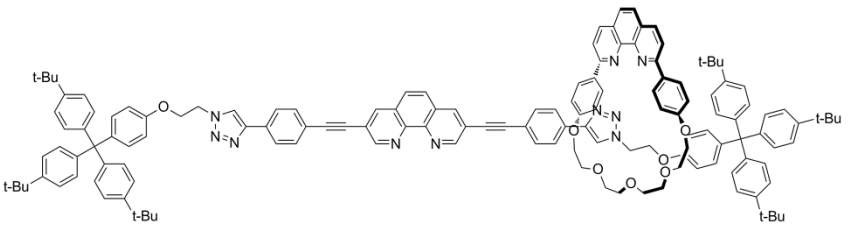

31

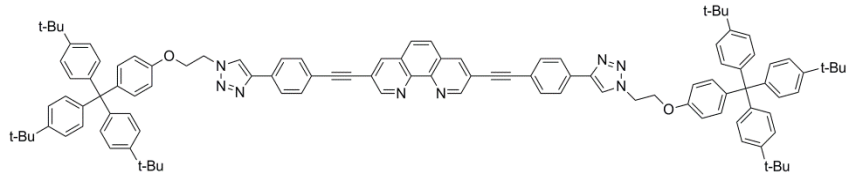

32

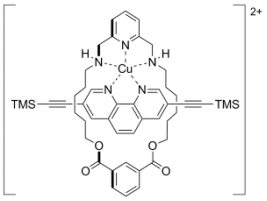

33

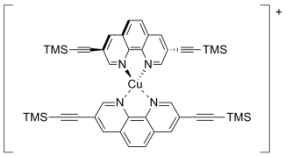

34

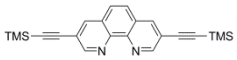

35

Chapter 2

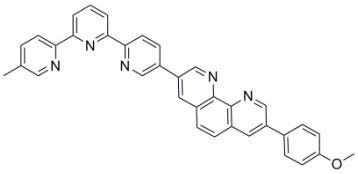

Ligand A

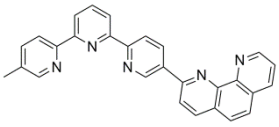

Ligand B

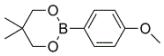

36

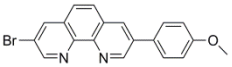

37

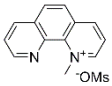

38

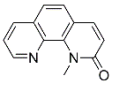

39

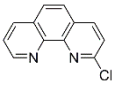

40

Chapter 3

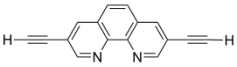

41

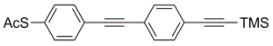

43

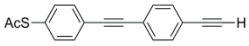

45

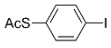

42

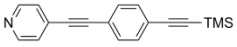

44

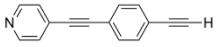

46

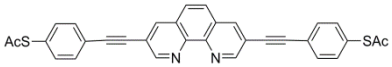

W1

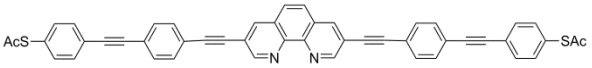

W2

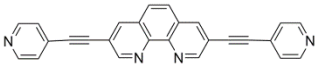

W3

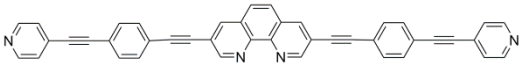

W4

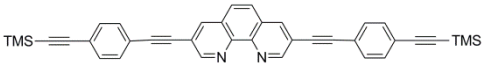

W5

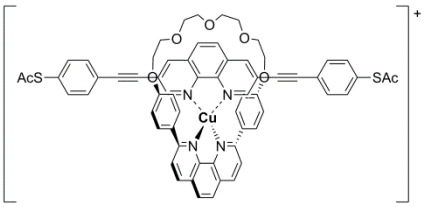

[Cu(**M2**)(**W1**)]$^{+}$

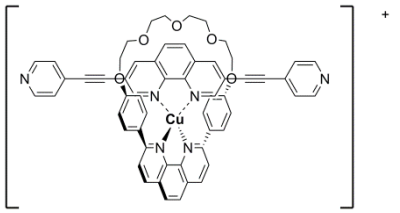

[Cu(**M2**)(**W3**)]$^{+}$

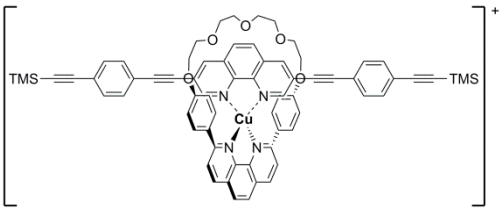

[Cu(**M2**)(**W5**)]$^{+}$

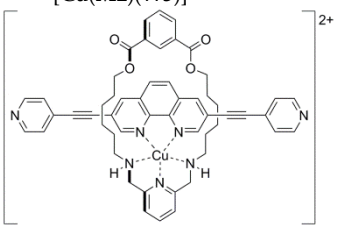

[Cu(**M4**)**W3**]$^{2+}$

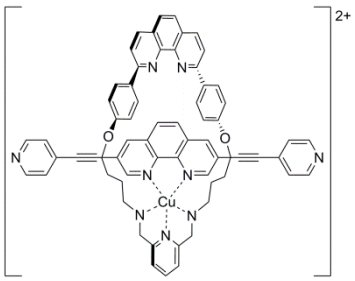

[Cu(**M2**)(**W3**)]$^{2+}$

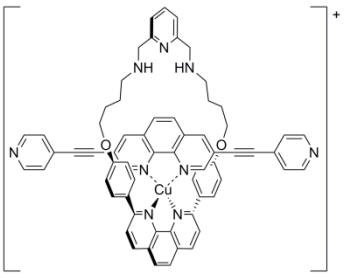

[Cu(**M3**)(**W3**)]$^{+}$

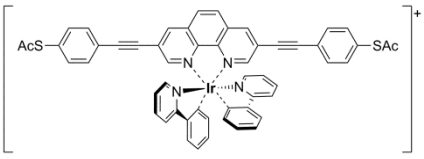

$[Ir(ppy)_2(\mathbf{W1})]^+$

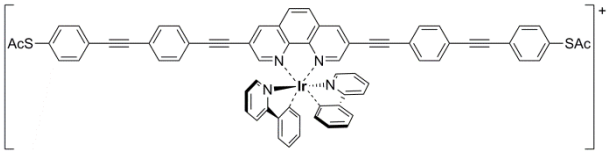

$[Ir(ppy)_2(\mathbf{W2})]^+$

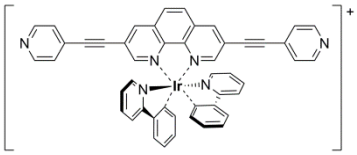

$[Ir(ppy)_2(\mathbf{W3})]^+$

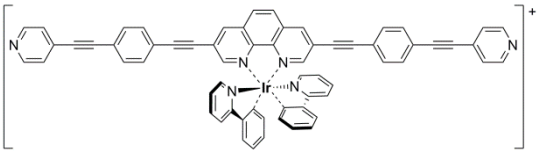

$[Ir(ppy)_2(\mathbf{W4})]^+$

Chapter 1

Copper rotaxanes

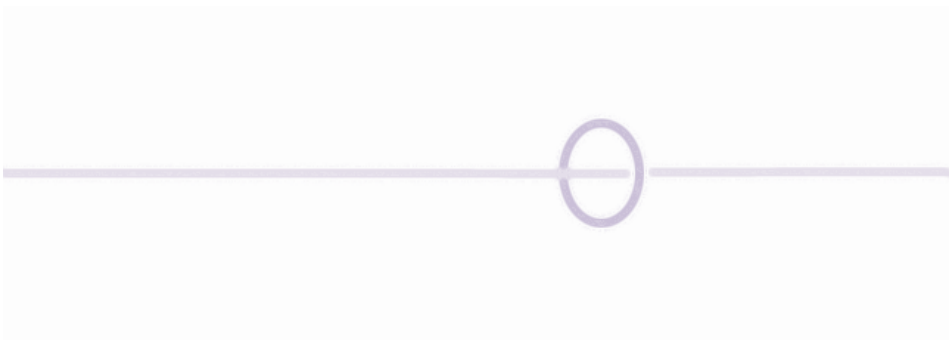

Introduction

Mechanically interlocked systems constitute a new class of compounds that surged from the incorporation of the entanglement concept into chemical systems. This name is assigned to superstructures composed by several molecular units which are intertwined in a way so that they cannot be separated without the breaking of a chemical bond, although they are not covalently bonded. Depending on the shape of their components and their entanglement we can distinguish between three different topologies that are represented in Figure 1.1: catenanes, rotaxanes and knots.[1]

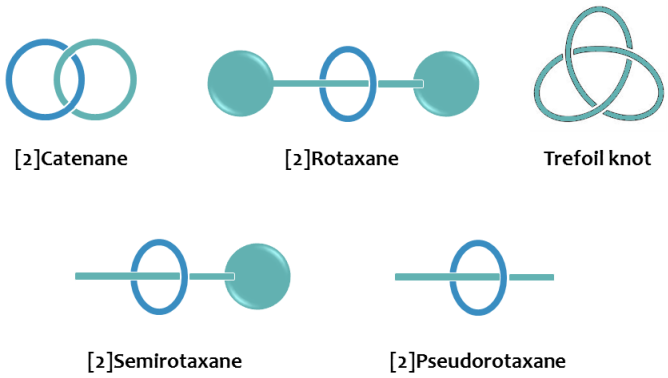

Figure 1.1 Principal interlocked structures.

The term **catenane** is used to describe multi-component systems, composed by two or more interlocked rings. On the other hand, when the systems are formed by a single closed but entangled curve, the superstructures are called **knots**. In the cases in which the ring component is encircling at least one axle with bulky stoppers on the extremes the structure is called **rotaxane**. The function of the stoppers is to prevent the ring unthreading, thus, if there is no stopper on at least one of the extremes the system will be open. The non-interlocked forms of rotaxanes are called **pseudorotaxanes** when no stopper is present at the ends of the axis, and **semirotaxanes** if there is only one. The nomenclature employed in these systems involves placing in square brackets the number of interlocked components before the name of the compound.[2]

Statistical[3] or covalent-bond strategies[4] have been employed for the construction of mechanically interlocked systems, but nowadays the efficient synthesis of such topologies relies on the use of template-directed methodologies.[5] This approach consists in bringing together the subcomponents in the appropriate relative orientation by the establishment of supramolecular interactions. Once the building blocks have been gathered together, the process finishes by the closure of the ring or the stoppering of the axis that will lock the components together in what is called a mechanical bond. The non-covalent interactions that have been employed for this purpose include: donor-acceptor interactions, hydrogen bonding, hydrophobic-hydrophilic interactions, π-π stacking interactions, electrostatic forces or metal coordination bonds.[6]

Usually, the same interactions that have been used in the templated synthesis are present in the final interlocked system fixing the subcomponents in a precise relative position or co-conformation. The term 'conformation' is referred to the different geometries that can be interconverted by the rotation around a single covalent bond. By analogy, 'co-conformation' is the term used to describe the different relative positioning that the components adopt in interlocked systems. When several recognition sites are present in an interlocked system, each one of them defines an energy minimum on the potential energy surface, as represented in Figure 1.2. If the different sites are non-degenerate, the interlocked system will adopt preferentially one co-conformation and the thermodynamic free energy difference (ΔG) between them will determine the population distribution in the equilibrium.

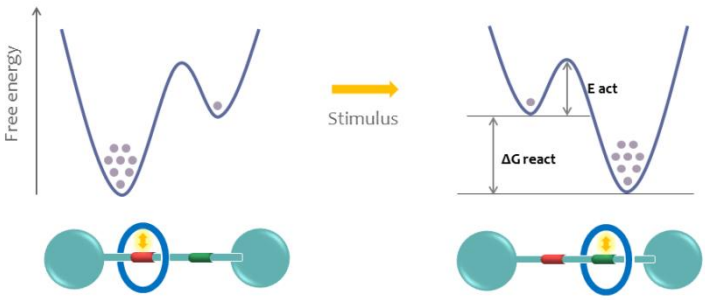

Figure 1.2 Potential energy profile for a stimuli-responsive switchable rotaxane. The different ground-state co-conformation are represented below.

When the binding affinity of the recognition sites can be chemically modified by an external impulse, the system is **stimuli-responsive**. This feature implies that the weakening of the interactions of the preferred site or the stabilization of the second site will push the system to adopt a different co-conformation, which involves a relative molecular translocation. Once the original affinities are restored, the system will come back to its original co-conformation. The second parameter that determines the behavior of a stimuli-responsive system is the activation energy (*Eact*). This energy is proportional to the time necessary to recover the equilibrium distribution once the stimulus has been applied, and thus, it is related to the lifetime of the unstable co-conformation.

The intense research in the area of stimuli-responsive catenanes and rotaxanes has led to a great variety of bistable interlocked molecules in which intramolecular motions can be induced by a wide variety of external stimuli, such as chemical reactions,[7] photochemical reactions,[8, 9] electrochemical impulses,[10-12] pH changes,[13] solvent changes[14] or heat.[15, 16] Among them, reversible redox-triggered motions are particularly appealing in terms of the potential applications since they allow remote, reagent-free and waste-free control over molecular co-conformations while they provide the opportunity of interfacing the molecular devices with the existing electronic technologies.[6]

In principle, any chemical system that can exist in at least two states with distinguishable spectral, electrochemical or magnetic properties can be considered a **molecular switch**, as long as the transition between the different states can be controlled by an external

stimulus and does not occur spontaneously.[17] Redox-active catenanes and rotaxanes can be reversibly shifted between two or more metastable states by the application of voltage impulse, thus, on that basis, they have been proposed as molecular switches. Besides, the associated conformational changes enable that, once the applied electrochemical potential is removed, the system does not return spontaneously to the initial state until a reset potential value is reached.[18] Thereby, they present a **hysteretic redox behavior** that can be exploited for the development of single-molecule memory units. The operation of a redox-based memory system is based in defining three different voltage values; one to switch the molecule to an 'ON' state (set voltage), one to interrogate the molecule (read voltage) and another one to switch back the molecule to the initial 'OFF' state (reset voltage).[19] These actions are illustrated in Figure 1.3.

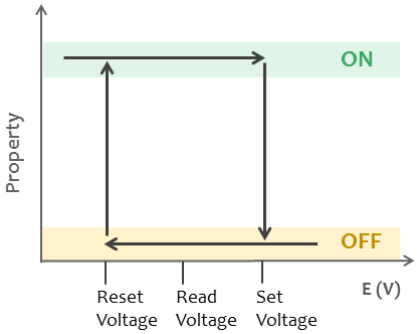

Figure 1.3 Redox hysteresis in a redox-switch.

Besides, there is another reason why bistability has been an intensively pursued feature in interlocked molecules. Comparing with other bistable molecules, the peculiarity that these systems resides in that the switching process is accompanied by a directional molecular motion that can be of large amplitude. This feature enables the possibility of transferring chemical, electrical or photochemical energy into controllable molecular motions and has inspired the vision of interlocked topologies as **molecular machine prototypes**.[20-23] Although fast controlled molecular motions have been reached in solution, the transfer of this behavior to the condensed phase is not a trivial issue. The arrangement of these molecular structures in an ordered way so that the collective effect

of all of them could be transduced into an observable macroscopic mechanical work, constitutes a big challenge.[24]

Depending on the direction of the molecular motion, bistable rotaxanes can be sub-divided in two groups: **pirouetting rotaxanes,** in which the ring describes a rotational movement around the axle while the distance of the ring to the stoppers remains unaltered; and **molecular shuttles,** in which the ring glides in a controlled fashion along the axle around which it has been threaded, leading to a linear motion. These differences are illustrated in Figure 1.4.

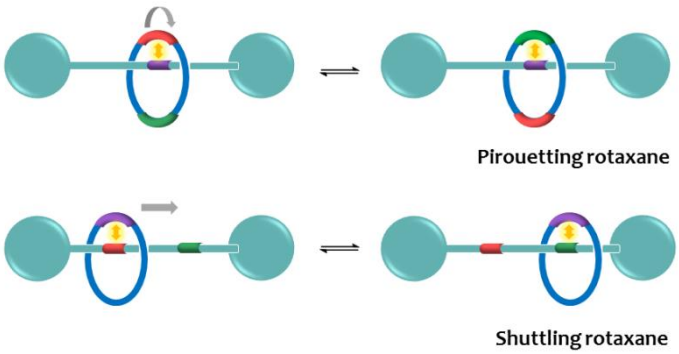

Figure 1.4 Representation of pirouetting and shuttling movements in bistable rotaxanes.

For practical reasons, electronic devices should operate at low response times and in a controlled and reproducible manner. Thus, the potential application of molecular systems as functional molecular devices requires the switching processes to be externally activated, quantitative, reversible and fast. Early attempts of constructing electronic devices from redox-bistable interlocked molecules have been leaded by the group of Professor J.F. Stoddart. This group has developed a whole family of redox-active rotaxanes and catenanes holded by donor-acceptor interactions, which, in collaboration with different groups, have been employed in the construction of the first examples of electronic memory devices[25-27] and mechanical actuators[28, 29] based on mechanically interlocked molecules. Our research on this topic will be focused on the study of bistable

rotaxanes based on the coordination of the Cu(I/II) couple firstly developed by Prof. J. P. Sauvage in Strasbourg.[30]

2.1 Copper-based interlocked systems

Copper, together with silver and gold, constitute the group nine of the transition metal elements. It possesses two stable oxidation states 1+ and 2+. Owing to the great affinity of copper for nitrogen ligands,[31] the most employed coordination units in copper-complexed interlocked systems have been polypyridinic ligands: 1,10-phenanthrolines (phen) or 2,2′-bipyridines (bipy) as bidentate, and 2,2′:6′,2′′-terpyridines (terpy) as tridentate ligands (see Figure 1.5).

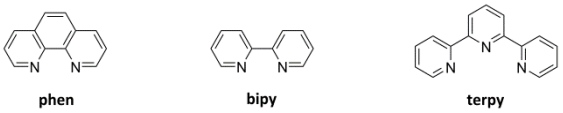

Figure 1.5 Chemical structure of the principal ligands employed in copper-complexed rotaxanes.

Cu(I) cation possess a d^{10} electronic configuration with the 3d shell completely filled that results in a symmetrical distribution of the electronic charge. For that reason, the preferred coordination environment is tetrahedral, since it minimizes the electrostatic repulsions between donor atoms. By contrast, Cu(II) complexes with diimine ligands present almost exclusively five or six coordination indexes because they lead to a better stabilization of the charge. As we can see in the crystal structure of $[Cu(dpp)_2](PF_6)$ (dpp = 2,9-diphenyl-phenanthroline), Figure 1.6, the coordination of Cu(I) to phenanthrolines leads to elongated tetrahedral geometries. In the crystal, the proximity of the aryl substituents to the phenanthroline core of the opposite ligand (3.4 Å) is indicative of the appearance of stabilizing intramolecular π-stacking interactions that forces the distortion of the D_{2d} geometry.[32] However, ^{1}H NMR studies indicate that the $[Cu(dpp)_2]^+$ complex is fluxional in solution, and both ligands are identical in the NMR timescale.

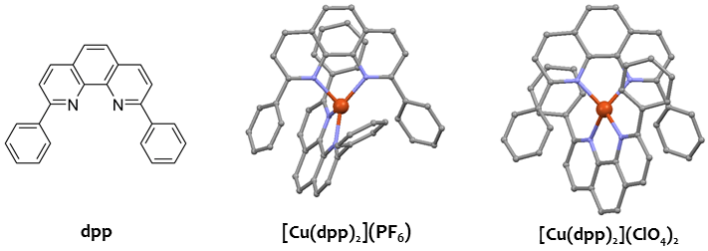

Figure 1.6 Crystal structure of $[Cu(dpp)_2](PF_6)$ and $[Cu(dpp)_2](ClO_4)_2$. Protons and anions are omitted for clarity. Structural data extracted from.[32]

Oxidation of Cu(I)-bis-phen complexes leads to the adoption of a flattened distribution that enables the approximation of a nucleophile to the metal center and promotes to the adoption of higher coordination indexes. In $[Cu(dpp)_2](ClO_4)_2$ the coordination of Cu(II) approaches to square planar (D_{2h}) evidencing this distortion, see Figure 1.6. In this particular case, the presence of the aryl substituents in 2- and 9- positions shields very effectively the copper center from the approximation of a nucleophile, and thus, it hampers the adoption of higher coordination indexes. That is the reason why, despite the tendency of Cu(II) complexes for the penta- or hexa-coordination, the crystal structure of tetracoordinated $[Cu(dpp)_2](ClO_4)_2$ could be resolved.

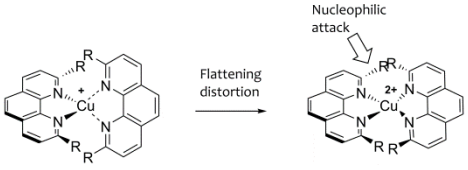

Figure 1.7 Flattening distortion upon oxidation of the complex and subsequent nucleophilic attack by solvent, counterion, or other molecules.

These geometric limitations are reflected in the photophysical and photochemical properties of copper bis-phen compounds. Steric congestion around the copper center has a significant stabilizing effect on cuprous state, and thus, the oxidation potential of $[Cu(phen)_2](PF_6)$, 0.19 V, rises up to 0.64 V in substituted $[Cu(dmp)_2](PF_6)$ (dmp = 2,9-dimethyl-phenanthroline) in dichloromethane solution.[33] Besides, the different oxidation states afforded also distinguishable visible spectra. Whereas four-coordinate Cu(I)

complexes are intense red species (439 nm, ε= 2570 $mol^{-1}Lcm^{-1}$), five-coordinate Cu(II) complexes are pale olive green (640nm, ε≈ 125 $mol^{-1}Lcm^{-1}$).

Several examples have been reported that exploit the different coordination preferences of the oxidation states of a metal ion to induce controlled motions at the molecular level.[34-37] But probably, the most relevant and sophisticated examples of dynamic metal-containing systems are the copper bistable interlocked systems developed by Prof. J. P. Sauvage.[38] These catenane and rotaxane molecules have been designed to undergo spontaneous molecular rearrangements upon the application of an electrochemical potential. The working principle of these systems relies in the existence of two different coordination environments, one tetracoordinated and one pentacoordinated, which are spatially separated. As mentioned above, whereas Cu(I) ions prefer tetrahedral coordination environments, Cu(II) tends to the penta or hexacoordination. On passing from the 1+ to the 2+ redox state, a metastable species is generated which spontaneously evolves to the pentacoordinated geometry carrying out the pertinent rearrangement. When the Cu(II) is reduced again to Cu(I) the system will return to the initial tetracoordinated geometry, carrying out the reverse translational movement. The process is schematized in Figure 1.8 for a pirouetting rotaxane.

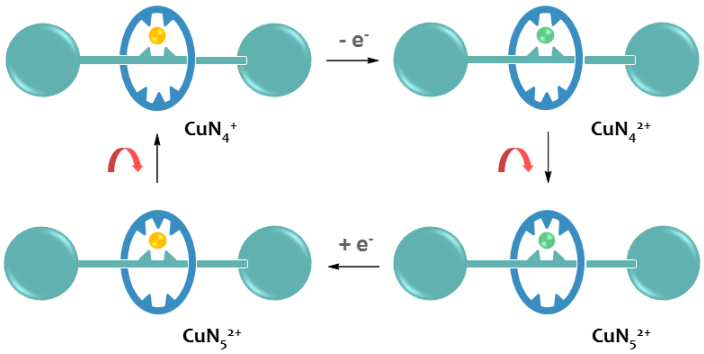

Figure 1.8 Electrochemically-induced movement in a pirouetting copper rotaxane. Cu(I) and Cu (II) ions are colored in orange and green respectively. The rotational movement of the ring around the axis is represented by red arrows. The subscript 4 or 5 indicates the number of nitrogen atoms coordinated to the metal.

2.2 Copper interlocked systems in motion

Bistable copper-complexed interlocked systems have been set in motion by either electrochemical signals, chemical reactions[39] or photochemical assisted processes.[11] The interaction holding the components together in these molecules are metal-ligand coordination bonds, which are significantly stronger (15-50 kcal/mol) than the rest of non-covalent interactions employed (0.5-10 kcal/mol) in dynamic interlocked systems, but far below that of organic covalent bonds (60-120 kcal/mol).[40] These systems are characterized by nearly quantitative conversions between co-conformers ($\Delta G >>$), and thus, determination of the equilibrium constants results unnecessary. Nevertheless, when compared to purely organic systems, the major drawback of copper-based bistable systems resides in their long response times. Hence, kinetic rates are the fundamental parameters describing their switching behavior.

In redox bistable rotaxanes and catenanes, electrochemical time-dependent methods have proven to be an extremely well-suited tool for studying the kinetic[12, 41] as well as the thermodynamic parameters[12, 42] intrinsic of the switching cycle. Since tetra- and penta-coordination geometries afford well separated potential values for the Cu(I/II) couple, the position of the ring can be monitored by cyclic voltammetry.[41] Electron-transfer processes are generally fast, and therefore, the rate of the intramolecular motion is controlled by the translational or rotational step. In particular, the typical limiting step in the switching cycle of copper interlocked molecules consists in the reorganization of the Cu(II) ion from the tetra to the pentacoordinated site.

$$CuN_4^+ \rightarrow CuN_4^{2+} + e^-$$

$$CuN_4^{2+} \overset{k}{\rightarrow} CuN_5^{2+}$$

The kinetic constant (k) of this process can be calculated from cyclic voltammetry experiments by applying the analysis methods described by Nicholson and Shain[43] for an oxidation followed by an irreversible chemical reaction. According to this work, for small values of k/a, being a directly related with the scan rate, the cyclic voltammogram

will show a Cu(I/II) redox couple for the tetracoordinated environment at positive potential, as represented in Figure 1.9 **A**. Since the reduction peak height (i_a) is proportional to the concentration of the reacting species (CuN_4^{2+}), with increasing the scan rate (v), the i_a/i_c ratio grows at a speed inversely related to the rate constant. Thereby, the rate constant can be calculated from a single cyclic wave by extrapolating from the working curve reported for the ratio of peak currents, i_a/i_c, as a function of $k\tau$.[43]

$$a = nFv/RT \qquad \tau = (E_\lambda - E_{\frac{1}{2}})/v$$

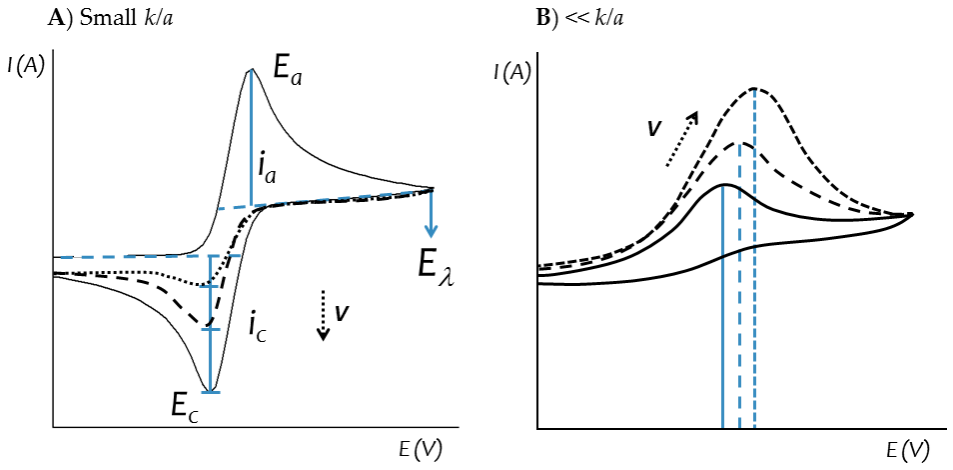

Figure 1.9 Representation of the evolution of the Cu(I/II) wave in the tetracoordinated environment with the scan rate (v); for small values of k/a (**A**) and large values of k/a (**B**). The fundamental parameters involved in the calculations are depicted in graph **A**.

As k/a becomes large, the CuN_4^{2+} species is quickly consumed, and the wave becomes irreversible. At the limit $\frac{i_a}{i_c} \ll$, the peak potential experiences an anodic shift with increasing the scan rate that is described by equation (i). In this case, the value of k can be estimated from this equation by measuring the evolution of the oxidation wave potential with the scan rate.

$$E_a = E_{1/2} - \left(\frac{RT}{nF}\right)\left(0.780 - ln\sqrt{\frac{k}{a}}\right) \qquad \text{(i)}$$

These two situations have been encountered in the bistable rotaxanes studied in this chapter and in both cases the kinetic rates of the rearrangement movements have been calculated.

As already mentioned, the main factor determining the kinetics of the motion cycle of copper catenanes and rotaxanes is the lability of the tetracoordinated environment. In addition, in the case of shuttling rotaxanes, the distance between the two recognition sites has also shown to have an influence on the switching rates. In the following we will discuss these factors in detail across the reported examples of dynamic catenanes and rotaxanes.

2.2.1 Influence of the tetracoordinated environment

The first example of dynamic interlocked molecule based on copper was a bistable [2]catenane.[44] It consisted in two intertwined macrocycles; one mono-chelating containing a bidentate dpp unit and one bis-chelating bearing a dpp and a tridentate terpy unit. Upon electrochemical reduction and oxidation of the system in solution one of the rings performed a reversible gliding motion along the other. The process could be monitored by cyclic voltammetry, visible absorption spectroscopy[44] and electron paramagnetic resonance spectroscopy (EPR).[45] In a later work, the entanglement of two analogous bis-chelating macrocycles, afforded a multistage [2]catenane with three distinct geometries; tetracoordinated $Cu(dpp)_2$, pentacoordinated Cu(dpp)(terpy) and hexacoordinated $Cu(terpy)_2$.[41] As can be observed in Figure 1.10, the three different coordination spheres afforded well separated potential values for the Cu(I/II) couple at +0.63 V, -0.05 V and -0.41 V, which were assigned to the tetra-, penta- and hexacoordinated complexes, respectively.

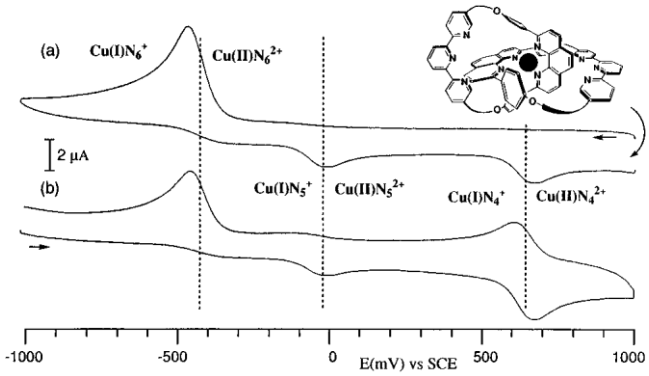

Figure 1.10 Cyclic voltammogram of a multistable [2]catenane (represented the inset) in acetonitrile /TBA(BF_4) 0.1M at 200 mV/s. The subscript 4, 5 or 6 indicates the number of nitrogen atoms coordinated to the metal. Figure extracted from reference.[41]

In Figure 1.10 a) we can see that, starting from a potential of +1.0 V, only the reduction of the hexacoordinated species $[Cu(terpy)_2]^{2+}$ was observed. On the way back to positive potential, the ring is detected first in the penta and then in the tetracoordinated position. When starting from -1.0 V, (curve b), the same sample showed a reversible signal corresponding to $[Cu(dpp)_2]^{+}$ formed by the reduction and subsequent rearrangement of the $[Cu(terpy)_2]^{2+}$ species. However this peak turned to be reversible, indicating that the rearrangement of the $[Cu(dpp)_2]^{2+}$ to the penta- and then the hexacoordinated geometry is too slow, and thus, not detectable in the timescale of the experiment. The reduction wave appearing in curve b) at negative potential is attributed, instead to the rotation of the catenane, to the starting hexacoordinated complex existing in the bulk solution. From this voltammogram it can be concluded that the rearrangement of the unstable $[Cu(dpp)_2]^{2+}$ occurs significantly slower than the rearrangement of the $[Cu(terpy)_2]^{2+}$. As expected, double-charged complexes are less labile than single-charged ones. It was assumed that the gliding process occurs via the breaking of the coordination bonds between the copper ion and one of the ligands.[46] Thus, the stability of coordinatively non-saturated intermediate species is greatly enhanced by the coordination of auxiliary molecules (solvent or anion). However, as mentioned in the section 1.1.2, the highly encumbering environment provided by the dpp ligands hampers the approximation of

an auxiliary molecule to the metal centre, increasing the activation energy of the gliding process.

The first reported example of a copper pirouetting rotaxane,[47] presented the same coordination moieties used in the previous [2]catenanes,[41, 44] dpp and terpy units, see rotaxane **A** in Figure 1.11. As in catenane molecules, the electrochemically induced rearrangement of the $[Cu(dpp)_2]^{2+}$ site to pentacoordinated spheres turned out to be the limiting step of the rotational motion. The rate constants (k) of the two rearrangement processes could be determined by recording cyclic voltammograms at different sweep rates. The half lifetime ($t_{1/2} = \ln 2/k$) obtained for the two environments was 56 ± 28 ms for $[Cu(terpy)(dpp)]^{+}$ and 120 ± 50 s for $[Cu(dpp)_2]^{2+}$.

The most reasonable strategy that was found to increase the kinetics of the Cu(I) reorganization, was to facilitate the access to the metal center. In that direction, the bidentate dpp chelate contained in the axis was replaced by a 3,8-substituted-2,2'-bipyridine chelate, rotaxane **B** in Figure 1.11.[46] Cyclic voltammetry revealed a significantly lower potential value for the new tetracoordinated site, 0.45 V vs SCE, and the measured kinetic constant of the rearrangement was nearly three orders of magnitude faster than in its sterically-hindered parent compound. Hence, the complete reversible movement of rotaxane **B** was completed in the millisecond timescale.

$$\boldsymbol{A_4^{2+}} \rightarrow \boldsymbol{A_5^{2+}} \qquad k = 8 \cdot 10^{-3}\ s^{-1}$$

$$\boldsymbol{B_4^{2+}} \rightarrow \boldsymbol{B_5^{2+}} \quad k = 5\ s^{-1}$$

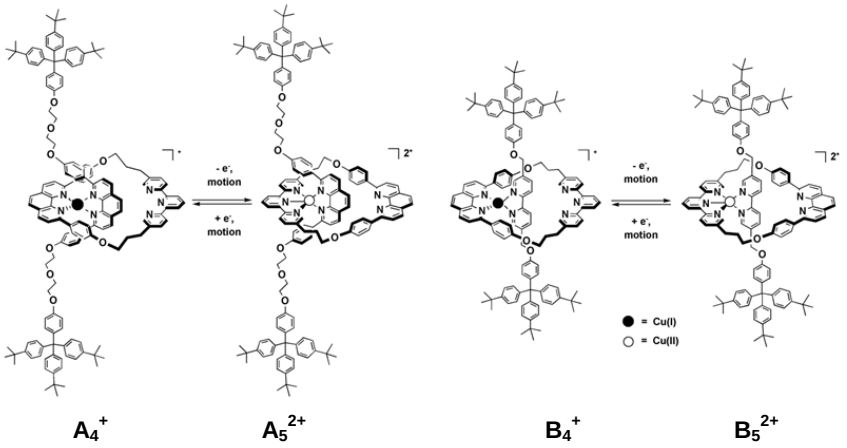

Figure 1.11 Pirouetting rotaxanes presenting a more sterically hindered (**A**)[47] and a less sterically hindered (**B**) coordination environments.[46]

In the search for the optimal tetracoordination environment, a comparative study of three different bidentate ligands was carried out.[48] Herein, three rotaxanes where prepared from the combination of the hetero-bischelating macrocycle used in previous works, Figure 1.11, and linear fragments of different nature; a dpp, a 2.9-diphenyl-2,2'-bipyridine (dpb), and a 8,8'-diphenyl-3,3'-biisoquinoline (dpbiiq). The chemical structures of the new bidentate chelates are shown in Figure 1.12.

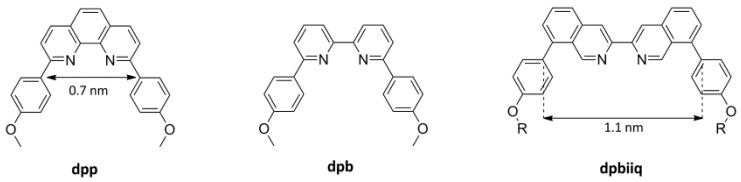

Figure 1.12 Chemical structure of the discussed chelates.

The comparison between dpp and dpb chelates showed that when these ligands bear exactly the same substitution, bipys afford one order of magnitude higher rate constants.[48] Besides, the dpbiiq ligand leads to rate constants 5 times higher than dpd. The enhanced lability of dpbiiq has been ascribed to the larger space between the copper centre and the phenyl rings, which enables the approximation of the nucleophiles to the metal centre. Nevertheless, the cyclic voltammetry of the dpabiiq pseudorotaxane

showed once again that the reduction of the steric hindrance around the copper tetracoordinated site is accompanied by a lowering of the oxidation potential and an increase of the kinetic rate constants. By contrast, the five-coordinate state is less sensitive to steric hindrance and its rearrangement is always visible in the timescale of the CV experiments.

The evolution of shuttling rotaxanes ran parallel to that of pirouetting rotaxanes, and the authors introduced analogous modifications on the tetracoordinated site in order to increase the kinetic rate constants.[49] The first shuttling rotaxane, here named **C**(PF_6), was constructed from the typical dpp and terpy units. Its chemical structure is shown in Figure 1.13. The substitution of the dpp chelate of the ring by the less hindering dpdiiq, resulted once again in a substantial increase on the rearrangement kinetics of the tetracoordinated Cu(II) species.[49] However, this rotaxane, **E**(PF_6) in Figure 1.13**,** included a second modification on carbon spacer linking both coordination sites. In order to evaluate accurately the dpbiiq effect, the rotaxane containing the same rigid thread and the sterically hindering dpp-based macrocycle was constructed, **D**(PF_6). The comparison between the electrochemical behavior of **E**(PF_6) and **D**(PF_6), corroborated an increase of several orders of magnitude in the kinetic rates ascribed only to the dpbiiq effect.[50]

$$\boldsymbol{C_4^{2+}} \rightarrow \boldsymbol{C_5^{2+}} \qquad k = 1.5 \cdot 10^{-4}\ s^{-1}$$

$$\boldsymbol{D_4^{2+}} \rightarrow \boldsymbol{D_5^{2+}} \qquad k \ll$$

$$\boldsymbol{E_4^{2+}} \rightarrow \boldsymbol{E_5^{2+}} \qquad k = 2\ s^{-1}$$

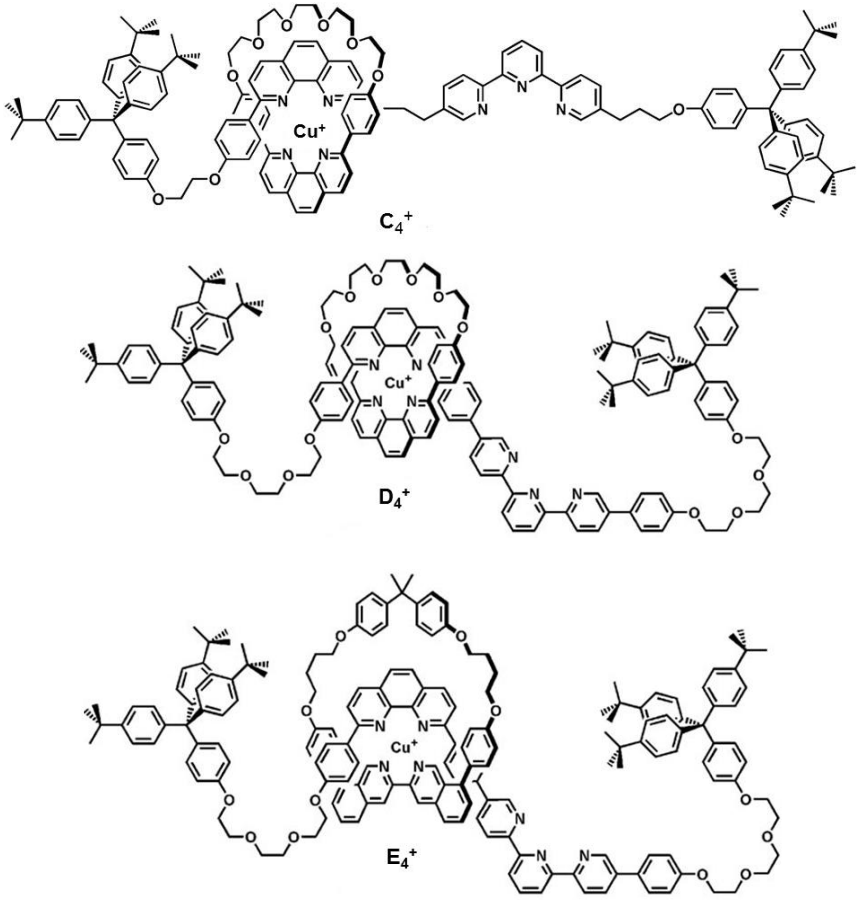

Figure 1.13 Chemical structure of shuttling rotaxanes **C**(PF_6), **D**(PF_6) and **E**(PF_6).[50, 51]

2.2.2 Influence of the spacer between the coordinating sites

The nature of the spacer has a main influence on the kinetics of shuttling rotaxanes since it defines the way of the linear translation between the recognition sites and several authors have studied the influence of the length and flexibility of the organic chain.[52-54]

The comparison between the rates of rotaxanes **C**(PF_6) and **D**(PF_6), whose chemical structure is shown in Figure 1.13, and which contain the same coordinating sites and only differ in the chemical structure of the spacer between them, evidenced that the

substitution a rigid phenyl by a flexible aliphatic chain leads to a great acceleration of the limiting tetracoordinated environment rearrangement.[51]

The next modifications performed on copper shuttling rotaxanes were directed to reach fast long-distance linear motions. It was expected that increasing the distance between the two coordination stations by the introduction of a rigid spacer will lead to a slower motion of the ring.[20, 55] The way found to facilitate the gliding of the ring along a longer thread consisted in introducing a third coordination station between the two external positions, a dpp and a terpy unit. The ring employed in this rotaxane was the rapidly moving dpdiiq macrocycle, and the coordination unit chosen for the middle position was a 2,2'-bipyridine (bipy) since its complexes afford intermediate thermodynamic stabilities between the dpp and terpy stations. For Cu(I) the order of stabilities goes: $[Cu(dpbiiq)(terpy)]^+$ <$[Cu(dpbiiq)(bipy)]^+$ <$[Cu(dpbiiq)(dpp)]^+$; and for Cu(II) $[Cu(dpbiiq)(dpp)]^{2+}$ <$[Cu(dpbiiq)(bipy)]^{2+}$ <$[Cu(dpbiiq)(terpy)]^{2+}$. The cyclic voltammogram of such rotaxane revealed a reversible shuttling motion of the ring from the terpy to the dpp station, and no signal coming from the intermediate bipy station was observed. This way, a long-distance (23 Å) and fast linear motion was achieved.

Long-distance molecular movements were previously attempted with little success. Trying to emulate the motion of skeletal muscles, a rotaxane dimer was designed to carry out a large-amplitude contraction/stretching movement.[39] The molecule consisted on two analogue ring-and-string conjugates assembled by a double threading reaction, as shown in Figure 1.14. Unfortunately, the electrochemical stimulus found a very high activation barrier and was unable to promote the intramolecular rearrangement of copper. Finally, the pentacoordinated station could be reached by a chemical reaction, removing Cu(I) ions and changing them by Zn(II). This way the rotaxane passed from a 18 Å contracted form to a final extended form of 36 Å.

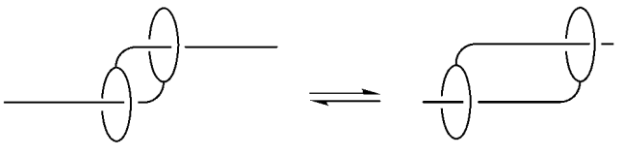

Figure 1.14 Extended and contracted conformation in a bistable rotaxane dimer.

2.3 Synthetic methods for rotaxane preparation

Preparation of copper rotaxanes can be divided in two main stages: the synthesis of the axis and macrocycle precursors and the templated locking of the threaded system.

The first stage consist in the preparation of simpler building blocks bearing the different recognition sites, which in the case of copper rotaxanes typically comprise polypyridinic ligands, and their following assembly. Cross-coupling reactions have been extensively used for these purposes since it constitutes a very efficient approach to link aryl and heteroaryl fragments due to its high regioselectivity and compatibility with a wide range of functional groups.[56, 57] In these reactions a new Csp^2-Csp^2 bond is formed between a halogen derivative and a carbon atom having an stannane group (in Stille couplings), or a boronic ester substituent (in Suzuki-Miyaura cross-couplings). The reaction takes place in the presence of a metallic catalyst, being Pd(0) complexes the most employed. The main advantage of Suzuki with respect to Stille cross-coupling reactions is the lower toxicity of the generated secondary products. Nevertheless, the use of Stille cross-coupling reactions results advantageous in some cases.

As far as the self-assembly and locking of rotaxanes are concerned, two main strategies can be distinguished, the **capping** and the **clipping**. The capping approach starts with a molecular ring and a non-stoppered axis precursor. After the copper-templated threading of the ring by the linear rod, the resulting pseudorotaxane is locked by the attachment of two bulky stoppers at both ends. By contrast, the clipping methodology consists in the cyclization of an initially opened macrocycle around the dumbbell axis that is linked to by non-covalent interactions.[58, 59] The gathering and locking steps are usually carried out in a one pot reaction.

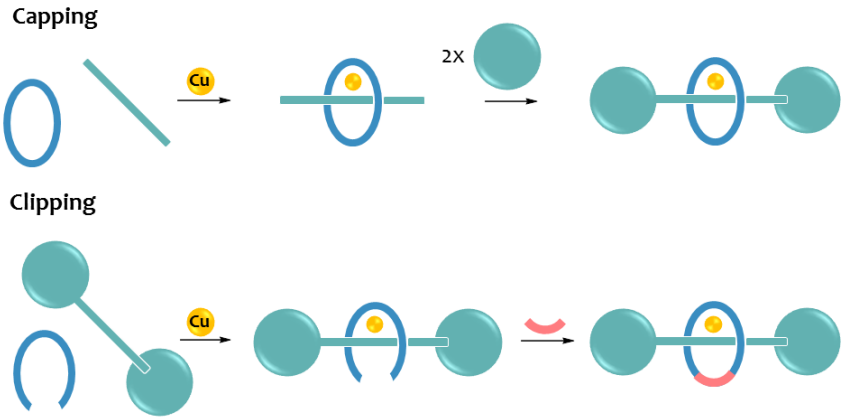

Figure 1.15 Schematic representation of capping and clipping strategies in the templated synthesis of copper rotaxanes.

In the self-assembly of copper rotaxanes, the coordination of the metal ion is acting as the template that brings the subcomponents together in the appropriate relative orientation for the final locking of the target threaded system. As mentioned before, Cu(I) complexes show a marked tendency for tetrahedral environments, whereas Cu(II) can lead to either penta or hexacoordinated species in their combination with nitrogen ligands. For that reason, the self-assembly of copper rotaxanes is commonly templated by Cu(I) ions.

Finally, the covalent closure of the precursors constitutes the critical step in the preparation of copper rotaxanes. Although the self-assembly of the pseudorotaxane is near quantitative, the attachment of the stoppering groups is sometimes problematic and tend to decrease significantly the overall yield of the process. In the first examples of copper rotaxanes, the stoppering procedures were based on the Williamson reaction.[46, 47, 60] This reaction consists of the substitution of a primary alkyl halide by an alkoxide ion via a S_N2 mechanism which leads to the formation of an ether (see Figure 1.16).

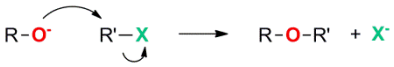

Figure 1.16 General mechanism of the Williamson reaction.

It is typically performed in aprotic polar solvents, and requires basic conditions for the generation of the alkoxide being the most commonly used bases carbonates, hydrides and hydroxides. This methodology enabled the preparation of a large family of copper interlocked systems.[41, 46, 47, 51, 61] However, the hard basic conditions promoted the partial unthreading of copper rotaxanes and thus, it led to moderate yields between 30-40%, which encouraged the search of more efficient procedures for the covalent attachment of the stoppers.

2.3.1 Click chemistry

In 2001, Sharpless *et al.* introduced the concept 'click chemistry' to describe a set of reactions useful to link quickly and reliably small building blocks in a covalent way.[62] This synthetic strategy tries to emulate the ability of living organisms to construct large organic frameworks as polynucleotides, polypeptides and polysacharides, from simple metabolites. The reactions included in the group of click chemistry must meet a series of requirements. They have to be *modular*, *wide in scope*, give very *high yields*, generate only *inoffensive byproducts* and be *stereospecific*. One of the most popular reaction within the click chemistry is the Huisgen 1,3-dipolar cycloaddition. It consists on the cycloaddition of alkynes and azides to give triazoles.[63] The general mechanism is shown in Figure 1.17. When it is carried out with terminal alkynes and in the presence of a Cu(I) catalyst the process is highly sterospecific and only 1,4-disubstituted 1,2,3-triazoles are obtained. The reaction takes place at room temperature and in a great variety of solvents, ranging from aqueous media to polar organic solvents.

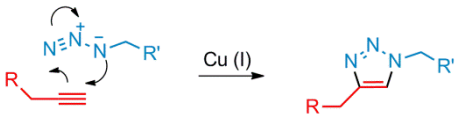

Figure 1.17 General mechanism of Huisgen 1,3-dipolar cycloaddition.

The mild conditions employed by the CuAAC (Copper-Catalyzed Azide-Alkyne Cycloadition), its tolerance to sensitive functional groups and its high yields make this

reaction a promising alternative for the stoppering of preliminary prepared pseudorotaxanes.[64] In the particular case of copper rotaxanes and catenanes, the use of click chemistry has afforded a wide range of systems in high yield,[65-70] even in the case of more labile rotaxanes.[71] In this one-pot procedure, the capping is carried out after the threading step by adding the stoppers, the base (typically Na_2CO_3), the Cu(I) catalyst and, in some cases, a mild reductant as sodium ascorbate to prevent the oxidation of Cu(I) in a deoxigenated mixture of dichloromethane and acetonitrile.

However, it has been observed that the presence of free chelating units in the precursors dramatically lowers the overall yield of the reaction.[72] Such effect is attributed to the complexation of the copper ions, which decreases its catalytic activity. This problem could be lowered by the use of a coordinatively saturated catalyst as [Cu(C18$_6$tren)]Br, shown in Figure 1.18, instead of the simple [Cu(CH_3CN)$_4$](PF_6) salt.[72]

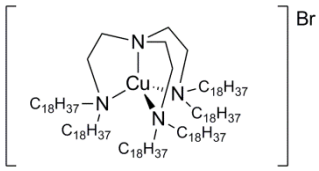

Figure 1.18 [Cu(C18$_6$tren)]Br catalyst

2.3.2 Imine covalent chemistry in interlocked systems

Dynamic Covalent Chemistry (DCC) has been proposed as a very useful tool for the generation of extended structures in supramolecular chemistry.[73] This chemistry is based in the use of highly reversible reactions that affords new covalent entities formed under thermodynamic control. The most extended functionality inside this category are imines. Their formation, schematized in Figure 1.19, takes place by the condensation between a primary amine and an aldehyde and implies the loss of one molecule of water. The regioselectivity of this reaction relies on the fast equilibration process that leads to the preferential formation of the thermodynamic products among other undesired kinetic

products. However, the high reversibility of the process makes imines very sensible to hydrolysis or to exchange in the presence of a second amine.[74]

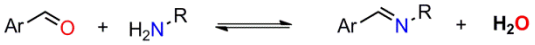

Figure 1.19 Imine condensation.

Imines bear a sp^2 nitrogen, which is a very good donor atom and form stable complexes with most transition-metals, lathanides and actinides.[75, 76] Thus far, in the presence of metal ions, imine-bond formation can be metal-templated. This approach has enabled the self-assembly of complex metal architectures, such as macrocycles or helicates,[77] upon the mixture of metal ions with primary amines and formyl fragments. However, it is on the synthesis of interlocked molecules where the use imine-covalent chemistry has got a bigger impact. One fascinating example are Borromean rings and Solomon knots.[78] In the former, represented in Figure 1.20, six Zn(II) metal ions direct the assembly of small organic precursors to create a highly symmetric mechanically interlocked species.

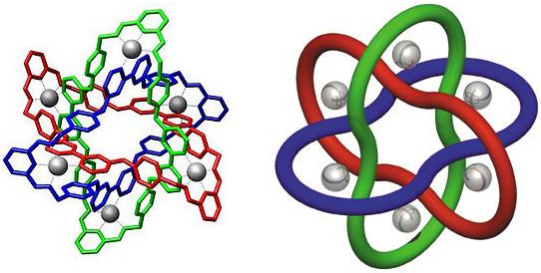

Figure 1.20 Crystal structure and schematic representation of a Borromean ring.

The templated formation of imines has also enabled the construction of interlocked catenanes[79, 80] and rotaxanes[81, 82] assisted by either metal ions or alkylammonium salts. Figure 1.21 shows a new class of rotaxanes generated by octahedral metal-templated imine condensation in a gathering and threading protocol.[83]

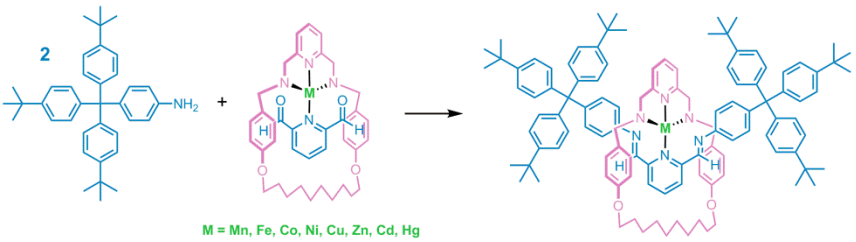

Figure 1.21 Self-assembly of [2]rotaxane by metal template imine formation.[83]

One additional feature of imine-based mechanically interlocked structures is that they can be preserved into non-exchanging forms by the reduction to secondary amines since it avoids the possibility of breaking of the imine bond while maintaining the coordination requests of the nitrogen.[79, 84] Therefore, this chemistry affords a new possibility for the locking catenane and rotaxane molecules.

Results and discussion

In the present section we describe the synthesis and characterization of two new bistable copper rotaxanes able of performing electrochemically-triggered shuttling and pirouetting motions, respectively (see Figure 1.22).

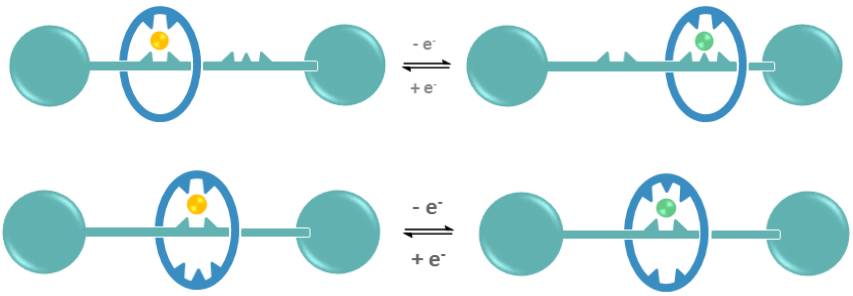

Figure 1.22 Schematic representation of a shuttling and a pirouetting copper rotaxane, respectively.

The possibility of externally controlling the Cu(I/II)-driven isomerization at room temperature envisions the potential of these kind of systems as molecular scale devices. Compared to other interlocked bistable systems,[12, 85] copper-based present very high switching ratios but moderate response times in solution. In this context, we wanted to contribute to the field by the optimization of the existing and by the introduction of new coordination environments that could enhance the dynamic properties of these systems. As shown in section 1.1.3, structural factors can have a very significant influence on the switching behaviour of Cu(II/I) based dynamic systems. The kinetic inertness of the primitive copper–based interlocked systems can be lowered by the modification of at least one of the bidentate ligands. However, this acceleration has always been accompanied by a lowering of the redox oxidation potential.[48] The separation between the redox potential of the copper tetra and pentacoordinated sites is going to define the width of the hysteresis cycle, and thus, the stability interval between ON and OFF states.

In the two systems proposed in this chapter we have explored the effect on the kinetics of changing the usual 2,9- for a 3,8-substitution in the phenanthroline ligand. This

configuration is expected to facilitate the access to nucleophilic species, and thus, to increase the lability of the complex, see Figure 1.23.

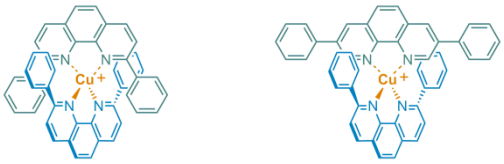

Figure 1.23 Different copper shielding in $[Cu(dpp)_2]^+$ and [Cu(dpp)(3,8-bisphenyl-phenanthroline)]$^+$ coordination spheres.

In contrast to the tetracoordinated site, the tridentate coordination chelate, based on 5,5''-disubstituted-2,2':6,2''-terpyridines, has been maintained invariant in time. Despite the improvements on the preparation of substituted terpy ligands carried out along the years, it still involves the use of time-consuming multi-step synthetic routes and highly toxic organostannane reagents.[86] With the aim of developing more feasible synthetic strategies for the construction of these beautiful and, at the same time, complicated molecules, we have introduced the use of dynamic covalent chemistry for the preparation of the tridentate coordinating unit.

2.4 A shuttling rotaxane based on a phen/terpy conjugate

Electrochemically-triggered linear motions have been successfully induced in stimuli-responsive rotaxanes in which the different recognition sites are distributed along the axle subcomponent.[87-90]

As pointed before, copper-coordination bonds are one of the interactions that have been successfully exploited for the construction of molecular shuttles.[39, 49, 60, 91] Along with the lability of the tetracoordinated environment there is a second factor determining the dynamic response of copper-based molecular shuttles, the spacer between the two coordination sites. Previous studies have shown that when the spacer between the phen and terpy chelates increases its flexibility, the gliding motion of the ring along the axle is accelerated.[49, 91] Herein, in order to study the effect of the distance between the two

coordinating sites we have designed and studied switchable rotaxane **R1**$^{+}$ whose structure is shown in Figure 1.24. In this system, the tridentated chelating unit, consisting on a terpy, has been directly bonded through its 5 position to a phen unit. This distribution reduces to a minimum the distance between the two coordination sites, and thus, it is expected to minimize the number of different conformations that the threaded system can adopt during the gliding motion.[92]

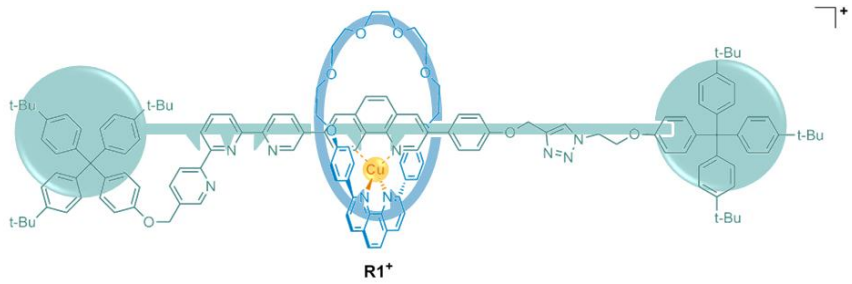

Figure 1.24 Rotaxane **R1**$^{+}$**.**

Besides, on the tetracoordinated site, the axle phenanthroline has been functionalized through its 3- and 8- positions to reduce the steric hindrance around copper, whereas, we have kept a dpp in the macrocycle **M1**[93] in order to reduce the destabilization of the cuprous oxidation state.

2.4.1 Synthesis

Synthesis of rotaxane **R1**$^{+}$ was carried out using the threading followed by stoppering approach.[58] We decided to use CuAAC methodology for the final capping of the [2]pseudorotaxane since these reactions are carried out under very mild conditions and have already to be proven very successful in the synthesis of other copper-interlocked systems.[66-70] Moreover, in order to enhance the yield of the final stage, only one single blocking group was incorporated in the capping, the other one being already present on the terpy extreme of the axle precursor.[69] Hence, the mono-stoppered thread was provided with a terminal alkyne, whereas the second stopper fragment was functionalized with an azide derivative.

2.4.1.1 Synthesis of the thread

The structure of linear ethynyl-terminated thread **2** is depicted in Scheme 1.1. It is composed by a terpy unit directly bonded through its 5- position to the 3- position of a phenanthroline moiety. Attached to the other terpy end of the axle there is also a tetraphenyl methane stoppering group. The synthesis of **2** was accomplished by the convergent assembly of its various constituent fragments: stopper **3**, terpy derivative **4** and bromophen **5**.

Synthesis of phenolic blocking group **3** was carried out in two steps from 1-bromo-4-*tert*-buthylbenzene, p-*tert*-buthylbenzoate and phenol, according to reported literature procedures.[94] Preparation of the terpy and phen fragments **4** and **5** is depicted in Scheme 1.1. We decided to use unsymmetrical derivatives of both terpy and phen ligands in order to increase the bonding selectivity during the assembly of **2**. Thereby, both extremes of **4** were functionalized with groups of very different reactivity, an aryl bromide, to be reacted in palladium-catalyzed cross-coupling reactions, and a benzylic bromide, which is very reactive in nucleophilic substitution reactions. For the same reason, phen **5** was equipped in its 3- and 8- positions with a bromide and a protected phenol derivative.

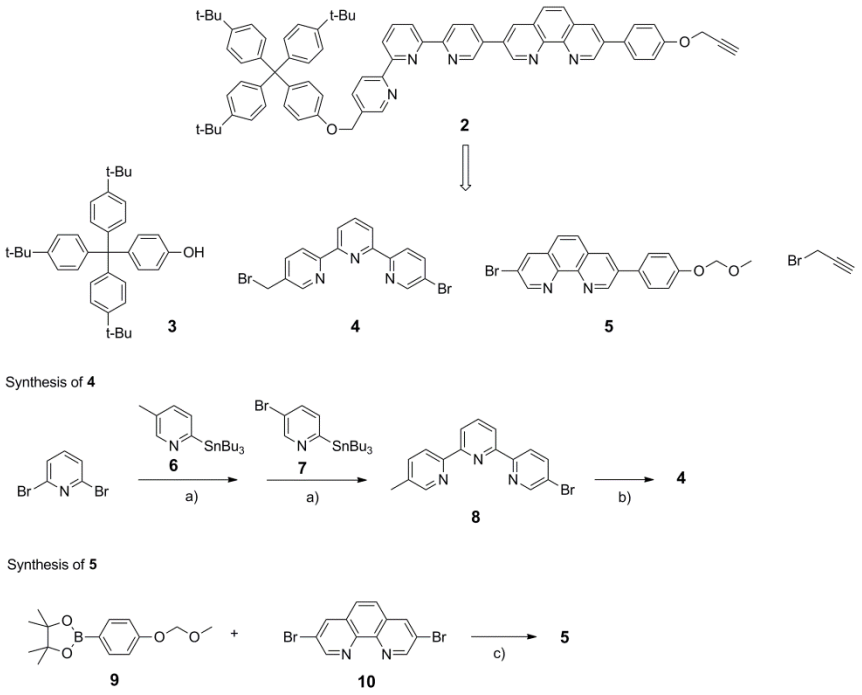

Scheme 1.1 Retrosynthesis of axle precursor **2**. Synthesis of building blocks **4** and **5**: **a)** $Pd(PPh_3)_4$, toluene (65%); **b)** NBS, dichloromethane, H_2O, light (77%); **c)** $Pd(PPh_3)_4$, DMF, K_2CO_3, H_2O (33%).

Asymmetric terpy **4** was prepared in good yield (77 %) by photobromination of the benzylic position of **8** with NBS in a dichloromethane/water biphasic media. The synthesis of **8** was carried out in the presence of catalytic amounts of $Pd(PPh_3)_4$, as it was described in a previous communication from our group,[95] in 42% overall yield using two consecutive Stille cross-coupling reactions between 2,6-dibromopyridine and stannyl-pyridines **6**[96] and **7.**

Asymmetric phen **5** was prepared by the cross-coupling of 3,8-dibromophenanthroline (**10**)[97] with one equivalent of aryl boronic ester **9**. This reactant was prepared from commercially available 4-hydroxyphenylboronic acid pinacol ester and chloromethyl methyl ether. Although there are several examples in the literature describing Suzuki cross-couplings performed in the presence of free phenol groups, in our case the protection of the phenol group as a methoxymethyl ether (MOM) resulted convenient in

order to avoid deboronation processes[98, 99] and to increase the solubility of the final products. In addition, MOM group is resistant to the basic cross-coupling media used in a later synthetic stage and can be cleaved under very mild conditions.[100]

The linkage of the different building blocks to form thread **2** was attempted by several approaches. The first synthetic route planned, consisted on the first obtaining of the phen-terpy conjugate, followed by the attachement of the stoppering group in a second stage. The former steps of this route were directed to the conversion of **5** into the corresponding boronate or stannane derivative, to be further coupled with bromoterpy **8** by Stille or Suzuki protocols. However, these attempts resulted unsuccessful. The treatment of **5** with Mg, *n*-BuLi or *tert*-BuLi for a metal-halide exchange reaction followed by the addition of different electrophiles such as $B(OMe)_3$, *i*-PrOBPin or Bu_3SnCl, as well as the reaction under cross-coupling conditions with $Pd(ddpf)Cl_2$ or $Pd(PPh_3)_4$ in the presence of pin_2B_2, yielded the unaltered starting material.[101]

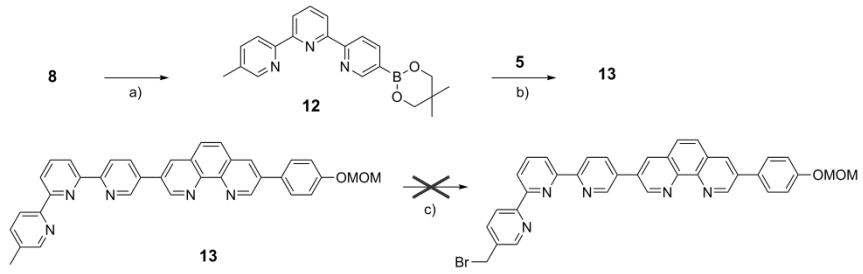

Scheme 1.2 Failed synthetic route: **a)** neo_2B_2, [$PdCl_2$(dppf)ferrocene], DMSO 80ºC (65%); **b)** $Pd(PPh_3)_4$, DMF, K_2CO_3, H_2O (51%); **c)** NBS, AIBN, CH_2Cl_2, H_2O, light.

Nevertheless, the terpy and phen fragments could be coupled by the conversion of **8** into its neopentil boronic ester under Miyaura conditions, in the presence of neo_2B_2 and using $Pd(ddpf)Cl_2$ as catalyst,[95] as schematized in Scheme 1.2. Compound **12** was isolated in good yield.[102, 103] Following, coupling of **12** with bromophen **5** afforded the phen-terpy conjugate **13**. Unfortunately, this synthetic route was finally discarded due to the impossibility of brominating the methyl group in the 5''-position of the terpy unit. We attribute this result to the low solubility of starting compound **13** in common halogenated solvents.

Finally, molecular thread **2** was assembled by first attaching the bulky group **3** to the bromomethyl terpy derivative **4** and then coupling with phen **5**. This synthetic route is described in Scheme 1.3 and involved: a) the initial nucleophilic attack of the phenolic stopper **3** to the benzylic bromide group in **4** under typical Williamson conditions to afford intermediate **14**, b) the conversion of **14** to its neopentil boronic ester **15** under Miyaura conditions using neo_2B_2 and $Pd(ddpf)Cl_2$ as catalyst,[102, 103] and c) the Suzuki cross-coupling between **15** and bromophenanthroline **5** to afford **16** in a reasonable yield (28 %); d) the cleavage of the MOM-protecting group in **16** to yield phenol **17** under the mild acidic media resulting from the visible-light irradiation of catalytic amounts of carbon tetrabromide in 2-propanol;[100] and e) the final nucleophilic substitution reaction between **17** and propargyl bromide under Williamson conditions to afford axle **2** in 80% yield. The final stoppering reaction of the [2]pseudorotaxane by CuAAC required the incorporation of an azide or a ethynyl functionality in the rotaxane axis-precursor. The nucleophilic character of both sodium azide and the phenol group present in **17**, allowed us to discard the incorporation of the azide function into the thread.

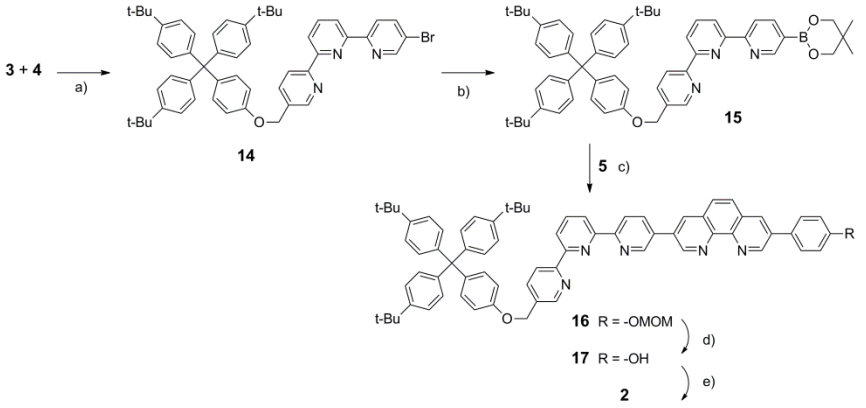

Scheme 1.3 a) K_2CO_3, DMF 80 ^{0}C (55%); **b)** neo_2B_2, [$PdCl_2$(dppf)ferrocene], DMSO 80 ^{0}C (49%); **c)** $Pd(PPh_3)_4$, DMF, K_2CO_3, H_2O (28%); **d)** CBr_4, 2-propanol, light (81%); **e)** NaH, propargyl bromide, THF 45 ^{0}C (80%).

Azide-functionalized stopper **20** was synthesized in 69 % yield in only two steps from previously described 2-(4-(tris(4-(*tert*-butyl)phenyl)methyl)phenoxy)ethan-1-ol, which was prepared from the reaction of **3** with 2-bromo-ethanol (see Scheme 1.4).[60] Alcohol **18**

was first transformed into the mesylate derivative **19**, and then directly reacted with NaN_3 in DMF to obtain the azide-functionalized stopper **20** in good yield (74%).[104] Such efficient substitution of the mesylate by the azide nucleophile permitted us to simplify in two-steps the transformation of the aliphatic alcohol into the azide functionality, instead of the common strategy that also involves an iodide intermediate.[105]

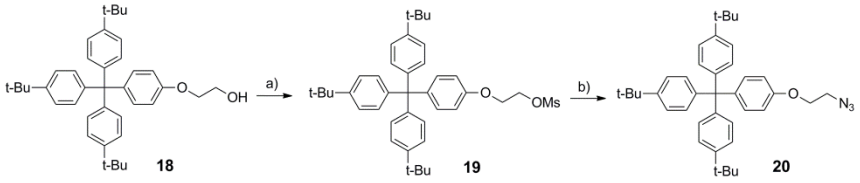

Scheme 1.4 a) MsCl, TEA, CH_2Cl_2 (93%); **b)** NaN_3, DMF (74%).

2.4.1.2 Threading and capping

Threading of the linear fragment **2** through the coordinating ring, and stoppering of the axle was carried out in one pot. First, equimolecular amounts of mono-stoppered axle **2**, the previously reported macrocycle **M1**[11] and $[Cu(CH_3CN)_4](PF_6)$ were dissolved in a dichloromethane/acetonitrile mixture under an inert atmosphere. The solution rapidly turned into dark-red, indicating the formation of [2]pseudorotaxane $[Cu(\mathbf{M1})(\mathbf{2})]^+$. The ensuing addition of Na_2CO_3, sodium ascorbate and a copper catalyst promoted the CuAAC reaction of the intermediate pseudorotaxane with azide stopper **20** as described in Scheme 1.5. The election of the Cu(I) catalyst for the CuAAC capping was an important issue. Although $[Cu(CH_3CN)_4](PF_6)$ can be used as catalyst in CuAAC reactions, some reports found recommendable the use of coordinatively saturated Cu(I) complexes as catalysts in the coupling of metal-chelating substrates.[72, 106, 107] In our case, we opted for the complex [Cu(Me6tren)]Br which has been described as an efficient catalyst in CuAAC[108] and it can be easily prepared by mixing equimolecular amounts of CuBr and commercial tris[2-(dimethylamino)ethyl]amine ligand (Me6Tren) in degassed acetonitrile. After the CuAAC capping, treatment of the reaction crude with aqueous KCN afforded after column chromatography a mixture containing demetallated rotaxane **21** and 13% of unthreaded axle **22** as a by-product. Copper-complexed rotaxane

R1^{+} could be finally obtained in an overall 11% yield by the remetallation of the mixture with one equivalent of [Cu(CH_3CN)$_4$](PF_6) and further purification by column chromatography.

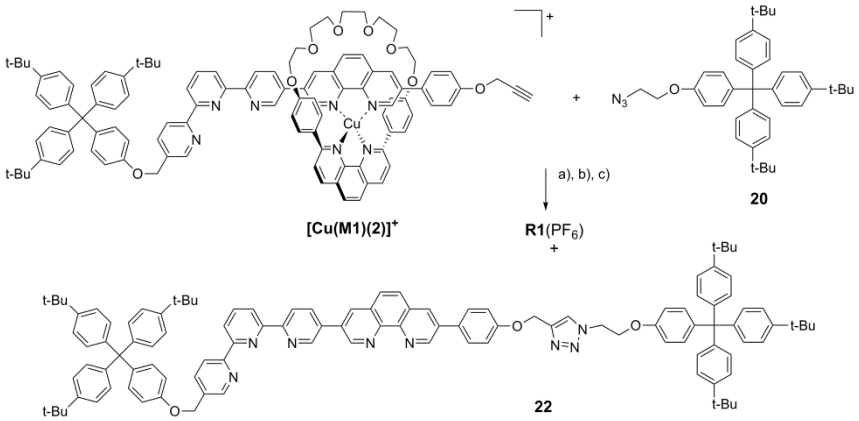

Scheme 1.5 Capping of **R1**$^{+}$: **a)** Cu(Me_6Tren)Br, Na_2CO_3, Sodium ascorbate, CH_3CN, CH_2Cl_2.; **b)** KCN aq.; **c)** [Cu(CH_3CN)$_4$](PF_6), CH_3CN, CH_2Cl_2 (11%).

2.4.2 Characterization

The structure of rotaxane **R1**$^{+}$ was confirmed by High Resolution Mass Spectrometry and ^{1}H NMR spectroscopy. Assignment of the signals in Figure 1.25 could be done by the combined use of 1D and 2D (COSY, NOE) ^{1}H NMR spectroscopy and comparison with the spectra of precursors **2** and **M1**. The precise coordination of copper to the axle phenanthroline and to the macrocycle was evidenced in the NMR spectrum of **R1**$^{+}$ by the appearance of a doublet below 6.0 ppm, corresponding to Mm-protons under the effect of the aromatic ring current of the phen moiety of the axle.[60] Furthermore, the location of the ring on the phenanthroline station of the axle was evidenced by the noticeably shift experienced by P2, P5, P6 and P9 protons. By contrast, all the protons coming from the terpy moiety appeared at chemical shifts similar to those found in the uncoordinated axle with the exception of T6, which is the closest to the macrocycle. Thereby, ^{1}H NMR confirms that the terpy site remains uncoordinated.

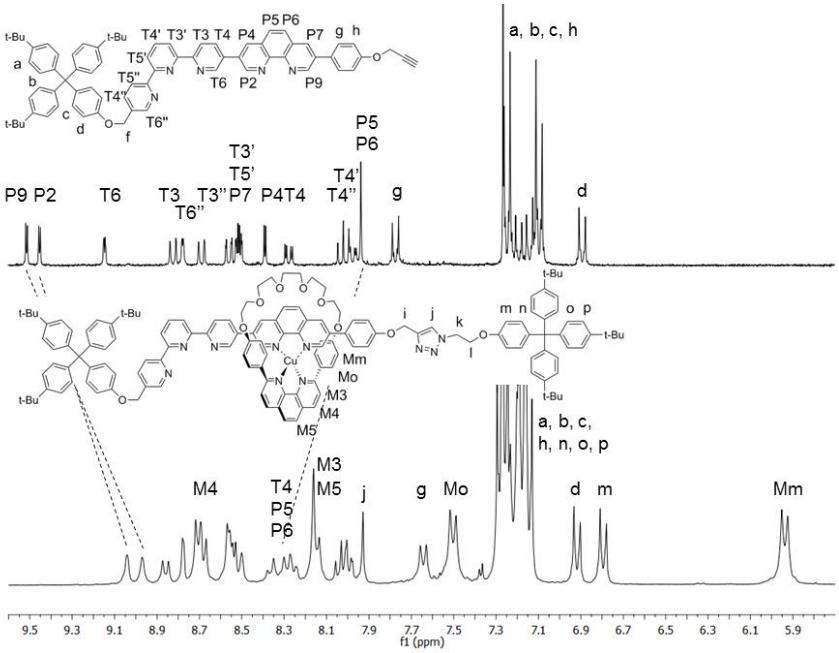

Figure 1.25 ^{1}H NMR spectra of axle precursor **2** and rotaxane **R1**(PF_6) recorded in $CDCl_3$ and CD_2Cl_2 respectively.

The identity of P2 and P9 protons was confirmed by NOE experiments (see Figure 1.26). Irradiation of the proton at δ = 9.04 ppm generates a NOE effect at protons Mo (7.50 ppm), whereas the irradiation of the peak at 8.97 ppm results in a NOE effect at protons g and Mo. Since they both lay close to Mo, these protons correspond to P2 and P9, being P9 the proton at 8.97 ppm, due to its proximity to g, and P2 the one appearing at 9.04 ppm.

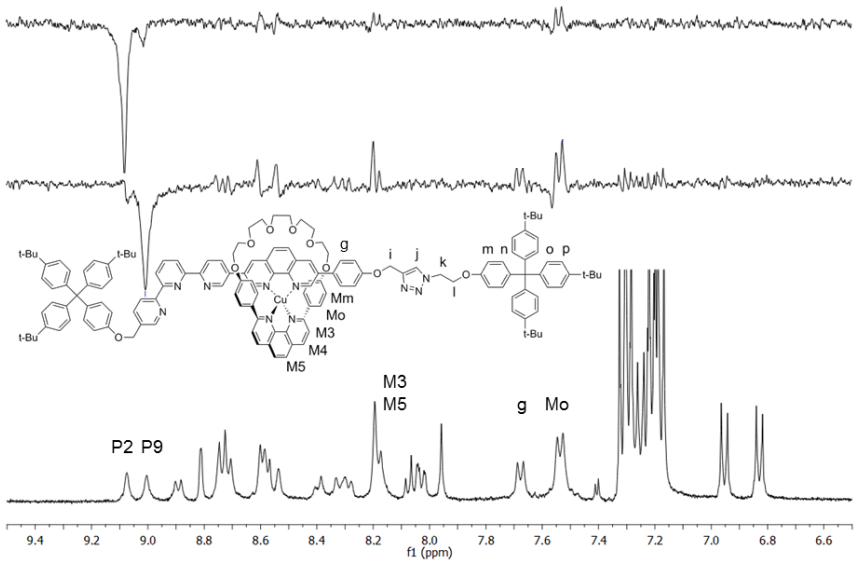

Figure 1.26 1D NOE experiments with **R1**(PF_6) carried out in CD_2Cl_2.Irradiation of the proton at δ= 9.04 ppm generates a NOE effect at protons Mo (7.50 ppm). Irradiation of the peak at 8.97 ppm results in a NOE effect at protons Hg and Mo. The phen protons of the the axle closest to Mo are P2 and P9. If the proton at 8.97 is near to Hg, it must be P9. Thus P2 is the peak at 9.04 ppm.

The UV-Vis spectra of **22** and the Cu(I) and Cu(II) forms of rotaxane **R1**(PF_6) recorded in $1 \cdot 10^{-5}$ M dichloromethane solution are shown in Figure 1.27. The absorption UV-Vis spectra of axle **18** presented an intense absorption band (343 nm, 68000 $M^{-1}cm^{-1}$) in the UV region, associated to π-π* ligand-centered (LC) transitions.[109] The spectrum of **R1**(PF_6) showed red-shifted LC transitions due to the coordination of copper and low-intensity overlapping Metal-to-Ligand Charge Transfer (MLCT) bands extending from 420 to 650 nm with absorption maxima at 439 nm (3900 $M^{-1}cm^{-1}$) and 570 nm (1700 $M^{-1}cm^{-1}$).[110] These MLCT bands, responsible of the characteristic red color of tetrahedral $[Cu(phen)_2]^+$ complexes, disappeared upon the oxidation of **R1**(PF_6) with $NO(BF_4)$ turning the colour of the solution into yellow. The original red color could be recovered by the addition of hidrazine. These facts can be ascribed to the oxidation/reduction of the copper center and subsequent reorganization of its coordination sphere.

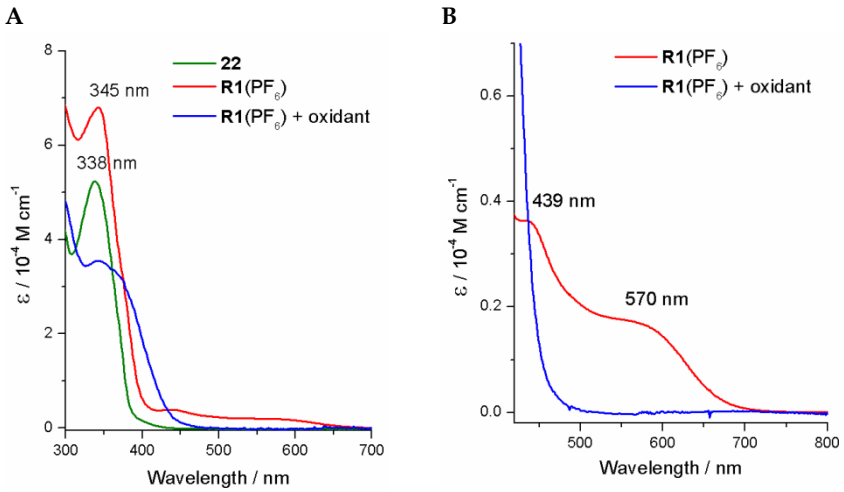

Figure 1.27 A) UV-Visible spectra of molecular axle **22**, and the reduced and oxidized forms of rotaxane **R1**(PF_6). **B)** Absorption spectra in the visible region of the reduced and oxidized forms of rotaxane **R1**(PF_6). Data recorded in dichloromethane $1 \cdot 10^{-5}$ M (oxidant: $NOBF_4$).

2.4.2.1 Electrochemical studies

Cyclic voltammetry studies were carried out in order to evaluate the electrochemical response of shuttling rotaxane **R1**(PF_6). The cyclic voltammograms in dichloromethane/acetonitrile (1:9) solution at different scan rates are shown in Figure 1.28. The electrochemically induced gliding of the ring along the axis was evidenced in the different waves observed in the cyclic voltammogram. On scanning from 0 V to positive potentials a redox process associated with the oxidation of Cu(I) in a tetrahedral environment appeared at $E_{1/2}$ = + 0.48 V. This value is below to that reported[41] for $Cu(dpp)_2$ and is close to that reported for other 2,9/3,8-substituted copper complexes like heteroleptic Cu(dpp)(dpbiiq).[48] As expected, the reduction of the steric hindrance around the tetracoordinated site is reflected in the destabilization of the cuprous state. According to the electrochemical potential of other $Cu(terpy)(dpp)^+$ like complexes,[41, 60] the irreversible wave at 0 V found in the reversal scan was associated to the reduction of Cu(II) in the pentacoordinated environment.

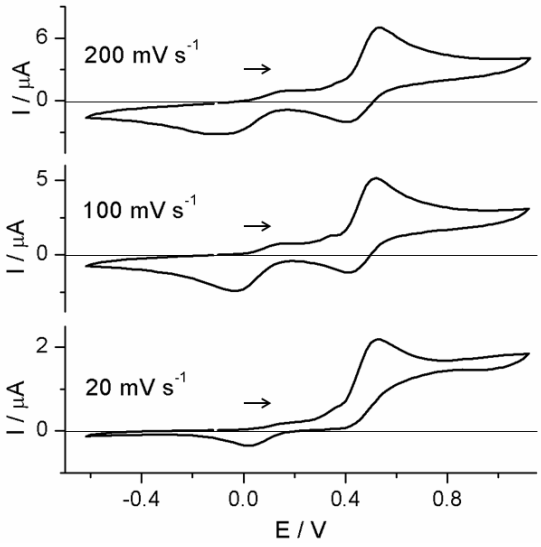

Figure 1.28 Cyclic voltammograms at 200, 100 and 20 mV/s scan rate of rotaxane **R1**(PF_6) ($1 \cdot 10^{-3}$ M) in dichloromethane/acetonitrile (1:9) using TBA(PF_6) 0.1 M as supporting electrolyte. Electrochemical potentials have been referenced to SCE using the Ferrocene/Ferricinium couple as internal standard.

On decreasing the scan rate from 200 to 20 mV/s, the electrochemically induced gliding of the ring, was further evidenced by the decrease in the intensity of the reduction wave corresponding to the Cu(II) in the tetracoordinated environment, see Figure 1.28. As previously observed, whereas the translational movement of the unstable Cu(I) pentacoordinated species is very fast in the timescale of the measurement, the rearrangement of tetracoordinated Cu(II) occurs at lower rates.[44, 47, 60] Making use of the working curve reported by Nicholson and Shain,[43] a value for the kinetic constant of the limiting reorganization process of k = 0.3 s^{-1} could be estimated from the peak height ratio of the waves at 0.48 V. When the rate constant was evaluated in 6:4 dichloromethane/acetonitrile mixtures, a value of 0.15 s^{-1} was obtained, see Figure 1.29. This observation supports the idea that solvent molecules coordinate copper during the rearrangement process, facilitating ligand exchange. In such case, a higher proportion of a more coordinating solvent like acetonitrile will lead to higher kinetic rates.

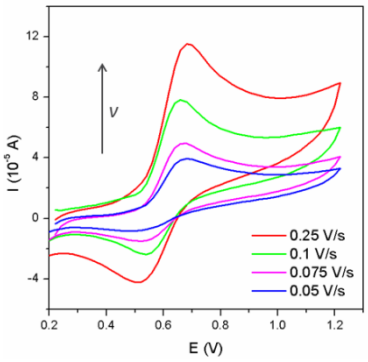

Figure 1.29 Evolution with the scan rate of the Cu(I/II) couple in the tetrahedral environment in rotaxane **R1**(PF_6) in dichloromethane/acetonitrile (6:4) mixtures.

If we compare with similar shuttling rotaxanes based on $Cu(dpp)_2$ environments measured in 1:9 dichloromethane/acetonitrile mixtures,[50, 60] in our case the rate constant is more than 100 times higher than that described for a shuttling rotaxane where the phen and terpy units are linked by an aliphatic or a single phenyl spacer. Considering that the change on the substitution on the bidentate site from 2,9-[48] to 3,8-[46] positions results only in an approximately 5-fold increase of the rearrangement rate of the tetracoordinated Cu(II) species, the high motion rates observed in the shuttling movement of **1**$^+$ can not only be ascribed to the less encumbering substitution on the phenanthroline chelate, but also to the proximity of the two coordination sites.

2.4.3 Conclusions

In this section we have studied the effect of the distance between the coordination sites on the dynamics of a copper-complexed shuttling rotaxane. Rotaxane **R1**$^+$ contains a 3,8-disubstituted phen bidentate chelate directly connected through its 3-position to the 5-position of a terpy unit in the axle and the dpp unit in the ring. This configuration makes **R1**$^+$ the copper-based shuttling rotaxane with the minimum possible distance between tetra and pentacoordinated sites.

Cyclic voltammetry experiments performed at different scan rates confirmed the reversible electrochemically-triggered shuttling motion of the ring along the axle. However, the reorganization of the Cu(I) pentacoordinated unstable species was slow in the timescale of the experiments. The substitution of the phen in its 3,8- positions and the direct attachment of the phen and terpy coordination sites led to a significant increase of this shuttling rate (0.3 s^{-1}) that is not far below from the fastest copper shuttling rotaxane reported to date (2 s^{-1}).[49] Nevertheless, the sum of these two factors was expected to afford a faster electrochemical response to oxidation. Considering the higher reorganization rates obtained by the use of 3,8-bipyridines[46, 48] and dpdiiq[49, 50] chelates, the substitution of the phen by more flexible bipy coordination units in the rotaxane axle will probably lead to the development of even faster copper-based molecular shuttles.

2.5 A pyridine bisamine-containing pirouetting rotaxane

The present section reports the synthesis and characterization of a pyridine bis-amine-containing pirouetting copper rotaxane. The employment of this terdentate ligand constitutes the first incorporation of imine-based dynamic covalent chemistry into switchable copper-complexed interlocked molecules. In this system, the use of non-hindering 3,8-bis(phenylethynyl)phenanthroline and pyridine bis-amine ligands as chelating units, not only has led to a simplification of the synthetic procedures, but also to a bistable system with an enhanced energetic separation between states. Moreover, the switching cycle was accelerated to less than 2 ms.

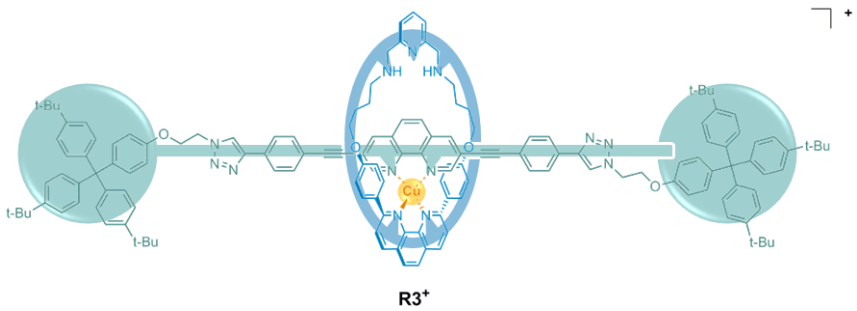

Figure 1.30 Rotaxane **R3**$^{+}$.

The chemical structure of pirouetting [2]rotaxane **R3**$^{+}$ is represented in Figure 1.30. This system is composed by a bis-chelating macrocycle threaded by a molecular axle bearing a phen moiety. Taking advantagee of its readily accessible synthesis, we wanted to explore the effects of substituying the classical terpy by the pyridine bis-amine coordinating unit for the construction of mechanically interlocked systems. The proposed 31-membered macrocycle, in short **M3**, bears two different coordination sites, one bidentate dpp, and one tridentate pyridine bis-amine moiety, connected by flexible buthyl chains (Figure 1.31).

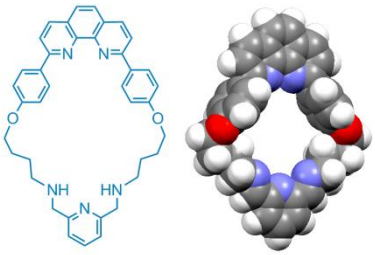

Figure 1.31 Molecular structure and DFT-optimized structure of **M3** macrocycle.

Pyridine bis-imine chelators have been proposed as a feasible alternative to tridentate terpy ligands.[80, 111] These ligands can be easily formed by one-pot condensation of commercially available 2,6-pyridinedicarbaldehyde with primary amines[112] and form very stable ML_2 octahedral complexes with a great number of soft metal ions such as Mn (II), Fe (II), Co (II), Ni (II), Cu (II), Zn (II), Cd (II), Hg (II).[113] The reduction of the imine bonds to the corresponding amines, transforms this chemically labile chelate into the non-exchanging pyridine bis-amine form (Figure 1.32).[114] In general, imine nitrogens lead to larger metal binding constants than their saturated analogues due to the ability of unsaturated nitrogen to act not only as σ-donor but also as π-acceptor.[115] That fact has been evidenced by the evaluation of the stability constants of a series of divalent metal complexes in which pyridine units have been sequentially introduced in linear polyamine ligands.[116] On the other hand, the substitution of imine by amine nitrogens increases the flexibility of the chelate. In the particular case of Cu(II), this is particularly important since it enables the adoption of less strained square pyramidal geometries in pentacoordinated spheres. Thereby, pyridine bis-amines provide a larger stabilization of the cupric state than terpys or fully-saturated triamine ligands.[117, 118]

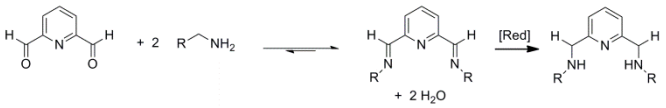

Figure 1.32 Pyridine bisamine formation.

The second coordination site of **M3** is constituted by a dpp, which has demonstrated to provide a very stable coordination environment for Cu(I).[119] Moreover, the presence of

rigid phenyl groups in 2 and 9 positions of the phen sterically prevents the binding of the two chelating units of one ring to the same copper center, which would lead to the saturation of the coordination requests of copper, avoiding the threading of the axle.

On the other hand, the molecular axle comprises a 3,8-disubstituted phen in which the chelate has been symmetrically bonded to the stoppers by a phenylethynyl spacer. The ethynyl groups of the axis were chosen for molecular resistance considerations, as will be discussed in the third chapter. This substitution has demonstrated to fulfill the two main requirements: it affords very stable Cu(I) heteroleptic complexes in combination with dpp ligands which, at the same time, are labile upon oxidation.

In order to better evaluate the dynamic properties of **R3**$^+$ we prepared rotaxane **R2**$^+$, in which the same molecular axle is threaded by a monochelating macrocycle (**M2**) comprising the dpp bidentate moiety, as shown in Figure 1.33.

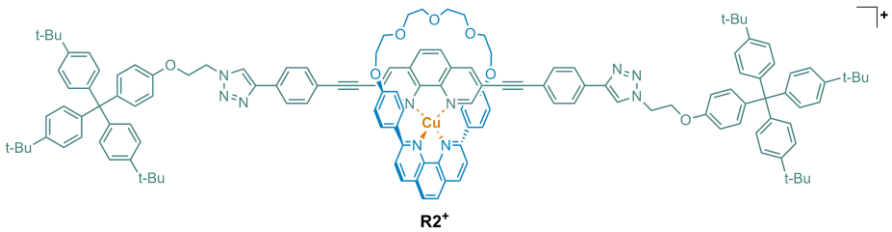

R2$^+$

Figure 1.33 Rotaxane **R2**$^+$.

2.5.1 Synthesis

On first instance, we decided to synthesize rotaxanes **R2**(PF_6) and **R3**(PF_6) via the threading followed by CuAAC stoppering.[59] The three macrocycles used in this work are presented in Scheme 1.6. Macrocyle **M2** was synthesized as described elsewhere.[93] The synthesis of heteroditopic ring **M3** was carried out in three steps, as shown in Scheme 1.6, starting from 2,9-bis(*p*-hydroxyphenyl)-1,10-phenanthroline (**23**),[93] which was prepared following previously described procedures.[120] In a first step, a substitution reaction of **23** with 4-(Boc-amino)butyl bromide under basic conditions afforded **24** in reasonable yield

(42%). Subsequent deprotection of the boc-protected amines with trifluoroacetic acid in dichloromethane afforded diamine **25** in 85% yield. Next, the ring closure of **25** was promoted by its double condensation with 2,6-pyridinedicarbaldehyde. This reaction was carried out under high dilution conditions in order to avoid oligomers as by-products. Finally, the imine bonds were reduced in situ with $NaBH_4$ in order to obtain the final non-labile pyridine bis-amine macrocycle **M3** in high yield.[114]

For comparative reasons, a third macrocycle named **M4**, containing just one coordinating pyridine bis-amine tridentate chelate, was prepared. This macrocycle was synthesized in three steps starting from 2,6-pyridine carboxaldehide in good 65% overall yield (Scheme 1.6). In a first step, **26** was obtained in one-pot by double imine condensation between 2,6-pyridine carboxaldehide and 6-aminohexanol, followed by reduction with $NaBH_4$ and subsequent protection of the amino group with di-tert-butyl dicarbonate. Next, condensation of diol **26** with isophthaloyl chloride under high dilution conditions promoted the ring closure through a diester formation to yield **27**. Finally, the boc-amino protecting groups in **27** were cleaved with trifluoroacetic acid under standard conditions[121] affording macrocycle **M4**.

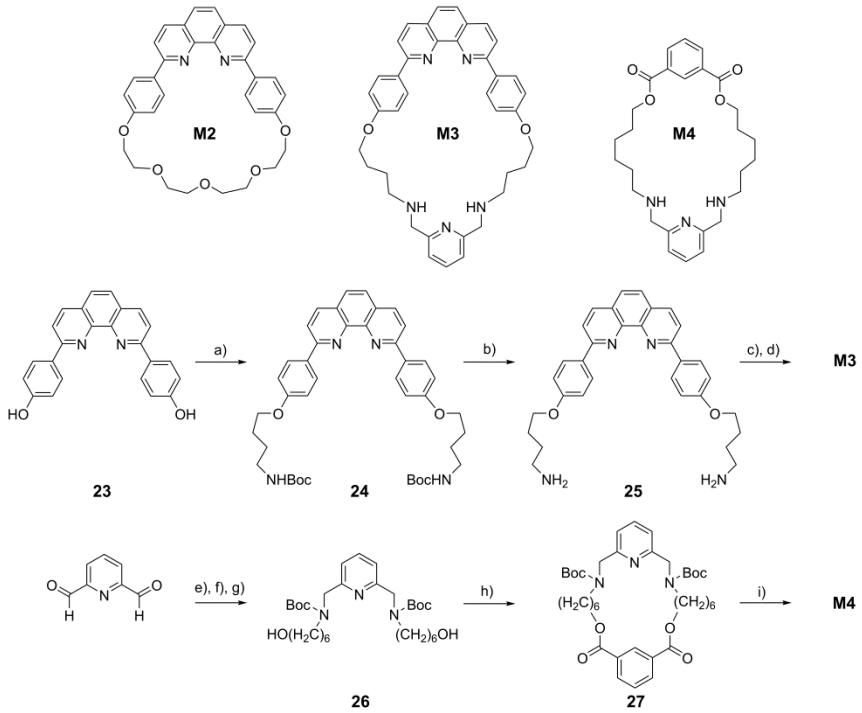

Scheme 1.6 Coordinating macrocycles **M2**, **M3** and **M4** (up). Synthesis of macrocycles **M3** (middle) and **M4** (bottom): **a)** 4-(Boc-amino)butyl bromide (2 eq), Na_2CO_3, DMF, 60 °C (42%); **b)** TFA, CH_2Cl_2 (85%); **c)** 2,6-pyridinedicarbaldehyde, MeOH/CH_2Cl_2; **d)** $NaBH_4$ (92%); **e)** 6-aminohexanol (2 eq), MeOH; **f)** $NaBH_4$; **g)** di-tert-butyl dicarbonate, triethylamine, reflux (97%); **h)** isophthaloyl chloride, CH_2Cl_2, TEA (68%); **i)** trifluoroacetic acid, CH_2Cl_2 (98%).

For the capping reaction, we decided to employ a CuAAC between diacetylenic axle precursor **30** and azide-functionalized stopper **20,** whose synthesis was described in the section 1.4.1.1. The synthesis of **30** is summarized in Scheme 1.7. Rigid phen derivative **29** was obtained in 50% yield from the reaction of 3,8-dibromo-1,10-phenanthroline[97] (**11**) and ((4-ethynylphenyl)ethynyl)trimethylsilane[122] (**28**) under Sonogashira cross-coupling conditions.[123] Cleavage of the terminal trimethylsilyl groups under basic conditions quantitatively yielded diacetylene **30**.

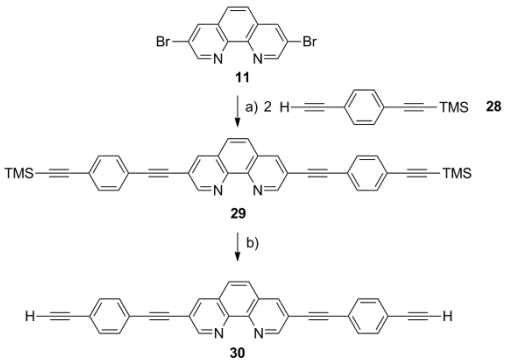

Scheme 1.7 a) $Pd(PPh_3)_2Cl_2$, CuI, THF, i-Pr_2NH (50%); **b)** K_2CO_3, MeOH (91%).

Rotaxane **R2**$^+$ was prepared as described in Scheme 1.8. In a first step, rod-like fragment **30** was threaded into macrocycle **M2** in the presence of Cu(I) to yield the copper-complexed pseudorotaxane intermediate. Next, [Cu(**M2**)**30**]$^+$ was reacted with two equivalents of the azide-terminated stopper **20** in the presence of [Cu(Me$_6$tren)]Br catalyst under CuAAC conditions. Once the capping process was complete, the resulting mixture was treated with aqueous KCN in order to remove the copper salts and then purified by silica column chromatography affording demetallated rotaxane **31** in 34% yield. Finally, **R2**$^+$ was obtained quantitatively by the re-metallation of **31** with one equivalent of [Cu($CH_3CN)_4$](PF_6) under an argon atmosphere.

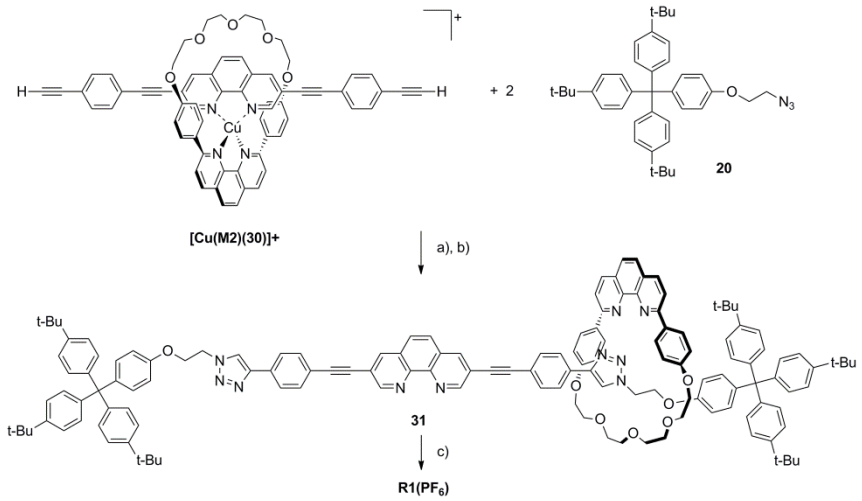

Scheme 1.8 Rotaxane **R2**$^{+}$ prepared by the threading followed by capping approach: **a)** Cu(Me$_6$tren)Br, Na_2CO_3, sodium ascorbate, CH_3CN, CH_2Cl_2; **b)** KCN aq; **c)** $[Cu(CH_3CN)_4](PF_6)$, CH_3CN-CH_2Cl_2 (97%).

Unfortunately, when the synthesis of **R3**$^{+}$ was attempted by the threading of **30** into **M3** followed by stoppering under the same conditions used for **R2**$^{+}$ the desired final product could not be obtained. As an alternative, and taking advantage of the dynamic nature of the reversible imine covalent bond, we decided to use a clipping methodology[73] for the preparation of **R3**$^{+}$. The clipping procedure used is illustrated in Scheme 1.9**.** First**,** we synthesized stoppered axle **32** in 70% yield by reacting fragment **30** with two equivalents of azide-terminated stopper **20** under CuAAC conditions. The intertwined copper-complex precursor [Cu(**25**)(**32**)]$^{+}$ was obtained upon mixing molecular axle **32**, diamine precursor **25** and Cu(I) in a 1:1:1 stoichiometry. In this complex, copper coordination holds **25** and **32** together in the right orientation for the clipping. In situ addition of 2,6-pyridine bis-aldehyde promoted the condensation of the two pendant primary amines around the axis, affording the pyridine bis-imine tridentate moiety. Finally, in situ reduction to the corresponding pyridine bis-amine with $NaBH_4$, followed by water quenching and column chromatography afforded rotaxane **R3**$^{+}$ in 22 % yield.

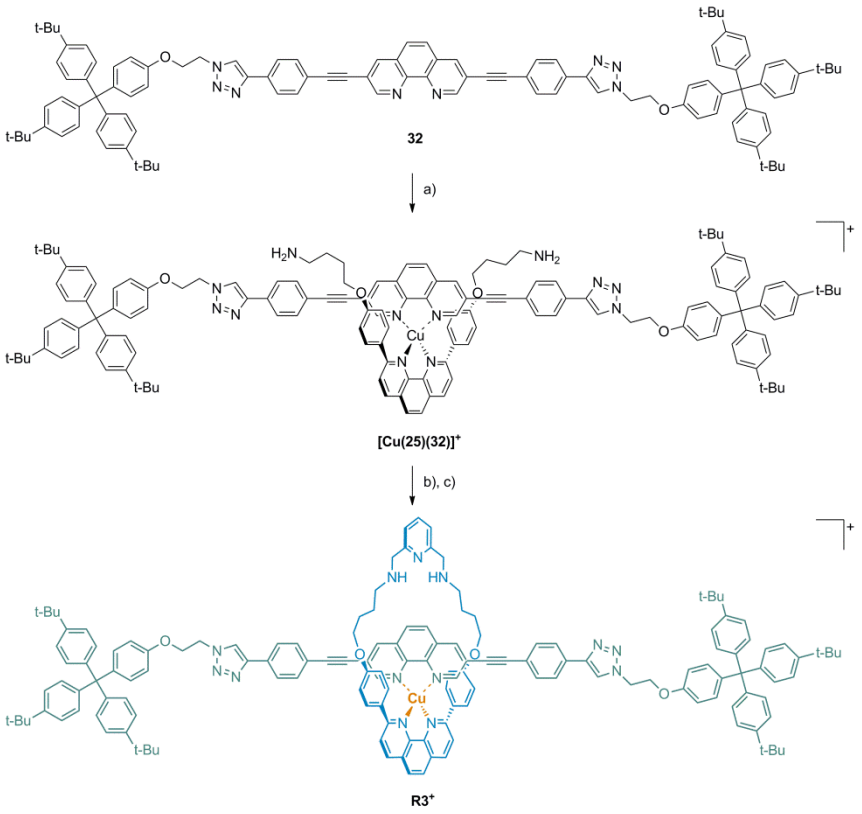

Scheme 1.9 Rotaxane **R3**$^{+}$ prepared in one pot by the clipping approach: **a) 22**, $[Cu(CH_3CN)_4](PF_6)$, CH_3CN, CH_2Cl_2; **b)** 2,6-pyridinedicarbaldehide, MeOH; **c)** $NaBH_4$ (22 %).

On the other hand, macrocycle **M4** was reacted with 3,8-bis((trimethylsilyl)ethynyl)-1,10-phenanthroline (**35**)[124] and $Cu(CH_3COO)_2{\cdot}H_2O$ to prepare pentacoordinated $[Cu(\mathbf{M4})(\mathbf{35})]^{2+}$ (**33**) complex. Complex **33** was used as a reference in the characterization of the oxidized of rotaxane **R3**$^{2+}$ (see later).

2.5.2 NMR characterization

The structures of rotaxanes **R2**(PF_6) and **R3**(PF_6) were confirmed by mass spectrometry and 1D and 2D (COSY, NOE) ^{1}H NMR spectroscopy. Comparative ^{1}H NMR spectra of both rotaxanes and axle **32** are shown in Figure 1.34. The appearance of the aromatic

signals below 6.0 ppm corresponding to the ring phenoxy moieties (Mm-protons) confirmed unambiguously the coordination of copper to the ring and the axis.[60] Furthermore, the down and up-field shifts experienced by protons P2 and P5 respectively, clearly reveals the participation of the axis phen in the complex. Two new aromatic signals corresponding to the pyridine chelate protons, Py3 and Py4, appeared in the ^{1}H NMR spectra of **R3**(PF_6). These signals present chemical shifts comparable to those of bare **M2** molecule, confirming the lack of participation of the pyridine diamine moiety in the coordination to the copper ion.

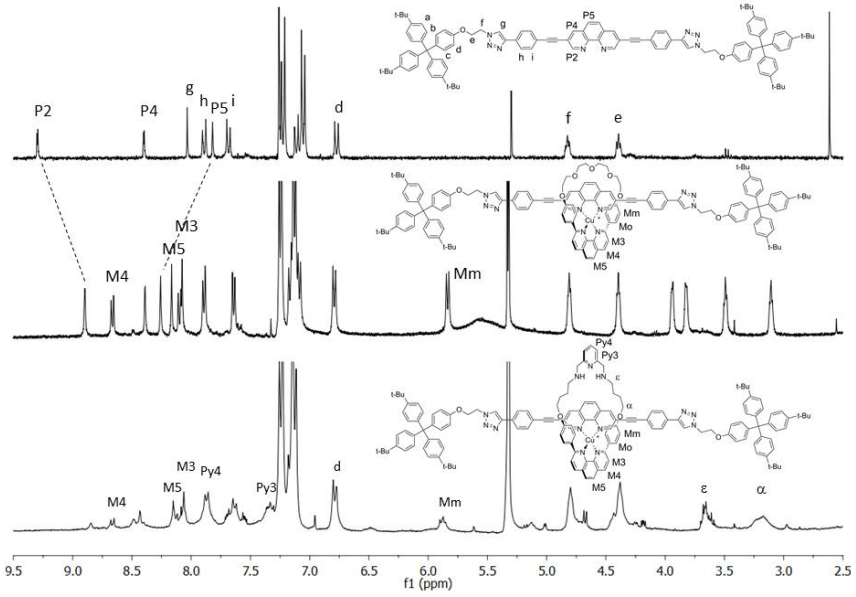

Figure 1.34 ^{1}H NMR spectra in CD_2Cl_2 of **32**, **R2**(PF_6) and **R3**(PF_6). Dashed lines denote the most representative proton displacements.

NOESY experiments, shown in Figure 1.35, were carried out in order to assign correctly two couples of protons: aliphatic protons e and f, and the phenylene protons h and i. The correlation between e and d protons supports the assignation of the 4.43 ppm triplet as the aliphatic proton closest to the stopper. On the other hand, correlation between the 7.92 doublet to g (8.11 ppm) identifies this proton as the closest to the triazole ring.

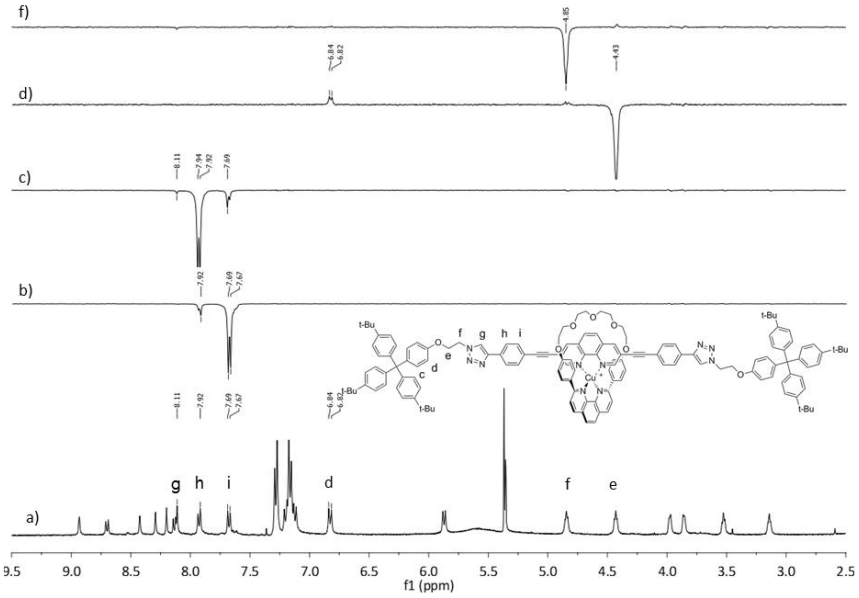

Figure 1.35 NOESY experiments in CD_2Cl_2 of **R2**(PF_6).

2.5.3 Chemical oxidation

In order to elucidate the coordination environment of the Cu(II) centre in the oxidized form of rotaxanes **R2**$^{+}$ and **R3**$^{+}$, the corresponding Cu(II) complexes **R2**$^{2+}$ and **R3**$^{2+}$ were prepared by the treatment of dichloromethane solutions of both rotaxanes with $NO(BF_4)$ and further precipitation with $K(PF_6)$. The identity of the target threaded Cu(II) species was evidenced by HRMS (ES) analysis of dichloromethane solutions in which peaks corresponding to **R2**$^{2+}$ (*m*/*z*: 1081.10) and **R3**$^{2+}$ (*m*/*z*: 1125.79) could be observed and further confirmed by comparative UV-vis, IR and EPR studies.

2.5.3.1 UV-vis characterization

Figure 1.36 A shows the UV-vis spectra of macrocycles **M2** and **M3**, axis **32** and rotaxanes **R2**(PF_6) and **R3**(PF_6). In all cases, the intense absorption bands (ε > 50000 $M^{-1}cm^{-1}$) below 400 nm are associated to π-π* LC transitions.[109]

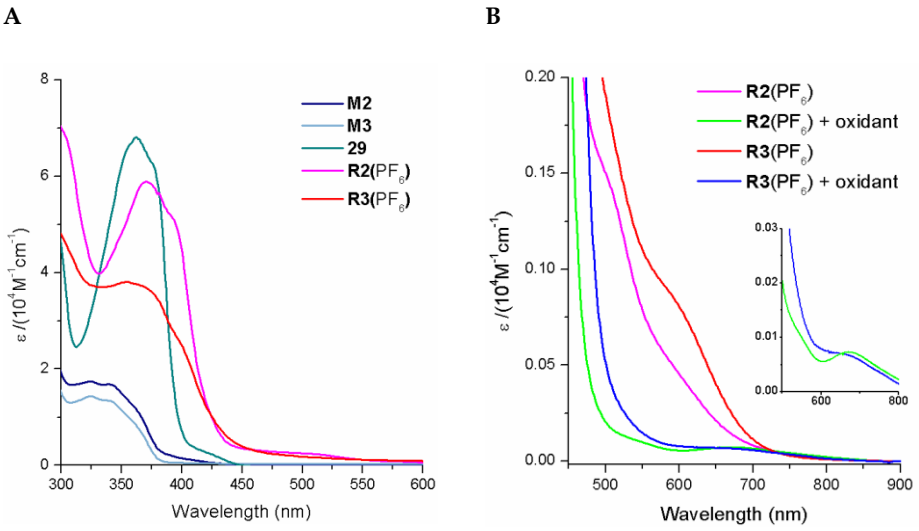

Figure 1.36 A) Absoption UV-Visible spectra of macrocycles **M2** and **M3**, molecular axis **32** and rotaxanes **R2(PF6)** and **R3(PF6)**. Data recorded in dichloromethane C =1·10^{-5} M. **B)** Absoption spectra of the reduced and oxidized forms of rotaxanes **R2**(PF6) and **R3**(PF6). Data recorded in dichloromethane 1·10^{-3} M (oxidant: NOBF4).

Upon coordination, the LC band experienced a red-shift of approximately 25 nm. Moreover, several new bands responsible of the characteristic red colour of tetrahedral [Cu(phen)2]$^{+}$ complexes appeared in the visible region.[110] These broader and less intense bands (ε < 2000 M^{-1}cm^{-1}) are assigned to MLCT transitions. Complexes of the [Cu(phen)2]$^{+}$ family typically present at least three bands in the visible region: band I (above 500 nm), band II (maximum around 430-480 nm, the most prominent), and band III (390-420 nm, often hidden by the onset of band II), whose intensities are related to the symmetry of the complex.[110] As can be seen in Figure 1.36 B, in **R2**$^{+}$ and **R3**$^{+}$ II and III bands are masked by the tail of the strong absorbing LC bands. However, band I is still visible above 500 nm. In addition, pronounced low-energy shoulders extending down to 650 nm are characteristic of copper complexes with dpp.[110] Spectral data are summarized in Table 1.1.

	λ_{max} (nm)	ε (M^{-1} cm^{-1})	λ_{max} (nm)	ε (M^{-1} cm^{-1})
M2	324	17400		
M3	324	14300		
32	363	68800		
R2(PF_6)	370	58900	505	1200
R3(PF_6)	355	38000	605	500

Table 1.1 Absorption spectroscopic data in dichloromethane for macrocycles **M2** and **M3**, axle **32** and Cu(I) complexes **R2**(PF_6) and **R3**(PF_6).

Chemical oxidation of $\mathbf{R2}^{+}$ and $\mathbf{R3}^{+}$ with $NOBF_4$ occurred with no appreciable change in the UV region, but with an instantaneous color change from red to pale yellow associated with the disappearance of the MLCT bands characteristic of Cu(I) complexes and the appearance of a very weak band centered around 670 nm and approx. ε = 70 $M^{-1}cm^{-1}$ (Figure 1.36 B). This band is similar to that reported for tetracoordinated $[Cu(dpp)_2]^{2+}$ [11] or pentacoordinated $[Cu(phen)(L)]^{2+}$ (L = macrocyclic triethylenamine derivate, λ_{max} = 670 nm, ε = 40 $M^{-1}cm^{-1}$)[125] and $[Cu(phen)(terpy)]^{2+}$ (λ_{max} =645 nm, ε = 8 $M^{-1}cm^{-1}$).[126] Hence, despite UV-Vis data supported the existence of coordinated Cu(II) metal ions, given the minimal expected differences in the UV-Vis spectrum of $\mathbf{R2}^{2+}$ and $\mathbf{R3}^{2+}$ species we were unable to discriminate if Cu(II) was tetra- o pentacoordinated in $\mathbf{R3}^{2+}$. Owing to that, we decided to characterize the rotaxane oxidized forms by EPR and Infra-red (IR) spectroscopy.

2.5.3.2 EPR studies

Subtle changes in the metal coordination geometry of paramagnetic metal centres are well reflected in the d-orbital splitting pattern of the EPR spectra. Figure 1.37 shows the powder and frozen acetonitrile solution EPR spectra of $\mathbf{R2}^{2+}$ and $\mathbf{R3}^{2+}$. Extracted g and parallel hyperfine coupling constants ($A_{\parallel}$) from solid samples of both rotaxanes are compiled in the right part of Figure 1.37. Analogous values were obtained from frozen solution samples.

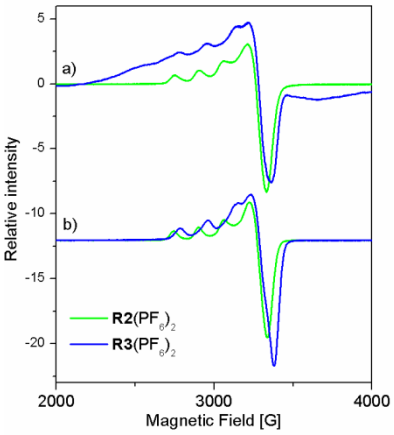

	$g_\perp$	$g_\parallel$	$A_\parallel$ (G)
R2$(PF_6)_2$	2.065	2.269	150
R3$(PF_6)_2$	2.063	2.225	172
$[Cu(dpp)_2](PF_6)_2$	2.073	2.276	
$[Cu(dpp)(terpy)](PF_6)_2$	2.045	2.233	166

Figure 1.37 X-band EPR spectra of $\mathbf{R2}^{2+}$ and $\mathbf{R3}^{2+}$ recorded at 4 K in frozen acetonitrile solution **(a)** and in powder **(b)** samples. Microwave frecuency was 9.4723 GHz. In the table are depicted g and $A_\parallel$ of rotaxanes $\mathbf{R2}^{2+}$ and $\mathbf{R3}^{2+}$**.** $[Cu(dpp)_2](PF_6)_2$ and $[Cu(dpp)(terpy)](PF_6)_2$ parameters have been added from comparision.[45]

For both complexes we obtained the characteristic pattern of axially elongated mononuclear Cu(II) complexes, with $g_\parallel > g_\perp > 2.04$ and a well-resolved hyperfine coupling of the parallel component with the $I = 3/2$ nuclear spin of the copper ion.[126, 127] However, on passing from $\mathbf{R2}^{2+}$ to $\mathbf{R3}^{2+}$ a decrease of $g_\parallel$ and an increase of $A_\parallel$ were observed. As predicted by ligand field theory and confirmed experimentally,[45] this is the expected evolution of $g_\parallel$ and $A_\parallel$ as the equatorial ligand field becomes stronger, or the axial field weaker.[127] This trend matches with the coordination of one additional imine nitrogen in $\mathbf{R3}^{2+}$ respect to $\mathbf{R2}^{2+}$. Moreover, the values of $A_\parallel$ and g obtained for $\mathbf{R2}^{2+}$ perfectly match these reported for tetracoordinated $[Cu(dpp)_2]^{2+}$,[45] whereas $\mathbf{R3}^{2+}$ parameters better fit with those reported for other pentacoordinated Cu(II) complexes in square pyramidal coordination geometries.[125, 127, 128] In addition, when compared to other Cu(II) terpyridine-containing complexes,[126] our higher $g_\parallel$ value supports the idea that the pyridine bis-amine chelate leads to a final square-pyramidal geometry less strained than in terpy-containing environments. Hence, EPR spectra fully confirmed that upon oxidation **M3** pirouettes around the central axis and copper changes his coordination geometry from tetrahedral to square pyramidal.

2.5.3.3 IR

Near-IR spectra of rotaxanes **R2**(PF_6) and **R3**(PF_6) showed the characteristic absorption bands of aromatic heterocyclic compounds. The oxidized forms of both rotaxanes presented a very similar IR spectrum with the exception of the 1800-1600 cm^{-1} region, zoomed in Figure 1.38, where a new intense band at 1720 cm^{-1} appeared in **R3**(PF_6)$_2$. Such band was also found in the IR spectra of reference Cu(II) complex **33** and has been previously observed in other Cu(II) pyridine bis-amine complexes.[129, 130] Such observation further supports the idea of the generation of a new pentacoordinated environment involving the pyridine bis-amine chelate upon oxidation of rotaxane **R3**$^+$.

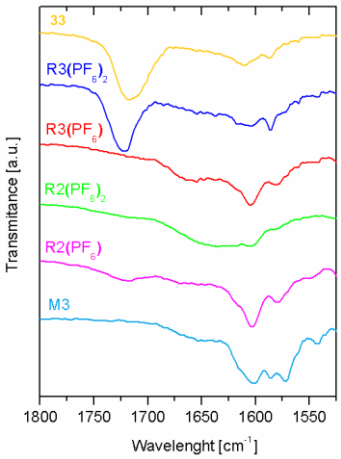

Figure 1.38 IR spectra between 1800 and 1525 cm^{-1} of macrocycle **M3**, reference compound **33,** rotaxanes **R2**$^+$ and **R3**$^+$ and their oxidized forms.

2.5.4 Electrochemical studies

The electrochemical behaviour of rotaxanes **R2**$^+$ and **R3**$^+$ was studied by cyclic voltammetry. As it has been shown, the existence of two different coordination sites in **M3** leads to the electrochemically-induced movement of the ring around the axis in **R3**$^+$, which is not possible in the case of **R2**$^+$. It has been observed that subtle structural factors, like electron-donating character of the ligands, the geometry or the steric congestion

around the metal, can have a very significant influence on the oxidation potential of the Cu(II/I) couple.[48, 49] In order to better evaluate these factors we measured the potentials of complexes [Cu(**M4**)(**35**)](PF$_6$)$_2$ (**33**) and [Cu(**35**)$_2$](PF$_6$) (**34**), depicted in Figure 1.39.

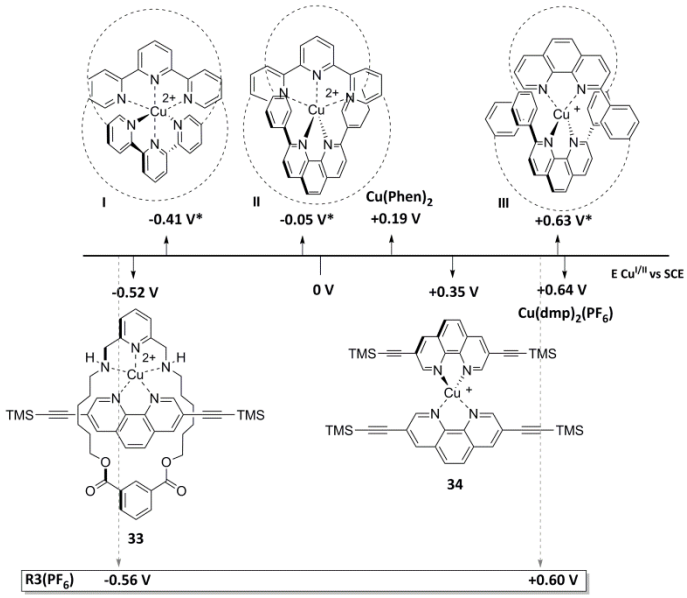

Figure 1.39 Cu(I/II) Redox potentials of **33** and **34,** and **R3**(PF$_6$). Potentials of reference complexes I-III and Cu(Phen)$_2$ in acetonitrile solution were extracted from the literature and are added for comparison.[41] Redox potentials were measured in TBA(PF$_6$) 0.1 M dichloromethane solution. A silver wire was used as pseudo-reference electrode. [Cu(dmp)$_2$](PF$_6$) was used as internal reference.

We can see from Figure 1.39 that the stabilization of the cuprous state in **34** is less pronounced than the one observed for tetracoordinated complex III. This responds to the reduced steric hindrance of the ethynyl groups, which facilitate the rearrangement into the more flat geometry adopted by Cu(II) bis(phen) complexes.[131] Nevertheless, the redox potential of **34** is still well above that of [Cu(phen)$_2$]$^+$ (0.19 V vs SCE). This fact has been attributed to the electro-donating character of trimethylsilylacethylene groups.[132] Regarding to the pentacoordinate environment of complexes **33** and II, the high negative potential observed (-0.52 V vs SCE), near to that reported for Cu(II) in comparable coordination environments,[117, 133] is indicative of a great stabilization of the cupric state provided by the pyridine bisamine chelate, which was previously suggested in the EPR

characterization of rotaxane **R3**$^{+}$. Such redox potential is even lower than the one reported for the hexacoordinate divalent complex I (-0.41 V vs SCE).[41] We ascribe this fact to the greater basicity of amines compared to pyridines and the enhanced flexibility of the chelate that minimizes the strain in the preferred square pyramidal geometry.[32]

Rotaxane **R2**$^{+}$ in dichloromethane solution presented a reversible peak at 0.64 V vs SCE associated with the Cu(II/I) redox couple in the tetrahedral environment. The proximity of this value to the one reported for III in acetonitrile[41] is noteworthy. This fact reveals that the mixed 2,9/3,8-disubstituted phen environment, although less congested, is equally stable to oxidation than Cu(dpp)$_2$ environments. By contrast, as shown in Figure 1.40, in the case of rotaxane **R3**$^{+}$**,** the peak at 0.60 V associated to the oxidation of Cu(I) in the tetracoordinated environment becomes irreversible and a new peak at -0.56 V is now apparent. By comparison with the data obtained for reference compound **33,** the cathodic wave at -0.56 V was assigned to the reduction of the Cu(II) ion in the pentacoordinate environment. Upon scan reversal, no anodic wave was observed at this potential and the anodic peak at 0.64 V was recovered without any appreciable loss of intensity, thus confirming the reversible rearrangement of the Cu(I) ion into the original tetracoordinate site.

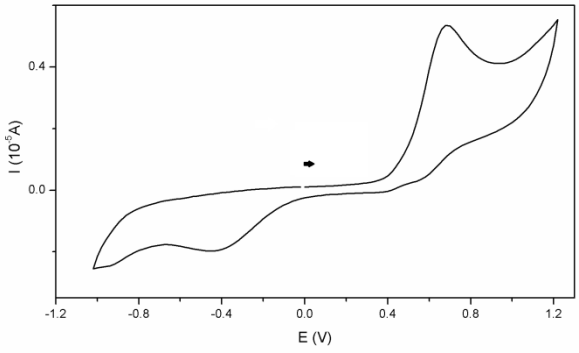

Figure 1.40 Cyclic voltammogram of rotaxane **R3**(PF_6) (C = 1·10^{-3} M) in TBA(PF_6) 0.1 M dichloromethane buffer solution. Scan rate: 0.1 Vs^{-1}.

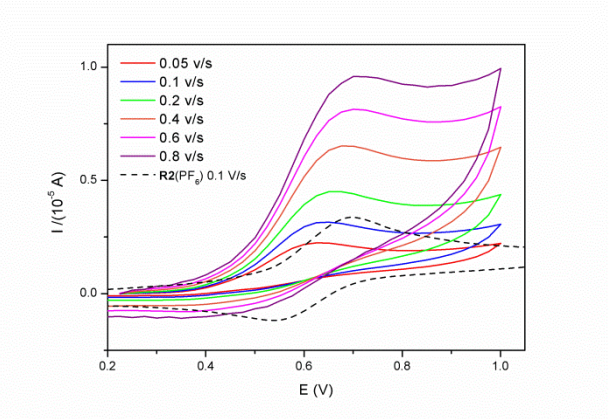

Figure 1.41 Cyclic voltammograms in TBA(PF_6) 0.1 M dichloromethane buffer solution of rotaxane **R3**(PF_6) at different scan rates (solid lines), and rotaxane **R2**(PF_6) at 0.1 Vs^{-1} (dashed line) $1{\cdot}10^{-3}$ M.

Upon repeated cycling in the -1.0/+1.2 V potential window, we did not observe any change in the shape of the voltammograms of **R3**$^+$, confirming the robustness of the gliding process. The cyclic voltammograms recorded between 50 and 1000 mV/s (the maximum scan rate accessible in our experimental setup) did not show the appearance of reversible waves in either oxidation or reduction processes. The evolution of the oxidation wave potential with the scan rate in the +0.2/ +1.0 V range is illustrated in Figure 1.41. As predicted by Nicholson and Shain,[43] the peak described an anodic shift with increasing the scan rate. By the application of equation (i) (see section 1.2) a value for the rate constant of the rearrangement of tetrahedrally coordinated Cu(II) to a pentacoordinated environment can be estimated. An approximated rate constant (k) of 620 s^{-1} was extracted from the linear fitting of the oxidation wave potential evolution (Ep) with the scan rate (v). The half-wave potential ($E_{1/2}$) of the reversible process was considered equal to the half-wave of rotaxane **R2**(PF_6) and non-compensated resistivity effects at each scan rate were extracted from the cyclic voltammogram of **R2**(PF_6) and corrected for the calculation of k in **R3**(PF_6).

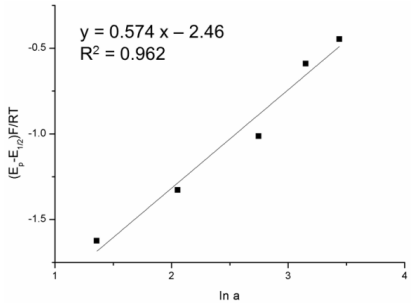

Figure 1.42 Linear fitting of the potential shift. The rate constant value was extracted from the y-interception.

The half-lifetime ($t_{1/2}$ = (ln2)/*k*) of the unstable tetrahedral Cu(II) species is 1.1 ms. Taking into account that this rearrangement constitutes the limiting step, these data prove that rotaxane **R3**$^{+}$ operates at the millisecond timescale even in a non-coordinating solvent as dichloromethane. The kinetic rates for the pirouetting processes are higher than those of the fastest pirouetting rotaxanes reported to date.[46]

2.5.5 Conclusions

In this section we have described the synthesis and dynamic properties of fast-moving pirouetting copper rotaxane **R3**(PF_6). This rotaxane is based on the use of a 3,8-bis(phenylethynyl)phenanthroline axle and a macrocyclic component with two different recognition sites: a dpp moiety and a pyridine bis-amine chelate. The use of the pyridine bis-amine instead of the classical terpyridine terdentate chelate offers a greater stabilization of the cupric state derived from its higher flexibility. Regarding to the tetrahedral coordination site, the mixed 2,9-/ 3,8-substituted phen environment has afforded a less congested coordination sphere around the copper ion with no lessening its redox stability. Thereby, the electrochemical potential of the reduced state is maintained while that of the oxidized state is increased, affording a bistable switchable rotaxane whose electronic states are separated by more than 1 V. Moreover, the high rate estimated for the limiting step of the switching processes, k = 620 s^{-1}, makes **R3**$^+$ the fastest copper rotaxane reported to date.

This rate is far above that presented by pirouetting rotaxane **B**$^+$ (see Figure 1.11) described by Poleschak *et al.* (5 s^{-1}).[46] Both rotaxanes present similar 2,9-/ 3,8-sustituted tetracoordinated environments. The main difference is that in **B**$^+$ the coordinating unit of the axle is a bipy, which has proven to be more labile than phen. Thus far, the reason for the high lability of **R3**$^+$ may reside, at least in some extend, on the novel pentacoordinated environment. Steric considerations avoids the possibility of a concerted mechanism in which the pyridine bis-amine chelate participates in the decoordination of the unstable Cu(II) environment. Nevertheless, according to Marcus theory, the kinetic rate (k) of a chemical reaction is related to its thermodynamic free energy difference (ΔG).[134] In rotaxane **B**$^+$, tetra and pentacoordinated electrochemical potentials are separated by 0.49 V, whereas in **R3**$^+$, the separation is 1.1 V. Thus far, we ascribe the fast kinetics found in **R3**$^+$ to the very favourable thermodymamics of the reorganizaton process.

General conclusions

The marked redox bistability of copper-interlocked systems make them excellent candidates for the construction of functional molecular devices.

One of the targets of this work was to simplify the chemical procedures employed in the preparation of this kind of complicated molecules. For the stoppering, which is one of the most troublesome stages in the synthesis of copper rotaxanes, we resolved to employ CuAAC in first instance. Despite the use of a coordinatively saturated copper catalyst, the obtained yields were still low, particularly in the case of bistable rotaxanes **R1**$^{+}$ (11 %) and **R3**$^{+}$ (0 %). This 11% yield is comparable to that obtained by other groups in the capping of bistable copper rotaxanes.[72] Thus far, although in the case of non-bistable rotaxanes CuAAC constitutes a suitable alternative to Williamsons reaction affording stoppering yields above 50 %,[38, 65-67, 69, 70, 107] it fails in the case of rotaxanes bearing free chelating sites, for which the yields obtained are below 10 %.[72] Aware of this problem, the group of Prof. Sauvage has recently proposed a strategy to enhance the efficiency of CuAAC stoppering reactions that consists in the use of cleavable coordinating rings to block the target free coordinating units.[135] However, in view of the promising results obtained by the clipping methodology employed in the synthesis of **R3**(PF_6), we considered that the use of imine condensation followed by reduction to amines, is a much more feasible alternative for the preparation of bistable copper rotaxanes. Indeed, although the yield of the last stoppering step is modest (22 % in **R3**(PF_6)), it is still above that obtained by click chemistry. Furthermore, it implies a great simplification of the synthetic route since it starts from very accessible derivatives and affords a very advantageous tridentate coordinating unit, the pyridine bis-amine ligand.

The second target of this chapter consisted in the optimization of the coordinating units in order to enhance the kinetic rates of the two dynamic systems, shuttling and pirouetting rotaxanes. The design of less congested tetrahedral sites comprising a 2,9-/ 3,8-sustituted phen ligands accelerated the typically limiting reorganization process of

the unstable Cu(II) tetracoordinated species to the second scale. Nevertheless, the kinetic rates obtained for **R1**$^{+}$ were still below that afforded by dpbiiq-containing rotaxanes. The high lability of these chelate resulted from the low shielding around the metal ion along with its high flexibility. Apart from that, the electrochemical response of this rotaxane evidenced that the reduction of the space between the coordinating sites can lead to an enhancement of the kinetics of shuttling copper rotaxanes. Thereby, although the electrochemical behavior of rotaxane **R1**$^{+}$, did not exceed the rates of the previously reported rotaxanes, we considered that this system has contributed to a better understanding of the structural factors affecting the dynamics of copper-based molecular shuttles.

In the case of **R3**$^{+}$, the chemical structure of the coordinating environments afforded a great stabilization of both redox oxidation states. This fact was translated into a large redox state separation. Remarkably, this feature was accompanied by a very high lability that features this pirouetting copper rotaxane as the fastest reported to date. All in all, the wide redox hysteresis exhibited by **R3**$^{+}$ as well as its fast electrochemical response, constituted very promising features for the further applications of this system as a molecular switch. Actually, early attempts of fabricating switching electronic molecular devices based on this molecular system will be presented in chapter 3.

Experimental

Spectroscopic measurements

^{1}H NMR spectra were acquired on a Bruker AVANCE DRX 300 spectrometer. The spectra were referred to residual proton-solvent references.[136]

Electrospray (ES) **mass spectra** were obtained with a Waters Micromass ZQ spectrometer in the positive ion mode. High-resolution (ES) mass spectra were recorded on a MICROMASS QUATTRO TM (Waters) spectrometer in the positive ion mode. High-resolution MALDI mass spectra were recorded in a 5800 MALDI TOFTOF (ABSciex) in positive reflector mode.

UV-Vis absorption spectra were recorded on a Shimadzu UV-2501PC spectrophotometer using quartz 1 cm path length cuvettes.

First derivative **EPR** spectra were recorded at 4 K in a Bruker ELEXYS E580 equipped with continuous-flow cryostats for liquid helium. Complexes solutions of approximate $1{\cdot}10^{-3}$ M were prepared in dry acetonitrile. Reported *g* values and hyperfine coupling constants (A), were obtained by the simulation of the experimental spectra with WINEPR SimFonia program Version 1.25.

IR spectra were recorded on a Nicolet 5700 FTIR spectrophotometer as pressed KBr pellets.

Elemental analyses of carbon, nitrogen, sulphur and hydrogen contents were determined by using an EA 1110 CHNS-O Elemental Analyzer from CE Instruments.

Electrochemical measurements

Electrochemical measurements were performed in a nitrogen glove box using an Autolab PGSTAT 128N potentiostat and a three-electrode electrochemical cell consisting

in a glassy carbon working electrode, a platinum wire counter electrode and a silver wire quasi-reference electrode. Ferrocene (0.45 V vs SCE in acetonitrile)[137] or [Cu(dmp)$_2$](PF$_6$) (0.64 V vs SCE in dichloromethane)[33] were used as internal references. Buffered supporting electrolytes were prepared from anhydrous dichloromethane (Sigma-Aldrich) and TBA(PF$_6$) (Sigma-Aldrich).

Non-compensated resistivity effects were corrected in the calculation of k from the single oxidation wave at 0.60 V vs SCE in the cyclic voltammetry of **R3**(PF$_6$). The value of the non-compensated resistance for a single wave was estimated as (ΔE – 0.059)/2 from the reversible Cu(I/II) couple in **R2**(PF$_6$).

Materials and general procedures

All chemicals used were purchased from commercial sources and used without further purification, except for NBS, which was recrystallized from water. Anhydrous dichloromethane, acetonitrile and tetrahydrofuran solvents were freshly distilled under argon over the appropriate drying agent (calcium chloride, calcium hydroxide and sodium respectively). Column chromatographies were carried out on silica or alumina gel (60 Å, 230-400 mesh).

A lamp equipped with two incandescent bulbs (General Electric, 220 V, 100 W) was used in benzilic bromination reactions.

Macrocycle *M1*

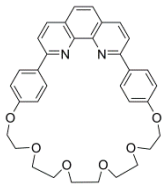

M1 was prepared according to a described procedure.[93]

NMR (300 MHz, $CDCl_3$) δ 8.41 (d, *J* = 8.9 Hz, 4H), 8.28 (d, *J* = 8.4 Hz, 2H), 8.07 (d, *J* = 8.4 Hz, 2H), 7.76 (s, 2H), 7.19 (d, *J* = 8.9 Hz, 2H), 4.35 (t, *J* = 5.3 Hz, 4H), 3.86 (t, *J* = 5.3 Hz, 4H), 3.78 – 3.67 (m, 12 H).

MS (ES): *m*/*z* (%): calcd for $[C_{34}H_{34}N_2O_6H]^+$: 567.2; found: 567.6 (100) $[MH]^+$.

Tris(p-tert-butylphenyl)-(4-hydroxyphenyl)methane ***3***

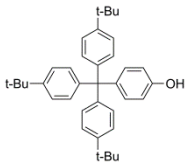

3 was prepared according to a described procedure.[94]

NMR (300 MHz, $CDCl_3$) δ 7.23 (d, *J* = 8.6 Hz, 6H), 7.06 (dd, *J* = 8.7, 8.6 Hz, 8H), 6.69 (d, *J* = 8.7 Hz, 2H), 1.30 (s, 27H).

5-Methyl-2-tributylstannylpyridine ***6***

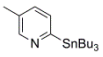

n-BuLi 2.5 M (29 mL, 72 mmol) was added over a degassed solution of 2-aminoethanol (4 mL, 36 mmol) in anhydrous hexane (30 ml) at 0 ^{0}C. After 30 min of stirring, an anhydrous hexane solution of 3-picoline (1.2 mL, 12 mmol) was added dropwise. After one hour, Bu_3SnCl (9.8 mL, 36 mmol) was added dropwise and the solution was then allowed to warm to room temperature. Finally, methanol (10 mL) was added and the reaction mixture was concentrated under reduced pressure affording the product as yellow oil (4.5 g, 97%) that was used in the following stage without further purification.

^{1}H NMR (300 MHz, $CDCl_3$): δ 8.58 (s, 1H), 7.32-7.30 (m, 2H), 2.28 (s, 3H), 1.61-1.49 (m, 6H), 1.32 (sext, *J*= 7.3 Hz, 6H), 1.10 (t, *J*= 8.1 Hz, 6H), 0.87 (t, *J*= 7.3 Hz, 9H).

6'-Bromo-5-methyl-2,2'-bipyridine **7**

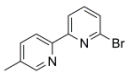

A mixture of 5-methyl-2-tributylstannylpyridine (**7**) (4.0 g, 10.5 mmol), 2,5-dibromopyridine (3.8 g, 15.7 mmol) and $Pd(PPh_3)_4$ (0.54 g, 0.47 mmol) and distilled toluene (100 mL) was degassed and refluxed under argon at 120 ^{0}C for 2 days. The insoluble precipitate formed was separated from the warm mixture by filtration. Evaporation of the solvent afforded a solid that was dissolved in 2.5 M HCl (100 mL). The aqueous layer was extracted with dichloromethane (4x 25 mL) and the organic layers extracted with HCl 2.5 M (4 x 30 mL). The combined aqueous phases were basified with NH_3 conc. at 0 ^{0}C until the apparition of a white precipitate. The solid was filtered and, if necessary, purified by column chromatography (Silica gel, CH_2Cl_2/MeOH) to yield the pure product as a white solid (1.70 g, 65%).

^{1}H NMR (300 MHz, $CDCl_3$): δ 8.48 (d, *J*= 2.0 Hz, 1H), 8.33 (dd, *J*= 7.8 and 0.8 Hz, 1H), 8.29 (d, *J*= 8.1 Hz, 1H), 7.64 (t, *J*= 7.8 Hz, 1H), 7.61 (dd, *J*= 8.1 and 2.0 Hz, 1H), 7.45 (dd, *J*= 7.8 and 0.8 Hz, 1H), 2.93 (s, 3H).

MS (ES): *m*/*z* (%): calcd for $[C_{11}H_9BrN_2H]^+$: 249.0; found: 249.0 (100) $[MH]^+$.

5-Bromo-2-tributylstannylpyridine **8**

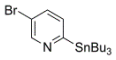

n-BuLi was added dropwise (2.5 M in hexane, 7.9 mL, 19.8 mmol) over a degassed solution of 2,5-dibromopyridine (4.0 g, 16.5 mmol) in anhydrous toluene (200 mL) at -78 ^{0}C. After 2h of stirring at -78 ^{0}C, Bu_3SnCl (5.4 mL, 19.0 mmol) was added dropwise and the solution was allowed to warm to room temperature overnight. After addition of water (150 ml) at 0 ^{0}C, the mixture was divided in two phases which were separated: the aqueous layer was extracted with dichloromethane (4 x 40 mL) and the combined organic fractions were dried over Na_2SO_4 and concentrated under reduced pressure. The

resulting oil was purified by column chromatography over alumina gel using hexane/ ether as eluent to afford the pure product as colourless oil (6.3 g, 85%).

^{1}H NMR (300 MHz, $CDCl_3$): δ 8.81 (d, *J*= 2.4 Hz, 1H), 7.63 (dd, *J*= 7.9 and 2.4 Hz, 1H), 7.29 (d, *J*= 7.9 Hz, 1H), 1.61-1.49 (m, 6H), 1.32 (sext, *J*= 7.25, 6H), 1.11 (t, *J*=8.1 Hz, 6H), 0.88 (t, *J* = 7.3 Hz, 9H).

5-Bromo-5''-methyl-2,2':6',2''-terpyridine **9**

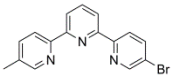

A mixture of 6'-bromo-5-methyl-2,2'-bipirydine (**7**) (1.87 g, 7.5 mmol), 5-bromo-2-tributylstannylpyridine (**8**) (3.52 g, 7.88 mmol), $Pd(PPh_3)_4$ (0.52 g, 0.45 mmol) and distilled toluene (200 mL) was degassed and refluxed under argon at 120 ^{0}C for 1 day. The insoluble precipitate formed was separated from the warm mixture by filtration. The filtrate was then concentrated under reduced pressure and the resulting solid was redissolved in 2.5 M HCl (100 mL). The aqueous layer was extracted with dichloromethane (4 x 25 mL) and the organic layers extracted with 2.5 M HCl (4 x 30 mL). The aqueous phase was basified with NH_3 conc. at 0 ^{0}C until the apparition of a white precipitate. The solid was filtered and, if necessary, purified by column chromatography (silica gel, CH_2Cl_2/MeOH) to yield **9** as a white solid (1.59 g, 65%).

^{1}H NMR (300 MHz, $CDCl_3$): δ 8.73 (d, *J*= 2.3 Hz, 1H), 8.54 (s, 1H), 8.53 (d, *J*= 2.3 Hz, 1H), 8.47 (d, *J*= 8.1 Hz, 1H), 8.43 (dd, *J*= 7.8 and 0.9 Hz, 1H), 8.39 (dd, *J*= 7.8 and 0.9 Hz, 1H), 7.96 (dd, *J*= 8.5 and 2.3 Hz, 1H), 7.94 (t, *J*= 7.8 Hz, 1H), 7.66 (dd, *J*= 8.1 and 2.3 Hz, 1H), 2.42 (s, 3H).

MS (ES): *m*/*z* (%): calcd for $[C_{16}H_{12}BrN_3H]^+$: 326.0; found: 326.2 (100) $[MH]^+$.

5-Bromo-5''-bromomethyl-2,2':6',2''-terpyridine **4**

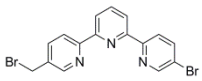

A mixture of 5-bromo-5''-methyl-2,2':6',2''-terpyridine (**9**) (0.16 g, 0.50 mmol), NBS (0.11 g, 0.60 mmol), dichloromethane (35 mL) and water (35 ml) was irradiated at reflux for 1 day using 100W light bulbs. Then, the solution was basified with Na_2CO_3 0.05 M and the aqueous phase was extracted with dichloromethane (4x20 mL). The combined organic phases were washed with aqueous $Na_2S_2O_3$ 15% (2x30 mL) and water (60 mL). After drying over Na_2SO_4, the solvent was eliminated under rotary evaporation to yield **4** as a brown solid (0.20 g, 77 %).

^{1}H NMR (300 MHz, $CDCl_3$): δ 8.74 (d, *J*= 2.2 Hz, 1H), 8.70 (d, *J*= 2.2 Hz, 1H), 8.57 (d, *J*= 8.2 Hz, 1H), 8.51 (d, *J*= 8.5 Hz, 1H), 8.46 (d, *J*= 7.9 Hz, 1H), 8.43 (d, *J*= 7.9 Hz, 1H), 7.98 (dd, *J*= 8.5 and 2.2 Hz, 1H), 7.96 (t, *J*= 7.9 Hz, 1H), 7.89 (dd, *J*= 8.2 and 2.2 Hz, 1H), 4.56 (s, 2H).

HRMS (MALDI): *m*/*z* (%) calcd. for $[C_{16}H_{12}Br_2N_3]^+$: 405.938; found: 405.852 (35) $[MH]^+$.

MOM-protected (p-hydroxyphenyl) boronic acid pinacol ester[138] **10**

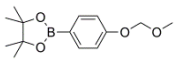

Chloromethyl methyl ether (0.30 g, 3.6 mmol) was added dropwise over a THF solution (5 mL) containing 4-hydroxyphenyl boronic acid pinacol ester (0.50 g, 2.3 mmol) and sodium hydride (60% in mineral oil, 0.12 g, 2.9 mmol) at 0 ^{0}C. The mixture was stirred at room temperature for 2 h. After this time, addition of water (40 mL) afforded two phases. The aqueous phase was separated and extracted with dichloromethane (4 x 10 mL). The combined organic layers were dried over Na_2SO_4 and the solvent was eliminated under reduced pressure to yield the pure product as brown oil (0.57 g, 94%).

^{1}H NMR (300 MHz, $CDCl_3$): δ 7.75 (d, *J*= 8.4 Hz, 2H), 7.02 (d, *J*= 8.4, 2H), 5.20 (s, 2H), 3.45 (s, 3H), 1.33 (s, 12H).

3,8-Dibromo-1,10-phenanthroline ***11***

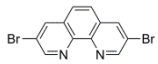

Pyridine (7.9 g, 100 mmol), S_2Cl_2 (13.5 g, 100 mmol), 1,10-phenanthroline (5.5 g, 30.4 mmol) and n-BuCl (220 mL) were placed under argon in a two-necked round bottom flask equipped with a $Na_2S_2O_3$/NaOH gas trap, and heated at 90 ^{0}C overnight. The mixture was then cooled to room temperature and the supernatant solvent separated. The remaining solid was dissolved in chloroform (200 mL) and NaOH 10% (200 mL) was added. The organic phase was separated and the aqueous phase was extracted with chloroform (4 x 50 mL). The combined organic phases were dried over Na_2SO_4 and concentrated under reduced pressure. The resulting solid was column cromatographed through silica gel using CH_2Cl_2/MeOH as eluent affording **11** as a white solid (5.4 g, 50%).

^{1}H NMR (300 MHz, $CDCl_3$): δ 9.19 (d, *J*= 2.3Hz, 2H), 8.40 (d, *J*= 2.3Hz, 2H), 7.75 (s, 2H)**.**

MS (ES): *m*/*z* (%): calcd for $[C_{12}H_6Br_2N_2H]^+$: 338.9; found: 339.0 (100) $[MH]^+$.

MOM-Protected 3-bromo-8-(p-hidroxyphenyl)-1,10-phenanthroline ***5***

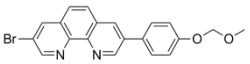

A toluene (120 mL) solution containing 3,8-dibromo-1,10-phenanthroline (**11**) (2.10 g, 6.2 mmol), MOM-protected boronic ester derivative **10** (1.90 g, 7.4 mmol) and $Pd(PPh_3)_4$ (0.40 g, 0.35 mmol) was added to a degassed aqueous solution of Na_2CO_3 2 M (36 mL) and refluxed under argon at 120 ^{0}C for 3 days. After the addition of water (100 mL), the organic layer was separated and the aqueous layer extracted with dichloromethane (4 x 40 mL). The combined organic phases were washed once again with water, dried over Na_2SO_4 and concentrated under reduced pressure. The crude product was chromatographed in a silica column using CH_2Cl_2/MeOH as eluent affording the desired monosubstituted product **5** as a yellow solid (0.82 g, 33%) followed by the disubstituted derivative as a secondary product.

^{1}H NMR (300 MHz, $CDCl_3$): δ 9.40 (d, *J*= 2.2 Hz, 1H), 9.19 (d, *J*= 2.2 Hz, 1H), 8.42 (d, *J*=2.2 Hz, 1H), 8.35 (d, *J*= 2.2 Hz, 1H), 7.89 (d, *J*= 8.6 Hz, 1H), 7.74 (d, *J*= 8.6 Hz, 1H), 7.72 (d, *J*= 8.5 Hz, 2H), 7.23 (d, *J*= 8.5 Hz, 2H), 5.27 (s, 2H), 3.53 (s, 3H).

MS (ES): *m*/*z* (%) calcd for $[C_{20}H_{15}BrN_2O_2H]^+$: 395.0; found: 395.3(100) $[MH]^+$.

Elemental Analysis calcd for $C_{20}H_{15}BrN_2O_2$: C, 60.78; H, 3.83; N, 7.09; found: C, 61.20; H, 4.14; N, 6.74.

MOM-protected 3,8-bis(p-methoxyphenyl)-1,10-phenanthroline (disubstituted derivative)

^{1}H NMR (300 MHz, $CDCl_3$): δ 9.40 (d, *J*= 2.3 Hz, 2H), 8.35 (d, *J*= 2.3 Hz, 2H), 7.87 (s, 2H), 7.73 (d, *J*= 8.7 Hz, 4H), 7.23 (d, *J*= 8.7 Hz, 4H), 5.27 (s, 4H), 3.53 (s, *6*H).

5-Neopentylglycolatoboryl-5''-methyl-2,2':6',2''-terpyridine **12**

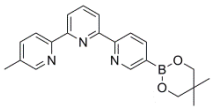

A degassed mixture of 5-bromo-5''-methyl-2,2':6',2''-terpyridine (**9**) (0.98 g, 3.0 mmol), bis(neopentyl glycolato)diboron (0.77 g, 3.3 mmol) and [$PdCl_2$(dppf)ferrocene] (0.073 g, 0.09 mmol) in anhydrous DMSO (15 mL) was stirred under argon at 80 ^{0}C for 5h. The insoluble precipitate formed was removed by filtration. Then dichloromethane (100 mL) was added to the filtrate and the organic solution was washed with water (4 x 25 mL), dried over Na_2SO_4 and concentrated under reduced pressure. The resulting red solid was recrystallized from EtOH/CH_2Cl_2 to yield **12** as a white solid (0.7 g, 65%).

^{1}H NMR (300 MHz, $CDCl_3$): δ 8.98 (s, 1H), 8.55-8.40 (m, 4H), 8.37 (d, *J*= 7.8 Hz, 1H), 8.18 (dd, *J*= 7.9 and 1.4 Hz, 1H), 7.89 (d, *J*= 7.8 Hz, 1H), 7.63 (dd, *J*= 8.1 and 1.9 Hz, 1H), 3.75 (s, 4H), 2.35 (s, 3H), 0.99 (s, 6H).

Phen-terpy conjugate ***13***

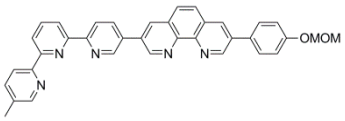

A mixture of phenanthroline **5** (10 mg, 0.25 mmol), 5-neopentylglycolatoboril-5''-methyl-2,2':6',2''-terpyridine (**12)** (90 mg, 0.25 mmol), $Pd(PPh_3)_4$ (23.1 mg, 0.20 mmol), K_2CO_3 (350 mg, 2.5 mmol), DMF (10 mL) and water (0.5 mL) was degassed and heated under argon at 80 ^{0}C for 18 h. The resulting solid was filtered and washed with a 8:2 DMF/CH_2Cl_2 mixture (10 mL), water (25 mL), NH_4Cl 1 M (10 mL), NH_3 conc. (10 mL) and water (25 mL). The solid was dried under vacuum to afford the pure product (white solid, 0.27 g, 51%).

^{1}H NMR (300 MHz, $CDCl_3$): δ 9.50 (d, *J*= 2.3 Hz, 1H), 9.44 (d, *J*= 2.3 Hz, 1H), 9.12 (d, *J*= 2.0 Hz, 1H), 8.82 (d, *J*= 8.3 Hz, 1H), 8.56 (d, *J*=2.3 Hz, 1H), 8.55 (d, *J*= 8.4 Hz, 1H), 8.52-8.47 (m, 2H), 8.45 (d, *J*= 2.3 Hz, 1H), 8.37 (d, *J*= 2.3 Hz, 1H), 8.26 (dd, *J*= 8.3 and 2.4 Hz, 1H), 7.99 (t, *J*= 7.8 Hz, 1H), 7.92 (s, 2H), 7.74 (d, *J*= 8.7 Hz, 2H), 7.70 (s, 1H), 7.10 (d, *J*= 8.7 Hz, 2H), 5.27 (s, 2H), 3.53 (s, 3H), 2.44 (s, 3H).

MS (ES): *m*/*z* (%): calcd for $[C_{36}H_{27}N_5O_2H]^+$: 562.2; found: 562.4 (10) $[MH]^+$.

Stoppered bromo terpyridine derivative ***14***

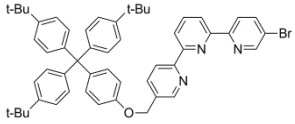

A mixture of tris(p-*tert*-butylphenyl)-(4-hydroxyphenyl)methane (**3**) (0.76 g, 1.5 mmol), 5-bromo-5''-bromomethyl-2,2':6',2''-terpyridine (**4**) (0.59 g, 1.45 mmol), anhydrous K_2CO_3 (2.1 g, 15.0 mmol) and anhydrous DMF (40 mL) was heated at 80 ^{0}C for 20 h. The warm mixture was filtered to remove the excess of K_2CO_3 and DMF was evaporated under reduced pressure to afford a solid which was redissolved in dichloromethane (60 mL).

The organic layer was washed with water (4x15 mL) and dried over Na_2SO_4. Evaporation of the solvent yielded a solid which was chromatographed over silica gel using CH_2Cl_2/MeOH as eluent (white solid, 0.98 g, 55%).

^{1}H NMR (300 MHz, $CDCl_3$): δ 8.81 (d, *J*= 1.9 Hz, 1H), 8.75 (d, *J*= 1.9 Hz, 1H), 8.62 (d, *J*= 8.2 Hz, 1H), 8.57 (d, *J*= 8.4 Hz, 1H), 8.51 (d, *J*= 7.5 Hz, 1H), 8.45 (d, *J*= 7.5 Hz, 1H), 8.03-7.95 (m, 3H), 7.24 (d, *J*= 8.6 Hz, 6H), 7.13 (d, *J*= 8.9 Hz, 2H), 7.08 (d, *J*= 8.6 Hz, 6H), 6.87 (d, *J*= 8.9 Hz, 2H), 5.15 (s, 2H), 1.30 (s, 27H).

HRMS (MALDI): *m*/*z* (%) calcd. for $[C_{35}H_{55}BrN_3O]^+$: 828.353; found: 828.364 (65) $[MH]^+$.

Stoppered boryl terpyridine derivative **15**

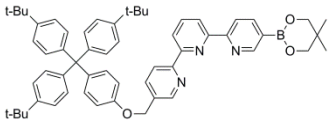

A degassed mixture of **14** (0.41 g, 0.49 mmol), bis(neopentyl glycolato)diboron (0.12 g, 0.55 mmol), [$PdCl_2$(dppf)ferrocene] (12 mg, 0.015 mmol) and anhydrous DMSO (15 mL) was stirred under argon at 80 ^{0}C during 5 h. The insoluble precipitate was removed by filtration. Dichloromethane (100 mL) was added and the organic layers were washed with H_2O (4x25 mL), dried over Na_2SO_4 and concentrated under reduced pressure. The resulting red solid was recrystallized from a CH_2Cl_2/EtOH mixture to yield **15** as a white solid (0.21 g, 49%).

^{1}H NMR (300 MHz, $CDCl_3$): δ 9.03 (d, *J*=1.7 Hz, 1H), 8.74 (d, *J*=1.7 Hz, 1H), 8.66 (d, *J*= 8.2 Hz, 1H), 8.57 (dd, *J*= 7.9 and 0.8 Hz, 1H), 8.50 (dd, *J*= 7.9 and 0.8 Hz, 1H), 8.45 (dd, *J*=7.9 and 0.8 Hz, 1H), 8.21 (dd, *J*=7.9 and 1.7 Hz, 1H), 7.98-7.94 (m, 2H), 7.24 (d, *J*= 8.7 Hz, 6H), 7.11 (d, *J*= 9.0 Hz, 2H), 7.08 (d, *J*= 8.7 Hz, 6H), 6.87 (d, *J*= 9.0 Hz, 2H), 5.14 (s, 2H), 3.82 (s, 4H), 1.30 (s, 27H); 1.06 (s, 6H).

HRMS (MALDI): *m*/*z* (%) calcd. for $[C_{58}H_{65}BN_3O_3]^+$: 862.512; found: 862.519 (100) $[MH]^+$.

MOM-protected thread ***16***

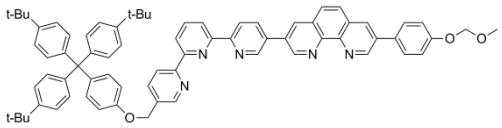

A degassed mixture of MOM-protected phenanthroline **5** (65 mg, 0.17 mmol), terpyridine derivative **15** (15 mg, 0.17 mmol), $Pd(PPh_3)_4$ (15 mg, 0.013 mmol), K_2CO_3 (230 mg, 1.6 mmol), water (0.4 mL) and DMF (8 mL) was heated under argon at 80 ^{0}C for 20 h. After evaporation of the solvents, 30 mL of water were added and the mixture was sonicated for at least 2 hours. The suspended solid was filtered, washed with water (20 mL), dried and further purified by silica gel column chromatography using CH_2Cl_2/ MeOH as eluent to obtain the pure product as a pale yellow solid (0.049 g, 28%).

^{1}H NMR (300 MHz, $CDCl_3$): δ 9.50 (d *J*= 2.1 Hz, 1H), 9.44 (d, *J*= 2.1 Hz, 1H), 9.13 (d, *J*= 1.7 Hz, 1H), 8.81 (d, *J*= 8.3 Hz, 1H), 8.78 (d, *J* = 1.7 Hz, 1H), 8.69 (d, *J* = 8.1 Hz, 1H), 8.57-8.45 (m, 3H), 8.37 (d, *J*= 2.1 Hz, 1H), 8.26 (dd, *J*= 8.3 and 1.7 Hz, 1H), 8.02 (t, J = 7.9 Hz, 1H), 7.97 (dd, *J*= 8.1 and 1.7 Hz, 1H), 7.94 (s, 2H), 7.75 (d, *J*= 8.9, 2H), 7.26 – 7.20 (m, 8H), 7.13 (d, *J* = 8.7, 2H), 7.09 (d, *J* =8.7 Hz, 6H), 6.89 (d, *J* = 8.9 Hz, 2H), 5.27 (s, 2H), 5.15 (s, 2H), 3.53 (s, 3H), 1.30 (s, 27H).

HRMS (MALDI): *m*/*z* (%): calcd for $[C_{73}H_{71}N_5O_3]^+$: 1064.548; found: 1064.427 (50) $[MH]^+$.

Deprotected thread ***17***

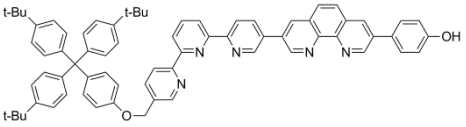

MOM-protected thread **16** (0.35 g, 0.33 mmol)**,** carbon tetrabromide (0.22 g, 0.66 mmol) and anhydrous 2-propanol (40 mL) were placed in a round-bottom flask and irradiated at reflux for 15 min using 100 W light bulbs. Then the reaction mixture was heated at reflux overnight. After the addition of 10 mL of dichloromethane the mixture was

washed with a pH 6 NH_4Cl buffer solution (2 x 20 mL) and water (2 x 20mL). Finally, evaporation of the solvents afforded the pure product as a yellow solid (0.28 g, 81%).

^{1}H NMR (300 MHz, $CDCl_3$) δ 9.51 (d, *J* = 2.2 Hz, 1H), 9.43 (d, *J* = 2.2 Hz, 1H), 9.14 (d, *J* = 1.6 Hz, 1H), 8.82 (d, *J* = 8.4 Hz, 1H), 8.77 (d, J = 1.6 Hz, 1H), 8.69 (d, *J* = 8.2 Hz, 1H), 8.58 – 8.47 (m, 3H), 8.38 (d, *J* = 2.2 Hz, 1H), 8.28 (dd, *J* = 8.4, 1.6 Hz, 1H), 8.04-7.96 (m, 2H), 7.93 (s, 2H), 7.70 (d, *J* = 8.9 Hz, 2H), 7.26 – 7.20 (m, 8H), 7.14 (d, *J* = 8.6 Hz, 2H), 7.09 (d, *J* = 8.6 Hz, 6H), 6.89 (d, *J* = 8.9 Hz, 2H), 5.16 (s, 2H), 1.30 (s, 27H).

Ethynyl-terminated thread **2**

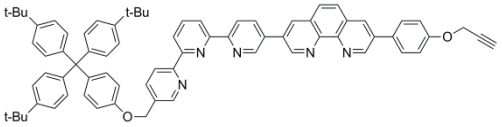

Sodium hydride (60 % dispersion in mineral oil, 0.26 g, 0.66 mmol) was added over a solution of **17** (0.34 g, 0.33 mmol) in anhydrous THF (20 ml). After stirring for 10 min, 20 equiv of propargyl bromide (80 wt. % solution in toluene, 0.70 mL, 0.66 mmol) were added. The mixture was stirred under argon at 45 ^{0}C for 5 days. Evaporation of the solvent afforded an orange solid that was suspended in water, filtered, washed with some more water, hexane and finally a 1:1 mixture of hexane/diethyl ether. The resulting brownish solid was purified by alumina column chromatography using a CH_2Cl_2/MeOH as eluent affording a pale yellow solid (0.28 g, 80%).

^{1}H NMR (300 MHz, $CDCl_3$) δ 9.51 (d, *J* = 2.3 Hz, 1H), 9.45 (d, *J* = 2.3 Hz, 1H), 9.14 (d, *J* = 2.3 Hz, 1H), 8.82 (d, *J*= 8.3 Hz, 1H), 8.77 (d, *J* = 1.9 Hz, 1H), 8.68-8.49 (m, 3H), 8.39 (d, *J* = 2.3 Hz, 1H), 8.27 (dd, *J* = 8.3 and 2.3 Hz, 1H), 8.01 (t, *J*= 7.8 Hz, 1H), 7.97 (dd, *J*= 7.9 and 1.9 Hz, 1H), 7.93 (s, 2H), 7.77 (d, *J* = 8.8 Hz, 2H), 7.24 (d, *J* = 8.7 Hz, 6H), 7.19 (d, *J* = 8.9 Hz, 2H), 7.13 (d, *J* = 8.9 Hz, 2H), 7.09 (d, *J* = 8.7 Hz, 6H), 6.89 (d, *J* = 8.8 Hz, 2H), 5.16 (s, 2H), 4.80 (d, *J* = 2.4 Hz, 2H), 2.58 (t, *J* = 2.4 Hz, 1H), 1.30 (s, 27H).

HRMS (MALDI): *m*/*z* (%): calcd for $[C_{74}H_{68}N_5O_2]^+$: 1058.537; found: 1058.525 (20) $[MH]^+$.

Hydroxyl stopper ***18***

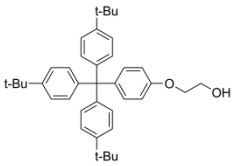

18 was prepared according to a described procedure.[60]

^{1}H NMR (300 MHz, $CDCl_3$): δ 7.23 (d, *J* = 8.7 Hz, 6H), 7.09 (dd, *J* = 8.7, 8.6 Hz, 8H), 6.78 (d, *J* = 9.0 Hz, 2H), 4.08 (t, *J* = 6.0 Hz, 2H), 3.95 dd, *J* = 8.7, 8.6 Hz (t, *J* = 6.0 Hz, 2H), 1.30 (s, 27H).

Mesylate-derivative stopper ***19***

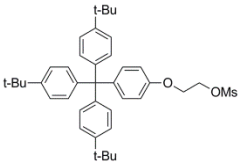

Triethylamine (13 mL) and methanesulfonyl chloride (0.62 mL, 8.0 mmol) were added dropwise to a stirred solution of **18** (1.13 g, 2.00 mmol) in dry dichloromethane (20 mL) at 0 ^{0}C. The mixture was stirred for 2 h at 0 ^{0}C, and then it was allowed to reach room temperature overnight. The resulting mixture solution was washed with water (4 x 40mL), dried over Na_2SO_4, and concentrated under reduced pressure to obtain the pure product as a white solid (1.19 g, 93%) without further purification.

1H NMR (300 MHz, $CDCl_3$): δ 7.23 (d, J = 8.5 Hz, 6H), 7.11 (d, J = 8.9 Hz, 2H), 7.07 (d, J = 8.5 Hz, 6H), 6.76 (d, J = 8.9 Hz, 2H), 4.59 – 4.53 (m, 2H), 4.25 – 4.19 (m, 2H), 3.08 (s, 3H), 1.30 (s, 27H).

Elemental Analysis calcd for $C_{40}H_{50}O_4S$: C, 76.64; H, 8.04; S, 5.11; found: C, 75.56; H, 8.36; S, 5.44.

Azide-derivative stopper **20**

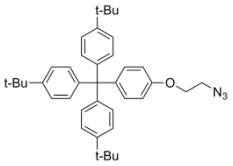

A mixture of **19** (0.38 g, 0.62 mmol) and NaN_3 (0.20 g, 3.10 mmol) was dissolved in 10 mL of DMF and stirred at 50 ^{0}C for 24. After evaporation of the solvent, the resulting solid was dissolved in dichloromethane. The organic layer was washed with water (3 x 30 mL), dried over anhydrous Na_2SO_4 and concentrated under reduced pressure affording a white solid that was purified by silica gel column chromatography using hexane/CH_2Cl_2 to yield **20** as a white solid (0.27 g, 74%).

^{1}H NMR (300 MHz, $CDCl_3$): δ 7.23 (d, *J* = 8.7 Hz, 6H), 7.09 (m, 8H), 6.78 (d, *J* = 9.0 Hz, 2H), 4.13 (t, *J* = 6.0 Hz, 2H), 3.58 (t, *J* = 6.0 Hz, 2H), 1.30 (s, 27H).

MS (ES): *m*/*z* (%): calcd for $[C_{39}H_{47}N_3O]^+$: 591.4; found: 591.4 (100) $[MNH_4]^+$.

Elemental Analysis calcd for $C_{39}H_{47}N_3O$: C, 81.63; H, 8.26; N, 7.32; found: C, 81.22; H, 8.04; N, 6.93.

Cu(M1)22(PF$_6$) ***R1(PF$_6$)***

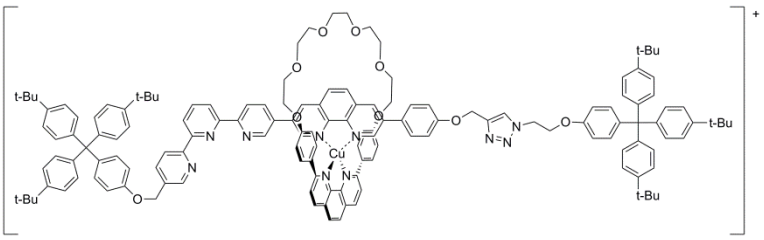

A solution of $[Cu(CH_3CN)_4][PF_6]$ (37 mg, 0.10 mmol) in dry degassed acetonitrile (5 mL) was added to a degassed solution of macrocycle **M1** (57 mg, 0.10 mmol) in dry dichloromethane (5 mL). After 30 min of stirring under argon, a degassed solution of ethynyl-terminated thread **2** (11 mg, 0.10 mmol) in dichloromethane (8 mL) was added via cannula. The mixture turned immediately into dark red and was left to react for

another 30 minutes. After that time the solvents were removed under reduced pressure. Azide stopper **20** (0.072g, 0.125 mmol), Na_2CO_3 (0.003g, 0.025 mmol) and sodium ascorbate (0.02g, 0.1 mmol) were added to the remaining solid and the mixture was dissolved in degassed dichloromethane (4 mL). In a separated flask, CuBr (3.7 mg 0.025 mmol) and Me_6Tren (7 μL, 0.025 mmol) were heated in degassed acetonitrile (2 mL) at 60 ^{0}C for 30 minutes. The resulting green solution was added via cannula to the reaction mixture. After 7 days of stirring under argon at room temperature the crude was treated with 5 mL of aqueous KCN (30 mg, 0.46 mmol) and some more dichloromethane (10 mL). After vigorous stirring for 4 h, the phases were separated and the organic layer was washed with water, dried over Na_2SO_4 and concentrated under reduced pressure. The crude was purified by silica column chromatography using CH_2Cl_2/MeOH as eluent affording unthreaded axle **22** (57 mg, 13%) as a by-product and a mixture containing **R1**$^+$. The rest of the material was remetallated in a degassed mixture of dichloromethane (2 mL) and acetonitrile (1 mL) with $[Cu(CH_3CN)_4][PF_6]$ (19 mg, 0.05 mmol). After 1 hour of stirring the solvents were evaporated under reduced pressure and the resulting solid was purified by silica gel column chromatography using CH_2Cl_2/MeOH to afford pure rotaxane **R1**(PF_6) as a brown solid (72 mg, 11%).

Unthreaded axle 22

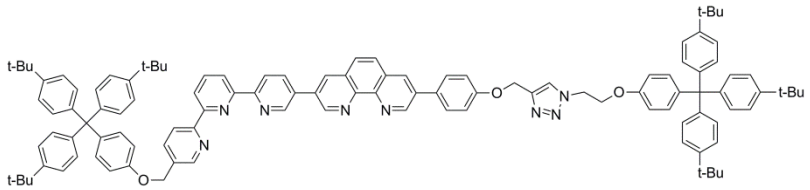

^{1}H NMR (300 MHz, $CDCl_3$): δ 9.51 (d, *J* = 2.5 Hz, 1H), 9.44 (d, *J* = 2.2 Hz, 1H), 9.14 (d, *J* = 1.4 Hz, 1H), 8.81 (d, *J* = 8.3 Hz, 1H), 8.77 (d, *J* = 1.6 Hz, 1H), 8.68 (d, *J* = 8.1 Hz, 1H), 8.55 (d, *J* = 7.8 Hz, 1H), 8.53 – 8.47 (m, 3H), 8.38 (d, *J* = 2.3 Hz, 1H), 8.27 (dd, *J* = 8.3, 2.3 Hz, 1H), 8.01 (t, *J* = 7.8 Hz, 2H), 7.97 (dd, *J* = 8.0, 2.1 Hz, 1H), 7.93 (s, 2H), 7.74 (dd, *J* = 8.8, 1.4 Hz, 2H), 7.23 (m, 12H), 7.15-7.05 (m, 18H), 6.89 (d, *J* = 9.0 Hz, 2H), 6.75 (d, *J* = 9.0 Hz, 2H), 5.27 (s, 2H), 4.79 (t, *J* = 4.8 Hz, 2H), 4.35 (t, *J* = 4.8 Hz, 2H), 1.30 (s, 27H).

HRMS (MALDI): *m*/*z* (%) calcd. for $[C_{113}H_{115}N_8O_3]^+$: 1631.913; found: 1632.705 (20) $[MH]^+$.

Copper-complexed rotaxane R1(PF_6)

^{1}H NMR (300 MHz, CD_2Cl_2): δ 9.04 (s, 1H), 8.97 (s, 1H), 8.86 (d, *J* = 8.1 Hz, 1H), 8.78 (s, 1H), 8.74 – 8.64 (m, 4H), 8.59 – 8.47 (m, 4H), 8.40-8.22 (m, 3H), 8.20-8.10 (m, 4H), 8.10-7.96 (m, 2H), 7.93 (s, 1H), 7.64 (d, *J* = 8.7 Hz, 2H), 7.50 (d, *J* = 8.6 Hz, 4H), 7.32 – 7.10 (m, 30H), 6.92 (d, *J* = 8.9 Hz, 2H), 6.79 (d, *J* = 8.9 Hz, 2H), 5.94 (d, *J* = 8.6 Hz, 4H), 5.26 (s, 2H), 5.16 (s, 2H), 4.78 (t, *J* = 4.8 Hz, 2H), 4.37 (t, *J* = 4.9 Hz, 2H), 3.81 (s, 4H), 3.76-3.66 (m, 4H), 3.65-3.55 (m, 4H), 3.50-3.35 (m, 8H), 1.31 (s, 27H), 1.29 (s, 27H).

HRMS (MALDI): *m*/*z* (%) calcd. for $[CuC_{147}H_{148}N_{10}O_9]^+$: 2261.08; found: 2261.04 (15) $[M]^+$.

Macrocycle **M2**

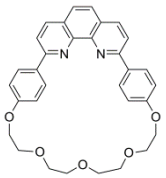

M2 was prepared according to a described procedure.[93]

^{1}H NMR (300 MHz, $CDCl_3$) δ 8.43 (d, *J* = 9.0 Hz, 4H), 8.25 (d, *J* = 8.4 Hz, 2H), 8.06 (d, *J* = 8.4 Hz, 2H), 7.73 (s, 2H), 7.28 (d, *J* = 9.0 Hz, 4H), 4.41 (t, *J* = 4.9 Hz, 4H), 3.80 (t, *J* = 4.9 Hz, 4H), 3.70 (s, 8H).

MS (ES): *m*/*z* (%): calcd for $[C_{32}H_{30}N_2O_5H]^+$: 523.2; found: 523.5 (100) $[MH]^+$.

2,9-Bis(p-hidroxyphenyl)-1,10-phenanthroline **23**

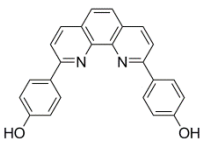

23 was prepared according to a described procedure.[93]

^{1}H NMR (300 MHz, $CDCl_3$) δ 8.38 (d, *J* = 8.5 Hz, 2H), 8.27 (d, *J* = 8.7 Hz, 4H), 8.14 (d, *J* = 8.5 Hz, 2H), 7.82 (s, 2H), 6.97 (d, *J* = 8.7 Hz, 4H).

N-Boc protected diamine **24**

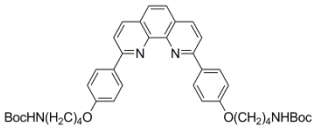

A solution of 4-(boc-amino)butyl bromide (2.00 g, 9.0 mmol) in 10 mL of dry DMF was added dropwise to a flask containing **23** (1.11 g, 3 mmol), K_2CO_3 (3.37g, 24.4 mmol) and 20 mL of dry DMF. The mixture was stirred at 60 ^{0}C for 5 days. The solvent was removed under reduced pressure and the resulting solid was dissolved in dichloromethane (40 mL). The organic phase was washed twice with 0.5 M aqueous NH_4Cl and then with distilled water. Then it was dried over Na_2SO_4 and concentrated under reduced pressure. The resulting yellow oil was purified by silica column chromatography (CH_2Cl_2/MeOH) to afford 0.32 g (15 %) of the targeted disubstituted product **24**, 0.49 g (30 %) of the monosubstituted product and 0.37 g (21 %) of the starting material. The starting material and the monosubstituted product were reacted again with 4-(boc-amino)buthyl bromide under the same conditions to afford **24** in a global 42 % yield.

^{1}H NMR (300 MHz, $CDCl_3$): δ 8.41 (d, *J* = 8.8 Hz, 4H), 8.24 (d, *J* = 8.5 Hz, 2H), 8.06 (d, *J* = 8.5 Hz, 2H), 7.72 (s, 2H), 7.09 (d, *J* = 8.8 Hz), 4.67 (s, 2H), 4.09 (t, *J* = 6.2 Hz, 4H), 3.23 (dd, *J* = 12.9, 6.5 Hz, 4H), 1.87 (m, 4H), 1.71 (dt, *J* = 13.1, 6.4 Hz, 4H), 1,46 (s, 18 H).

MS (ES): *m*/z (%): calcd for $[C_{42}H_{50}N_4O_6H]^+$: 707.4; found: 707.3 (100) $[MH]^+$.

Monosubstituted derivative

^{1}H NMR (300 MHz, $CDCl_3$): δ 8.44 (d, J = 8.8 Hz, 2H), 8.41 (d, J = 8.8 Hz, 2H), 8.26 (d, J = 8.5 Hz, 2H), 8.09 (d, J = 8.5 Hz, 2H), 7.12 (d, J = 8.8 Hz, 2H), 7.09 (d, J = 8.8 Hz, 2H), 4.10 (t, J = 6.2 Hz, 2H), 3.15 (dd, J = 13.3, 6.6 Hz, 2H), 1.87 (m, 2H), 1.71 (m, 2H), 1,46 (s, 9 H).

MS (ES): m/z (%): calcd for $[C_{33}H_{33}N_3O_4H]^+$: 536.25; found: 536.33 (100) $[MH]^+$.

Diamine **25**

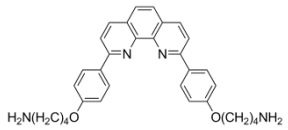

Boc-amino protected compound **24** (0.91 g, 1.30 mmol) was dissolved in 30 mL of a 9:1 mixture of dichloromethane: trifluoroacetic acid and stirred at room temperature for 24 h. The solvent was removed under reduced pressure affording a yellow oil that was then mixed with aqueous 1 M NaOH and extracted with dichloromethane. The organic phase was washed with water, dried over Na_2SO_4 and concentrated under reduced pressure to yield **25** as a yellow solid (0.53 g, 85%).

^{1}H NMR (300 MHz, $CDCl_3$): δ 8.48 (d, J = 8.9 Hz, 4H), 8.26 (d, J = 8.5 Hz, 2H), 8.08 (d, J = 8.5 Hz, 2H), 7.74 (s, 2H), 7.10 (d, J = 8.9 Hz, 4H), 4.11 (t, J = 6.4 Hz, 4H), 2.81 (t, J = 7.1 Hz, 4H), 1.98 – 1.81 (m, 4H), 1.67 (dt, J = 10.3, 7.1 Hz, 4H).

MS (ES): m/z (%): calcd for $[C_{32}H_{34}N_4O_2H]^+$: 507.3; found: 507.6 (25) $[MH]^+$; calcd for $[C_{32}H_{34}N_4O_2H]^{2+}$: 254.6; found: 254.4(100) $[M_2H]^{2+}$.

Macrocycle M3 ***M3***

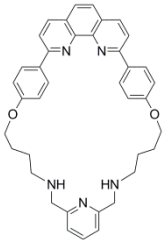

Diamine **25** (0.20 g, 0.40 mmol) was placed in a round bottom flask under argon and dissolved in a mixture of dichloromethane (40 mL) and anhydrous methanol (20 mL). Then 0.054 g (0.4 mmol) of 2,6-pyridinedicarbaldehyde were added and the mixture was stirred at room temperature 30 minutes. After that time, $NaBH_4$ (0.045 g, 1.2 mmol) was added in small portions and the yellowish solution was stirred overnight. Solvents were

removed under reduced pressure affording a yellow oil that was redissolved in dichloromethane and washed with 0.5 M NH_4Cl until the pH of the discarded aqueous phase was 7. The organic layer was dried over Na_2SO_4 and concentrated under reduced pressure to yield macrocycle **M3** as an off-white solid (0.23g, 92%).

^{1}H NMR (300 MHz, $CDCl_3$): δ 8.41 (d, *J* = 8.9 Hz, 4H), 8.25 (d, *J* = 8.4 Hz, 2H), 8.06 (d, *J* = 8.4 Hz, 2H), 7.74 (s, 2H), 7.65 (t, *J* = 7.6 Hz, 1H), 7.24 (d, *J* = 7.6 Hz, 2H), 7.10 (d, *J* = 8.9 Hz, 4H), 4.17 (t, *J* = 6.7 Hz, 4H), 3.96 (s, 4H), 2.81 (t, *J* = 7.5 Hz , 4H), 1.98 – 1.86 (m, 4H), 1.84 – 1.70 (m, 4H).

MS (ES): *m*/*z* (%): calcd for $[C_{39}H_{39}N_5O_2H]^+$: 610.3; found: 610.5 (100) $[MH]^+$.

IR: (KBr) = 3403 (br), 3185 (br), 2932 (m), 2864 (m), 1601 (s), 1572 (s), 1487 (s), 1400 (s), 1240 (s), 1174 (s), 828 cm^{-1} (m).

Boc-protected pyridine-2,6-diylbis(methylene))bis((6-hydroxyhexyl) **26**

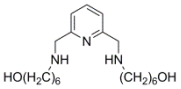

2,6-Pyridine carboxaldehide (0.34 g, 2.50 mmol) was added to a solution of 6-aminohexanol in 50 mL of anhydrous methanol. After stirring for 1 h at room temperature, $NaBH_4$ (0.26g, 7.00 mmol) was added and the reaction mixture was left to stir overnight. 5 ml of triethylamine and 2.9 ml of di-*tert*-butyl dicarbonate were added to the colourless mixture and the whole was refluxed during 4 h. Solvents were removed under reduced pressure and the resulting white semisolid was dissolved in dichloromethane (40 mL) and washed four times with distilled water. The organic layer was dried over Na_2SO_4 and concentrated under reduced pressure to afford the targeted product as colorless oil (1.30 g, 97 %).

^{1}H NMR (300 MHz, $CDCl_3$): 7.61 (t, *J* = 7.8 Hz, 1H), 7.07 (m, 2H), 4.49 (m, 4H), 3.61 (t, *J* = 6.3 Hz, 4H), 3.26 (d, *J* = 28.2 Hz, 4H), 1.65-1.40 (m, 12H), 1.38 (s, 18H).

Boc-protected macrocycle M4 **27**

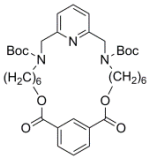

A solution of isophthaloyl chloride (0.51 g, 2.50 mmol) in distilled dichloromethane (100 ml) was added dropwise over a stirred solution of **26** (1.30 g, 2.50 mmol) and triethylamine (1.6 mL, 11.25 mmol) in distilled dichloromethane (250 ml). The reaction mixture was stirred under argon at room temperature for 3 days. The solvent was partially evaporated and the remaining solution was washed four times with water and dried over Na_2SO_4. Evaporation of the solvent led to an uncolored oil which was purified by column chromatography (silica gel, CH_2Cl_2/MeOH) to yield the pure product as a white solid (1.14 g, 68%).

^{1}H NMR (300 MHz, $CDCl_3$): δ 8.59 (t, *J* = 1.6 Hz, 1H), 8.25 (dd, *J* = 7.8, 1.6 Hz, 2H), 7.66 – 7.51 (m, 2H), 7.22 – 7.03 (m, 2H), 4.49 (m, 4H), 4.35 (t, *J* = 6.0 Hz, 4H), 3.95 (s, 4H), 3.26 (m, 4H), 1.88 – 1.68 (m, 4H), 1.50-1.46 (m, 8H), 1.39 (s, 18H).

MS (ES): *m*/*z* (%): calcd for $[C_{37}H_{53}N_3O_8H]^+$: 667.4; found: 668.5 $[MH]^+$; calcd for $[C_{37}H_{53}N_3O_8Na]^+$: 690.4; found: 690.5 $[MNa]^+$.

Pyridine bis-amine macrocycle M4 ***M4***

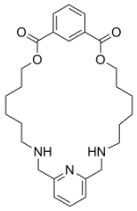

Boc-protected macrocycle **27** (0.18 g, 0.28 mmol) was dissolved in 10 mL of a mixture of dichloromethane and trifluoroacetic acid (9:1) and stirred at room temperature for 24 h. The solvent was then removed under reduced pressure affording an oil that was mixed

with 1 M aqueous NaOH and extracted with dichloromethane. The organic phase was washed with water, dried over Na_2SO_4 and concentrated under reduced pressure to afford macrocycle **M4** as a white solid (0.13 g, 98%).

^{1}H NMR (300 MHz, $CDCl_3$): δ 8.59 (t, J = 1.7 Hz, 1H), 8.25 (dd, J = 7.8, 1.7 Hz, 2H), 7.54 (dd, J = 11.8, 4.3 Hz, 1H), 7.26 (s, 1H), 7.06 (d, J = 7.6 Hz, 2H), 4.35 (t, J = 6.3 Hz, 4H), 3.88 (s, 4H), 2.67 (t, J = 6.7 Hz, 4H), 1.79 (dd, J = 8.4, 6.3 Hz, 4H), 1.69 – 1.36 (m, 13H).

MS (ES): *m*/z (%): calcd for $[C_{27}H_{37}N_3O_4H]^+$: 468.3; found: 468.6 $[MH]^+$.

((4-Ethynylphenyl)ethynyl)trimethylsilane **28**

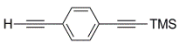

A solution of 1,4-diethynylbenzene (2.00 g, 16 mmol) in anhydrous THF (200 mL) was placed in a two neck round-bottom flask under argon, and cooled to -78 °C. n-BuLi was added dropwise (10 ml, 1.6 M in hexane, 16 mmol). After stirring for 1 h at -78 °C, chlorotrimethylsilane (3 mL, 24 mmol) was then added dropwise and the solution was then allowed to warm to room temperature overnight. The reaction was quenched with water and THF was eliminated under reduced pressure. Diethyl ether (70 mL) was added, and the organic phase was washed with water and dried over Na_2SO_4. Evaporation of the solvent led to a yellow solid composed by 68% of the desired compound **28**, 12% of the diprotected derivative and 20% of starting material. The excess of starting material was evaporated under vacuum and the resulting mixture of mono and diprotected compounds was used in the following stage without further purification.

^{1}H NMR ($CDCl_3$, 300 MHz): δ 7.41 (s, 4H), 3.15 (s, 1H), 0.25 (s, 9H).

1,4-bis((trimethylsilyl)ethynyl)benzene

^{1}H NMR ($CDCl_3$, 300 MHz): δ 7.38 (s, 4H), 0.24 (s, 18H).

3,8-bis((4-((trimethylsilyl)ethynyl)phenyl)ethynyl)-1,10-phenanthroline **29**

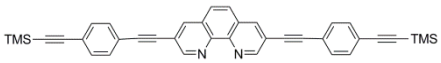

The previous mixture of mono and disylilated derivatives (1.62 g, ca. 6.80 mmol of **28**), 3,8-dibromo-1,10-phenanthroline (**11**) (0.92 g, 2.72 mmol), CuI (0.05 g, 0.27 mmol), $PdCl_2(PPh_3)_2$ (0.11 g, 0.16 mmol), $(i\text{-}Pr)_2EtN$ (8 mL) and anhydrous THF (20 mL) were heated under argon at 60 ^{0}C for 4 days. The resulting mixture was filtered and the solid washed with dichloromethane (40 mL). The combined organic solutions were washed with water (4x15 mL) and dried over Na_2SO_4. The solution was filtered and the solvent was removed. The resulting solid was chromatographed over silica gel using CH_2Cl_2/MeOH as eluent to yield **29** as a yellow solid (0.77 g, 50%).

^{1}H NMR (300 MHz, $CDCl_3$): δ 9.26 (d, *J* = 2.1 Hz, 2H), 8.36 (d, *J* = 2.1 Hz, 2H), 7.55 and 7.49 (AB system, 8H), 0.26 (s, 18H).

HRMS (ES): *m*/*z* (%): calcd for $[C_{38}H_{32}N_2Si_2H]^+$: 573.217; found: 573.217 (100) $[MH]^+$.

3,8-bis((4-ethynylphenyl)ethynyl)-1,10-phenanthroline **30**

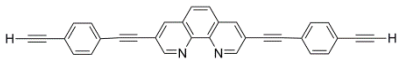

A suspension of the bis-silylated phenanthroline **29** (0.77 g, 1.35 mmol) and K_2CO_3 (0.19 g, 1.35 mmol) in 30 mL of methanol was stirred at room temperature for 1 h. Evaporation of the solvent yielded a solid which was suspended in water, filtered and washed with plenty of water affording the pure product as an off-white solid (0.50 g, 91%).

^{1}H NMR (300 MHz, $CDCl_3$): δ 9.30 (d, *J* = 2.1 Hz, 2H), 8.42 (d, *J* = 2.1 Hz, 2H), 7.84 (s, 2H), 7.60 and 7.55 (AB system, 8H), 3.23 (s, 2H).

Demetallated R2 ***31***

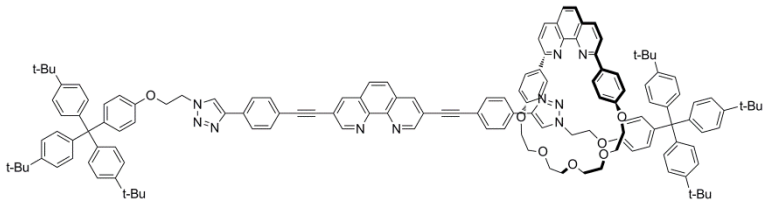

A degassed solution of $[Cu(CH_3CN)_4][PF_6]$ (0.02 g, 0.05 mmol) in dry acetonitrile (4 mL) was added to a degassed solution of macrocycle **M2** (0.03 g, 0.05 mmol) in dichloromethane (4 mL). After 30 min of stirring under argon, a degassed solution of phenanthroline diacetylene **30** (0.02 g, 0.05 mmol) in dichloromethane (20 mL) was added via cannula. The mixture immediately turned into dark brown and was left to react for another 30 min at room temperature. Then the solvents were removed under reduced pressure. Azide stopper **20** (0.07 g, 0.13 mmol), Na_2CO_3 (0.003 g, 0.025 mmol) and sodium ascorbate (0.02 g, 0.10 mmol) were added to the remaining solid and the mixture was dissolved in 4 mL of degassed dichloromethane. In a separated flask, 3.7 mg (0.025 mmol) of CuBr and 6.7 μL (0.025 mmol) of Me_6Tren in degassed acetonitrile (2 mL) were heated for 30 min at 60 ^{0}C and the resulting green solution was added via cannula to the reaction mixture. After 7 days of stirring under argon at room temperature the crude was treated with 20 mL of aqueous KCN (120 mg, 0.46 mmol) and dichloromethane (10 mL). After 4 h of vigorous stirring, the phases were separated and the organic layer was washed with water, dried over Na_2SO_4 and concentrated under reduced pressure. The crude product was purified by silica column chromatography using CH_2Cl_2/MeOH as eluent to yield demetallated rotaxane **31** as a yellow solid (0.354 g, 34 %).

^{1}H NMR (300 MHz, $CDCl_3$): δ 9.35 (s, 1H), 9.25 (s, 1H), 9.04 (s, 1H), 8.67 (s, 1H), 8.31 (s, 1H), 8.26 (d, *J* = 8.3 Hz, 2H), 8.02 (s, 1H), 7.91 – 7.76 (m, 11H), 7.73 – 7.43 (m, 10H), 7.21 (t, *J* = 6.9 Hz, 14H), 7.15 – 6.90 (m, 20H), 6.72 (d, *J* = 8.7 Hz, 9H), 4.81 (s, 2H), 4.38 (s, 5H), 4.22 (s, 3H), 4.11 (s, 5H), 3.76 (s, 9H), 3.56 (s, 5H), 1.29 (s, 27H).

MS (EI): *m*/*z* (%): calcd for $[C_{142}H_{141}N_{10}O_7]^+$: 2099.1; found: 2099.0 (100) $[MH^+]$.

Rotaxane R2 ***R2(PF$_6$)***

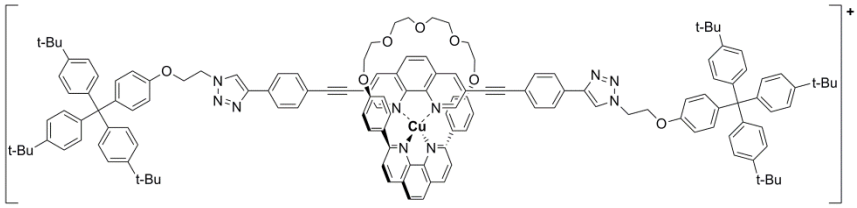

Under an argon atmosphere, an acetonitrile solution (1 mL) of [Cu(CH$_3$CN)$_4$](PF$_6$) (3.3 mg, 0.01 mmol) was cannulated over a solution of demetallated rotaxane **31** (0.02 g, 0.01 mmol) in distilled dichloromethane (2 mL). The resulting red-brown solution was stirred for 1 h and the solvents were evaporated under reduced pressure affording the metallated rotaxane **R2**(PF$_6$) as a brown solid (2.2 mg, 97%).

^{1}H NMR (300 MHz, CD$_2$Cl$_2$): δ 8.89 (d, *J* = 1.7 Hz, 2H), 8.66 (d, *J* = 8.3 Hz, 2H), 8.39 (d, *J* = 1.7 Hz, 2H), 8.26 (s, 2H), 8.16 (s, 2H), 8.10 (d, *J* = 8.3 Hz, 2H), 8.08 (s, 2H), 7.89 (d, *J* = 8.3 Hz, 4H), 7.64 (d, *J* = 8.2 Hz, 4H), 7.25 (d, *J* = 8.5 Hz, 12H), 7.20 – 7.05 (m, 20H), 6.79 (d, *J* = 8.9 Hz, 4H), 5.83 (d, *J* = 8.6 Hz, 4H), 4.81 (t, *J* = 4.6 Hz, 4H), 4.39 (t, *J* = 4.6 Hz, 4H), 3.93 (d, *J* = 4.9 Hz, 4H), 3.82 (d, *J* = 4.9 Hz, 4H), 3.49 (t, *J* = 4.8 Hz, 4H), 3.10 (t, *J* = 4.8 Hz, 4H), 1.28 (s, 54H).

MS (ES): *m*/*z* (%): calcd for [CuC$_{142}$H$_{140}$N$_{10}$O$_7$]$^+$: 2161.0; found: 2161.9 (100) [M$^+$].

IR: (KBr) = 3440 (br), 3143 (br), 2958 (m), 2866 (m), 2207 (w), 1718 (w), 1603 (m), 1505 (m), 1400 (m), 1246 (s), 842 (s), 557 cm^{-1} (m).

Oxidized rotaxane R2 ***R2(PF$_6$)$_2$***

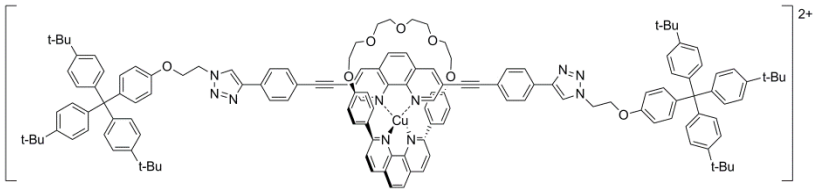

A freshly prepared acetonitrile solution of $NOBF_4$ (0.5 mL, 0.01 M) was added over a solution of **R2**(PF_6) (8.8 mg, 0.005 mmol) in dichloromethane (3 mL). After 10 minutes of stirring, the color of the solution completely changed from red-brown to green-yellow. Once the solvents were evaporated, the solid was redisolved in acetonitrile (3 mL) and precipitated with a 0.1 M aqueous solution of KPF_6 (8 mL). The resulting precipitate was filtered and washed with water affording the pure product as a yellow solid (1.2 mg, 98%).

HRMS (ES): *m*/*z* (%) calcd for $[CuC_{142}H_{140}N_{10}O_7]^+$: 1081.12; found: 1081.10 (10) $[M^{2+}]$.

Stoppered axis **32**

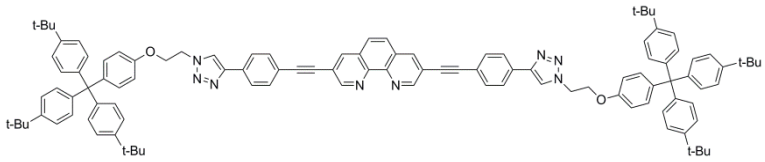

Phenanthroline diacetylene **30** (0.04 g, 0.1 mmol), azide-functionalized stopper **20** (0.14 g, 0.25 mmol) and hydrazine monohydrate (1.2 μL, 0.025 mmol), were dissolved in 10 mL of dichloromethane. In a separated flask, CuBr (7.0 mg, 0.05 mmol) and Me_6tren (13 μL, 0.05 mmol) were dissolved in degassed acetonitrile (4 mL) and stirred for 30 minutes. The greenish catalyst mixture was added via a cannula to the reaction mixture and stirred under argon at room temperature for 5 days. Aqueous KCN (6 mg/mL, 5 mL) and dichloromethane (10 mL) were added to the crude in order to eliminate the copper. After 4 hours of stirring, the phases were separated and the organic phase was washed with water, dried over Na_2SO_4 and concentrated under reduced pressure. The crude product was purified by silica column chromatography using CH_2Cl_2/MeOH as eluent to afford **32** as a yellow solid (0.11 g, 70%).

^{1}H NMR (300 MHz, $CDCl_3$): δ 9.30 (d, *J* = 2.0 Hz, 2H), 8.40 (d, *J* = 2.0 Hz, 2H), 8.04 (s, 2H), 7.89 (d, *J* = 8.4 Hz, 4H), 7.82 (s, 2H), 7.69 (d, *J* = 8.4 Hz, 4H), 7.23 (d, *J* = 8.7 Hz, 12H), 7.11

(d, *J* = 9.0 Hz, 4H), 7.06 (d, *J* = 8.7 Hz, 12H), 6.77 (d, *J* = 9.0 Hz, 4H), 4.83 (t, *J* = 4.6 Hz, 4H), 4.40 (t, *J* = 4.6 Hz, 4H), 1.29 (s, 54H).

HRMS (MALDI): *m*/*z* (%) calcd for $C_{110}H_{110}N_8O_2$: 1576.10; found: 1576.98(100) [M^+].

Rotaxane R3 ***R3(PF$_6$)***

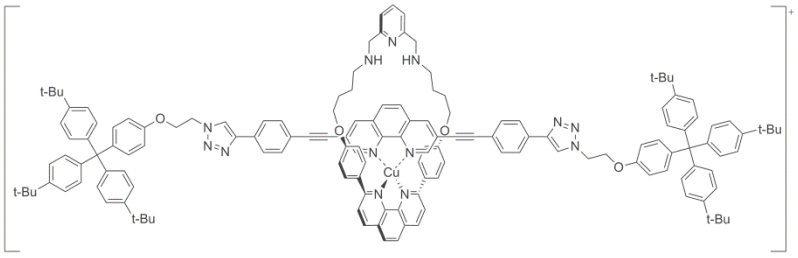

A solution of $[Cu(CH_3CN)_4](PF_6)$ (1.7 mg, 0.045 mmol) in dry degassed CH_3CN (6 mL) was added to a degassed solution of stoppered axle **32** (7.1 mg, 0.045 mmol) in dichloromethane (50 mL). After 20 min of stirring under argon, a degassed solution of diamine **25** (2.3 g, 0.045 mmol) in dichloromethane (10 mL) and methanol (1 mL) was added via cannula. The mixture turned immediately into dark brown and was left to react for another 30 min. Then, a degassed solution of 2,6-pyridine dicarbaldehide in dichloromethane (8 mL) was added. After 1 h of stirring a degassed solution of $NaBH_4$ (0.068 g, 1.8 mmol) in methanol (10 mL) was added via cannula and the reaction mixture was stirred for another 4 h. The resulting brown solution was filtered and purified by silica column chromatography using CH_2Cl_2/MeOH as eluent to yield a red-brown solid (0. 022 g, 22 %).

^{1}H NMR (300 MHz, CD_2Cl_2): δ 8.84 (s, 2H), 8.66 (d, *J* = 8.4 Hz, 2H), 8.50 (s, 2H), 8.42 (d, *J* = 1.8 Hz, 2H), 8.14 (d, *J* = 7.1 Hz, 2H), 8.15-8.06 (m, 4H), 7.88 (d, *J* = 8.4 Hz, 4H), 7.78 (s, 1H), 7.63 (d, *J* = 8.4 Hz, 4H), 7.40-7.25 (m, 6H)), 7.24 (d, *J* = 8.6 Hz, 12H), 7.20-7.10 (m, 16H), 6.79 (d, *J* = 8.8 Hz, 4H), 5.90-5.86 (m, 4H), 4.85-4.75 (m, 4H), 4.50-4.30 (m, 8H), 3.75-3.60 (m, 4H), 3.28-3.15 (m, 4H), 2.10-1.60 (m, 10H), 1.28 (s, 54H).

HRMS (MALDI): *m*/*z* (%) calcd for $CuC_{149}H_{149}N_{13}O_4$: 2248.12; found: 2248.14 (20) [M^+].

IR: (KBr) = 3422 (br), 3147 (br), 2959 (m), 2866 (m), 2206 (w), 1605 (m), 1505 (m), 1400 (m), 1246 (s), 844 (s), 558 cm^{-1} (m).

Oxidized rotaxane R3 ***R3(PF$_6$)$_2$***

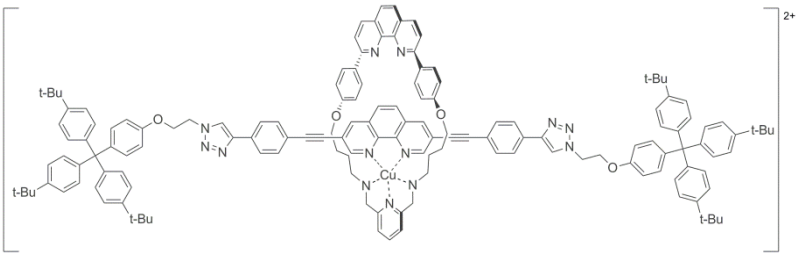

A freshly prepared acetonitrile solution of $NOBF_4$ (0.5 mL, 0.01 M) was added over a solution of **R3**(PF_6) (4.8 mg, 0.002 mmol) in dichloromethane (3 mL). After 10 minutes of stirring, the color of the solution completely changed from red-brown to green-yellow. Once the solvents were evaporated, the solid was redisolved in acetonitrile (3 mL) and precipitated with a 0.1 M aqueous solution of KPF_6 (8 mL). The resulting precipitate was filtered and washed with water affording the pure product as a yellow solid (4.9 mg, 98%).

HRMS (ES): *m*/*z* (%) calcd for $CuC_{142}H_{140}N_{10}O_7$: 1125.81; found: 1125.79 (10) [M^{2+}].

IR: (KBr) = 3431 (br), 3144 (br), 2958 (m), 2210 (w), 1721 (s), 1605 (w), 1504 (w), 1413 (s), 1400 (s), 1264 (m), 1103 (s), 842 (m), 723 (m), 558 cm^{-1} (w).

3,8-bis((trimethylsilyl)ethynyl)-1,10-phenanthroline ***35***

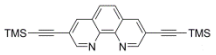

Over a degassed mixture of 3,8-dibromo-1,10-phenanthroline (**11**) (0.34 g, 1.00 mmol), CuI (0.02 g, 0.12 mmol), $PdCl_2(PPh_3)_2$ (0.04 g, 0.06 mmol) and diisopropylamine (2 mL) in anhydrous THF (5 mL) were added 0.34 mL (4 mmol) of ethynyltrimethylsilane. The mixture was heated under argon at room temperature for 3 days. The organic solvent

was evaporated under reduced pressure and the residue was dissolved in dichloromethane (20 mL) and treated with aqueous KCN (10 mL, 6 g/mL) for 4 h. The two layers were separated and the aqueous phase was washed with CH_2Cl_2 (4x 15 mL). Combined organic layers were washed with water (4x 20 mL), dried over Na_2SO_4, filtered and concentrated. The resulting dark solid was chromatographed over silica gel using CH_2Cl_2/MeOH as eluent to yield **35** as a brownish solid (0.27 g, 73%).

^{1}H NMR (300 MHz, $CDCl_3$): δ 9.21 (d, *J* = 2.0 Hz, 2H), 8.34 (d, *J* = 2.0 Hz, 2H), 7.76 (s, 2H), 0.32 (s, 18H).

Cu(M4)TMSPhen(PF$_6$)$_2$ ***33(PF$_6$)$_2$***

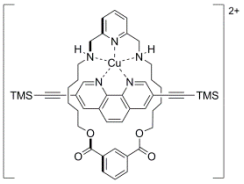

A solution of $Cu(CH_3COO)_2{\cdot}H_2O$ (6.0 mg, 0.03 mmol) and **35** (11.0 mg, 0.03 mmol) in methanol (2 mL) was added to a solution of **M4** (14.0 mg, 0.03 mmol) in 2 mL of methanol. After 1 h of stirring an excess of KPF_6 was added to the blue resulting mixture and precipitated with water. The precipitate was filtered, affording the target compound as a blue solid (0.026g, 85%).

MS (ES): *m*/*z* (%) calcd for $CuC_{30}H_{54}N_6PF_6$: 706.3; found: 706.5 (20) [M^+].

IR: (KBr) = 3448 (br), 3275 (br), 3120 (br), 2957 (m), 2159 (w), 1718 (s), 1610 (w), 1428 (w), 1384 (w), 1250 (s), 12141 (w), 1076 (w), 843 (s), 733 (w), 559 cm^{-1} (m).

Cu(TMSPhen)$_2$(PF$_6$) ***34(PF$_6$)$_2$***

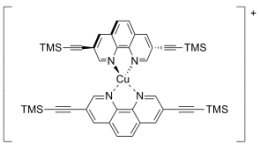

Under an argon atmosphere, an acetonitrile solution (4 mL) of [Cu(CH_3CN)$_4$](PF_6) (9.3 mg, 0.025 mmol) was cannulated over a solution of **35** (19 mg, 0.05 mmol) in distilled dichloromethane (8 mL). The resulting brown solution was stirred for 1 h and the solvents were evaporated under reduced pressure affording the desired complex as a brown solid (0.019g, 79%).

MS (EI): *m*/*z* (%) calcd for $CuC_{44}H_{48}N_4Si_4$: 807.2; found: 807.4 (100) [M^+].

^{1}H NMR (300 MHz, CD_2Cl_2): δ 8.89 (s, 2H), 8.64 (s, 2H), 8.09 (s, 2H), 0.25 (s, 18H).

References

References

(1) Schill, G. In ***Catenanes, Rotaxanes, and Knots***; Organic Chemistry Monographs; Academic Press: 1971; , pp 192.

(2) Amabilino, D. B.; Stoddart, J. F. *Chem. Rev.* **1995**, *95*, 2725-2828.

(3) Harrison, I. T.; Harrison, S. *J. Am. Chem. Soc.* **1967**, *89*, 5723-5724.

(4) Schill, G.; Lüttringhaus, A. *Angew. Chem. , Int. Ed.* **1964**, *3*, 546-547.

(5) Qu, D. H.; Tian, H. *Chem. Sci.* **2011**, *2*, 1011-1015.

(6) Tian, H.; Wang, Q. C. *Chem. Soc. Rev.* **2006**, *35*, 361-374.

(7) Iijima, T.; Vignon, S. A.; Tseng, H. R.; Jarrosson, T.; Sanders, J. K. M.; Marchioni, F.; Venturi, M.; Apostoli, E.; Balzani, V.; Stoddart, J. F. *Chem. -Eur. J.* **2004**, *10*, 6375-6392.

(8) Qu, D. H.; Wang, Q. -.; Tian, H. *Angew. Chem. , Int. Ed.* **2005**, *44*, 5296-5299.

(9) Balzani, V.; Clemente-León, M.; Credi, A.; Ferrer, B.; Venturi, M.; Flood, A. H.; Stoddart, J. F. *Proc. Natl. Acad. Sci. U. S. A.* **2006**, *103*, 1178-1183.

(10) Collier, C. P.; Wong, E. W.; Belohradský, M.; Raymo, F. M.; Stoddart, J. F.; Kuekes, P. J.; Williams, R. S.; Heath, J. R. *Science* **1999**, *285*, 391-394.

(11) Livoreil, A.; Sauvage, J. P.; Armaroli, N.; Balzani, V.; Flamigni, L.; Ventura, B. *J. Am. Chem. Soc.* **1997**, *119*, 12114-12124.

(12) Fioravanti, G.; Haraszkiewicz, N.; Kay, E. R.; Mendoza, S. M.; Bruno, C.; Marcaccio, M.; Wiering, P. G.; Paolucci, F.; Rudolf, P.; Brouwer, A. M.; Leigh, D. A. *Nat. Nanotechnol.* **2008**, *130*, 2593-2601.

(13) Keaveney, C. M.; Leigh, D. A. *Angew. Chem. , Int. Ed.* **2004**, *43*, 1222-1224.

(14) Da Ros, T.; Guldi, D. M.; Morales, A. F.; Leigh, D. A.; Prato, M.; Turco, R. *Org. Lett.* **2003**, *5*, 689-691.

(15) Bottari, G.; Dehez, F.; Leigh, D. A.; Nash, P. J.; Pérez, E. M.; Wong, J. K. Y.; Zerbetto, F. *Angew. Chem. , Int. Ed.* **2003**, *42*, 5886-5889.

(16) Qu, D. H.; Wang, Q. C.; Tian, H. *Mol. Cryst. Liq. Cryst.* **2005**, *430*, 59-65.

(17) Szacilowski, K. *Chem. Rev.* **2008**, *108*, 3481-3548.

(18) Lehn, J. M. In *Molecular and Supramolecular Devices;* Supramolecular Chemistry: Concepts and Perspectives; VCH: Weinheim, 1995; .

(19) Periyasamy, G.; Collin, J. P.; Sauvage, J. P.; Levine, R. D.; Remacle, F. *Chem. -Eur. J.* **2009**, *15*, 1310-1313.

(20) Tseng, H. R.; Vignon, S. A.; Stoddart, J. F. *Angew. Chem. , Int. Ed.* **2003**, *42*, 1491-1495.

(21) Balzani, V.; Credi, A.; Silvi, S.; Venturi, M. *Chem. Soc. Rev.* **2006**, *35*, 1135-1149.

(22) Champin, B.; Mobian, P.; Sauvage, J. P. *Chem. Soc. Rev.* **2007**, *36*, 358-366.

(23) Kay, E. R.; Leigh, D. A.; Zerbetto, F. *Angew. Chem. , Int. Ed.* **2007**, *46*, 72-191.

(24) Coskun, A.; Banaszak, M.; Astumian, R. D.; Stoddart, J. F.; Grzybowski, B. A. *Chem. Soc. Rev.* **2012**, *41*, 19-30.

(25) Collier, C. P.; Mattersteig, G.; Wong, E. W.; Luo, Y.; Beverly, K.; Sampaio, J.; Raymo, F. M.; Stoddart, J. F.; Heath, J. R. *Science* **2000**, *289*, 1172-1175.

(26) Mendes, P. M.; Flood, A. H.; Stoddart, J. F. *Appl. Phys. A: Mater. Sci. Process.* **2005**, *80*, 1197-1209.

(27) Green, J. E.; Wook Choi, J.; Boukai, A.; Bunimovich, Y.; Johnston-Halperin, E.; Deionno, E.; Luo, Y.; Sheriff, B. A.; Xu, K.; Shik Shin, Y.; Tseng, H. R.; Stoddart, J. F.; Heath, J. R. *Nature* **2007**, *445*, 414-417.

(28) Liu, Y.; Flood, A. H.; Bonvallet, P. A.; Vignon, S. A.; Northrop, B. H.; Tseng, H. R.; Jeppesen, J. O.; Huang, T. J.; Brough, B.; Baller, M.; Magonov, S.; Solares, S. D.; Goddard, W. A.; Ho, C. -.; Fraser Stoddart, J. *J. Am. Chem. Soc.* **2005**, *127*, 9745-9759.

(29) Juluri, B. K.; Kumar, A. S.; Liu, Y.; Ye, T.; Yang, Y. -.; Flood, A. H.; Fang, L.; Stoddart, J. F.; Weiss, P. S.; Huang, T. J. *ACS Nano* **2009**, *3*, 291-300.

(30) Durot, S.; Reviriego, F.; Sauvage, J. P. *Dalton Trans.* **2010**, *39*, 10557-10570.

(31) Cotton, F. A.; Wilkinson, G. In *Advanced inorganic chemistry: a comprehensive text;* Wyley: New York, 1980; .

(32) Miller, M. T.; Gantzel, P. K.; Karpishin, T. B. *Inorg. Chem.* **1998**, *37*, 2285-2290.

(33) Ruthkosky, M.; Castellano, F. N.; Meyer, G. J. *Inorg. Chem.* **1996**, *35*, 6406-6412.

(34) Potts, K. T.; Keshavarz-K, M.; Tham, F. S.; Abruña, H. D.; Arana, C. *Inorg. Chem.* **1993**, *32*, 4436-4449.

(35) Zelikovich, L.; Libman, J.; Shanzer, A. *Nature* **1995**, *374*, 790-792.

(36) Amendola, V.; Fabbrizzi, L.; Mangano, C.; Pallavicini, P. *Acc. Chem. Res.* **2001**, *34*, 488-493.

(37) Hawthorne, M. F.; Zink, J. I.; Skelton, J. M.; Bayer, M. J.; Liu, C.; Livshits, E.; Baer, R.; Neuhauser, D. *Science* **2004**, *303*, 1849-1851.

(38) Collin, J. P.; Durola, Fabien and Sauvage, J.P In *Electrochemically driven molecular machines based on transition -metal complexed catenanes and rotaxanes;* John Wiley & Sons, Inc., Ed.; Electrochemistry of functional supramolecular systems; 2010; Vol. 14, pp 425.

(39) Jimenez-Molero, M. C.; Dietrich-Buchecker, C.; Sauvage, J. P. *Chem. -Eur. J.* **2002**, *8*, 1456-1466.

(40) Chakrabarty, R.; Mukherjee, P. S.; Stang, P. J. *Chem. Rev.* **2011**, *111*, 6810-6918.

(41) Cárdenas, D. J.; Livoreil, A.; Sauvage, J. P. *J. Am. Chem. Soc.* **1996**, *118*, 11980-11981.

(42) Fahrenbach, A. C.; Barnes, J. C.; Li, H.; Benítez, D.; Basuray, A. N.; Fang, L.; Sue, C. H.; Barin, G.; Dey, S. K.; Goddard III, W. A.; Stoddart, J. F. *Proc. Natl. Acad. Sci. U. S. A.* **2011**, *108*, 20416-20421.

(43) Nicholson, R. S.; Shain, I. *Anal. Chem.* **1964**, *36*, 706-723.

(44) Livoreil, A.; Dietrich-Buchecker, C. O.; Sauvage, J. P. *J. Am. Chem. Soc.* **1994**, *116*, 9399-9400.

(45) Baumann, F.; Livoreil, A.; Kaim, W.; Sauvage, J. P. *Chem. Commun.* **1997**, 35-36.

(46) Poleschak, I.; Kern, J. M.; Sauvage, J. P. *Chem. Commun.* **2004**, *10*, 474-476.

(47) Raehm, L.; Kern, J. M.; Sauvage, J. P. *Chem. -Eur. J.* **1999**, *5*, 3310-3317.

(48) Collin, J. P.; Durola, F.; Mobian, P.; Sauvage, J. P. *Eur. J. Inorg. Chem.* **2007**, 2420-2425.

(49) Durola, F.; Sauvage, J. P. *Angew. Chem. , Int. Ed.* **2007**, *46*, 3537-3540.

(50) Durola, F.; Lux, J.; Sauvage, J. P. *Chem. -Eur. J.* **2009**, *15*, 4124-4134.

(51) Collin, J. -.; Gaviña, P.; Sauvage, J. P. *New J. Chem.* **1997**, *21*, 525-528.

(52) Furusho, Y.; Sanno, R.; Oku, T.; Takata, T. **2004**, *25*, 1641-1644.

(53) Günbas, D. D.; Brouwer, A. M. *J. Org. Chem.* **2012**, *77*, 5724-5735.

(54) Cao, J.; Fyfe, M. C. T.; Stoddart, J. F.; Cousins, G. R. L.; Glink, P. T. *J. Org. Chem.* **2000**, *65*, 1937-1946.

(55) Lane, A. S.; Leigh, D. A.; Murphy, A. *J. Am. Chem. Soc.* **1997**, *119*, 11092-11093.

(56) Carey, F. A. In *Advanced Organic Chemistry. Part B: Reaction and Synthesis, 3th Edition;* Springer: .

(57) Li, J. J.; Gribble, W. G. In *Palladium in Heterocyclic Chemistry, 1st Edition;* Elsevier Science: Oxford, 2000; .

(58) Aricó, F.; Badjic, J. D.; Cantrill, S. J.; Flood, A. H.; Leung, K. C. F.; Liu, Y.; Stoddart, J. F. *Top. Curr. Chem.* **2005**, *249*, 203-259.

(59) Gaviña, P.; Tatay, S. *Curr. Org. Synth.* **2010**, *7*, 24-43.

(60) Armaroli, N.; Balzani, V.; Collin, J. P.; Gavina, P.; Sauvage, J. P.; Ventura, B. *J. Am. Chem. Soc.* **1999**, *121*, 4397-4408.

(61) Dietrich-Buchecker, C. O.; Edel, A.; Kintzinger, J. P.; Sauvage, J. P. *Tetrahedron* **1987**, *43*, 333-344.

(62) Kolb, H. C.; Finn, M. G.; Sharpless, K. B. *Angew. Chem. , Int. Ed.* **2001**, *40*, 2004-2021.

(63) Rostovtsev, V. V.; Green, L. G.; Fokin, V. V.; Sharpless, K. B. *Angew. Chem. , Int. Ed.* **2002**, *41*, 2596-2599.

(64) Dichtel, W. R.; Miljanić, O. S.; Spruell, J. M.; Heath, J. R.; Stoddart, J. F. *J. Am. Chem. Soc.* **2006**, *128*, 10388-10390.

(65) Megiatto Jr., J. D.; Schuster, D. I. *J. Am. Chem. Soc.* **2008**, *130*, 12872-12873.

(66) Collin, J. P.; Sauvage, J. P.; Trolez, Y.; Rissanen, K. *New J. Chem.* **2009**, *33*, 2148-2154.

(67) Collin, J. P.; Frey, J.; Heitz, V.; Sauvage, J. P.; Tock, C.; Allouche, L. *J. Am. Chem. Soc.* **2009**, *131*, 5609-5620.

(68) Collin, J. P.; Durola, F.; Frey, J.; Heitz, V.; Reviriego, F.; Sauvage, J. P.; Trolez, Y.; Rissanen, K. *J. Am. Chem. Soc.* **2010**, *132*, 6840-6850.

(69) Collin, J. P.; Durot, S.; Keller, M.; Sauvage, J. P.; Trolez, Y.; Cetina, M.; Rissanen, K. *Chem. -Eur. J.* **2011**, *17*, 947-957.

(70) Durot, S.; Mobian, P.; Collin, J. P.; Sauvage, J. P. *Tetrahedron* **2008**, *64*, 8496-8503.

(71) Mobian, P.; Collin, J. P.; Sauvage, J. P. *Tetrahedron Lett.* **2006**, *47*, 4907-4909.

(72) Collin, J. P.; Durot, S.; Sauvage, J. P.; Trolez, Y. *New J. Chem.* **2011**, *35*, 2009-2012.

(73) Belowich, M. E.; Stoddart, J. F. *Chem. Soc. Rev.* **2012**, *41*, 2003-2024.

(74) Meyer, C. D.; Forgan, R. S.; Chichak, K. S.; Peters, A. J.; Tangchaivang, N.; Cave, G. W. V.; Khan, S. I.; Cantrill, S. J.; Stoddart, J. F. *Chem. -Eur. J.* **2010**, *16*, 12570-12581.

(75) Gupta, K. C.; Sutar, A. K. *Coord. Chem. Rev.* **2008**, *252*, 1420-1450.

(76) Fenton, D. E.; Vigato, P. A. *Chem. Soc. Rev.* **1988**, *17*, 69-90.

(77) Sarma, R. J.; Nitschke, J. R. *Angew. Chem. , Int. Ed.* **2008**, *47*, 377-380.

(78) Meyer, C. D.; Joiner, C. S.; Stoddart, J. F. *Chem. Soc. Rev.* **2007**, *36*, 1705-1723.

(79) Hutin, M.; Schalley, C. A.; Bernardinelli, G.; Nitschke, J. R. *Chem. -Eur. J.* **2006**, *12*, 4069-4076.

(80) Leigh, D. A.; Lusby, P. J.; Teat, S. J.; Wilson, A. J.; Wong, J. K. Y. *Angew. Chem. , Int. Ed.* **2001**, *40*, 1538-1543.

(81) Wu, J.; Leung, K. C. -.; Stoddart, J. F. *Proc. Natl. Acad. Sci. U. S. A.* **2007**, *104*, 17266-17271.

(82) Yin, J.; Dasgupta, S.; Wu, J. *Org. Lett.* **2010**, *12*, 1712-1715.

(83) Hogg, L.; Leigh, D. A.; Lusby, P. J.; Morelli, A.; Parsons, S.; Wong, J. K. Y. *Angew. Chem. , Int. Ed.* **2004**, *43*, 1218-1221.

(84) Hutin, M.; Bernardinelli, G.; Nitschke, J. R. *Proc. Natl. Acad. Sci. U. S. A.* **2006**, *103*, 17655-17660.

(85) Fahrenbach, A. C.; Bruns, C. J.; Cao, D.; Stoddart, J. F. *Acc. Chem. Res.* **2012**, *45*, 1581-1592.

(86) Colasson, B. X.; Dietrich-Buchecker, C.; Sauvage, J. P. *Synlett* **2002**, 271-272.

(87) Bissell, R. A.; Cordova, E.; Kaifer, A. E.; Stoddart, J. F. *Nature* **1994**, *369*, 133-137.

(88) Altieri, A.; Gatti, F. G.; Kay, E. R.; Leigh, D. A.; Martel, D.; Paolucci, F.; Slawin, A. M. Z.; Wong, J. K. Y. *J. Am. Chem. Soc.* **2003**, *125*, 8644-8654.

(89) Clark, P. G.; Day, M. W.; Grubbs, R. H. *J. Am. Chem. Soc.* **2009**, *131*, 13631-13633.

(90) Dawson, R. E.; Lincoln, S. F.; Easton, C. J. *Chem. Commun.* **2008**, 3980-3982.

(91) Collin, J. P.; Durola, F.; Lux, J.; Sauvage, J. P. *Angew. Chem. , Int. Ed.* **2009**, *48*, 8532-8535.

(92) Nygaard, S.; Leung, K. C. F.; Aprahamian, I.; Ikeda, T.; Saha, S.; Laursen, B. W.; Kim, S. Y.; Hansen, S. W.; Stein, P. C.; Flood, A. H.; Stoddart, J. F.; Jeppesen, J. O. *J. Am. Chem. Soc.* **2007**, *129*, 960-970.

(93) Dietrich-Buchecker, C.; Sauvage, J. P. *Tetrahedron* **1990**, *46*, 503-512.

(94) Gibson, H. W.; Lee, S. H.; Engen, P. T.; Lecavalier, P.; Sze, J.; Shen, Y. X.; Bheda, M. *J. Org. Chem.* **1993**, *58*, 3748-3756.

(95) Gaviña, P.; Tatay, S. *Tetrahedron Lett.* **2006**, *47*, 3471-3473.

(96) Mathieu, J.; Gros, P.; Fort, Y. **2001**, *42*, 1879-1881.

(97) Saitoh, Y.; Koizumi, T.; Osakada, K.; Yamamoto, T. *Can. J. Chem.* **1997**, *75*, 1336-1339.

(98) Cammidge, A. N.; Crépy, K. V. L. *J. Org. Chem.* **2003**, *68*, 6832-6835.

(99) Cammidge, A. N.; Crépy, K. V. L. *Tetrahedron* **2004**, *60*, 4377-4386.

(100) Lee, A. S. Y.; Hu, Y. J.; Chu, S. F. *Tetrahedron* **2001**, *57*, 2121-2126.

(101) Tatay, S. Complejos Metálicos Biestables para la Electrónica Molecular: Síntesis y Organización sobre superfícies de Rotaxanos y Moéculas Imán, Universidad de Valencia, 2008.

(102) Ishiyama, T.; Murata, M.; Miyaura, N. *J. Org. Chem.* **1995**, *60*, 7508-7510.

(103) Fang, H.; Kaur, G.; Yan, J.; Wang, B. *Tetrahedron Lett.* **2005**, *46*, 1671-1674.

(104) Balamurugan, D.; Muraleedharan, K. M. *Tetrahedron* **2009**, *65*, 10074-10082.

(105) Chambron, J. C.; Sauvage, J. P.; Mislow, K.; De Cian, A.; Fischer, J. *Chem. -Eur. J.* **2001**, *7*, 4086-4096.

(106) Durola, F.; Durot, S.; Heitz, V.; Joosten, A.; Sauvage, J. P.; Trolez, Y. *J. Inclusion Phenom. Macrocyclic Chem.* **2011**, 1-9.

(107) Joosten, A.; Trolez, Y.; Collin, J. P.; Heitz, V.; Sauvage, J. P. *J. Am. Chem. Soc.* **2012**, *134*, 1802-1809.

(108) Golas, P. L.; Tsarevsky, N. V.; Sumerlin, B. S.; Matyjaszewski, K. *Macromolecules* **2006**, *39*, 6451-6457.

(109) Kim, K. Y.; Farley, R. T.; Schanze, K. S. *J. Phys. Chem. B* **2006**, *110*, 17302-17304.

(110) Armaroli, N. *Chem. Soc. Rev.* **2001**, *30*, 113-124.

(111) De Bruin, B.; Bill, E.; Bothe, E.; Weyhermüller, T.; Wieghardt, K. *Inorg. Chem.* **2000**, *39*, 2936-2947.

(112) Alyea, E. C.; Merrell, P. H. *Synth. React. Inorg. Met. -Org. Chem.* **1974**, *4*.

(113) Leigh, D. A.; Lusby, P. J.; McBurney, R. T.; Morelli, A.; Slawin, A. M. Z.; Thomson, A. R.; Walker, D. B. *J. Am. Chem. Soc.* **2009**, *131*, 3762-3771.

(114) Zhong, Z.; Postnikova, B. J.; Hanes, R. E.; Lynch, V. M.; Anslyn, E. V. *Chem. -Eur. J.* **2005**, *11*, 2385-2394.

(115) Timmons, J. H.; Martell, A. E.; Harris, W. R.; Murase, I. *Inorg. Chem.* **1982**, *21*, 1525-1529.

(116) Rothermel Jr., G. L.; Miao, L.; Hill, A. L.; Jackels, S. C. *Inorg. Chem.* **1992**, *31*, 4854-4859.

(117) Anbu, S.; Kandaswamy, M.; Selvaraj, M. *Polyhedron* **2012**, *33*, 1-8.

(118) Ganeshpandian, M.; Loganathan, R.; Ramakrishnan, S.; Riyasdeen, A.; Akbarsha, M. A.; Palaniandavar, M. *Polyhedron* **2013**, *52*, 924-938.

(119) Schmittel, M.; Michel, C.; Liu, S. X.; Schildbach, D.; Fenske, D. *Eur. J. Inorg. Chem.* **2001**, 1155-1166.

(120) Dietrich-Buchecker, C. O.; Sauvage, J. P. *Tetrahedron Lett.* **1983**, *24*, 5091-5094.

(121) Greene, T. W.; Wuts, P. G. M. In *Protective Groups in Organic Synthesis;* Wyley: 1999; .

(122) Ziessel, R.; Suffert, J.; Youinou, M. *J. Org. Chem.* **1996**, *61*, 6535-6546.

(123) Quek, S. Y.; Kamenetska, M.; Steigerwald, M. L.; Choi, H. J.; Louie, S. G.; Hybertsen, M. S.; Neaton, J. B.; Venkataraman, L. *Nat. Nanotechnol.* **2009**, *4*, 230-234.

(124) Ciszek, J. W.; Tour, J. M. *Tetrahedron Lett.* **2004**, *45*, 2801-2803.

(125) Saha, S.; Ravikumar, I.; Ghosh, P. *Chem. Commun.* **2011**, *47*, 6272-6274.

(126) Arena, G.; Bonomo, R. P.; Musumeci, S.; Purrello, R.; Rizzarelli, E.; Sammartano, S. *J. Chem. Soc. , Dalton Trans.* **1983**, 1279-1283.

(127) Fernandes, A. S.; Cabral, M. F.; Costa, J.; Castro, M.; Delgado, R.; Drew, M. G. B.; Félix, V. *J. Inorg. Biochem.* **2011**, *105*, 410-419.

(128) Nunes, R. M.; Delgado, R.; Cabral, M. F.; Costa, J.; Brandão, P.; Félix, V.; Goodfellow, B. J. *Dalton Trans.* **2007**, 4536-4545.

(129) Lu, T.; Chen, S.; Mao, Z.; Martell, A. E.; Ji, L. *Inorg. Chem. Commun.* **2003**, *6*, 1068-1070.

(130) Jagoda, M.; Warzeska, S.; Pritzkow, H.; Wadepohl, H.; Imhof, P.; Smith, J. C.; Krämer, R. *J. Am. Chem. Soc.* **2005**, *127*, 15061-15070.

(131) Scaltrito, D. V.; Thompson, D. W.; O'Callaghan, J. A.; Meyer, G. J. *Coord. Chem. Rev.* **2000**, *208*, 243-266.

(132) Kabehie, S.; Xue, M.; Stieg, A. Z.; Liong, M.; Wang, K. L.; Zink, J. I. *J. Am. Chem. Soc.* **2010**, *132*, 15987-15996.

(133) Ganeshpandian, M.; Loganathan, R.; Ramakrishnan, S.; Riyasdeen, A.; Akbarsha, M. A.; Palaniandavar, M. *Polyhedron* **2013**, *52*, 924-938.

(134) Marcus, R. A. *Discuss. Faraday Soc.* **1960**, *29*, 21-31.

(135) Joosten, A.; Trolez, Y.; Heitz, V.; Sauvage, J. P. *Chem. -Eur. J.* **2013**, *19*, 12815-12823.

(136) Fulmer, G. R.; Miller, A. J. M.; Sherden, N. H.; Gottlieb, H. E.; Nudelman, A.; Stoltz, B. M.; Bercaw, J. E.; Goldberg, K. I. **2010**, *29*, 2176-2179.

(137) Bao, D.; Millare, B.; Xia, W.; Steyer, B. G.; Gerasimenko, A. A.; Ferreira, A.; Contreras, A.; Vullev, V. I. *J. Phys. Chem. A* **2009**, *113*, 1259-1267.

(138) Steinke, N.; Jahr, M.; Lehmann, M.; Baro, A.; Frey, W.; Tussetschläger, S.; Sauer, S.; Laschat, S. *J. Mater. Chem.* **2009**, *19*, 645-654.

Chapter 2

Supramolecular metallostructures

Introduction

The self-assembly between transition metal ions and organic ligands bearing several coordination sites have afforded a wide variety of discrete multinuclear supramolecular architectures.[1-6] Depending on its shape and dimensionality, they can be classified in chains, stacks and helices (1D), metallacycles and grids (2D) and cages (3D), represented in Figure 2.1.[7] These supramolecular assemblies constitute a way of pre-organizing several metal centres in a well-defined discrete structure. Metal ions possess very accessible redox and spin states and their proximity in a regular array can lead to new cooperative effects in their redox or magnetic properties.[8-11] Besides, attending to memory storage applications, the 2D-grid like motif has been a particularly pursued topology since it constitutes a regular way of electrically addressing functional metal centres in 2D. Thereby, the electronic information contained in the metal centres can be read by spatially resolved techniques as Scanning Transmission Microscopy (STM).[12, 13] Furthermore, the self-organization of these structures onto surfaces has opened the possibility of having long-range ordered metal assemblies.[8, 14, 15]

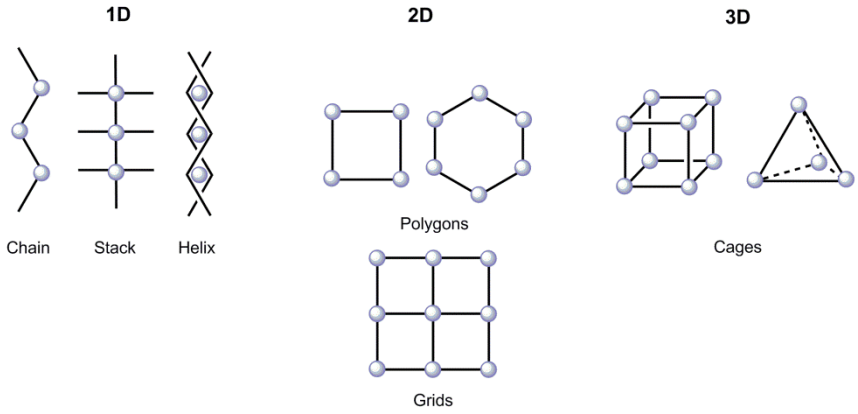

Figure 2.1 Supramolecular architectures of different dimensionality.

3D architectures, the so-called coordination cages, attract a special interest, not only because of their intrinsic aesthetical appeal, but also due to the presence of inner hollow

cavities that can encapsulate guest molecules giving rise to very rich and interesting host-guest chemistry.[16-20] Such cavities have demonstrated their capacities for host-guest recognition and anion sensing, and ultimately they have provided very reactive media for catalytic transformations.[21]

The construction of metallic superstructures requires the design and synthesis of polytopic ligands, whose coordination abilities, along with the coordination demands of the metal ions employed, are going to determine the nuclearity and stoichiometry of the resulting assembly. Coordination-driven self-assembly processes are governed by the 'maximal site occupancy' principle,[22] consisting in the highest fulfilment of the coordination requirements of both ligands and metal ions. According to this principle, and taking advantage of the high directionality of the coordination bond, the proper election of the ligand and metal ions enables a good control over the final shape of the supramolecular assembly. Besides, due to the high kinetic reversibility of coordination bonds, the system rapidly evolves to these thermodynamically favoured species, and thus, a high degree of selectivity can be reached.[7]

Figure 2.2, illustrates the two main strategies that can be distinguished in the construction of supramolecular architectures: the coplanar and the non-coplanar strategy.[23] The first one relies on the use of exotopic ligands and affords structures in which the metal center and the ligand axis remain in the same plane. The second one is based on the use of endotopic ligands, and leads to structures in which the ligands constitute the edges of the polygons or cages in the final assembly. This last can be further divided in interwoven or parallel arrays depending on the relative orientation of the different chelating units in the same ligand.

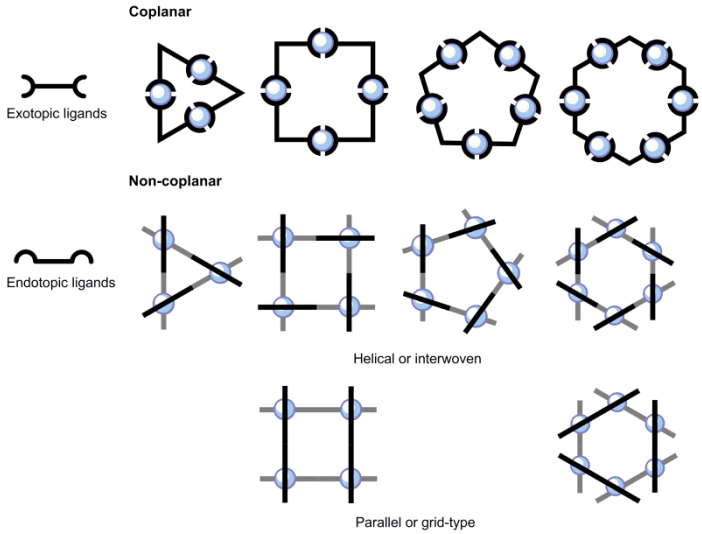

Figure 2.2 Scheme of the different strategies employed in the construction of metallacycles.

Results and discussion

Few years ago, our group initiated the employment of terpy and phen conjugates for the construction of supramolecular metallostructures. The first ligand explored, **A**,[24] surged from the synthesis of shuttling copper-based rotaxanes (see chapter 1) and comprised two different coordination sites, a terpy and a phen unit connected along their 5- and 3-position respectively, see Figure 2.3. **A** is an endotopic ligand in which the presence of one bidentate and another tridentate chelating site can be used for the construction of unusual supramolecular assemblies with metal ions presenting coordination indices from 4 to 6.

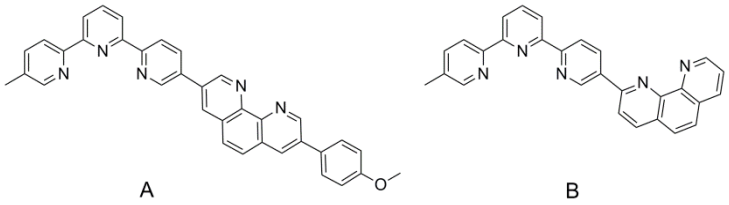

Figure 2.3 Chemical structure of ligands **A** and **B**.

For example, when heteroditopic ligand **A** was combined with Cu(II) in a 1:1 stoichiometry, due to the known tendency of Cu(II) ion to form pentacoordinated complexes with pyridine-type ligands,[25] the self-assembly process afforded homometallic metallacycles with M_nL_n stoichiometries. Triangles turned out to be the predominant species in solution, along with some contributions of tri, tetra and pentanuclear species. However, in the solid state, a hexanuclear interwoven metallacycle could be isolated.[23] In this assembly, six equivalent Cu(II) ions were coordinated by a phen and a terpy unit of two different ligands, affording (2+3) coordination indexes. This structure constituted the first molecular hexagon of the grid-type family based on a hexanuclear Cu(II) complex of a heteroditopic ligand.

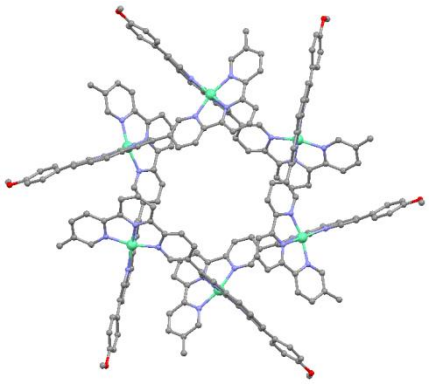

Figure 2.4 Crystal structure of the $[Cu_6\mathbf{A}_6](PF_6)_{12}$ metallacycle. Counterions have been omitted for clarity.[23]

Continuing with this work, during this thesis we have explored the combination of ligand **A** with tetra and hexacoordinated metal ions for the construction of metallostructures with different shapes and nuclearities.

Next experiments were directed to the combination of ligand **A** with Fe(II) ions. In this case, the preference of the metal for octahedral geometries could be satisfied by its combination with **A** in a 5:6 (M:L) stoichiometry that fully saturates the coordination demands of both, metal and ligand. The resulting structure consisted on a trigonal bipyramid cage comprising iron atoms in two different coordination environments, $[Fe(phen)_3]^{2+}$ (2+2+2) and $[Fe(terpy)_2]^{2+}$ (3+3), as illustrated in Figure 2.5, centre.[26] The preparation and characterization of this cage will be discussed in the following section.

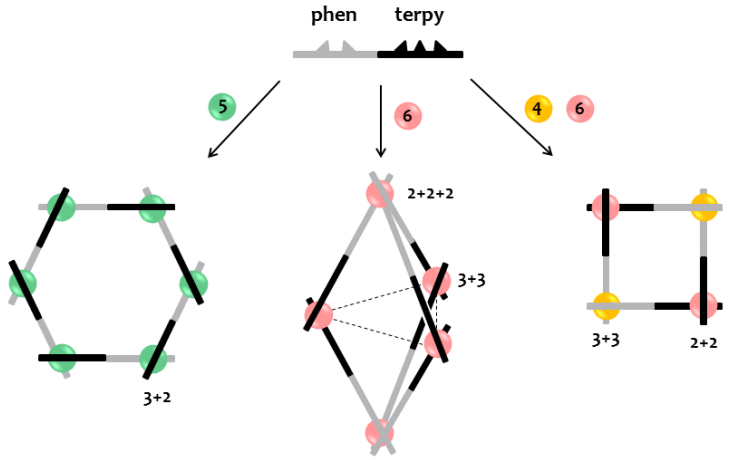

Figure 2.5 Self-assembly of a (3+2) hexagon (left), a (2+2+2)-(3+3) cage (middle) and a (2+2)-(3+3) square (right) superstructures from a phen-terpy conjugate with metal ions of specified coordination indexes.

Finally, in view of the well-known stability of tetrahedral $[Cu(phen)_2]^+$ (2+2) and octahedral $[Fe(terpy)_2]^{2+}$ (3+3) complexes, we have explored the possibility of using these two different metal ions for the preparation of heterometallic square metallacycles with conjugate **A** in a (2+2), (3+3) fashion (Figure 2.5, right). However, the exploitation of this ligand for the construction of heterometallic grids did not yield to the quantitative formation of the pursued [2x2] grid. When 1:1:2 mixtures of Cu(I), Fe(II) and **A** were analyzed by mass spectroscopy they presented a high number of peaks, but only a couple of them could be assigned to the $[Fe_2Cu_2\mathbf{A}_4]^{6+}$ stoichiometry (annex). Very basic modelling suggested that in this case the resulting species were highly tensioned. As a result we hypothesized that any modification in the phen/terpy connectivity that reduces this strain should improve the results. That idea inspired the synthesis of ligand **B** in which the same coordination moieties present in **A** are linked in a different way: instead of connecting the phen and terpy moieties by their 3- and 5- positions in this case the 2-position of the phen is bonded to the 5-position of the terpy (see Figure 2.3).

According to the predictions, the new relative orientation of the two chelating sites in ligand **B** resulted in a decrease of the tension of the supramolecular assembly which

enabled the easy isolation of a series of heterometallic square grids that would be described in this section. By contrast, reaction of **B** with metal salts in the same conditions employed in the preparation of the Cu(II) metallacycles and the pentanuclear Fe(II) cage from **A,** did not afford any closed structure.

2.1 Self-assembly of a Fe(II) pentanuclear cage

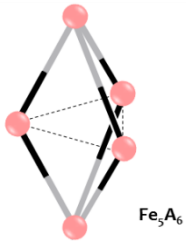

A very common strategy for obtaining metallosupramolecular cages consists in the use of relatively labile octahedral metal centers and linear homoditopic bis-bidentate bridging ligands capable of coordinating transition metal ions in a non-coplanar situation. Thereby, architectures with $M_{2n}L_{3n}$ stoichiometry are obtained, being M_4L_6 tetrahedral cages the most common structures.[5, 27-33] The 2M : 3L ratio reflects the coordinative demands of the metal ions; while each metal requires six coordinating atoms to complete its coordination sphere, each ligand provides only four donor atoms. This results in the formation of tetrahedral cages in which metals occupy the vertex of the polyhedron while bridging ligands spans along the edges as illustrated on top Figure 2.6. By contrast, the use of homoditopic bis-tridentate ligands with octahedral metal centres mostly results in the formation of planar metallacycles[3, 34-36] or 2-stranded helicates in a M_nL_n stoichiometry.[37-43]

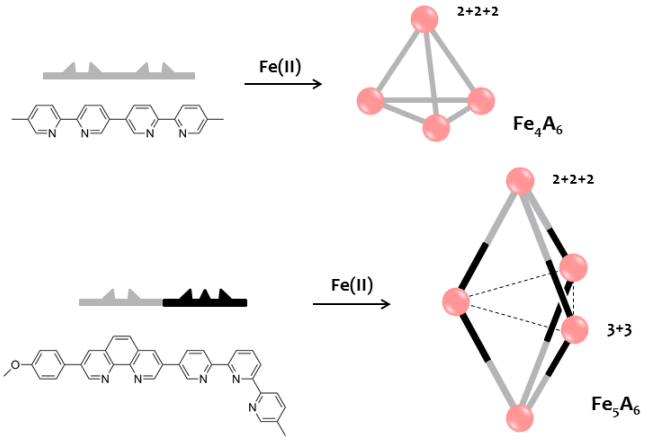

Figure 2.6 Different coordination cages based on Fe(II).

According to the maximum occupancy principle, heterotopic ligand **A**, which possesses five donor atom in total, was combined with Fe(II) octahedral metal centers in 6:5 ratio for the formation of a supramolecular cage of formula $[Fe_5\mathbf{A}_6](PF_6)_{10}$. This metallostructure presents a trigonal-bipyramidal geometry in which, in order to saturate the coordination demands of the Fe(II), equatorial positions are constituted by three units $Fe(phen)_3$, while two $Fe(terpy)_2$ units rest on the two remaining apical positions, as represented in Figure 2.6.

2.1.1 Synthesis and characterization

Scheme 2.1 shows the synthesis of ligand **A** carried out by the Suzuki cross-coupling of neopentil boronic ester **12**, seen in the previous chapter, with 3-Bromo-8-(p-methoxyphenyl)-1,10-phenanthroline, as described in a previous publication.[24] Asymmetric phen **37** was previously prepared from 3-bromo-phenanthroline **11** and 4-methoxyphenyl neopentyl boronic (**36**) ester in similar conditions to that used in the preparation of **5**.

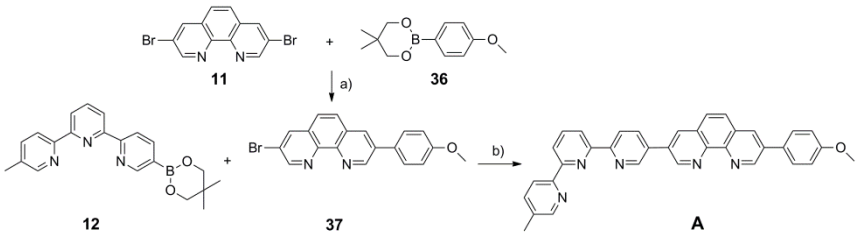

Scheme 2.1 Synthesis of ligand **A**: **a)** $Pd(PPh_3)_4$, toluene, Na_2CO_3, H_2O (80 %); **b)** $Pd(PPh_3)_4$, DMF, K_2CO_3, H_2O (67 %).

The reaction of **A** with $FeSO_4{\cdot}7H_2O$ in refluxing 1:1 acetone: water mixture, resulted in a deep red solution characteristic of low-spin $Fe(terpy)_2^{2+}$ and $Fe(phen)_3^{2+}$ chromophores. Anion exchange with excess of KPF_6 led to the isolation of the pentanuclear complex as a dark red precipitate in quantitative yield. Acetonitrile solutions of $[Fe_5\mathbf{A}_6](PF_6)_{10}$ yielded UV-Vis spectra showing intense absorption bands in the UV region associated with the ligand, and a band centred in the visible region (λ_{max} = 534 nm, ε = 23700·M^{-1}·cm^{-1}) associated with a MLCT transition as reported for other similar Fe(II)-oligopyridyl complexes (see annex).[44-46]

When solutions of $[Fe_5\mathbf{A}_6](PF_6)_{10}$ in acetonitrile at different concentrations were analyzed by ESMS (Figure 2.7) only signals of the intact pentanuclear cluster and the mononuclear compound $[Fe\mathbf{A}_2]^{2+}$ can be detected in the mass spectra. A clear sequence of peaks corresponding to the successive losses of PF_6^- anions was observed for the species $[Fe_5\mathbf{A}_6(PF_6)_{10-n}]^{n+}$ with *n* typically in the range 3-6. All isotopic profiles were in accordance with the theoretical predicted shapes. The absence of any signal attributable to other oligomeric structures in these experiments proved the selective formation in solution of discrete metallo-supramolecular species of formula $[Fe_5\mathbf{A}_6]^{10+}$

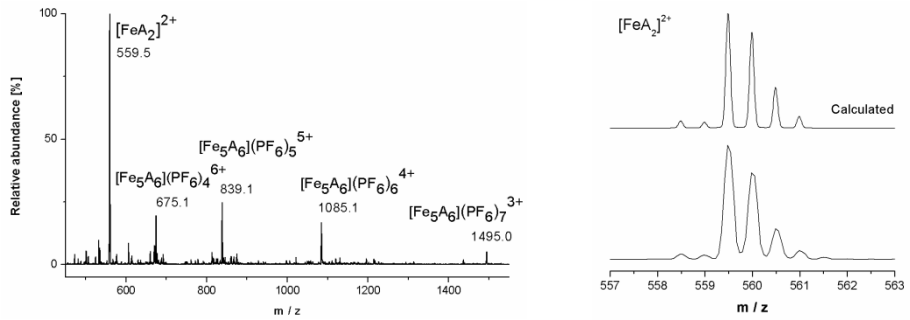

Figure 2.7 Positive ESMS spectra in acetonitrile of 1:1:2 mixtures of 5:6 Fe: **A** and isotopic profile of the [Fe**A**$_2$]$^{2+}$ peak.

Mononuclear complex [Fe**A**$_2$](PF$_6$)$_2$ was synthesized for comparison purposes by refluxing in acetone-water a 2:1 mixture of **A** and FeSO$_4$, followed by anion exchange with KPF$_6$. The aromatic part of the ^{1}H NMR spectra of ligand **A**, and complexes Fe**L**$_2$ and Fe$_5$**L**$_6$ are depicted in Figure 2.8. All the peaks were assigned with the aid of standard 2D COSY, NOESY and ROESY experiments and by comparison with other octahedral Fe(II) polypyridine complexes (see annex). On passing from **A** to Fe**A**$_2$, protons T6 and T6" of the terpy moiety undergo an important upfield shift ($\Delta\delta$~ 1.6-1.8 ppm) due to the proximity of these protons to the diamagnetic field of the opposite terpy pyridine rings in the Fe(terpy)$_2^{2+}$ complex, whereas proton T4' is downfield shifted due to coordination of the pyridine ring to the metal ion. Peaks corresponding to the free phen unit do not experiment significant changes, with the only exception of proton P2, which resonates at lower frequency probably due to the shielding ring currents of the opposite terpy fragment. This is also confirmed by the observation of a ROE effect between protons P2 and T6 (see annex), indicating a *cis* conformation of the terpy and phen moieties of the ligand **A** in the mononuclear complex.

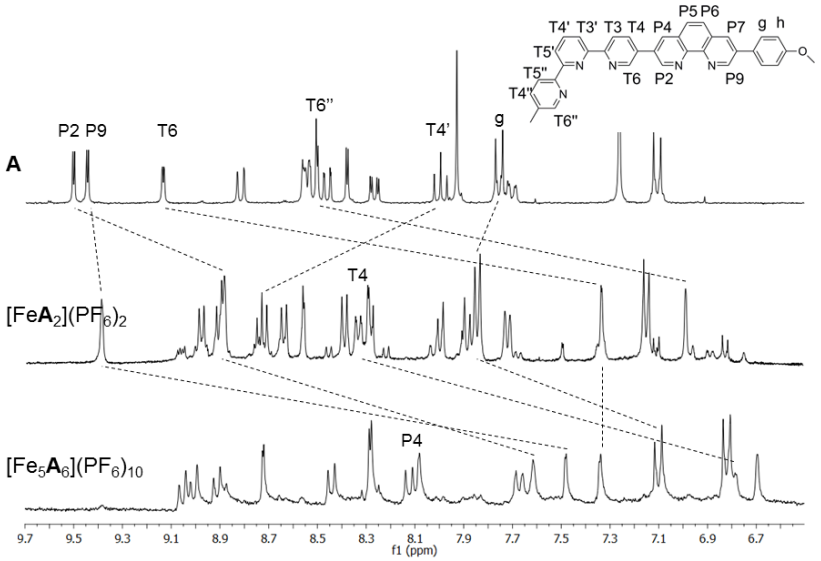

Figure 2.8 Partial ^{1}H NMR spectra of **A** ($CDCl_3$), [Fe**A**$_2$]$(PF_6)_2$ (CD_3CN) and [Fe$_5$**A**$_6$]$(PF_6)_{10}$ (CD_3CN).

^{1}H NMR spectra of [Fe$_5$**A**$_6$]$(PF_6)_{10}$ in acetonitrile-d_6 shows only one set of signals for the protons of **A**, which is in accordance with the presence in solution of a highly symmetric single species, in which all the ligands are in equivalent environments. Comparison between the ^{1}H NMR spectrum of [Fe$_5$**A**$_6$]$(PF_6)_{10}$ with that of [Fe**A**$_2$]$(PF_6)_2$ reveals an important shielding of the phen protons P9 and P2 ($\Delta\delta\sim$ 1.9 and 1.3 ppm) due to the coordination to Fe(II), and also a significant shielding of g protons. Most of the protons of the terpy moiety experimented little variations in their chemical shifts, except proton T4, which is also upfield shifted ($\Delta\delta\sim$ 1.5 ppm). This is the consequence of a *trans* disposition of the phen and terpy units in ligand **A**, which situates T4 on the shielding ring current of the phen ring of an opposite ligand (see Figure 2.10). This *trans* conformation was confirmed by ^{1}H-^{1}H NOESY experiments (see annex) which evidence correlations between protons P4 and T6 and protons P2 and T4.

The redox properties of [Fe$_5$**A**$_6$]$(PF_6)_{10}$ and [Fe**A**$_2$]$(PF_6)_2$ in acetonitrile were investigated by cyclic voltammetry and differential pulse voltammetry. Compound [Fe$_5$**A**$_6$]$(PF_6)_{10}$ undergoes a single quasi reversible oxidation process at 1.2 V (vs SCE), which can be assigned to the one-electron Fe(II/III) oxidation.[47] The absence of any electronic coupling

between metal centres has been previously observed for other polynuclear complexes based on ligand **A**,[23, 48] and has been ascribed to the high distance between the metal centres.

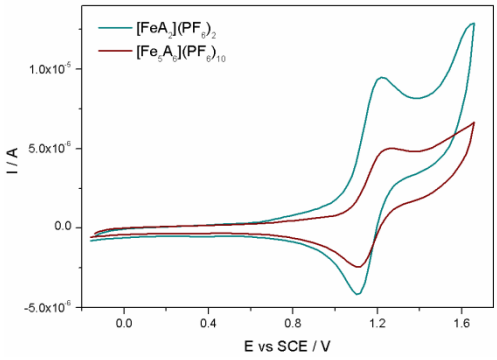

Figure 2.9 Cyclic voltammogram at 0.1 V/s scan rate ($1 \cdot 10^{-3}$ M based on Fe) in acetonitrile using TBA(PF_6) 0.1 M as supporting electrolyte. Electrochemical potentials have been referenced to SCE according to the potential of the Ferrocene/Ferricinium couple (0.45 V vs SCE in acetonitrile).[49]

All attempts to grow crystals of $[Fe_5\mathbf{A}_6](PF_6)_{10}$ suitable for X-ray diffraction were unsuccessful. Nevertheless, ESMS and 1D and 2D ^{1}H NMR data support the trigonal bipyramidal structure in which all the Fe(II) ions are situated in an octahedral coordination sphere.

To gain further insight into the structural characteristics of $[Fe_5\mathbf{A}_6](PF_6)_{10}$, density functional theory (DFT) calculations were undertaken for the energy minimized structure at the B3LYP level, considering the sole existence of **A** in a *trans* conformation as evidenced by the ^{1}H NMR data. Coordination around Fe atoms presents a pseudo-octahedral symmetry. The distances Fe-N are 2.03-2.08 Å, and the angles between opposite N atoms are around 175.4^0. In addition, ligand **A** is twisted around the bond between phen and terpy units giving rise to an angle of $32.2^0 - 32.6^0$.

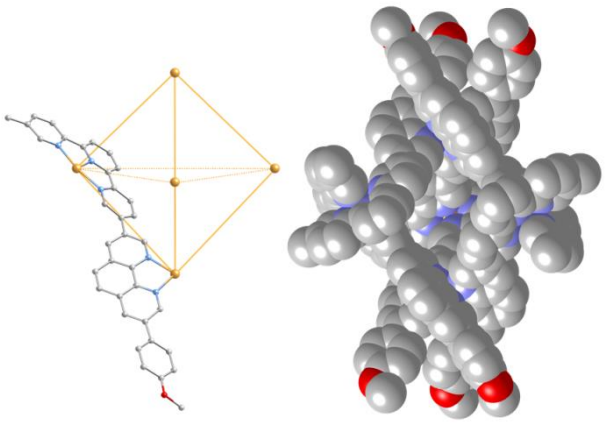

Figure 2.10 Schematic representation of $[Fe_5\mathbf{A}_6](PF_6)_{10}$ with only one ligand shown for clarity (left). Space-filling representation of the optimized DFT structure (right).

Only considering the metal centers, the optimized structure (see Figure 2.10) shows a D_{3h} symmetry, even though the organic ligand gives it some helical nature. The structure presents a distance of 13 Å between iron atoms in the central plane and 8.5 Å between the apical ones and this plane. From these distances we have estimated a 'door' of ca. 100 $Å^2$ and an internal cavity size of about 415 $Å^3$. This calculation has been done considering the molecule as a simple trigonal bipyramid with volumeless lines between the iron atoms.

In order to investigate the possible host-guest chemistry arising from the inner cavity of the cage we carried out some inclusion experiments with different anionic guests: PF_6^-, BF_4^-, SbF_6^- and $B(p\text{-}C_6H_5F)_4$. Since the cage is positively charged, first approaches were carried out with negatively charged guests. Additionally, we opted for fluorinated anions in order to study the host-guest properties by ^{19}F NMR in CD_3CN in a NMR tube.[5] Unfortunately, only one set of signals were obtained for each anion. In the case of the smaller anions (BF_4^-, PF_6^- and SbF_6^-), this result is ascribed to a fast exchange (in the NMR timescale) of the anion, in and out of the cage through the door of the cavity. In the case of the bulkier tetrakis(4-flurophenyl) borate, the anion may be too bulky to be encapsulated. Finally, we performed NMR tube assays at room temperature with the

neutral molecule trans-decaline,[32] but no evidence of two different environments for the guest molecule were detected by ^{1}H NMR.

Even though other late first-row octahedral transition metals such as Co(II) or Zn(II) have been used instead of iron, none of them afforded well-defined products. This fact highlights the strong binding and mutual stabilization between Fe(II) and imine ligands.

2.2 One-step preparation of [2x2] heterometallic grids from ligand B

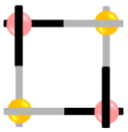

$M(II)_2M(I)_2B_4$

The self-assembly between ditopic ligands and metal ions has led to the preparation of a large family of homometallic [2x2] grids. However, up to date, only a few examples of heterometallic [2x2] grids with either homoditopic or heteroditopic ligands have been reported.[9, 10, 50-56] When homoditopic ligands are employed, the coordination sites are undistinguishable, and thus, the synthesis of heterometallic grids requires a sequential self-assembly starting from very stable corner-type precursors,[9, 10] or a stepwise protection/deprotection procedure.[10, 50] Stepwise procedures have also been employed with heteroditopic ligands[50-52, 56] although, when the coordination sites are different enough, heterometallic [2x2][53, 54] or [3x3][55, 57] grids can be formed in one single step by taking advantage of the different coordination preferences of the two metal ions involved.[53-55, 57] For instance, the mixing of Cu(I) and Zn(II) with a ligand possessing two binding sites, a bidentate α,α'-bipyridine and a tridentate unit including a 8-hydroxyquinoline, directs the formation of a [2x2] grid in a toposelective self-assembly process.[53]

In this case, the novel heteroditopic ligand **B** has demonstrated its ability for the construction of a family of heterometallic [2x2] grids by one-pot self-assembly with

different combinations of octahedral (Fe(II), Co(II)) and tetrahedral (Cu(I), Ag(I)) metal ions.

2.2.1 Synthesis of ditopic ligand B

Ligand **B** was prepared as depicted in Scheme 2.2 by the Suzuki cross-coupling of terpy boronic ester derivative **12** and 2-chloro-1,10-phenanthroline (**34**), in analogous conditions to that used in the synthesis of **A**. Compound **34** had previously been synthesized in 3 steps from commercial precursors. First, alkylation of 1,10-phenanthroline with methyl methanesulfonate gave 1-methyl-1,10-phenanthrolinium mesylate (**32**) in almost quantitative yield. Next, phenanthrolinium salt **32** was oxidized with MnO_2 as described by Johnson et *al*.[58] to give **33**. Finally, the treatment of **33** with PCl_5 and $POCl_3$ afforded the desired chlorophenanthroline **34**.[59]

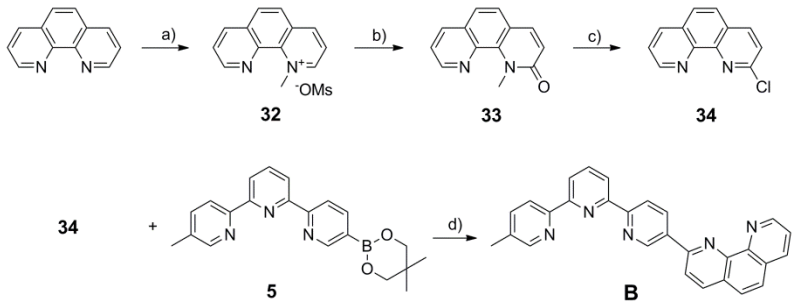

Scheme 2.2 Synthesis of ligand **B**: **a)** Methyl methanesulfonate, toluene, 100 ^{0}C (99%); **b)** MnO_2, THF, reflux (90 %); **c)** $POCl_3$, PCl_5, reflux (80 %); **d)** $Pd(PPh_3)_4$, DMF, K_2CO_3, H_2O, 100 ^{0}C (77%).

2.2.2 Self-assembly of the squares

When acetonitrile solutions of 1:1:2 Cu(I):Fe(II):**B** mixtures were analyzed by ESMS, peaks corresponding to $[Fe_2Cu_2\mathbf{B}_4]^{6+}$ were clearly identified. In order to obtain more information about the assembly process, the Fe(II) corner precursor $[Fe\mathbf{B}_2]^{2+}$ was studied by ^{1}H NMR spectroscopy. For that purpose, $Fe(BF_4)_2{\cdot}(H_2O)_6$ and ligand **B** were mixed in acetonitrile in a 1:2 molar ratio at room temperature, leading to the quantitative

formation of the iron corner complex within 30 min, as confirmed by ESMS. Precipitation with aqueous KPF_6 afforded $[Fe\mathbf{B}_2](PF_6)_2$ as a dark solid showing a deep purple colour characteristic of low spin $[Fe(terpy)_2]^{2+}$ complexes in solution.[44-46]

The ^1H NMR spectrum of $[Fe\mathbf{B}_2](PF_6)_2$ presented the same number of sharp signals than that of the free ligand (see Figure 2.11). This indicates that $[Fe\mathbf{B}_2]^{2+}$ is the only species present in solution and that the two coordinating ligands are equivalent. In the NMR spectra, the set of signals corresponding to the terpy moiety are considerably shifted compared to those of the free ligand. Particularly, T4' proton exhibited a large upfield shift, whereas signals coming from T6 and T6" protons are significantly downshifted. These last shifts can be explained by the octahedral geometry adopted by the two terpy around the iron atom that places these two protons in the diamagnetic field of the pyridine rings. By contrast, the signals corresponding to the phen moiety are only slightly downfield shifted. These facts confirm the hexacoordination of Fe(II) by the terpy moieties of two different ligands, leaving the phenanthroline moieties uncoordinated. Analogous displacements of the proton resonances were observed in the $[Fe\mathbf{A}_2](PF_6)_2$ complex.

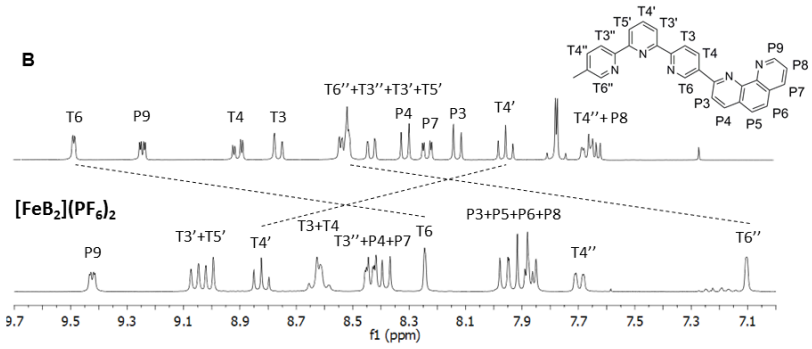

Figure 2.11 ^1H NMR spectra of ligand **B** and $[Fe\mathbf{B}_2](PF_6)_2$ in CD_3CN.

Heterometallic $[Fe_2Cu_2\mathbf{B}_4]^{6+}$ grid was prepared in one-pot in acetonitrile solution by either the direct combination of $Fe(BF_4)_2{\cdot}(H_2O)_6$ and $[Cu(CH_3CN)_4](PF_6)$ salts with **B** in a 1:1:2 molar ratio, or by the sequential addition of the two metal salts in the same

stoichiometry. The sequential procedure was carried out in one-pot by the first preparation of the $[Fe\mathbf{B}_2]^{2+}$ corner complex and following addition of the Cu(I) salt. After 30 minutes of stirring at room temperature, the presence of the heterometallic square of formula $[Fe_2Cu_2\mathbf{B}_4]^{6+}$ in the resulting deep red solutions was verified by ESMS (Figure 2.12 A). However, NMR spectra of the solution displayed only broad signals. This fact could respond to the fast exchange between species of different nuclearity.[16, 60]

The ESMS spectra showed 3 different signals for the tetranuclear species corresponding to the consecutive loss of PF_6^- anions. In addition, signals coming from dinuclear species of formula $[FeCu\mathbf{B}_2]^{3+}$ could be observed. In order to discern if these species were present in the solution or were a product of the fragmentation of the tetramer in the gas ionization phase, a study of the variations of ESMS peaks intensity with concentration and with extraction voltage was performed. These experiments revealed that the dimer/tetramer ratio decreased when the total concentration of the solution was increased (Figure 2.12 C). This fact can be clearly observed in Figure 2.12 B, in which the isotopic profile of the peak at *m*/*z* 557 (corresponding to both, the dimer and the tetramer) is represented as a function of the concentration. At a concentration of 0.5 mM (based on the ligand) the isotopic profile perfectly matches with that predicted for the $[FeCu\mathbf{B}_2](PF_6)^{2+}$ dimer, but at 8 mM the contribution of $[Fe_2Cu_2\mathbf{B}_4](PF_6)_2^{2+}$ becomes important. This is the expected tendency when there is a dynamic exchange between polynuclear species, that is, the formation of larger aggregates is favored at higher concentrations. By contrast, the dimer/tetramer ratio remained almost unchanged when extraction voltage was increased from 5 to 20V (Figure 2.12 D). According to this, the dimer would be the result of a dynamic equilibrium in solution, and thus, its appearance in the ESMS is not just a consequence of fragmentation of the tetramer in the gas-ionization process. This equilibrium between dimeric and tetrameric species in solution has been observed before in other metallostructures.[23]

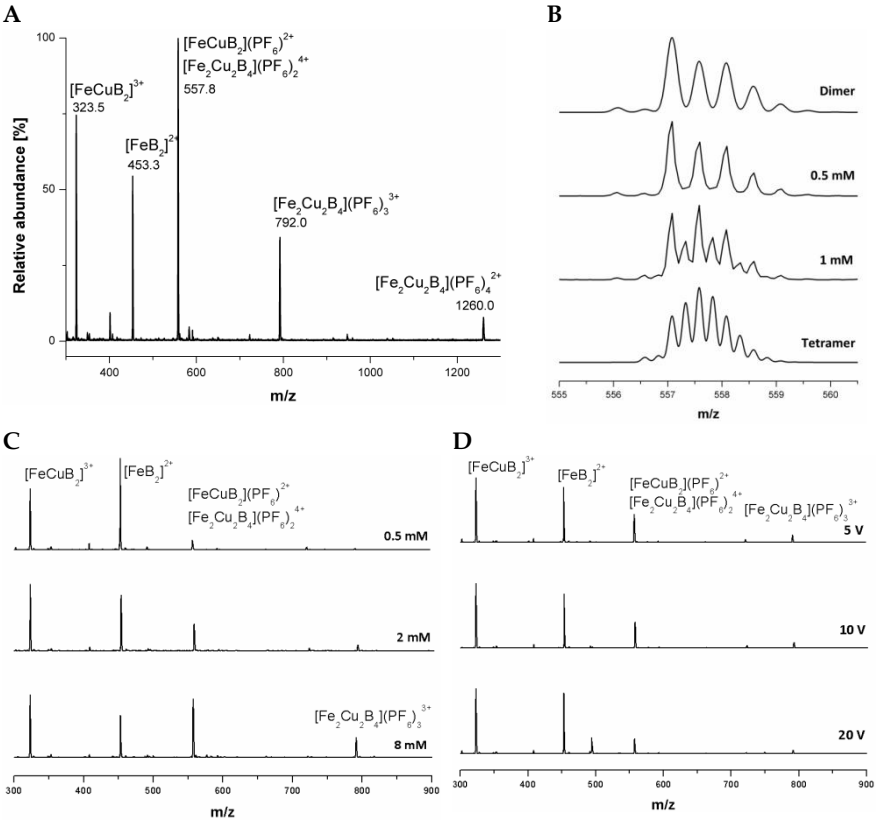

Figure 2.12 Positive ESMS spectra in acetonitrile of 1:1:2 mixtures of Fe:Cu:**B a)** ESMS spectra of 2 mM solutions; **b)** Experimental isotopic profile of peak m/z= 557 at a extraction voltage of 10V and calculated isotopic profiles of species $[FeCu\mathbf{B}_2](PF_6)^{2+}$(dimer) and $[Fe_2Cu_2\mathbf{B}_4](PF_6)_2^{4+}$ (tetramer); **c)** Complete spectra of different concentration solutions at a extraction voltage of 10V; **d)**. Complete spectra at different extraction voltages of 2 mM solutions. Concentration values are based on the ligand.

The redox properties of $[Fe\mathbf{B}_2](PF_6)_2$ and $[Fe_2Cu_2\mathbf{B}_4](PF_6)_6$ in acetonitrile were investigated by cyclic voltammetry and differential pulse voltammetry (Figure 2.13). Both complexes exhibit a single quasi reversible oxidation process at 1.1 V vs SCE associated to the one-electron Fe(II/III) oxidation[47] and a less intense wave at lower potentials. The oxidation wave corresponding to the Cu(I/II) was not visible in the cyclic voltammogram of $[Fe_2Cu_2\mathbf{B}_4](PF_6)_6$. As in the $[Fe_5\mathbf{A}_6](PF_6)_{10}$ cage, no electric coupling between metal centres was observed.

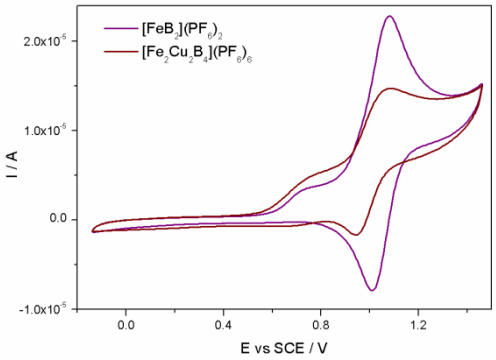

Figure 2.13 Cyclic voltammogram at 0.1 V/s scan rate ($1 \cdot 10^{-3}$ M based on Fe) in acetonitrile using TBA(PF_6) 0.1 M as supporting electrolyte. Electrochemical potentials have been referenced to SCE, according to the potential of the Ferrocene/Ferricinium couple (0.45 V vs SCE in acetonitrile).[49]

When diisopropyl ether was slowly diffused into 1:1:2 Fe(II):Cu(I):**B** acetonitrile mixtures, single crystals suitable for X-Ray diffraction, corresponding to the tetranuclear [2x2] coordination assembly, could be isolated. Within this structure four equivalent ligands define the sides of a molecular square with one metal ion placed in each vertex (Figure 2.14 A). Two copper atoms occupy opposite vertices and are tetracoordinated by two phen moieties, whereas two hexacoordinated iron atoms are placed in the other two vertices surrounded by two terpys. The ligands adopt a transoid orientation in which terpy and phen coordinating units are pointing into opposite directions with an angle of approximately 45 deg with respect to each other. The metal centres are separated by approximately 7.2 Å from one another.

Most surprisingly, the charge of the tetranuclear complex is balanced by seven PF_6^- counterions. This implies that, on average, one metal centre is oxidized in each square. Since the electrochemical potential of the [Fe(terpy)$_2$](II/III) couple[47] is considerably above than that of the [Cu(phen)$_2$](I/II) couple, 0.19 vs SCE,[61] and there are no $[Fe^{III}(terpy)_2]^{2+}$ complexes described in the literature, the oxidized metal would most probably correspond to Cu(II), leading to a species of formula [Fe(II)Cu(I)Cu(II)**B**$_4$](PF_6)$_7$. Notice that this 1:1 Cu(I)/Cu(II) ratio is not detected by ESI-MS in the initial solution or by microanalysis (EDAX) of the powder resulting from the precipitation of the complex with KPF_6.

Both iron atoms present a similar pseudooctahedral coordination sphere with terminal pyridine rings pulled into the metal center (N-Fe-N 162º) and Fe-N distances varying between 1.97-1.99 Å for external pyridines and 1.88-1.89 Å for the central pyridine rings. In both cases the terpy planes around the metal ion remain almost perpendicular. By contrast, the two copper centres of the square present dissimilar coordination geometries. This fact supports the assumption that one metal centre is Cu(I) and the other one is Cu(II). The distortion of the coordination sphere has been assessed by White's model, according to which an ideal tetrahedron possess $\theta_x = \theta_y = \theta_z = 90º$.[62] The parameters obtained for each copper ion from the crystal structure of the Fe-Cu grid are depicted in Table 2.1. The two coppers show heavily distorted tetrahedral coordination geometries, which are, at the same time, very different from each other. These differences are especially important in θ_z, whose deviation from 90º is related to the twisting between the two phen planes. For both ions Cu-N distances vary between 2.03 and 2.08 Å.

Table 2.1 Orientation angles (defined in reference[62]) for the Fe-Cu and Co-Cu grids.

	θ_x / º	θ_y / º	θ_z / º
Fe-Cu1	77.0	93.1	80.0
Fe-Cu2	73.9	101.8	101.0
Co-Cu1	91.2	110.5	92.0
Co-Cu2	93.1	110.0	94.2

Concerning the supramolecular packing of the [2x2] units, the crystal is stabilized by a relatively strong (3.32 Å) π-π stacking interaction between pyridyl rings of phenanthroline of neighbouring molecules, as illustrated in Figure 2.14 B.

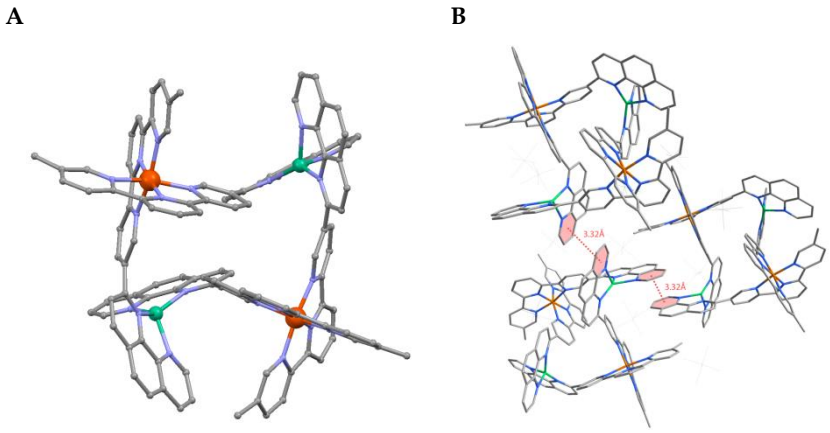

Figure 2.14 Crystal structure of the $[Fe_2Cu_2\mathbf{B}_4](PF_6)_7$ grid (**A**), and crystal packing (**B**). The π-π stacking is denoted. Counterions have been omitted for clarity.

The magnetic susceptibility of powder samples of $[Fe_2Cu_2\mathbf{B}_4](PF_6)_6$ tetranuclear system was recorded in the 300 K – 2 K temperature range under an external applied field of 1000 G. The χT product of $[Fe_2Cu_2\mathbf{B}_4](PF_6)_6$ remains approximately constant (0.002 emu.K.mol^{-1}) throughout the entire temperature range measured, consistent with that expected for isolated Fe(II) ions in a low spin state.

Despite we tested several crystallization conditions, in any case we were able to obtain single crystals of the dinuclear $[FeCu\mathbf{B}_2]^{3+}$ species observed in the ESMS spectra. This is in agreement with the predominance of square structures at high concentrations. Nevertheless, for this dinuclear species we propose a double-stranded helical arrangement with Fe(II) and Cu(I) respectively coordinated by two terpyridines and two phenanthrolines, that satisfy the coordination demands of both metal ions (see Figure 2.15). Similar helical arrangements have been previously observed in dinuclear complexes obtained upon the combination of polypyridine ditopic ligands with transition metal ions.[63-65]

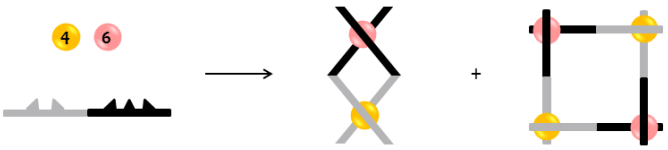

Figure 2.15 Self-assembly of an-equilibrating mixture of double helical and square [2x2] grid complexes from **B**, M(I) and M(II) ions.

Encouraged by the isolation of the Fe-Cu grid we decided to test the self-assembly of **B** with other transition metal ions such as octahedral Co(II) and tetrahedral Ag(I). Thus, the stirring an acetonitrile solution containing a 1:1:2 mixture of Co(II), Cu(I) and **B** at room temperature resulted in a deep orange solution in which the presence of the tetranuclear $[Co_2Cu_2\mathbf{B}_4]^{6+}$ complex was confirmed by mass spectrometry (Figure 2.16 A). As in the case of Fe:Cu:**B** acetonitrile solutions, both dinuclear and tetranuclear species could be observed in the mass spectra. The study of the dependence of the dimer/tetramer intensity ratio in the ESMS spectra with the concentration reflected the same tendency than in the case of the Fe-Cu pair, with the tetramer signals increasing with the concentration. This fact evidences again the dynamic equilibrium existing in solution between the dinuclear and tetranuclear species.

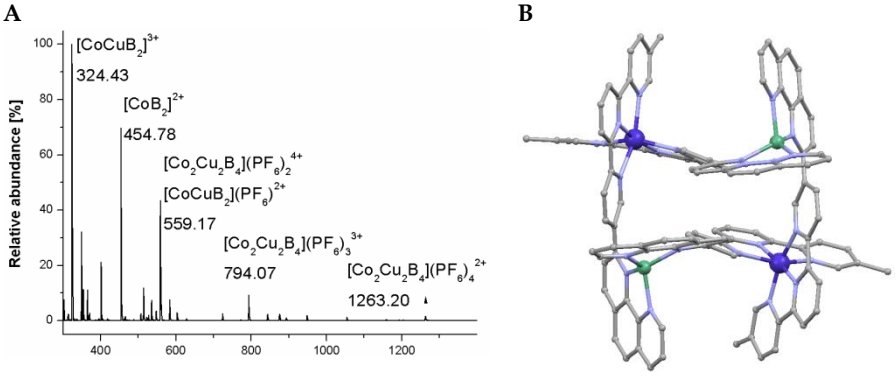

Figure 2.16. Positive ESMS in acetonitrile of 1:1:2 Co:Cu:**B** mixtures (**A**) and crystal structure of the grid $[Co_2Cu_2\mathbf{B}_4](PF_6)_6$ (**B**).

Slow diffusion of diisopropyl ether into the previous acetonitrile solution only afforded dark orange crystals of the tetranuclear complex $[Co_2Cu_2\mathbf{B}_4](PF_6)_6$. In contrast with the Fe-Cu tetramer, the four metal ions are distributed in a near-rectangular arrangement

with metal distances of 7.1 and 7.6 Å. The ligand adopts a transoid conformation in which the angles between terpy and phen moieties are 32º and 46º (Figure 2.16 B). In contrast to the [Fe_2Cu_2**B**$_4$] system, the crystals of [Co_2Cu_2**B**$_4$] are counterbalanced by 6 PF_6^- anions in agreement with the Co(II) and Cu(I) oxidation state of the starting metal salts. The two Co(II) ions placed at opposite corners of the rectangle adopt pseudooctahedral coordination geometries significantly different from one another. In one of the Co(II) ions, central pyridine rings are pulled into the metal centre affording 1.94 and 1.89 Å Co-$N_{central}$, and 2.18, 2.15, 2.00 and 1.99 Co-N_{distal} distances. The opposite Co(II) ion presents longer Co-$N_{central}$ distances of 2.06 and 2.03 Å and Co-N_{distal} distances of 2.16 Å on average. In both cases, the terpyridine planes around the metal remain almost perpendicular. On the remaining vertices of the rectangle, the distortion of the Cu(I) ions from tetrahedral geometries, that have been evaluated again according to White's model.[62] The resulting orientation angles are listed in Table 2.1. In this case both copper ions present similar distortions, in agreement with their analogous oxidation state. The magnetic properties of the [Co_2Cu_2**B**$_4$] square are currently under investigation.

Finally, the combination of **B** with Fe(II) and the tetracoordinated metal ion Ag(I), led once again to the formation of tetranuclear complexes. As in the previous cases, the recorded ESMS spectra of acetonitrile solutions containing 1:1:2 mixtures of Fe(II), Ag(I) and **B** confirmed the presence of the tetrameric [Fe_2Ag_2**B**$_4$]$^{6+}$ and dimeric [FeAg**B**$_2$]$^{3+}$ species (Figure 2.17). Additionally, a trinuclear [Fe_2Ag**B**$_3$]$^{5+}$ complex could also be detected in the mixture. Unfortunately, in this case, no crystals suitable for X-ray diffraction of the [Fe_2Ag_2**B**$_4$]$(PF_6)_6$ grid could be obtained.

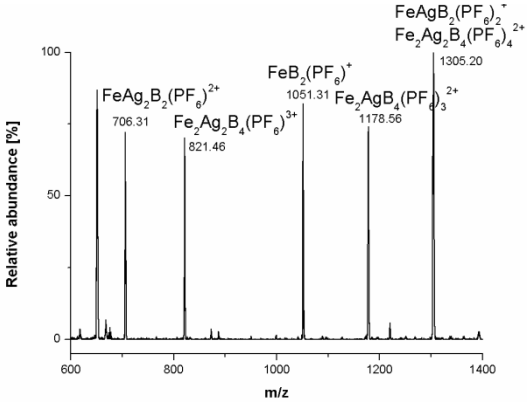

Figure 2.17. Positive ESMS of a 1:1:2 Fe(II):Ag(I):**B** mixture in acetonitrile.

Conclusions

The coordination entities described herein manifest the excellent capacities of phen/terpy conjugates **A** and **B** for the construction of discrete coordination supramolecular structures. Both ligands present analogous coordination sites but arranged in different orientations, which have given rise to very different architectures: whereas **A** generates homometallic metallacycles and cages with penta and hexacoordinated metal ions, **B** has demonstrated great abilities for the generation of heterobimetallic squares. In all cases the maximum occupancy principle is fulfilled. Nevertheless, the various resulting species evidenced how the geometry of the ligand can determine the final topology of the assembly. Accordingly, when rigid ligands are involved, not only the coordination demands of the metals but also the geometric limitations of the ligands must be taken into account in order to predict the result of the self-assembly.

To the best of our knowledge, the $Fe_5\mathbf{A}_6$ pentanuclear cage represents the first example of metal-coordination cage showing a trigonal bipyramid geometry. On the other hand, ligand **B** has shown excellent capacities for the toposelective self-assembly of heterometallic squares by its combination with different octahedral and tetrahedral metal ions pairs (Fe(II)-Cu(I), Co(II)-Cu(I) and Fe(II)-Ag(I)). Since all donor atoms present in ligand **B** are azaaromatic nitrogens, the selectivity of the process relies on the different denticity of the terpy and phen chelating units, and the different coordination demands of both metal ions. Besides, the isolation of single crystals of the $[Fe_2Cu_2\mathbf{B}_4](PF_6)_7$ and $[Co_2Cu_2\mathbf{B}_4](PF_6)_6$ [2x2] grids has contributed to increase the scarce list of reported heterometallic grid structures.

Summing up, we consider that a good level of control have been reached by the rational election of the metal ions and the stoichiometry in the coordination of phen/terpy conjugates. The combination of these ligands with tetra, penta and hexacoordinated transition metal ions according to the stoichiometries dictated by the maximum occupancy principle has afforded a wide variety of 2D and 3D structures. Nevertheless,

the distance between the two chelating units in phen/terpy conjugates **A** and **B** has avoided the appearance of cooperative effects in the redox or magnetic properties of the iron multinuclear assemblies.

Experimental

For mass spectrometry, ^{1}H NMR, IR and UV-Vis spectroscopy and elemental analysis details see the experimental section of chapter 1.

X-ray photoelectron spectroscopy (XPS, K-ALPHA, Thermo Scientific) was performed at Universidad de Alicante. All spectra were collected using Al-Kα radiation (1486.6 eV), monochromatizedby a twin crystal monochromator, yielding a focused X-ray spot with a diameter of 400 μm, at 3 mA × 12 kV. The alpha hemispherical analyzer was operated in the constant energy mode with survey scan pass energies of 200 eV to measure the whole energy band and 50 eV in a narrow scan to selectively measure the particular elements. Thus, XPS was used to provide the chemical bonding state as well as the elemental composition of the samples. Charge compensation was achieved with the system flood gun that provides low energy electrons and low energy argon ions from a single source.

Metallic atomic composition of bulk samples was determined by means of electron probe microanalysis (EPMA) performed in a Philips Model SEM-XL30 system equipped with an EDAX microprobe. Neat samples were prepared on aluminum sample holders, placed under general 10^{-6} mBar pressures and analysed with a 20 kV electron beam at a working height of 10 cm.

Computational Details

Geometrical optimization of the structure was performed with the density functional theory (DFT) approach using the Becke's three parameter exchange with the Lee–Yang–Parr correlation functional (B3LYP).[66-68] The basis used was 6-31G for C, H, O and N atoms and Los Alamos LANL2DZ split-valence set[69-71] for Fe atoms. The optimization convergence criteria were set to a maximum step size of 0.001 a.u. and an RMS force of 0.0003 a.u. All computations were performed with the GAUSSIAN 03 program.[72]

4-Methoxyphenyl neopentyl boronic ester ***36***

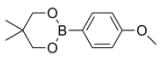

A solution of 4-bromoanisol (9.3 g, 50.0 mmol) in anhydrous THF (5 mL) was slowly added to a suspension of Mg turnings (1.3 g, 55.0 mmol) in THF (5 mL) under an argon atmosphere while the mixture was heated using a hot air gun to initialize the Grignard reaction. Generally the addition was concluded in 1h. The mixture was refluxed for another hour, cooled to room temperature and then added dropwise using a double tipped needle over a -78 ^{0}C cooled solution of $B(OMe)_3$ (8.8 g, 85.0 mmol) in anhydrous THF (40 mL). The mixture was allowed to reach room temperature overnight and THF was then evaporated under reduced pressure. Neopentylglycol (8.4 g, 60.0 mmol), p-TsOH·H_2O (0.24 g, 1.25 mmol) and toluene (350 mL) were added to the resulting solid and the mixture was refluxed under argon for 20h. The insoluble precipitate was separated by filtration. Evaporation of the toluene afforded a solid which was dissolved in diethyl ether (200 mL) and washed with water (4x 50 mL). The organic phase was dried over Na_2SO_4, the solvent was removed under reduced pressure and the resulting solid column cromatographied over silica gel using hexane/CH_2Cl_2 as eluent to yield pure product as a white solid in 70% yield. (7.70 g).

^{1}H NMR ($CDCl_3$, 300 MHz): δ 7.74 (d, *J*= 8.6 Hz, 2H), 6.89 (d, *J*= 8.6 Hz, 1H), 3.82 (s, 3H), 3.75 (s, 4H), 1.02 (s, 6H).

3-Bromo-8-(p-methoxyphenyl)-1,10-phenanthroline ***37***

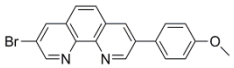

A solution containing 3,8-dibromo-phenanthroline (**11**) (1.88 g, 5.6 mmol), 4-methoxyphenyl neopentyl boronic ester (**36**) (0.98 g, 4.5 mmol), $Pd(PPh_3)_4$ (0.32 g, 0.28 mmol) and toluene (100 mL) was added to a degassed 2M Na_2CO_3 (30 mL) aqueous solution. The resulting emulsion was degassed again and refluxed under argon at 110 ^{0}C

for 24 h. After addition of 100 mL of water, the organic layer was separated and the aqueous layer extracted with chloroform (4x 40 mL). The combined organic extracts were washed once again with water, dried over Na_2SO_4 and concentrated under reduced pressure. Purification by silica gel column chromtography (CH_2Cl_2/AcOEt) afforded the target compound (white solid, 1.31 g) in 80% yield together with the starting phen **11** (0.37 g, 20%).

^{1}H NMR ($CDCl_3$, 300 MHz): δ 9.39 (d, *J*= 2.3 Hz, 1H) 9.17 (d, *J*= 2.3 Hz, 1H), 8.39 (d, *J*= 2.3 Hz, 1H), 8.32 (d, *J*= 2.3 Hz, 1H), 7.86 (d, *J*= 8.8 Hz, 1H), 7.74-7.67 (m, 3H), 7.08 (d, *J*= 8.8 Hz, 2H), 3.89 (s, 3H).

HRMS (ES): *m*/*z* (%) calcd for $[C_{19}H_{13}BrN_2O]^+$: 364.01; found: 364.01 (100) $[MH]^+$.

Ligand **A**

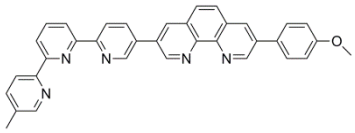

A was prepared according to a described procedure.[24] 3-Bromo-8-(p-methoxyphenyl)-1,10-phenanthroline (**37**) (0.49 g, 1.35 mmol), 5-neopentylglycolatoboril-5''-methyl-2,2':6',2''-terpyridine (**12**) (0.49 g, 2.0 mmol), $Pd(PPh_3)_4$ (0.12 g, 0.11 mmol), K_2CO_3 (1.87 g, 13.5 mmol), DMF (40 mL) and water (2 mL) were degassed and heated under argon at 80 ^{0}C for 24 h. The resulting solid was filtrated and washed with 10 mL of a 8:2 DMF/CH_2Cl_2 mixture, and then with water (25mL), 1.5 M HCl (50 mL), conc. NH_3 (50 mL) and water (25 mL). The solid was dried under vacuum affording the pure product as a brownish solid (0.53 g, 74%).

^{1}H NMR ($CDCl_3$, 300MHz): δ 9.50 (d, *J*= 2.3 Hz, 1H), 9.44 (d, *J*= 2.3 Hz, 1H), 9.12 (d, *J*= 2.0 Hz, 1H), 8.82 (d, *J*= 8.3 Hz, 1H), 8.56 (d, *J*=2.3 Hz, 1H), 8.55 (d, *J*= 8.4 Hz, 1H), 8.52-8.47 (m, 2H), 8.45 (d, *J*= 2.3 Hz, 1H), 8.37 (d, *J*= 2.3 Hz, 1H), 8.26 (dd, *J*= 8.3 and 2.4 Hz, 1H), 7.99 (t,

J= 7.8 Hz, 1H), 7.92 (s, 2H), 7.74 (d, *J*= 8.7 Hz, 2H), 7.70 (s, 1H), 7.10 (d, *J*= 8.7 Hz, 2H), 3.91 (s, 3H) 2.44 (s, 3H).

HRMS (FAB): *m*/*z* (%) calcd for $[C_{35}H_{25}N_5O]^+$: 531.21; found 531.20 (100) $[MH]^+$.

Cage [Fe$_5$A$_6$](PF$_6$)$_{10}$

A solution of $FeSO_4 \cdot 7H_2O$ (28 mg, 0.10 mmol) in water (5 mL) was added dropwise to a stirred solution of **A** (64 mg, 0.12 mmol) in refluxing acetone (5 mL). After stirring under argon at 60 ^{0}C for 30 min the mixture was cooled to room temperature and excess of aqueous KPF_6 was added. The resulting precipitate was filtered off, washed with water and dried under vacuum to afford **1** (97 mg, quantitative) as a deep red solid.

IR (KBr): $\bar{\nu}$ = 3422 (s), 3072, 2360, 1606 (s), 1518, 1435, 1251 (s), 841 (vs) and 557 (s) cm^{-1}.

UV-Vis (acetonitrile): λ_{max} = 534 nm (ε = 23700 $M^{-1}cm^{-1}$).

^{1}H NMR (300 MHz, CD_3CN): δ 9.06 (d, *J* = 8.0 Hz, 1H; $T_{5'}$), 9.02 (d, *J* = 8.0 Hz, 1H; $T_{3'}$), 8,91 (t, *J* = 8.0 Hz, 1H; $T_{4'}$), 8.73 (d, J = 1.6 Hz, 1H; P_7), 8.45 (d, *J* = 8.2 Hz, 1H; $T_{3''}$), 8.29 (d, *J* = 2.7 Hz, 2H; P_5, P_6), 8.13 (d, J = 8.4 Hz, 1H; T_3), 8.09 (d, *J* = 1.6 Hz, 1H; P_4), 7.68 (br. d, *J* ~ 8.2 Hz, 1H; $T_{4''}$), 7.61 (d, *J* = 1.6 Hz, 1H; P_2), 7.49 (d, *J* = 1.6 Hz, 1H; P_9), 7.35 (d, *J* = 1.6 Hz, 1H; T_6), 7.11 (d, *J* = 8.9 Hz, 2H; H_o), 6.83 (d, *J* = 8.9 Hz, 2H; H_m), 6.80 (dd, *J* = 8.4 and 1.6 Hz, 1H, T_4), 6.70 (s 1H; $T_{6''}$), 3.71 (s, 3H; OCH_3), 1.93 (s, 3H; CH_3); ^{19}F NMR (282 MHz, CD_3CN): δ -73.1 (d, J = 707 Hz).

MS (ES): *m*/*z* (%) = 1495.0 (5) $[Fe_5\mathbf{A}_6](PF_6)_7^{3+}$ (calcd 1495.2), 1085.1 (17) $[Fe_5\mathbf{A}_6](PF_6)_6^{4+}$ (calcd 1085.4), 839.1 (25) $[Fe_5\mathbf{A}_6](PF_6)_5^{5+}$ (calcd 839.6), 675.1 (20) $[Fe_5\mathbf{A}_6](PF_6)_4^{6+}$ (calcd 675.6), 559.5 (100) $[Fe\mathbf{A}_2]^{2+}$ (calcd 559.7).

Elemental analysis (%) calcd. for $C_{210}H_{150}N_{30}O_6P_{10}F_{60}Fe_5(H_2O)_8$: C, 49.82; H, 3.31; N, 8.30. Found: C, 49.88; H, 3.39; N, 8.50.

Complex [FeA$_2$](PF$_6$)$_2$

A solution of $FeSO_4 \cdot 7H_2O$ (28 mg, 0.10 mmol) in water (5 mL) was added dropwise to a stirred solution of **A** (0.11 g, 0.20 mmol) in refluxing acetone (10 mL). After stirring under argon at 60 ^{0}C for 30 min the mixture was cooled to room temperature and excess of aqueous KPF_6 was added. The resulting precipitate was filtered off, washed with water and dried to yield **2** (140 mg, quantitative) as a dark red solid.

IR (KBr): $\bar{\nu}$ = 3415 (s), 2925 (m), 2360, (m), 1606 (s), 1519 (m), 1436 (s), 1249 (m), 833 (vs) (P-F) and 559 (vs) (F-P-F) cm^{-1}.

^{1}H NMR (400 MHz, CD_3CN): δ 9.39 (d, *J* = 2.0 Hz, 1H; P_9), 8.98 (d, *J* = 8.0 Hz, 1H; $T_{3'}$), 8.90 (d, *J* = 8.0 Hz, 1H; $T_{5'}$), 8.89 (d, *J* = 2.0 Hz, 1H; P_2), 8.73 (t, *J* = 8.0 Hz, 1H, $T_{4'}$), 8.64 (d, *J* = 8.2 Hz, 1H; T_3), 8.56 (d, *J* = 2.0 Hz, 1H; P_7), 8.39 (d, *J* = 8.0 Hz, 1H; $T_{3''}$), 8.33 (dd, *J* = 8.2 and 1.6 Hz, 1H; T_4), 8.29 (d, *J* = 2.0 Hz, 1H; P_4), 7.99 (d, *J* = 9.0 Hz, 1H; P_6), 7.88 (d, *J* = 9.0 Hz, 1H; P_5), 7.84 (d, *J* = 8.8 Hz, 2H; H_o), 7.72 (d, *J* = 8.0 Hz, 1H; $T_{4''}$), 7.33 (d, *J* = 1.6 Hz, 1H; T_6), 7.15 (d, J = 8.8 Hz, 2H, H_m), 6.98 (s, 1H; $T_{6''}$), 3.88 (s, 3H; OCH_3), 2.01 (s, 3H; CH_3);

MS (ES): *m*/*z* (%) = 727.53 (26) [Fe**A**$_2$](PF$_6$)$_2$Na^{2+} (calcd 727.63), 716.57 (11) [Fe**A**$_2$](PF$_6$)$_2$HNa^{2+} (calcd 716.64), 643.56 (46) [Fe**A**$_2$](PF$_6$)Na^{2+} (calcd 643.66), 632.60 [Fe**A**$_2$](PF$_6$)H^{2+} (calcd 632.67), 559.60 (100) [Fe**A**$_2$]$^{2+}$ (calcd 559.68).

1-Methyl-1,10-phenanthrolinium mesylate ***38***

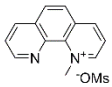

38 was prepared according to a described procedure.[58] 1,10-Phenanthroline monohydrate (5.0 g, 27.7 mmol) and 150 mL of toluene were heated at reflux in a round bottom flask equipped with a Dean-Stark trap until all water was removed. The mixture was cooled to 60 ^{0}C and methyl methanesulfonate was added dropwise via syringe. The mixture was further stirred at 60 ^{0}C for 36 h and the resulting precipitate was collected

by filtration, washed with toluene and diethyl ether, and dried under vacuum to afford the pure product as a white powder (7.3 g, 99%).

^{1}H NMR ($CDCl_3$, 300 MHz): δ 10.30 (d, *J*= 6.0 Hz, 1H), 9.28 (d, *J*= 6.0 Hz, 1H), 9.09 (d, *J*= 8.1 Hz, 1H), 8.56 (m, 2H), 8.16 (m, 2H), 7.91 (dd, *J*= 8.1 Hz, *J*= 4.2 Hz, 1H), 5.52 (s, 3H), 2.84 (s, 3H).

1-Methyl-1,10-phenanthrolin-2(1H)-one **39**

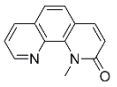

39 was prepared according to a described procedure.[58] 1-Methyl-1,10-phenanthrolinium mesylate (**38**) (3.0 g, 10.3 mmol) and activated 85% MnO_2 (26.4 g, 258 mmol) were refluxed in anhydrous THF (400 mL) under argon for 22 h. After the mixture was cooled to room temperature, MnO_2 was removed by filtration, and the flitrate was evaporated under reduced pressure. The resulting solid was purified by silica column chromatography (CH_2Cl_2/MeOH). The desired product was eluted first (white solid, 2.0 g, 90%) but also a minor amount of the phenanthroline 4-one isomer was isolated.

^{1}H NMR ($CDCl_3$, 300 MHz): δ 8.95 (dd, *J*= 4.2 Hz, *J*= 1.8 Hz, 1H), 8.19 (dd, *J*= 8.1 Hz, *J*= 1.8 Hz, 1H), 7.80 (d, *J*= 9.3 Hz, 1H), 7.57 (s, 1H), 7.56 (s, 1H), 7.51 (dd, *J*= 8.1 Hz, *J*= 4.2 Hz, 1H), 6.92 (d, *J*= 9.3 Hz, 1H), 4.49 (s, 3H).

2-Chloro-1,10-phenanthroline **40**

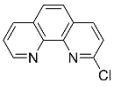

40 was prepared according to a described procedure.[59] 1-Methyl-1,10-phenanthrolin-2(1H)-one (**39**) (6.0 g, 28.5 mmol), phosphorous pentachloride (7.20g, 25 mmol) and phosphorus (V) oxychloride (54 mL, 579 mmol) were refluxed under argon for 8h. After that time, phosphorus (V) oxychloride was distilled under reduced pressure and the

resulting solid was suspended in iced water (150 mL) and basified with concentrated ammonia. The resulting insoluble precipitate was collected by filtration and purified by silica column chromatography (CH_2Cl_2/AcOEt) to yield the pure product as a white solid (4.9g, 80%).

^{1}H NMR ($CDCl_3$, 300 MHz): δ 9.24 (dd, *J*= 4.7 Hz, *J*= 1.7 Hz, 1H), 8.28 (m, 2H), 7.84 (m, 2H), 7.68 (m, 2H).

Ligand B

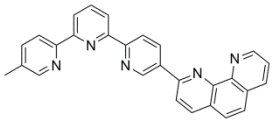

A mixture of 2-chloro-1,10-phenanthroline (**40**) (0.33 g, 1.54 mmol), 5-neopentylglicolatoboryl-5″-methyl-2,2′:6′,2″-terpyridine (**12**) (0.50 g, 1.40 mmol), $[Pd(PPh)_3]_4$ (0.13 g, 0.11 mmol), K_2CO_3 (1.90 g, 14.0 mmol), DMF (42 mL) and water (3.5 mL) were degassed and heated under argon at 100 ^{0}C for 24h. Next, the solvent was removed under reduced pressure and suspended in water (60 mL) was added. The suspension was filtered and the solid was washed with water. Purification by silica column chromatography (CH_2Cl_2:MeOH) afforded the pure product (white solid, 0.46 g, 77%).

^{1}H NMR (500 MHz, $CDCl_3$): δ 9.51 (d, *J* = 2.3 Hz, 1H), 9.27 (dd, *J* = 4.3, 1.7 Hz, 1H), 8.96 (dd, *J* = 8.3, 2.3 Hz, 1H), 8.80 (dd, *J* = 8.3 Hz, 1H), 8.59 – 8.51 (m, 3H), 8.45 (dd, *J* = 7.8, 1.0 Hz, 1H), 8.38 (d, *J* = 8.4 Hz, 1H), 8.29 (dd, *J* = 8.1, 1.7 Hz, 1H), 8.19 (d, *J* = 8.4 Hz, 1H), 7.98 (t, *J* = 7.8 Hz, 1H), 7.86 (d, *J* = 8.8 Hz, 1H),7.82 (d, *J* = 8.8 Hz, 1H), 7.74 – 7.65 (m, 2H), 2.43 (s, 3H).

^{13}C NMR (126 MHz, $CDCl_3$): δ 156.83 (s), 155.74 (s), 155.13 (s), 155.08 (s), 153.86 (s), 150.60 (s), 149.68 (s), 148.44 (s), 146.47 (s), 146.35 (s), 137.99 (s), 137.66 (s), 137.33 (s), 136.68 (s), 135.20 (s), 133.65 (s), 129.34 (s), 128.10 (s), 126.95 (s), 126.53 (s), 123.31 (s), 121.31 (s), 121.22 (s), 121.05 (s), 120.99 (s), 120.70 (s), 18.57 (s).

HRMS (ES): *m*/*z* (%) calcd for $[C_{42}H_{23}N_4]^+$: 425.16; found: 425.16 (100) $[MH]^+$.

Elemental analysis (%) calcd. for $C_{28}H_{19}N_5(H_2O)$: C, 75.83; H, 4.77; N, 15.79. Found: C, 75.03; H, 4.56; N, 15.49.

Complex [FeB$_2$](PF$_6$)$_2$

A mixture of ligand **B** (21 mg, 0.05 mmol), $Fe(BF_4)\cdot(H_2O)_6$ (8 mg, 0.025 mmol) and freshly distilled acetonitrile (4 mL) was stirred for 30 minutes resulting in a dark purple solution. A solution of KPF_6 0.1 M in water (20 mL) was added and the resulting precipitate was filtered off, washed with water and dried under vacuum to afford [Fe**B**$_2$](PF$_6$)$_2$ (135 mg, quantitative) as a deep purple solid.

^{1}H NMR (500 MHz, CD_3CN): δ 9.43 (dd, *J* = 4.1, 1.5 Hz, 1H), 9.61 (d, *J* = 8.0 Hz, 1H), 9.10 (d, *J* = 8.0 Hz, 1H), 8.83 (t, *J* = 8.0 Hz, 1H), 8.64 (d, *J* = 8.5 Hz, 1H), 8.60 (d, *J* = 8.5 Hz, 1H), 8.43 (m, 2H), 8.38 (d, *J* = 8.5 Hz, 1H), 8.25 (d, *J* = 1.0 Hz, 1H), 7.96 (d, *J* = 8.5 Hz, 1H), 7.94 - 7.86 (m, 3H), 7.70 (d, *J* = 8.2 Hz, 1H), 7.10 (s, 1H), 2.01 (s, 3H).

^{13}C NMR (126 MHz, CD_3CN): δ 161.55 (s), 160.98 (s), 158.91 (s), 156.29 (s), 154.32 (s), 153.09 (s), 151.42 (s), 146.62 (s), 146.47 (s),140.27 (s), 139.72 (s), 139.07 (s), 138.81 (s), 138.68 (s), 137.37 (s), 136.94 (s), 130.34 (s), 129.58 (s), 128.83 (s), 127.13 (s), 125.75 (s), 124.68 (s), 124.50 (s), 124.30 (s), 120.87 (s), 18.43 (s).

MS (ES): *m*/*z* (%) = 1051.18 (5) $[FeB_2(PF_6)]^+$ (calcd 1051.22), 453.41 (100) $[FeB_2]^{2+}$ (calcd 453.14).

Elemental analysis (%) calcd. for $C_{56}H_{38}N_{10}P_2F_{12}(H_2O)_4$: C, 53.01; H, 3.65; N, 11.04. Found: C, 53.91; H, 4.02; N, 9.98.

UV-Vis (acetonitrile): λmax = 569 nm (ε = 1500 $M^{-1}cm^{-1}$).

EDAX (calculated for [Fe**B**$_2$](PF$_6$)$_2$): Found Fe = 36.73% (33.33%); P = 63.27% (66.66%).

General method for the stepwise synthesis of heterobimetallic squares

Ligand **B** (42 mg, 0.1 mmol) and $M(II)(BF_4)_2$ (M(II) = Fe or Co) (0.05 mmol) were mixed in distilled acetonitrile (8 mL) and stirred at room temperature for 2h. Then, a solution of $M(I)(PF_6)$ (M(I) =Cu or Ag) (0.05 mmol) in degassed acetonitrile (8 mL) was added and stirred for another 24h. A solution of KPF_6 0.1 M in water (20 mL) was added and the resulting precipitate was filtered off, washed with water and dried under vacuum to afford $[M(II)_2M(I)_2\mathbf{B}_4](PF_6)_6$ in near quantitative yield.

General method for the single-step synthesis of heterobimetallic squares

A mixture of ligand **B** (42.5 mg, 0.1 mmol), $M(II)(BF_4)_2$ (M(II) = Fe or Co) (0.05 mmol) and $M(I)(PF_6)$ (M(I) = Cu or Ag) (0.05 mmol) was stirred at room temperature in distilled acetonitrile (16 mL) for 24h. The resulting mixture was precipitated with KPF_6 0.1 M in water (20mL), filtered off, washed with water and dried under vacuum to afford $[M(II)_2M(I)_2\mathbf{B}_4](PF_6)_6$ in near quantitative yield.

Square $[Fe_2Cu_2B_4](PF_6)_6$

Deep red solid. UV-Vis (acetonitrile): λmax = 560 nm (ε = 9000 $M^{-1}cm^{-1}$).

MS(ES): *m/z* (%) = 1260.14 (5) $[Fe_2Cu_2B_4(PF_6)_4]^{2+}$ (calcd 1260.13), 791.90 (35) $[Fe_2Cu_2B_4(PF_6)_3]^{3+}$ (calcd 791.77), 557.36 (100) $[FeCuB_2(PF_6)]^{2+}$ (calcd 557.09), 453.42 (60) $[FeB_2]^{2+}$ (calcd 453.14), 323.33 (75) $[FeCuB_2]^{3+}$ (calcd 323.07).

Elemental analysis (%) calcd. for $C_{112}H_{76}N_{20}P_6F_{36}Fe_2Cu_2(H_2O)_7$: C, 45.81; H, 3.09; N, 9.54. Found: C, 45.97; H, 3.20; N, 9.25.

UV-Vis (acetonitrile): λmax = 565 nm (ε = 2300 $M^{-1}cm^{-1}$).

EDAX (calculated for $[Fe_2Cu_2\mathbf{B}_4](PF_6)_6$): Found Fe = 17.69% (20.00%); Cu= 20.87% (20.00%); P = 61.44% (60.00%).

Square [$Co_2Cu_2B_4$]$(PF_6)_6$

Deep orange solid.

MS(ES): *m*/*z* (%) = 1263.35 (3) $[Co_2Cu_2B_4(PF_6)_4]^{2+}$ (calcd 1263.13), 794.07 (10) $[Co_2Cu_2B_4(PF_6)_3]^{3+}$ (calcd 793.77), 558.90 (44) $[CoCuB_2(PF_6)]^{2+}$ (calcd 558.59), 455.08 (70) $[CoB_2]^{2+}$ (calcd 455.64), 324.43 (100) $[CoCuB_2]^{3+}$ (calcd 324.07).

Elemental analysis (%) calcd. for $C_{112}H_{76}N_{20}P_6F_{36}Co_2Cu_2(H_2O)_2$: C, 47.16; H, 2.83; N, 9.82. Found: C, 47.18; H, 2.98; N, 10.04.

EDAX (calculated for $[Co_2Cu_2\mathbf{B}_4](PF_6)_6$): Found Co = 13.62% (20.00%); Cu= 18.43% (20.00%); P = 67.65% (60.00%).

Square [$Fe_2Ag_2B_4$]$(PF_6)_6$

Deep purple solid. UV-vis (acetonitrile): λmax = 569 nm (ε = 9128 $M^{-1}cm^{-1}$).

Elemental analysis (%) calcd. for $C_{112}H_{76}N_{20}P_6F_{36}Fe_2Ag_2(H_2O)_4$: C, 45.27; H, 2.85; N, 9.43. Found: C, 45.97; H, 2.88; N, 9.68.

MS(ES): *m*/*z* (%) = 1305.20 (100) $[FeAgB_2(PF_6)_2]^{+}$ (calcd 1303.10), 1178.43 (72) $[Fe_2AgB_4(PF_6)_3]^{2+}$ (calcd 1178.17), 1051.31 (80) $[FeB_2(PF_6)]^{+}$ (calcd 1051.22), 821.65 (70) $[Fe_2Ag_2B_4(PF_6)]^{3+}$ (calcd 821.42), 706.31 (70) $[FeAg_2B_2(PF_6)_2]^{2+}$ (calcd 706.00).

UV-Vis (acetonitrile): λmax = 569 nm (ε = 1100 $M^{-1}cm^{-1}$).

Annex

NMR experiments

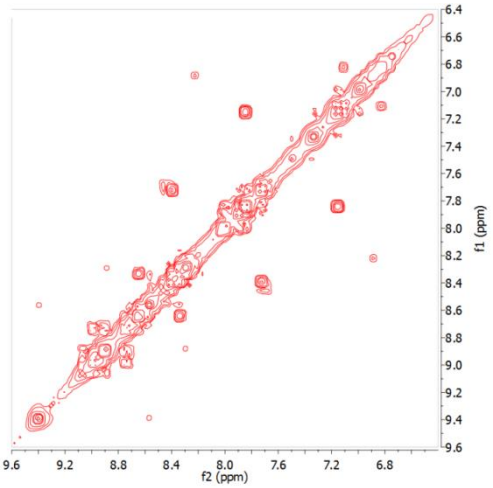

Figure 2.18 Partial 1H-1H COSY spectrum (CD_3CN, 400 MHz) of [Fe**A**$_2$](PF_6)$_2$.

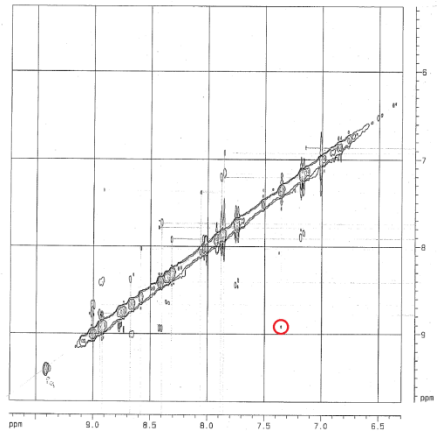

Figure 2.19 Partial ROESY spectrum (CD_3CN, 400 MHz) of [Fe**A**$_2$](PF_6)$_2$.

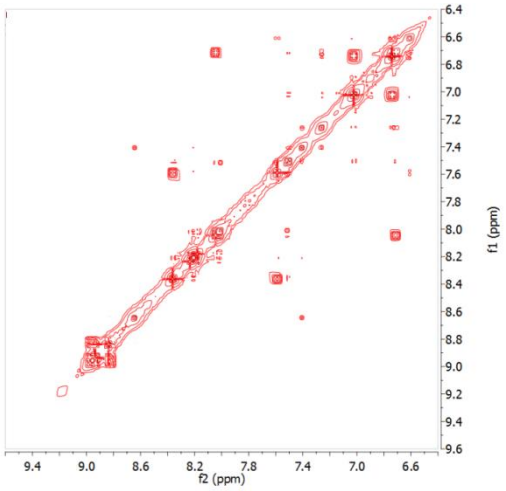

Figure 2.20 Partial COSY spectrum (CD_3CN, 400 MHz) of $[Fe_5\mathbf{A}_6](PF_6)_{10}$.

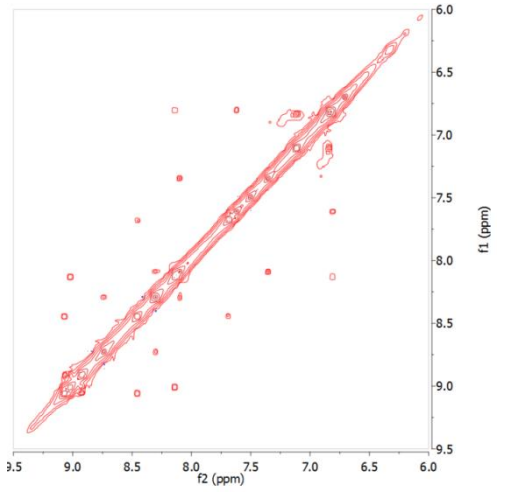

Figure 2.21 Partial 1H-1H NOESY spectrum (CD_3CN, 400 MHz) of $[Fe_5\mathbf{A}_6](PF_6)_{10}$.

ESMS

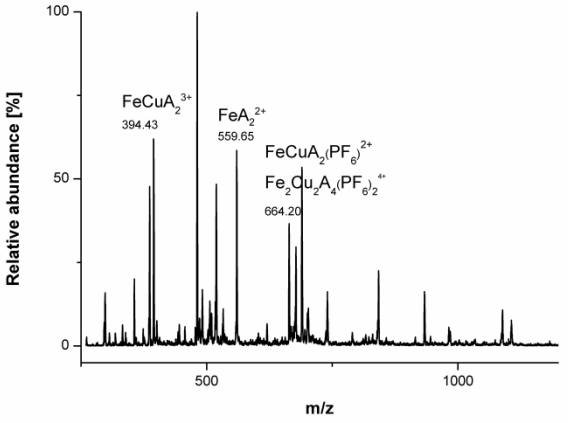

Figure 2.22 Positive ESMS spectra in acetonitrile of 2 mM 1:1:2 mixtures of Fe:Cu:**A**.

UV-Vis

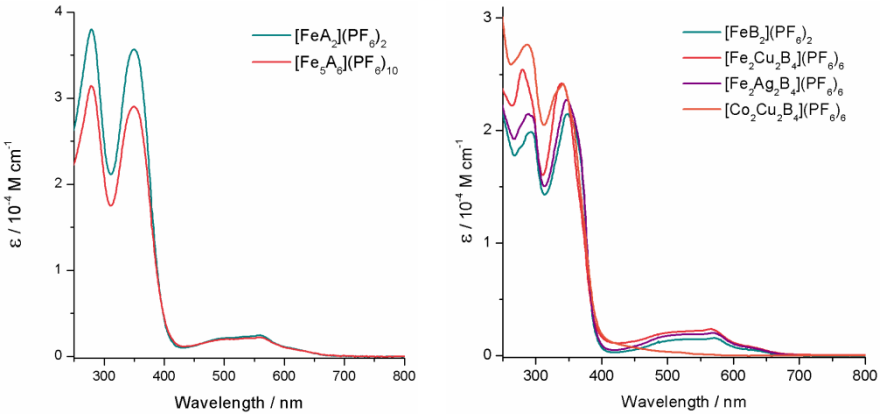

Figure 2.23 UV-Visible spectra of [Fe**A**$_2$](PF$_6$)$_2$ and [Fe$_5$**A**$_6$](PF$_6$)$_{10}$ (left), and of the Fe(II) corner complex and the supramolecular squares (right). Data recorded in acetonitrile 1·10^{-5} M.

References

References

(1) J. P. Sauvage In *Transition metals in supramolecular chemistry ;* John Wiley & Sons Ltd., Ed.; Perspectives in Supramolecular Chemistry; New York, 1999; Vol. 5.

(2) Fujita, M.; Tominaga, M.; Hori, A.; Therrien, B. *Acc. Chem. Res.* **2005**, *38*, 369-378.

(3) Ruben, M.; Rojo, J.; Romero-Salguero, F. J.; Uppadine, L. H.; Lehn, J. M. *Angew. Chem. , Int. Ed.* **2004**, *43*, 3644-3662.

(4) Saalfrank, R. W.; Maid, H.; Scheurer, A. *Angew. Chem. , Int. Ed.* **2008**, *47*, 8795-8824.

(5) Glasson, C. R. K.; Lindoy, L. F.; Meehan, G. V. *Coord. Chem. Rev.* **2008**, *252*, 940-963.

(6) De, S.; Mahata, K.; Schmittel, M. *Chem. Soc. Rev.* **2010**, *39*, 1555-1575.

(7) Chakrabarty, R.; Mukherjee, P. S.; Stang, P. J. *Chem. Rev.* **2011**, *111*, 6810-6918.

(8) Zhao, L.; Xu, Z.; Grove, H.; Milway, V. A.; Dawe, L. N.; Abedin, T. S. M.; Thompson, L. K.; Kelly, T. L.; Harvey, R. G.; Miller, D. O.; Weeks, L.; Shapter, J. G.; Pope, K. J. *Inorg. Chem.* **2004**, *43*, 3812-3824.

(9) Parsons, S. R.; Thompson, L. K.; Dey, S. K.; Wilson, C.; Howard, J. A. K. *Inorg. Chem.* **2006**, *45*, 8832-8834.

(10) Bassani, D. M.; Lehn, J. M.; Serroni, S.; Puntoriero, F.; Campagna, S. *Chem. -Eur. J.* **2003**, *9*, 5936-5946.

(11) Schneider, B.; Demeshko, S.; Dechert, S.; Meyer, F. *Angew. Chem. , Int. Ed.* **2010**, *49*, 9274-9277.

(12) Alam, M. S.; Strömsdörfer, S.; Dremov, V.; Müller, P.; Kortus, J.; Ruben, M.; Lehn, J. M. *Angew. Chem. , Int. Ed.* **2005**, *44*, 7896-7900.

(13) Petukhov, K.; Alam, M. S.; Rupp, H.; Strömsdörfer, S.; Müller, P.; Scheurer, A.; Saalfrank, R. W.; Kortus, J.; Postnikov, A.; Ruben, M.; Thompson, L. K.; Lehn, J. M. *Coord. Chem. Rev.* **2009**, *253*, 2387-2398.

(14) Ziener, U.; Lehn, J. M.; Mourran, A.; Möller, M. *Chem. -Eur. J.* **2002**, *8*, 951-957.

(15) Safarowsky, C.; Merz, L.; Rang, A.; Broekmann, P.; Hermann, B. A.; Schalley, C. A. *Angew. Chem. , Int. Ed.* **2004**, *43*, 1291-1294.

(16) Baxter, P. N. W.; Lehn, J. M.; Rissanen, K. *Chem. Commun.* **1997**, 1323-1324.

(17) Dalgarno, S. J.; Power, N. P.; Atwood, J. L. *Coord. Chem. Rev.* **2008**, *252*, 825-841.

(18) Yoshizawa, M.; Klosterman, J. K.; Fujita, M. *Angew. Chem. , Int. Ed.* **2009**, *48*, 3418-3438.

(19) Rebek Jr., J. *Acc. Chem. Res.* **2009**, *42*, 1660-1668.

(20) Ward, M. D. *Chem. Commun.* **2009**, 4487-4499.

(21) Amouri, H.; Desmarets, C.; Moussa, J. *Chem. Rev.* **2012**, *112*, 2015-2041.

(22) Lehn, J. M. In *Self-Processes - Programmed Supramolecular Systems;* Supramolecular Chemistry: Concepts and Perspectives; VCH: Weinheim, 1995; .

(23) Coronado, E.; Galan-Mascaros, J. R.; Gaviña, P.; Martĩ-Gastaldo, C.; Romero, F. M.; Tatay, S. *Inorg. Chem.* **2008**, *47*, 5197-5203.

(24) Gaviña, P.; Tatay, S. *Tetrahedron Lett.* **2006**, *47*, 3471-3473.

(25) Hathaway, B. J. *Coord. Chem. Rev.* **1983**, *52*, 87-169.

(26) Cardona-Serra, S.; Coronado, E.; Gavina, P.; Ponce, J.; Tatay, S. *Chem. Commun.* **2011**, *47*, 8235-8237.

(27) Saalfrank, R. W.; Stark, A.; Bremer, M.; Hummel, H. -. *Angew. Chem. , Int. Ed.* **1990**, *29*, 311-314.

(28) Saalfrank, R. W.; Burak, R.; Breit, A.; Stalke, D.; Herbst-Irmer, R.; Daub, J.; Porsch, M.; Bill, E.; Müther, M.; Trautwein, A. X. *Angew. Chem. , Int. Ed.* **1994**, *33*, 1621-1623.

(29) Caulder, D. L.; Powers, R. E.; Parac, T. N.; Raymond, K. N. *Angew. Chem. , Int. Ed.* **1998**, *37*, 1840-1843.

(30) Argent, S. P.; Riis-Johannessen, T.; Jeffery, J. C.; Harding, L. P.; Ward, M. D. *Chem. Commun.* **2005**, 4647-4649.

(31) Biros, S. M.; Yeh, R. M.; Raymond, K. N. *Angew. Chem. , Int. Ed.* **2008**, *47*, 6062-6064.

(32) Mal, P.; Schultz, D.; Beyeh, K.; Rissanen, K.; Nitschke, J. R. *Angew. Chem. , Int. Ed.* **2008**, *47*, 8297-8301.

(33) Custelcean, R.; Bosano, J.; Bonnesen, P. V.; Kertesz, V.; Hay, B. P. *Angew. Chem. , Int. Ed.* **2009**, *48*, 4025-4029.

(34) Bark, T.; Von Zelewsky, A.; Rappoport, D.; Neuburger, M.; Schaffner, S.; Lacour, J.; Jodry, J. *Chem. Eur. J.* **2004**, *10*, 4839-4845.

(35) Barboiu, M.; Ruben, M.; Blasen, G.; Kyritsakas, N.; Chacko, E.; Dutta, M.; Radekovich, O.; Lenton, K.; Brook, D. J. R.; Lehn, J. M. *Eur. J. Inorg. Chem.* **2006**, 784-792.

(36) Klingele, J.; Boas, J. F.; Pilbrow, J. R.; Moubaraki, B.; Murray, K. S.; Berry, K. J.; Hunter, K. A.; Jameson, G. B.; Boyd, P. D. W.; Brooker, S. *Dalton Trans.* **2007**, 633-645.

(37) Piguet, C.; Bernardinelli, G.; Hopfgartner, G. *Chem. Rev.* **1997**, *97*, 2005-2062.

(38) Albrecht, M. *Chem. Rev.* **2001**, *101*, 3457-3497.

(39) Al-Rasbi, N. K.; Adams, H.; Harding, L. P.; Ward, M. D. *Eur. J. Inorg. Chem.* **2007**, 4770-4780.

(40) Wu, D. Y.; Wu, G. H.; Huang, W.; Duan, C. -. *Polyhedron* **2008**, *27*, 947-954.

(41) Warr, R. J.; Willis, A. C.; Wild, S. B. *Inorg. Chem.* **2008**, *47*, 9351-9362.

(42) Amendola, V.; Boiocchl, M.; Brega, V.; Fabbrizzi, L.; Mosca, L. *Inorg. Chem.* **2010**, *49*, 997-1007.

(43) Constable, E. C.; Zhang, G.; Housecroft, C. E.; Neuburger, M.; Zampese, J. A. *Eur. J. Inorg. Chem.* **2010**, 2000-2011.

(44) Ruminski, R. R.; Petersen, J. D. *Inorg. Chim. Acta* **1985**, *97*, 129-134.

(45) Constable, E. C.; Ward, M. D.; Corr, S. *Inorg. Chim. Acta* **1988**, *141*, 201-203.

(46) Braterman, P. S.; Song, J. I. *Inorg. Chim. Acta* **1991**, *180*, 145-146.

(47) Ayers, T.; Scott, S.; Goins, J.; Caylor, N.; Hathcock, D.; Slattery, S. J.; Jameson, D. L. *Inorg. Chim. Acta* **2000**, *307*, 7-12.

(48) Coronado, E.; Gaviña, P.; Tatay, S.; Groarke, R.; Vos, J. G. *Inorg. Chem.* **2010**, *49*, 6897-6903.

(49) Bao, D.; Millare, B.; Xia, W.; Steyer, B. G.; Gerasimenko, A. A.; Ferreira, A.; Contreras, A.; Vullev, V. I. *J. Phys. Chem. A* **2009**, *113*, 1259-1267.

(50) Bassani, D.; Lehn, J.; Fromm, K.; Fenske, D. *Angew. Chem. , Int. Ed.* **1998**, *37*, 2364-2367.

(51) Uppadine, L. H.; Lehn, J. M. *Angew. Chem. , Int. Ed.* **2004**, *43*, 240-243.

(52) Uppadine, L. H.; Gisselbrecht, J. P.; Kyritsakas, N.; Nättinen, K.; Rissanen, K.; Lehn, J. M. *Chem. -Eur. J.* **2005**, *11*, 2549-2565.

(53) Petitjean, A.; Kyritsakas, N.; Lehn, J. M. *Chem. Commun.* **2004**, *10*, 1168-1169.

(54) Moroz, Y. S.; Szyrwiel, L.; Demeshko, S.; Kozowski, H.; Meyer, F.; Fritsky, I. O. *Inorg. Chem.* **2010**, *49*, 4750-4752.

(55) Newton, G. N.; Onuki, T.; Shiga, T.; Noguchi, M.; Matsumoto, T.; Mathieson, J. S.; Nihei, M.; Nakano, M.; Cronin, L.; Oshio, H. *Angew. Chem. , Int. Ed.* **2011**, *50*, 4844-4848.

(56) Stefankiewicz, A. R.; Harrowfield, J.; Madalan, A.; Rissanen, K.; Sobolev, A. N.; Lehn, J. M. *Dalton Trans.* **2011**, *40*, 12320-12332.

(57) Bao, X.; Liu, W.; Mao, L. L.; Jiang, S. D.; Liu, J. L.; Chen, Y. C.; Tong, M. L. *Inorg. Chem.* **2013**, *52*, 6233-6235.

(58) Johnson, M. R.; Bell, D.; Shanaman, L. *Heterocycles* **1997**, *45*, 1059-1069.

(59) Halcrow, B. E.; Kermack, W. O. *J. Chem. Soc.* **1946**, 155-157.

(60) Weilandt, T.; Troff, R. W.; Saxell, H.; Rissanen, K.; Schalley, C. A. *Inorg. Chem.* **2008**, *47*, 7588-7598.

(61) Scaltrito, D. V.; Thompson, D. W.; O'Callaghan, J. A.; Meyer, G. J. *Coord. Chem. Rev.* **2000**, *208*, 243-266.

(62) Dobson, J. F.; Green, B. E.; Healy, P. C.; Kennard, C. H. L.; Pakawatchai, C.; White, A. H. *Aust. J. Chem.* **1984**, *37*, 649.

(63) Constable, E. C.; Ward, M. D.; Tocher, D. A. *J. Chem. Soc. , Dalton Trans.* **1991**, 1675-1683.

(64) Chotalia, R.; Constable, E. C.; Neuburger, M.; Smith, D. R.; Zehnder, M. *J. Chem. Soc. , Dalton Trans.* **1996**, 4207-4216.

(65) Zong, R.; Thummel, R. P. *Inorg. Chem.* **2005**, *44*, 5984-5986.

(66) Becke, A. D. *Phys. Rev. A* **1988**, *38*, 3098-3100.

(67) Lee, C.; Yang, W.; Parr, R. G. *Phys. Rev. B* **1988**, *37*, 785-789.

(68) Becke, A. D. *J. Chem. Phys.* **1993**, *98*, 5648-5652.

(69) Hay, P. J.; Wadt, W. R. *J. Chem. Phys.* **1985**, *82*, 299-310.

(70) Hay, P. J.; Wadt, W. R. *J. Chem. Phys.* **1985**, *82*, 270-283.

(71) Wadt, W. R.; Hay, P. J. *J. Chem. Phys.* **1985**, *82*, 284-298.

(72) Frisch, M. J.; Trucks, G. W.; Schlegel, H. B.; Scuseria, G. E.; Robb, M. A.; Cheeseman, J. R.; Montgomery, J. A.; Vreven, T.; Kudin, K. N.; Burant, J. C.; Millam, J. M.; Iyengar, S. S.; Tomasi, J.; Barone, V.; Mennucci, B.; Cossi, M.; Scalmani, G.; Rega, N.; Petersson, G. A.; Nakatsuji, H.; Hada, M.; Ehara, M.; Toyota, K.; Fukuda, R.; Hasegawa, J.; Ishida, M.; Nakajima, T.; Honda, Y.; Kitao, O.; Nakai, H.; Klene, M.; Li, X.; Knox, J. E.; Hratchian, H. P.; Cross, J. B.; Bakken, V.; Adamo, C.; Jaramillo, J.; Gomperts, R.; Stratmann, R. E.; Yazyev, O.; Austin, A. J.; Cammi, R.; Pomelli, C.; Ochterski, J. W.; Ayala, P. Y.; Morokuma, K.; Voth, G. A.; Salvador, P.; Dannenberg, J. J.; Zakrzewski, V. G.; Dapprich, S.; Daniels, A. D.; Strain, M. C.; Farkas, O.; Malick, D. K.; Rabuck, A. D.; Raghavachari, K.; Foresman, J. B.; Ortiz, J. V.; Cui, Q.; Baboul, A. G.; Clifford, S.; Cioslowski, J.; Stefanov, B. B.; Liu, G.; Liashenko, A.; Piskorz, P.; Komaromi, I.; Martin, R. L.; Fox, D. J.; Keith, T.; Laham, A.; Peng, C. Y.; Nanayakkara, A.; Challacombe, M.; Gill, P. M. W.; Johnson, B.; Chen, W.; Wong, M. W.; Gonzalez C. and Pople, J. A. In *Gaussian 03, Revision B.03;* Gaussian, I., Wallingford CT., Ed.; 2003; .

Chapter 3

Molecular devices

Introduction

Molecular electronics is the scientific area that deals with electrical conduction through molecules.[1] This research field emerged in 1974 when Aviram and Ratner[2] first envisioned the use of tailored individual molecules as the functional building blocks in electronic devices. In this work, the authors proposed the use of a single organic molecule as a current rectifier, but later, it was suggested that molecules could perform all the basic functions of digital electronics: rectification, amplification and storage.[3, 4]

At the beginning, the replacement of the ordinary basic electronic elements (wires and transistors), based on silicon, by molecules was expected to give rise to a tremendous decrease of size of the microelectronic counterparts.[5] However, the silicon industry has carried out great advances on the miniaturization of circuit components. Nowadays 22 nm-size transistors form part of commercial devices and 14 nm-transistors have been announced for this year.[6] Nevertheless, the advantages offered by molecules go far beyond the size issue.

Molecules are discrete entities susceptible to an enormous structural variability that is not afforded by silicon technology, and which leads to highly tuneable properties. Hence, molecular electronics takes advantage of chemical synthesis as a very powerful tool for the fabrication of tailored-made components.[7] Nevertheless, to fully exploit the potential of molecules, the design of chemical structures requires the comprehensive understanding of charge transport at the single-molecule level. For that reason, the establishment of structure-function correlations is a fundamental pre-requisite in the development of functional molecular devices.[8]

Nowadays, several techniques, being STM[9] and Mechanically Controlled Break Junctions (MCBJs)[9] the most extended, enable the evaluation of single-molecule conduction and have provided crucial information on molecular charge transport insights. This investigation has stated that electrical conduction through single-molecules is governed by quantum mechanics, and thus, manifests some unique behaviours associated to the

nanoscale that have no analogue in bulk materials.[10] In addition, the theoretical and experimental investigation of molecular junctions under the effects of mechanical forces, thermal gradients or optical illumination, or in spin-unpaired molecular systems enables the study of mechanics, thermoelectronics, optoelectronics and spintronics at the molecular level. Thus far, hybrid molecular-electronic devices have revealed singular properties which can lead to unforeseen applications.[11] Nevertheless, despite nanofabrication techniques are advancing quickly, there are still significant problems that this technology has to face in order to constitute a realistic alternative.

In the next introductory sections we will summarize the charge transport fundaments in single molecules and we will discuss the basic principles involved in the design of molecular devices. Finally, the most remarkable measuring approaches and proposed molecular devices will be reviewed.

3.1 Charge transport in single molecules

Attending to the temperature dependence we can discriminate between two different transport regimes: **tunneling**, characterized to be temperature independent; and **hopping**, which is thermally activated. This last is typical of long molecules, except some remarkable cases as carbon nanotubes. Therefore, in short molecules or in molecules at low temperatures, tunneling mechanisms will dominate the transport.[1]

In resonant tunneling models, molecules are viewed as confined electronic systems coupled by tunnel barriers to source and drain electrodes, as represented in Figure 3.1. When a bias voltage is applied, the tunneling current passing through a molecule will be determined by the relative position of the molecular levels with respect to the Fermi level. Thereby, when a molecular level lies in between the voltage-bias window of source and drain, the resistance to the current flow along the junction will decrease. The energy of the molecular orbital closer to the Fermi level, and thus, the one that dominates the transport, is denoted as ε_o, which, in most situations, corresponds to the energy of the HOMO or LUMO level. Three terminal devices (3TD) enable the possibility of modifying

the energy of the molecular orbitals by sweeping the voltage of a third gate-electrode. Hence, in these configurations the junction can pass from high to low resistance zones by adjusting the gate-voltage due to the alignment of the molecular levels with the bias-voltage window.[12]

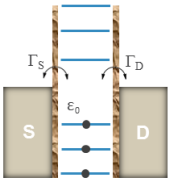

Figure 3.1 Schematic picture of the energy levels of a molecule connected to source and drain electrodes via tunnel barriers.

Nevertheless, the electronic structure of an isolated molecule does not fit exactly with that of the bound system. When a molecule is connected to one or more electrodes, the interaction between them causes a hybridization of both wavefunctions, which results in a broadening of the molecular electronic levels. The magnitude of this interaction is quantified by the coupling factor Γ that is the sum of the coupling with the two electrodes, $\Gamma = \Gamma_S + \Gamma_D$. As the coupling factor grows, the probability of coming into resonance with the electrodes is higher.[12, 13] When the molecule is equally coupled to both electrodes ($\Gamma_S = \Gamma_D$), the shape of the I-V curves will be symmetric. Thereby, according to the resonant tunneling model, two main factors determine the metal-molecule-metal resistance, the energy difference between the closest molecular level (ε_o) and the Fermi level of the electrodes and the coupling factor (Γ). These factors are determined by the chemical structure of the molecule, its conformation in the junction, and its chemical binding to the electrodes.[1, 13, 14] Nowadays, although the correlation between molecular conductance (*G*), junction stability and molecular structure is not completely understood, there are some trends that should be taken into account in the design of organic molecular wires.

3.2 Molecular wires design

First, we will treat the factors associated with the molecular chain.[1, 14] Along the wire the tunnel current depends exponentially on molecular length (L) and a tunneling attenuation factor, β, as shown in equation (iii).

$$G = G_o\, e^{-\beta L} \quad \text{(iii)}$$

The β factor has demonstrated to be characteristic of the chemical structure of the chain, although it can vary with the experimental conditions and measuring setup. Its experimental quantification in organic molecules has clearly evidenced that conjugated wires present much larger β values (0.2 to 0.4 $Å^{-1}$) than aliphatic chains, in which β values stay in the range from 0.8 to 1.2 $Å^{-1}$. This fact is ascribed to the lower HOMO-LUMO gap of π-systems (~ 3 eV) compared to saturated molecules (~ 8 eV) that leads to a better alignment with the electrodes Fermi level.[14] The value of the β parameter have been evaluated for a series of conjugated organic wires; twisted polyphenyl (t-PP), planar polyphenyl (p-PP), poly furan (PF), oligo phenylene vinylene (OPV), oligo phenylene ethylene (OPE), *cis-trans*-polyacetylene (ct-PA) and all *trans*-polyacetylene; whose chemical structure is shown in Figure 3.2. These values follow the order: t-PP› p-PP› OPE› OPV› PF› ct-PA › t-PA.[15]

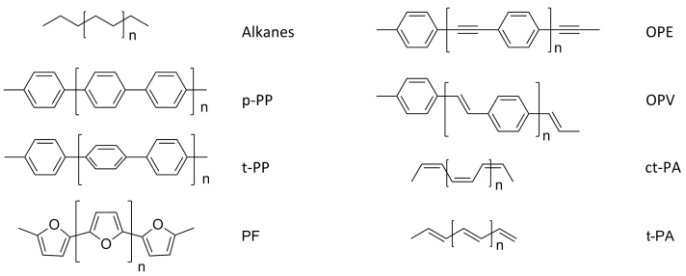

Figure 3.2 Chemical structure of some representative molecular wires.

The larger value found for p-PP compared to t-PP polymer indicates that, not only the nature but also the configuration of the chain has an effect on molecular conductance. The more planar configuration, and thus the larger extent of the conjugation, is reflected

in lower attenuation factors. In agreement with these results, different detailed studies performed on functionalized biphenyls showed a $\cos^2 \Phi$ dependence of molecular conductance with the torsion angle between phenyl rings (Φ), see Figure 3.3.[16-18]

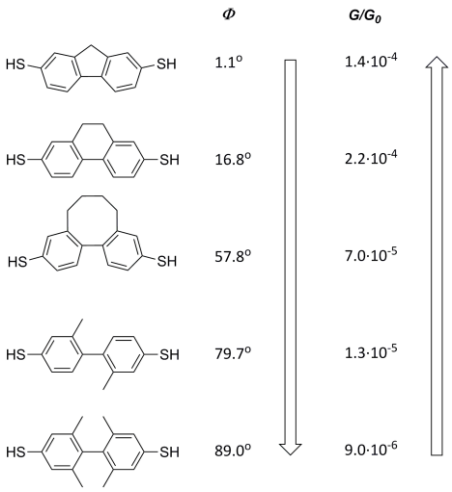

Figure 3.3 Experimental conductance vs torsion angle in a series of dithiolated biphenyls. Data extracted from ref.[17]

3.2.1 Anchoring groups

The way in what molecules bond to the electrodes, is the second factor determining the conductance of molecular junctions. Electrical contacts can be considered potential barriers whose magnitude is related to the coupling strength between the electrons in the molecules and those in the electrodes. In general, the physisorption of a molecule on the interface leads to weak couplings, whereas chemisorption involves the formation of strong covalent bonds between the anchoring groups and the electrodes, and hence, leads to higher couplings.[13] In a weak coupling situation, the resistance may be largely determined by the contact and no by the molecule under study.[12] For that reason, in molecular transport studies, the functionalization with suitable anchoring groups results highly recommendable.

The nature of the anchoring groups is closely related to the coupling parameter Γ, and thus, it plays a main role in the electrical characteristics of tunnel junctions. Ideal anchoring groups should provide, not only a strong coupling within the electrodes, but also reproducible and mechanically-stable contacts. Although a wide variety of anchoring groups have been reported to date,[13] herein we would limit the discussion to those included in Figure 3.4.

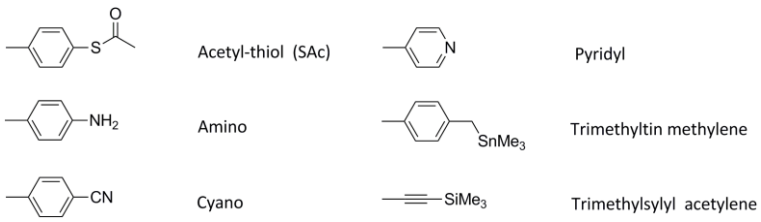

Figure 3.4 Chemical structure of the main anchoring groups treated.

So far, thiols have been the most employed anchoring groups in single-molecule measurements. The great affinity of sulfur for gold -the gold-thiolate bond has an strength of 2 eV or 50 kcal/mol- and its strong coupling with metal electrodes makes thiols excellent candidates for this means. Nevertheless, recent works reported that these derivatives usually lead to a lack of reproducibility in measured conductance.[19, 20] Charge transport in phenylene-thiol molecules is typically mediated by the highest occupied molecular orbital (HOMO) because is the closets level to the metal Fermi level.[21] The use of free phenyl thiols has proved to be problematic since, in solution, these molecules are very prone to suffer rapid oxidative disulfide formation.[5] For that reason, it is customary to work with thiol-protected derivatives. Among other capping groups, the acetylenic protected form of the thiol is the most commonly used,[22-26] since it is resistant to Pd-catalyzed coupling conditions, typically used in the synthesis of conjugated wires, and it also presents the advantage that it can be easily cleaved in the presence of metallic gold, even without the assistance of any deprotecting agent.[27]

The second most studied family of anchors is composed by nitrogen based groups: amino,[28-30] pyridyl[31-34] and cyano[35, 36] substituents. In general, these groups lead to a weaker coupling than thiols, and thus, to a higher barrier to the tunneling current.

However, although the coordination of nitrogen to gold is not such strong as sulfur, these groups still present high probability of junction formation. Additionally, they form very stable contacts and the particularly well-defined binding geometry that these molecules adopt between the leads, affords much more reproducible conductance values than the aforementioned thiols.[32-34] From the chemical point of view, the use of nitrogen-ended derivatives results very advantageous because they are compatible with a wide variety of reaction conditions and do not need to be protected in palladium-catalyzed reactions. Particular interest has attracted the promising characteristics presented by the pyridyl group.[32] It has been assessed that in these derivatives the electron transport occurs through the LUMO.[32]

Another anchoring groups tested include carboxilic acids,[28] and fullerenes.[37] However, more recently, some groups have explored different approaches for the direct binding of the carbon backbone to the gold leads in molecular junctions.[38-40] Either trimethyltin ($SnMe_3$, TMT) protected methylenes or trimethylsylyl ($SiMe_3$, TMS) protected acetylenes are cleaved off on gold surfaces with (TMS) or without (TMT) the assistance of a chemical agent, leading to the formation of an Au-C covalent σ-bond. These anchoring groups have given rise to very high conductance values, which in the case of TMT methylenes reach values up to 100 times larger than the analogous oligophenyl molecules with the amine termination.[39]

The position of the anchoring atom in aryl-terminated molecular wires is also a relevant issue. Sulfur or nitrogen substituents in *para* respect to the molecular axis are in resonance with the conduction pathway, and thus, the measured conductance values are higher. By contrast, when the anchoring groups are placed in *meta* the conjugation along the π-system is broken and the wires present a higher resistance to the current flow, as represented in Figure 3.5.[41]

Figure 3.5 Variation of molecular conductance with the position of the anchoring group.[41]

3.2.2 Charge transport through metal complexes

Electronic transport studies on individual molecules have been mainly focused on conjugated organic molecules due to its low resistance and high tunnability. However, the integration of metal complexes into electronic circuits is attracting an increasing interest[42, 43] since it combines the high tunnability of organic ligands with the special features of metal ions. Due to the special relevance of coordination compounds in this thesis, we would dedicate a short section to transport measurements through metal complexes.

As in the case of purely organic wires, to have a good coupling within the electrodes, metallic complexes are usually provided with metal-lead anchoring groups. Depending on the location of the anchoring, contacted metal complexes can fall into two different categories. In the first one, represented in Figure 3.6 A, the anchoring groups are placed in two separated ligands. Hence, the charge current is forced to pass through the metal ion, and in the absence of the metal center the molecule breaks down. [24, 44-48] In the second one, illustrated in Figure 3.6 B**,** the anchoring groups are placed on both ends of the same ligand. In this case, current will flow through the ligand even in the absence of the metal ion.

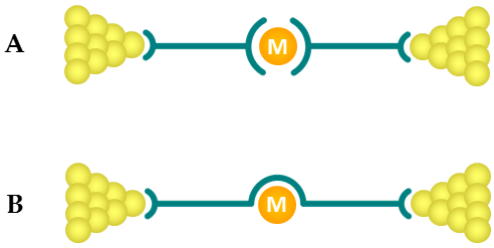

Figure 3.6. Schematic representation of the two different configurations of metallic complexes in single-molecule junction: **A)** Metal-complex junction with the two anchoring groups located in different ligands. **B)** Single-metal-complex junction with the two anchoring groups are located in the same ligand.

Metal complexes present particularly low HOMO-LUMO gaps, which in some cases can lead to a better alignment with the gold Fermi level, and thus, to low attenuation factors.[48-54] Some of these studies have tried to assess the effect of the metal ion on **A** type configurations by the comparison with purely organic wires,[48, 51, 52] nevertheless, from our point of view, the proper evaluation of the metal coordination influence on the conduction of organic wires requires the use of **B** type configurations, see Figure 3.7. This approach offers the possibility of investigating electronic transport either in the presence or absence of a metal center.[55-58] Indeed, the conductance response to the binding of a metal ion has been proposed as an example of single molecular sensor.[55]

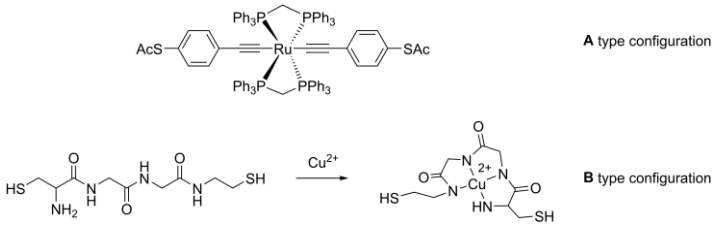

Figure 3.7 Examples of transition metal complexes implemented into molecular junction in **A** type[51] and **B** type[55] configurations.

In addition, metal complexes usually possess accessible redox and spin states whose alteration in the junction can lead to measurable changes in molecular conductance.[44, 45, 59] Hence, several metal-containing molecular switches have been proposed based on the manipulation of the redox state.[44, 45, 60, 61] Besides, the presence of a metal ion in the conduction pathway has specially employed in the search of Kondo effect evidences at

the single-molecule level. This effect appears when molecules possessing a net magnetic moment are involved in electronic transport. Its main feature is the appearance of molecular resonance at zero-bias. The Kondo resonance was observed for the first time at the single-molecule level in a Co(II) complex embedded in an electromigrated break junction.[47] More recently, the switching of the Kondo resonance has been induced by a gate voltage in a dinuclear cobalt complex with two coupled spins that transits between singlet and triplet states.[62]

3.3 Measuring single-molecule conductance

Over the last decades the attention awaked by the emerging field of molecular electronics has encouraged the development of new and even more sophisticated setups for studying electron transport in molecular junctions. The great advances carried out in lithographic and metal deposition techniques have enabled the fabrication of nanometer-sized gaps between metal electrodes by a wide variety of techniques. Metal electrodes can be obtained in a controlled and reproducible way by electrochemical or chemical deposition methods, [63] by shadow masks evaporation (see Figure 3.8 A), e-beam lithography, or by the rupture of a narrow thin metal wire by electromigration (Figure 3.8 B). Another recent approach for creating molecular-scale gaps are based in the use of nano-objects like carbon nanotubes[64] or gold nanoparticles, see Figure 3.8 C and D.[65-68] Further information concerning the fabrication of electrodes can be found in recent reviews.[63, 69]

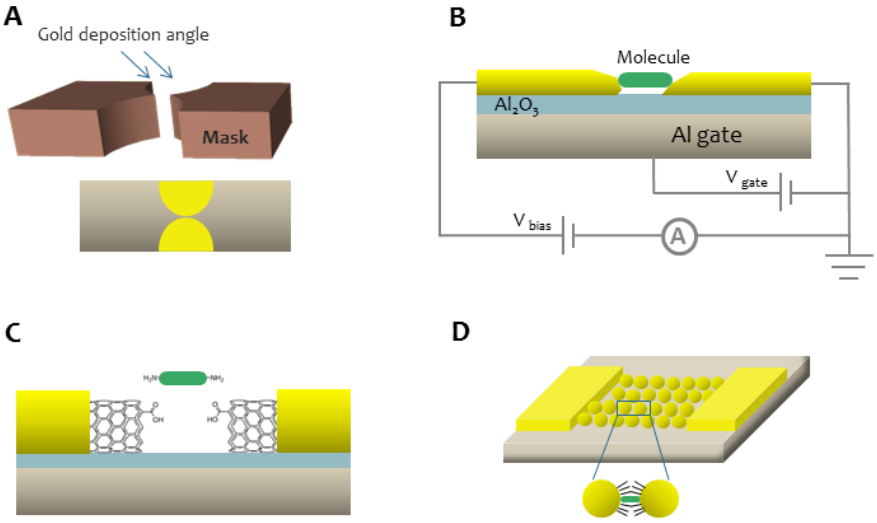

Figure 3.8 Schematic diagrams of several nanogap-formation techniques: **A)** Oblique angle shadow evaporation technique; [63] **B)** Electromigrated thin metal molecular junction on top of a Al/Al_2O_3 gate electrode;[12] **C)** Nanogap formed by an etched carbon nanotube contacted by metal electrodes. The carboxylic groups dangling at the ends of the conducting nanotubes react with the amine groups incorporated in the target molecules to form covalently attached molecular junctions; **D)** 2D-Nanoparticle network connected to evaporated metal electrodes. Nearest-neighbour nanoparticles are connected by molecular bridges.

Among all the reported techniques, STM and MCBJ provide the most accurate control over the electrode-gap size. Scanning probe techniques constitute a very powerful method for electron transport measurements since they combine high-resolution imaging (STM) and spatially resolved electrical microscopy (Scanning Tunnel Spectroscopy, STS). In these setups, I-V measurements can be recorded at different positions over an individual molecule lying flat on a surface (Figure 3.9 A) or along standing-up molecules that have grown onto a substrate as a SAM. To avoid interactions between target molecules they can be isolated by embedding them on a matrix of self-assembled inert molecules such as alkanethiols (Figure 3.9 B). In STM experiments there is no contact between the molecule and the tip, and thus, the junction results asymmetric.[51]

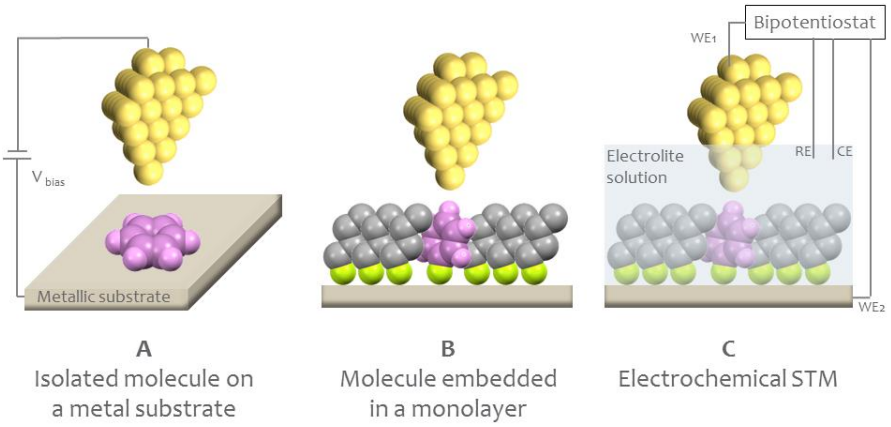

Figure 3.9 Schematic diagrams of different scanning probe techniques on single molecules.

In MCBJ, the molecular junction is formed by bending the substrate over which a metallic wire has been deposited on a three-point support in the presence of the molecules under study, as represented in Figure 3.10. Once the metallic wire is broken one of these molecules may get trapped between the two electrodes creating an electrical contact. At this point, histograms of the conductance evolution as a function of the electrode distance can be performed by further pushing this flexible substrate. The MCBJ method affords highly symmetrical junctions of tunable nanometric size with an impressive mechanical stability.[70]

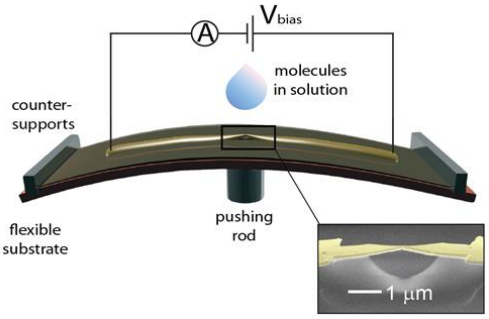

Figure 3.10 Layout of a MCBJ setup. Inset: scanning electron micrograph of a MCBJ device.

Scanning Tunneling Microscopy Break Junctions (STM-BJs) represents an innovative method that surged from the combination of STM and MCBJs techniques.[18, 71, 72] It

consists in approaching an STM tip to a molecule lying flat on a conducting substrate. When a contact is established, the tip is gently retracted and the molecule is lifted from the surface. Thereby, conductance histograms of isolated molecules can be recorded. This 'fishing' method affords more symmetric junctions than classical STM experiments.

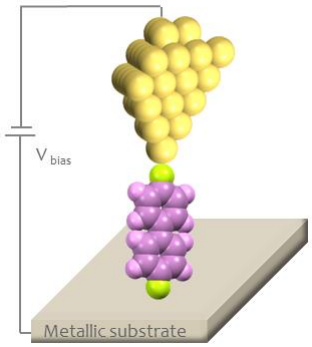

Figure 3.11 Schematic diagram of molecular junction formed in a STM-BJ.

In some cases, a third gate electrode that enables the access to the electronic exited states of the molecule can be incorporated into the setup.[12] 3TD have been intensely pursued since it enables the fabrication of molecular field-effect transistors (FETs) with electrochemically switchable molecules. The immersion of the device in an electrolytic solution along with reference and counter electrodes makes possible to control the charge of the molecule during the transport measurement using a potentiostat. These liquid electrochemical cells have been successfully implemented in STM setups, as schematized in Figure 3.9 C.[73] However, in the solid state, 3TD have to deal with several technical and geometric limitations that make difficult to achieve high gate couplings.[74]

Although all the methods described above may be valid for the determination of molecular conductivity, in many cases, the results reported for analogous molecular systems in different conditions are not consistent enough. Therefore, the complementary use of different molecular-conductivity measuring techniques can be a good help to understand and corroborate relevant phenomena.

3.4 Molecular electronic devices

Molecular wires are molecules that can efficiently transport charge and provide interconnections in electrical circuits.[4] However, computing applications demand molecules to work, not only as wires, but as active elements capable of performing active functions like current rectification. Another pursued function consists in the switching of the electrical conductance by an external impulse, which envisions the application of molecular junctions as memory units. Many of these behaviors have been achieved on 'many molecules' junctions, however, herein we would limit the discussion to single-molecule approaches.

3.4.1 Rectifiers

Rectifiers, or diodes, are devices that allow the electrical current to pass in one direction but block it in the opposite one. This effect is reflected in asymmetric I-V curves. Since it was proposed in 1974 by Aviram and Ratner,[2] the challenge of creating molecular-based rectifiers have been achieved by different groups. This work predicted the appearance of a rectifying behavior in connected molecules possessing separated donor and acceptor groups, see Figure 3.12. Charge transport measurements have finally confirmed the appearance of a molecular rectifying behavior in donor-acceptor structures[75] and also in non-symmetrical molecules (see Figure 3.12).[76]

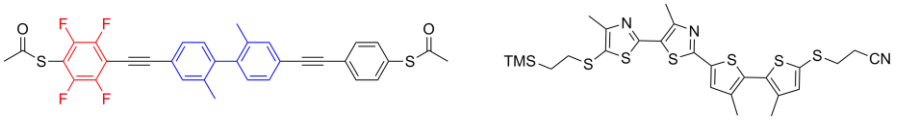

Figure 3.12 Two molecules presenting current-rectifying behaviour, based on donor-acceptor[75] systems and in asymmetric structures.[76]

3.4.2 Switches

Switches are electronic devices whose resistance to the current flow can be tuned by the application of an external impulse. As pointed out in the introduction of the first chapter, the denomination of molecular switch is generally applied to any chemical system that can exist in at least two states with distinguishable spectral, electrochemical or magnetic properties, as long as the transition between the different states could be controlled by an external stimulus and does not occur spontaneously.[77] However, for the realization of electronic devices, this switching may lead to a measurable change in molecular conductance.

In general, it is expected that molecular systems retain its functionality after contacted; however, the molecule-electrode coupling is a determining factor able to transform a switchable molecule into a passive junctions, as well as transforming passive molecules into junctions with switchable properties. Hence, we could find two different types of molecular switches; **intrinsic switches**, that are bistable molecules that retain its functionality in the device; and **extrinsic switches**, formed by non-active molecules that present switching properties when they are integrated on a measuring setup.[78]

The extrinsic switching phenomenon is generally induced on molecules by electrical current or field, but the mechanisms are, generally, not very well understood. Lörtscher *et al.* reported the voltage-triggered switching behavior of a rod-like molecule with nitro substituents embedded in a MCBJ (Figure 3.13). [79]

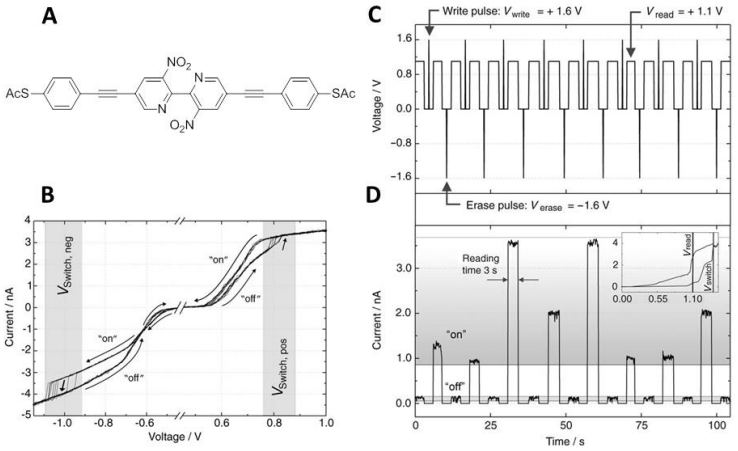

Figure 3.13 Controlled switching of a BPDN-dithiol molecule (shown in **A)** contacted in a MCBJ at 100K. If the voltage applied exceeds a positive threshold value ($V_{Switch,pos}$), switching from the initial OFF to the ON state occurs. A negative voltage sweep or a pulse below the negative threshold value ($V_{Switch,neg}$) resets the molecule to the initial 'off' state. **B)** Hysteretic I-V curves. **C)** Write, read and erase voltage pattern applied. **D)** Resulting switching between OFF and ON state.

In intrinsic switching devices, light, current and electric field are the external stimuli that have been employed to induce molecular changes. Depending on the nature of this process, switchable molecules can be classified in conformational or redox switches. In this classification pure conformational switches do not involve a redox-state alteration; however, changes in the molecular redox state are usually accompanied by conformational changes of different magnitude.

3.4.2.1 Conformational switches

Conformational switches are molecules whose isomers possess different 3D structures. One example of conformational change is the hydrogen tautomerization reaction found in the naphthalocyanine molecules. This process was induced by the tunnel current in an STM setup and led to considerable changes in the conductance.[80]

Another stimulus used to induce conformational changes in molecules is light. The two main photoswitchable systems studied in molecular devices have been azobenzenes and diarylethenes, illustrated in Figure 3.14. Since the *cis-trans* isomerization in azobenzenes

implies a large change on the molecular length, most of the work performed on azobenzenes has been performed in STM setups. By these means, light-induced switching have been detected on azobenzenes lying flat on a substrate,[81] or rather mixed on alkanethiols SAMs.[82, 83]

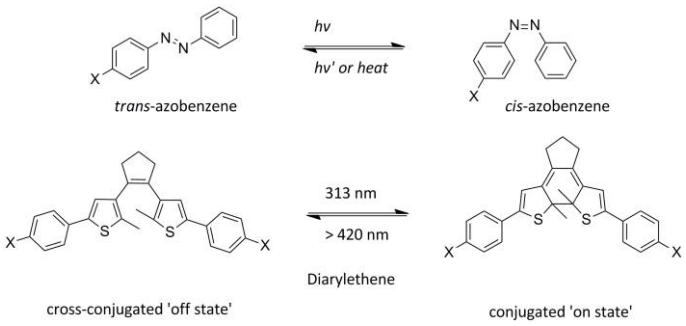

Figure 3.14 Photoisomerization in azobenzene and diarylethene molecules.

On second place, the case of diarylethenes constitutes an example of quenching of the switching molecular behavior caused by the electrode attachment. First attempts performed on these molecules showed that the strong coupling of the HOMO level with the electrodes avoided the photoinduced switching of the molecule back to the 'ON' state.[84] Fortunately, this problem could be solved by introducing groups that decreased the conjugation, and thus, reduced the metal-molecule coupling. By this strategy, the light-controlled conductance switching of diarylethenes, could be finally observed.[67, 85]

3.4.2.2 Redox switches

Charge switching involves a redox process on the molecule that leads to a permanent change in the number of electrons. This change can be achieved in a two-terminal device by the application of a high bias[86, 87] or by the use of a third gate electrode.[12] The observation of charge switching requires the permanent charging of the molecules implied. In solid state devices, when molecules are strongly coupled to the electrodes, electrons flow freely and permanent charging is not possible. In STM setups, this process can be avoided by the introduction of an ultrathin insulating film that decreases the

coupling with the conducting substrate. By using this strategy, different charge states could be detected in isolated single metal atoms and complexes. [88, 89]

The difficulties found in introduction of a third gate electrode in solid-state measuring setups makes that the examples of charge switching are rather scarce.[45, 47, 90] By contrast, the introduction of a third electrode in liquid cells results much more feasible. Electrochemical STM setups have provided a very prolific platform for the observation of the redox switching behavior. In these experiments the molecular redox state can be modified by independently controlling the tip and the substrate potentials with respect to a reference electrode immersed in the solution and the new charge introduced in the molecule is compensated by liquid electrolytic media.[91] An electrochemically triggered switching behavior could be observed by this approach in either STM[92, 93] or STM-BJs setups;[91, 94, 95] and in different redox-active systems like: viologens[92, 94], perylene bisimide derivatives [91, 95] or metal complexes.[44, 93] An impressive case was presented by Tao *et al*, in which a perylene tetracarboxylic diimide (represented in Figure 3.15) was used to control the current with a gate electrode over nearly 3 orders of magnitude, at room temperature.[91]

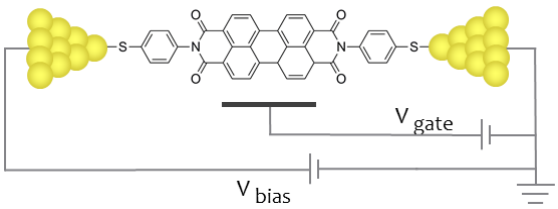

Figure 3.15 Scheme of a single molecule transistor based on a perylene tetracarboxylic diimide molecule with an electrochemical gate.[91]

3.4.3 Mechanically Interlocked devices

Switchable mechanically interlocked molecules integrated in electronic circuits could fall in both of the previous categories, conformational or redox switches, since the switching is generally promoted by a change in the molecule oxidation state. Nevertheless, due to their peculiar characteristics and their relevance in this thesis they will be treated in a

separated section. As pointed out in the first chapter, the redox hysteresis that characterizes these systems makes them very promising candidates for the fabrication of memory molecular devices.

Till the date, all the reported examples have been based on redox switches.[96-104] Most of the research performed in this field has been carried out by Prof. J.F. Stoddart, in collaboration with J. Heath and S. Williams groups, and has been recently reviewed.[105] Stoddart´s rotaxanes and catenanes are conformed by a π-electron deficient cyclobis(paraquat-*p*-phenylene) ($CBPQT^{4+}$) ring that moves between two π-electron-rich aromatic subunits (typically 1,4-dioxybenzene and TTF). The charge state of the TTF (tetrathiafulvalene) moiety (TTF or TTF^{2+}) determines the preference of the $CBPQT^{4+}$ ring for one station or the other.

Such systems have been tested in two-dimensional molecular arrays sandwiched between metal electrodes of different nature but no single-molecule approaches have ever been attempted. The investigation of charge transport was performed in two terminal configurations. It used a short voltage at low bias to interrogate the molecule (+0.2 V) and pulses at higher bias (+/- 1.5 V) to switch to the ON/OFF redox state.[101] When a combination of titanium and silicon or single-wall carbon nanotubes was used as top/bottom electrodes, the authors found a current-induced switching of the conductance in Langmuir-Blodgett monolayers of rotaxanes that was ascribed to the topoisomerization of the interlocked system.[98, 101, 104] The lifetime of the metastable species went from 1 s in solution to 10 min in tunnel junctions. Further studies at different temperatures demonstrated that the switching process in tunnel junctions was thermally activated.[106] By contrast, a large switching behavior was found in molecular devices constructed with a combination of Pt/Ti top/bottom electrodes that demonstrated to be molecule-independent, and thus, not associated to topoisomerization processes.[100] Finally, the only example that reports the measurement of these molecules in three-terminal configurations showed a molecular independent conductance response that was assessed to interfacial states; hence, no field-induced switching could be observed. [99] Therefore, these examples evidenced that when switchable mechanically

interlocked are introduced into high viscosity polymer matrices or in self-assembled monolayers deposited on metal surfaces, the thermodynamics that characterize its switching behavior remain approximately constant whereas the kinetics are significantly slowed down with respect to the solution phase. This fact has been ascribed to the dense packing of the media.[105] By contrast, this resistance to molecular motions is not expected when the measurements are performed on isolated molecules, like in MCBJ setups.

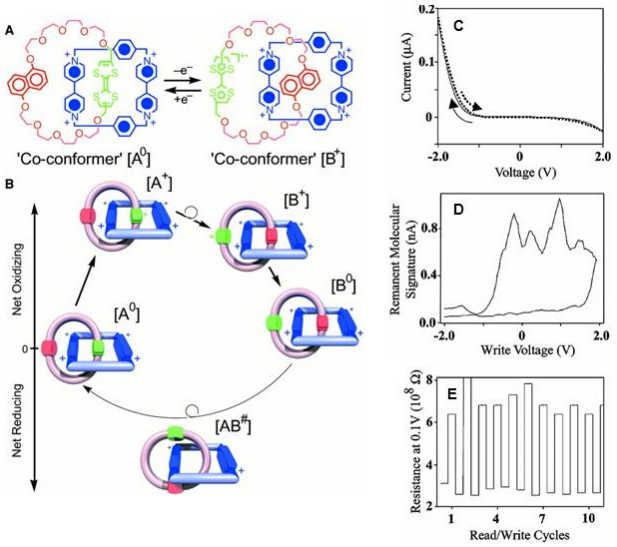

Figure 3.16 Conductance switching of a catenane-based molecular device.[107] **A)** Two states of the catenane **B)** Proposed switching mechanism in the device. When the [2]-catenane is oxidized (Bias voltage of -2V), the TTF groups (green) are positively charged, leading to the movement of the $CBPQT^{4+}$ (blue) to the neutral red station $[B^+]$. Reduction of TTF and partial reduction of the $CBPQT^{4+}$ (at 12 V bias) is necesary to regenerate $[A^o]$. **C)** I (V) hysteresis loop of one of the devices. **D)** The remnant signature of the device, measured by varying the write voltage in 40 mV stepsand by reading the device at -0.2 V. **E)** Switching operation of the device. The junction resistance was read at 0.1V as the device was alternatively opened at + 2V and closed at -2V. The authors relate the OFF state to $[A^0]$ and the ON state to $[B^0]$.

Results and discussion

This chapter is devoted to investigate the effect of metal coordination in the single-molecular conductance of conjugated wires, as well as to take advantage of the redox and optical properties of two different metal complexes for the development of functional molecular devices.

First, with the aim of studying the redox switching behavior of bistable rotaxane **R3**$^{+}$ in two-terminal MCBJ, we prepared a series of molecular wires by substituting the stoppers of the axis of this rotaxane by metal-anchoring groups of different nature. This gave rise to a family of symmetric ligands bearing a phen chelating site. The synthesis and electrical properties of these isolated backbone molecules is described in section 3.5.

These molecular backbones were designed to enable the measurement of electronic transport either in the presence or absence of a metal centre. Thus, in first instance, they were employed for the investigation of the Cu(I) coordination effect on molecular conductance, discussed in section 3.6. Although the influence of metal ions in the conduction pathway had been studied before, the effect of metal coordination avoiding changes on molecular conformation has been evaluated here for the first time. Besides, the electrical characterization performed on the Cu(I) complexes with the different wires, allowed us to choose the most suitable molecular backbone for the construction of the bistable threaded system.

The synthesis and characterization of the bistable copper pseudorotaxane system functionalized with electrode anchoring groups is described in section 3.7. This represents the first attempt of studying the conductance response of a mechanically interlocked system at the single-molecule level. Previous examples performed on mechanically interlocked molecular junctions reported a voltage-triggered switching behavior even when no bistable molecules were embedded between the electrodes, thus indicating that they are not associated to a molecular motion.[100] Herein, in order to assess

the origin of the conductance response to the current impulse, the two redox states of the bistable threaded system will be characterized separately in a single-molecule junction.

Finally, owing to the versatility of the phen chelate, these ligands will also be employed in the preparation of a family of photoactive Ir(III) molecular wires (section 3.9). Light excitation on cyclometallated Ir(III) complexes leads to a considerable perturbation of the electronic structure, and thus, it is expected that the molecular conductance of this Ir(III) wires will be greatly affected by light irradiation. With the aim of getting further insights into the nature of the ground and photoexcited state we have carried out the complete electrochemical and photophysical characterization of this wires. This study will help in the further assessment of photoconductance effects.

The work presented herein have been performed in collaboration with the experimental physics group of Prof. Herre Van der Zant from T.U. Delft, who carried out the single-molecule electronic transport measurements here described, the Electronic Structure Theoretical group led by Prof. Eliseo Ruiz from Universitat de Barcelona, who performed Non Non-equilibrium Green Functions together with DFT calculations (NEGF+DFT) of sections 3.6 and 3.7, and the Theoretical Chemistry Research Unit leaded by Prof. Enrique Ortí from the ICMol that carried out the DFT calculations and Dr. Nacho Vayá form the organic chemistry department in Universitat Politècnica de Valencia, who carried out part of the photophysical study included in 3.8 section. Therefore, the results described in this chapter are the result from an intense feedback between the experimental physicists, the theoretical/computational chemists and us, the synthetic chemists who designed, prepared and characterized the molecules.

3.5 Molecular wires bearing one coordinating site

Looking for a reliable and highly conductive molecular platform for the investigation of electronic transport through metal complexes, we designed and synthesized a family conjugated ligands with different lengths and anchoring groups, whose chemical structure is presented in Figure 3.17. These structures possess the same coordination core than **R3**$^{+}$, consisting on a phen unit symmetrically functionalized on 3- and 8- positions, since these wires were designed in first instance for implementing this bistable rotaxane into a MCBJ.

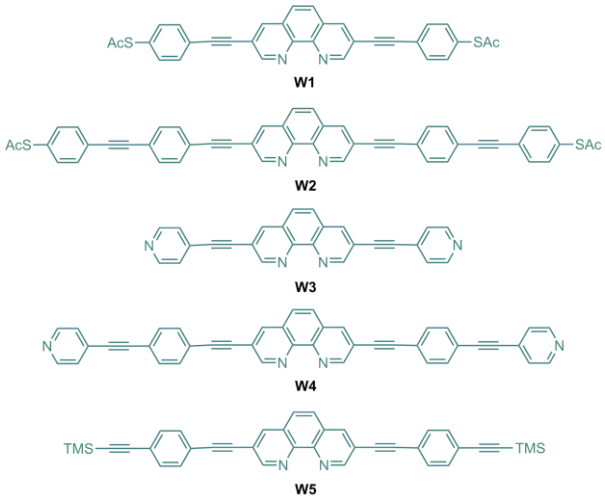

Figure 3.17 Chemical structure of the wires. The approximate molecular length between anchoring atoms is 2.4 nm for **W1**, 3.7 nm for **W2,** 2.1 nm for **W3**, 3.4 nm for **W4** and 2.6 nm for **W5**.

Metal coordination, apart from a redistribution of the electronic density, can induce conformational changes on the ligands that considerably affect the electronic transport.[55-58] Nevertheless, in phen ligand the torsional degree of freedom is suppressed and imine nitrogens are fixed in a *cis*- conformation even before metal interaction, see Figure 3.18.

Hence, any change in conductance after metal chelation in our molecular wires must be directly derived from the effect of metal, with minor contributions coming from changes in molecular conformation.[18]

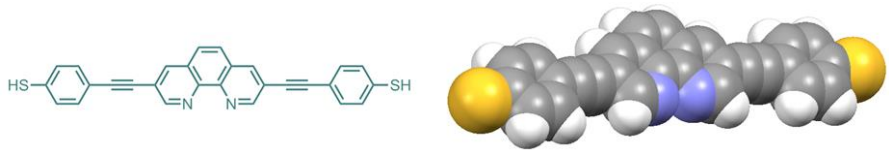

Figure 3.18 Chemical structure and DFT-optimized structure of deprotected **W1**.

On the other hand, it is well known that the nature of the anchoring groups greatly affects the electrical conduction through the junction.[28, 32, 108] Therefore, we provided the phen-based molecular backbones with different terminations in *para* to the backbone axis searching for the most suitable contact with the electrodes. The three anchoring groups tested have been: thiols (**W1** and **W2**), pyridines (**W3** and **W4**) and acetylenes (**W5**).

Finally, in order to add some distance between the metallic center and the electrodes, the phen core has been linked to the anchoring groups by phenylethynyl spacers of different length. The OPE-like system is expected to provide high conductance values along the molecular axis due to the low OPE tunneling attenuation factor (β 0.24 - 0.16 $Å^{-1}$).[23, 109] Besides, these spacers present the advantage that they do not give rise to isomers and have the ability of extending the conjugation along the wire regardless of the relative orientation of the phenyl groups. From a synthetic point of view, the ethynyl group is also very attractive since it is chemically stable, and easy to attach through Sonogashira coupling protocols.

3.5.1 Synthesis of the wires

The synthesis of ligands **W1-W5** was accomplished by a sequence of Sonogashira-type cross-coupling reactions between 3,8-dibromo-1,10-phenanthroline and substituted phenylacetylenes**,** resumed in Scheme 3.1. Preparation of **W1** and **W3** has been already described[110, 111] and its synthesis was accomplished following a slight modification of

described synthetic procedures. However, their molecular transport features had remained unexplored until now. By contrast, the synthesis of **W2**, **W4** and **W5** is described here for the first time.

For the synthesis of short molecular wires **W1** and **W3**, 3,8-dibromo-1,10-phenanthroline[112] (**11**), was coupled with commercial ethynyltrimethylsilane, to afford **35** in good yield. Following desilylation under basic conditions (K_2CO_3 in methanol) afforded diethynyl intermediate **41** in 97 % yield[113] which was then coupled with two equivalents of 4-iodopyridine or 1-(S-Acetylthio)-4-iodobenzene (**42**) under Sonogashira conditions to afford the desired **W1** and **W3** in high yield. [114, 115] The yield of the synthesis of **W1** could be enhanced from 21 to 40 % by the use of the $Pd(dba)_2$ catalyst during the last-step, as described by Flatt *et al*.[115]

The synthesis of **W5** has been carried out by the coupling of **11** with 2 equivalents of ((4-ethynylphenyl)ethynyl)trimethylsilane (**28**) in the same coupling conditions than that used in the case of **35.** Backbone **W5** was previously prepared by the reaction of 1,4-diethynylbenzene with n-BuLi and subsequent quenching by the addition of chlorotrimethylsilane, as already mentioned in the previous chapter (compound **29**).[116]

Longer wires **W2** and **W4**, were prepared from the desilylation of **W5** under basic conditions to afford **30**, and following coupling with two equivalents of 4-iodopyridine or 1-(S-Acetylthio)-4-iodobenzene (**42**) to obtain desired molecular rods **W2** and **W4** in very good yield (63 and 96 %). [114, 115]

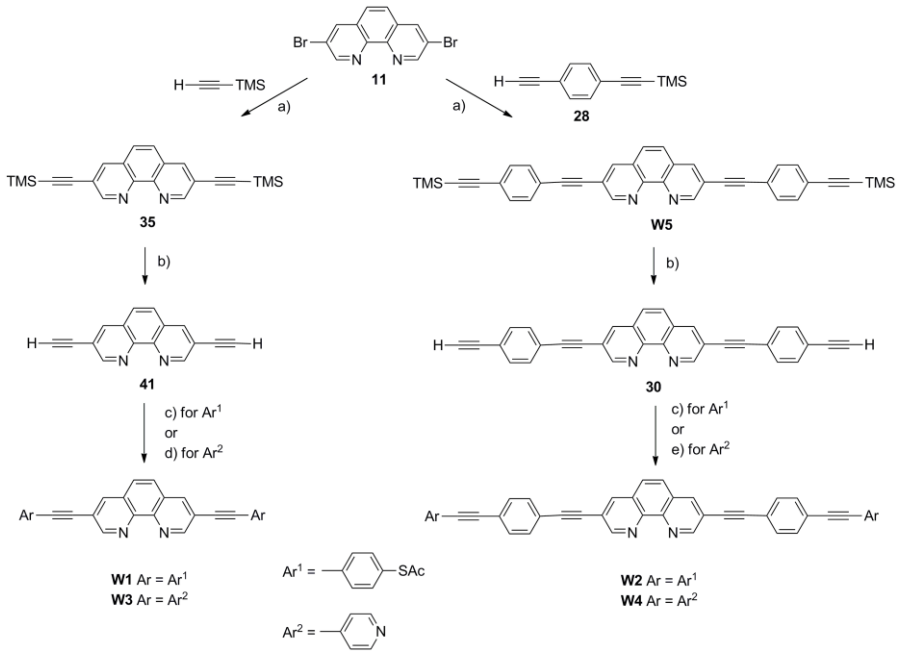

Scheme 3.1 Synthesis of molecular wires **W1-W5**: **a)** $Pd(PPh_3)Cl_2$, CuI, THF, i-Pr_2NH (74% for **35**, 50% for **W5**); **b)** K_2CO_3, MeOH (97% for **41** and **30**); c) 2 **42**, $Pd(dba)_2$, PPh_3, CuI, THF, DIEA (40% for **W1**, 63% for **W2**); **d)** 2 4-Iodopyridine, $Pd(PPh_3)_4$, CuI, THF, DIEA (84%); **e)** 2 4-Iodopyridine, $Pd(dba)_2$, PPh_3, CuI, THF, DIEA (96%).

Whereas, 4-iodopyridine is commercially available, the synthesis of **42** was accomplished in 95% yield by the reduction of 4-iodobenzenesulphonyl chloride[117] (Scheme 3.2). This method turned out to be much more efficient that the lithiation method described by Tour et al.[118] for the preparation of this acetyl protected thiol, widely used in molecular electronics.

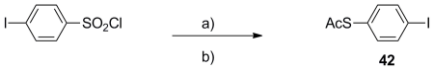

Scheme 3.2 Synthesis of **42. a)** Zn, $(CH_3)SiCl_2$, DMA, $ClCH_2CH_2Cl$; **b)** AcCl (98 %).

Alternatively, we attempted a different synthetic pathway for the preparation of the extended wires **W2** and **W4**, consisting in building the molecules from the extremes to the center (Scheme 3.3).

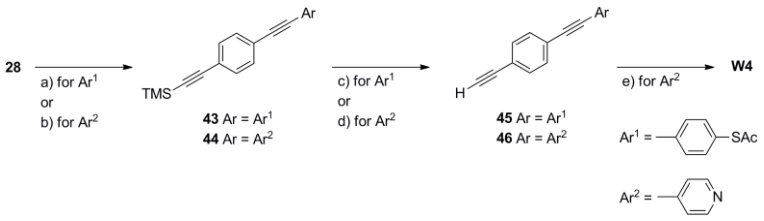

Scheme 3.3 a) 42, $Pd(PPh_3)Cl_2$, CuI, THF, DIEA, 43%; **b)** 4-Bromopyridine hydrochloride, $Pd(PPh_3)_2Cl_2$, CuI, i-Pr_2NH, 74%; **c)** TBAF, AcOH, AcOAc, 93%; **d)** K_2CO_3, MeOH, 100%; **e) 11**, $Pd(PPh_3)_4$, CuI, TEA, THF 60ºC, 41%.

First, compounds **43**[119] and **44**[120] were efficiently prepared by the reaction of **28** with 4-bromo-pyridine and **42** respectively under standard Sonogashira conditions.[115, 121] Cleavage of the trimethylsilyl group for the pyridine-ending derivatives was carried out in basic conditions (K_2CO_3 in methanol), but in the case of the sulfur derivatives these conditions promote the cleavage of the thioacetate group. For this reason, compound **43** was deprotected with TBAF in the presence of an excess of acetate.[115]

This route afforded molecular rod **W4** in moderate 24% overall yield from compound **11**, by its coupling with two equivalents of ethynyl derivative **46**, but unfortunately, it was unsuccessful for preparation of rod **W2**. The coupling of two equivalents of **45** with **11** did not afford the target molecule **W2**. Although **11** double coupled with **28** and **46** in moderate yield, it was not reacting with acetylene **45**, probably due to its low solubility. For this reason, for the preparation of molecular wires **W2** and **W4** we opted for the general first synthetic approach (Scheme 3.1).

3.5.2 Electronic transport features

The single-molecule conductance features of molecular backbones **W1-W5** at room temperature were investigated using the MCBJ technique in the low-bias regime (see the details in the experimental section). Thousands of breaking traces were collected by measuring the conductance (G = I/V) as a function of electrode displacement (z) with a bias voltage of 0.1 V applied across the electrodes. Compared with the empty gold junctions, individual breaking traces measured on electrodes exposed to pure solvents

(see Figure 3.52 A in the experimental section) did not introduce additional features. By contrast, when the MCBJ devices were exposed to solutions containing the target molecules, additional conductance plateaus were observed for sub-G_0 conductance values (Figure 3.19, insets).

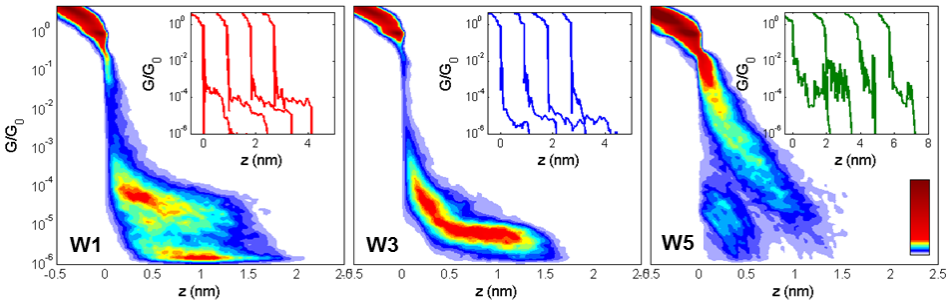

Figure 3.19 Trace histograms obtained from 1000 breaking traces as those shown in the insets for junctions exposed to 0.5 mM solutions of **W1**, **W3** and **W5**. The bias voltage was 0.1 V and the electrode displacement speed 12 nm/s. The colour scale indicates the number of counts found at each conductance value for a certain electrode displacement. The areas with high counts denote the most probable evolution during the formation of the molecular junctions.

Typical trace histograms obtained from 1000 consecutive breaking traces measured in the presence of short backbones **W1**, **W3** and **W5** are shown in Figure 3.19. To build these 2D-trace histograms, the individual breaking traces without any data selection, have been shifted along the horizontal electrode displacement-axis to fix the rupture of one-atom gold contact at zero. The histograms for **W1** and **W3** show the occurrence of conductance plateaus with distinguishable conductance values, but traces measured in the presence of **W5** appear noisier. According to their length, these plateaus observed just after the breaking of the metallic contact correspond to the formation of single-molecule junctions, where the anchoring groups provide the mechanical and electrical connection between the gold electrodes and the individual molecule.[122] However, at shorter electrode displacements the phen unit may compete with the terminal anchoring groups and contribute to the conductance.[123-125]

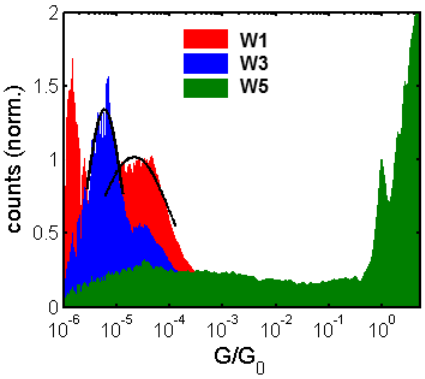

Figure 3.20 One dimensional conductance histogram obtained from the trace histograms displayed in Figure 3.19.

Figure 3.20 shows the 1D-conductance histograms for **W1**, **W3** and **W5** obtained from data in Figure 3.19. These histograms reveal well-defined peaks only in the case of **W1** and **W3**. A Gaussian fit to these peaks was used to identify the most probable conductance for a single-molecule junction. In the case of **W1**, a broad peak is centred at $2.1 \cdot 10^{-5}$ G_0, while for molecule **W3** the peak is centred at $5.8 \cdot 10^{-6}$ G_0. Although single-molecule transport through thiolated BPE (bipyridyl oligophenyleneethynylene) molecules has been studied before,[56, 126] authors did not report any low-bias conductance value to compare with. Nevertheless, **W1** exhibits a conductance value close to the value of $2.1 \cdot 10^{-5}$ G_0 reported for the biphenylene oligophenyleneethynylene dithiolated derivative reported by Zhang *et al.*[127] As in the case of **W1**, in this compound the central aromatic rings are forced to remain planar through proper chemical substitution. Thus, the phen moiety affords a molecular resistance value comparable to that reported for a planar biphenyl unit. . In agreement with its molecular length, molecular backbone **2** presents a molecular conductance value intermediate between that reported for OAE3 and OAE4 (OAE = oligo(aryleneethylene)s) with terminal pyridyl groups measured in MCBJ.[128] Besides, previous works on tolane molecules in MCBJ reported by Hong *et al.*,[32, 40] describe a comparable increase of the resistance on passing from acetylenes to thiols and then to pyridines, G (acetylenes) > G (thiols) > G (pyridines), and described the following sequence for junction formation probability and stability: pyridines, acetylenes

> thiols. However, under our experimental conditions, acetylenes did not afford well-defined conductance plateaus in the measured *breaking traces (*Figure 3.19).

The trace histograms obtained for junctions exposed to longer wires **W2** and **W4** did not show any molecular signature, see Figure 3.21. We attribute this result to the higher length of these molecules which leads to a higher resistance. According to equation (iii): $G = Go\, e^{-\beta L}$,[1] and considering the attenuation factor reported for OPE polymers[15] (β= 0.19 Å^{-1}), the drop of molecular conductance caused by the elongation of wires **W1** and **W3** to **W2** and **W4** (ΔL= 14 Å) could be roughly estimated in Δlog G = -2.6 G_0. According to the molecular conductance values found for **W1** (log G = -4.7 G_0) and **W3** (log G = -5.2 G_0), the conductance of **W2** and **W4** must be below the detection limit of the experimental setup (log G = -6 G_0).

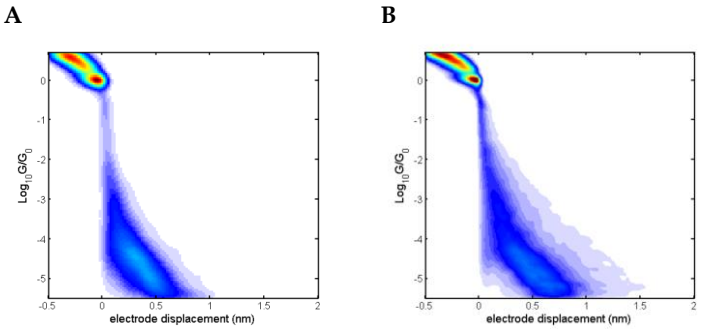

Figure 3.21 Trace histograms obtained for junctions exposed pure solvent (**A**) and **W4** (**B**) after 1 day of deposition.

3.5.2 Conclusions

The electronic transport features of the family **W1**-**W5** have been measured at room temperature by the MCBJ technique. Most probable conductance values could be extracted from the trace histograms of thiol and pyridine-ended wires **W1** and **W3**. The values obtained for these molecular backbones are in good agreement with that reported for similar structures. By contrast, acetylene derivatives did not show clearly defined plateaus and no precise conductance values could be obtained. The single-molecule conductance of longer wires **W2** and **W4** was below the detection limit of our setup.

Even though, we want to note that this fact does not imply that the conductance of these molecules cannot be measured. It is expected that this limitation could be overcome by the use of 'many molecule' approaches,[129] and thus, these molecules could find application in other transport measuring setups.

3.6 Effect of copper coordination on the conductance of single molecular wires

In this section will study the conductance response of our conjugated molecular wires to the coordination of Cu(I). The evaluation of the metal coordination effect on the conductance of a conjugated wire in **B** type configurations has only been performed on peptides[55] and on ligands of the 2,2'-bipyridine family.[56-58] All these examples reported an increase of molecular conductance upon coordination, which is obscured by a change in molecular configuration. Both, phen and bipy are considered excellent coordination chelates capable of forming stable complexes with most transition metal ions. However, whereas in bipy both pyridine rings can rotate respect each other, in phens the torsional degree of freedom is suppressed. Accordingly, in our phen-based molecular wires, any change in conductance must derive from the effect of metal ion with minor contributions coming from changes in molecular configuration.[18] Thereby, we can isolate the effect of Cu(I) coordination on the conductance.

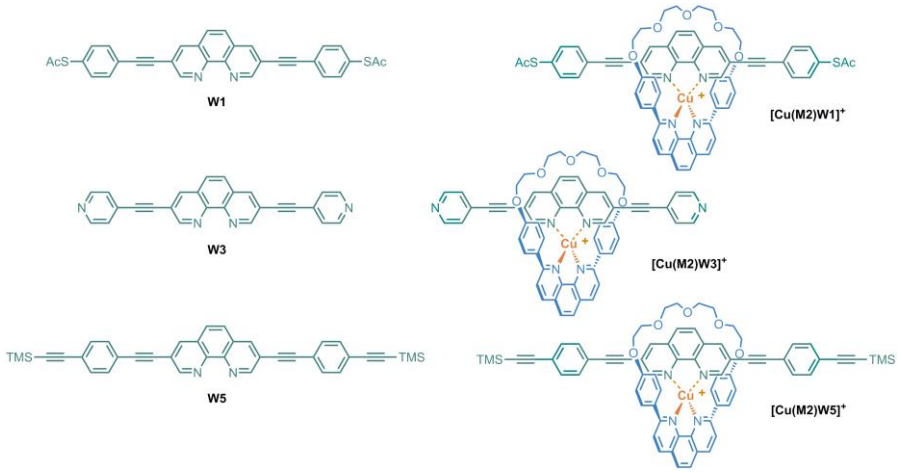

Figure 3.22 Chemical structure of molecular wires **W1**, **W3** and **W5** and their corresponding complexes [Cu(**M2**)**W1**]$^{+}$, [Cu(**M2**)**W3**]$^{+}$ and [Cu(**M2**)**W5**]$^{+}$.

In the following we have measured the electrical properties of short molecular wires **W1**, **W3** and **W5**, and their corresponding threaded systems: [Cu(**M2**)(**W1**)](PF_6), [Cu(**M2**)(**W3**)](PF_6) and [Cu(**M2**)(**W5**)](PF_6), whose structures are shown in Figure 3.22. This complexes were obtained by the self-assembly of the corresponding molecular backbone with Cu(I) and macrocycle **M2**. The use of **W2** and **W4** was discarded due to its lower conductivity, as already mentioned. The coordination of Cu(I) ion afforded a variable coordination effect on the conductance depending on the anchoring group employed, which will be rationalized in terms of electronic and DFT considerations.

3.6.1 Synthesis and chemical characterization

The synthesis of threaded copper complexes [Cu(**M2**)(**W**)](PF_6) is schematized in Figure 3.23. It was carried out by mixing equimolecular amounts of macrocycle **M2** and [Cu(CH_3CN)$_4$](PF_6) with molecular backbones **W1**, **W3** and **W5** under argon in a dichloromethane/acetonitrile mixture. Cu(I) and phen ligands form tetrahedral complexes which are kinetically labile. Despite that the presence of 2,9-aryl substituents on the phen moiety of macrocycle **M2**[130] affords a very stable coordination environment for Cu(I) ions and minimizes metal exchange,[131] its closed nature avoids the formation of

the homoleptic $[Cu(\mathbf{M2})_2]^+$ complex. For these reasons, the combination of Cu(I) ions with our 3,8-substituted molecular backbones (**W1, W3** and **W5**) and with macrocycle **M2** in a 1:1:1 stoichiometry, assures the selective formation of the heteroleptic $[Cu(\mathbf{M2})(\mathbf{W})]^+$ complexes.[132]

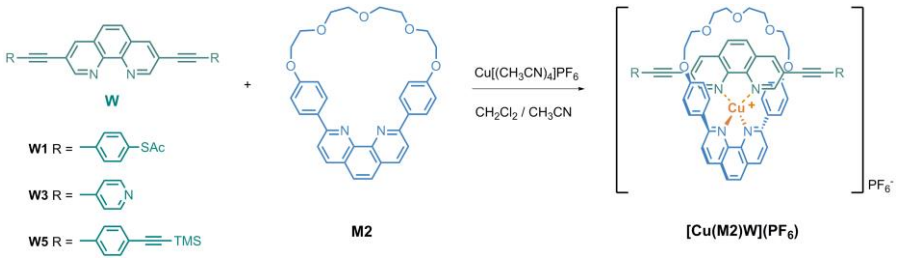

Figure 3.23 Copper-templated self-assembly of complexes $[Cu(\mathbf{M2})\mathbf{W}](PF_6)$.

The obtaining of the threaded species was evidenced by the rapid appearance of a red-brown colour characteristic of Cu(I) complexes with two aromatic diimine ligands[133, 134] and was further verified by ^{1}H NMR and MS. The C_{2v} symmetry of the complexes was evidenced by ^{1}H NMR since all the signals in the spectra integrated to at least 2H.

Photo and electrochemical characterization

Organic backbones **W1**, **W3** and **W5** and their corresponding $[Cu(\mathbf{M2})(\mathbf{W})](PF_6)$ complexes were characterized by means of UV-Vis spectroscopy and CV. As it can be observed in the UV-Vis spectra (Figure 3.24 A), the backbones present very intense absorption bands (ε > 50000 $M^{-1}cm^{-1}$) around 285 and 345 nm arising from π-π transitions.[135] The Cu(I) complexes show additional weak broad bands (ε < 4000 $M^{-1}cm^{-1}$) in the region between 400 and 550 nm associated to MLCT processes arising from the presence of the metal atom.[134, 136]

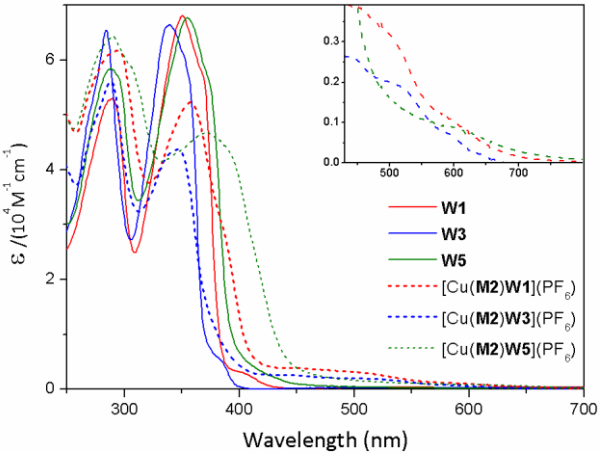

Figure 3.24 UV-Vis spectra in dichloromethane solution of organic backbones **W1, W3** and **W5** and their corresponding [Cu(**M2**)(**W**)](PF$_6$) complexes. The region between 410-700 nm is zoomed inset.

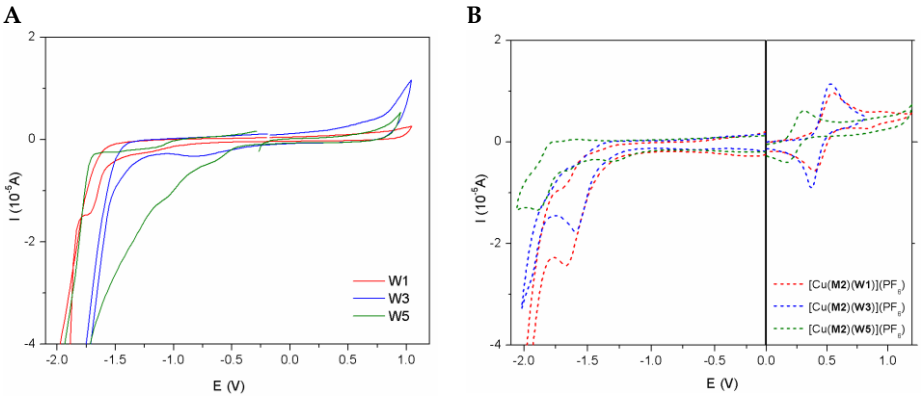

Figure 3.25 Cyclic voltammograms of organic backbones **W1, W3** and **W5** (**A**) and their corresponding [Cu(**M2**)(**W**)](PF$_6$) complexes (**B**) measured in TBA(PF$_6$) 0.1 M dichloromethane solution (1·10^{-3} M). Scan rate 0.1 V/s.

Cyclic voltammograms of molecular backbones **W1**, **W3** and **W5** present one non-reversible reduction process below -1.0 V (see Figure 3.25 A). In the corresponding Cu(I) complexes (Figure 3.25 B) these irreversible reduction processes become somewhat more defined and reduction peaks are observed. Additionally, a quasi-reversible peak associated with the Cu(I/II) couple appeared around 0.5 V.[133]

The optical HOMO–LUMO gap ($E_{g\text{-}opt}$) was estimated from the on-set of the lowest energy band. Besides, according to the empirical relationship proposed by Forrest *et al.* [137, 138] the ionization potential and electron affinity can be correlated with the on-set of the oxidation and reduction waves, respectively. According to that, we have estimated the LUMO energy levels of **W1**, **W3** and **W5** and [Cu(**M2**)(**W1/W3/W5**)](PF_6) and also the HOMO energy level and the HOMO-LUMO gap energies of the complexes from the electrochemical data ($E_{g\text{-}elec}$). In all cases, the onsets were calculated as the intersection between the baseline and the tangent line that touches the point of inflection. Results of the calculations and some other relevant data are summarized in Table 3.1.

Table 3.1 Electrochemical and Optical Properties, of wires **W1**, **W3** and **W5** and [Cu(**M2**)(**W1/W3/W5**)](PF_6).

Compound	$E_{½red}$	$E_{½ox}$	E_{HOMO}	E_{LUMO}	$E_{g\text{-}elec}$	λ_{max}	$E_{g\text{-}opt}$	$E_{g\text{-}DFT}$
W1	-1.67	-	-	-2.16	-	384	3.23	3.43
W3	-1.60	-	-	-2.21	-	371	3.34	3.65
W5	-1.10	-	-	-3.64	-	393	3.15	3.45
[Cu(**M2**)(**W1**)](PF_6)	-1.67	0.54	-4.35	-2.38	1.97	596	1.80	2.64
[Cu(**M2**)(**W3**)](PF_6)	-1.52	0.52	-4.25	-2.38	1.88	612	1.91	2.50
[Cu(**M2**)(**W5**)](PF_6)	-1.28	0.18	-4.84	-3.35	1.40	510	1.70	2.59

[a]Recorded $E_{1/2}$ values vs. SCE in CH_2Cl_2 with $TBAPF_6$ as supporting electrolyte. Concentration was 1mM and scan rate 100 mV/s. [b]HOMO and LUMO energies were determined from the onset of the first oxidation and the first reduction waves in cyclic voltammograms and/or difference pulse voltamperograms. [c]Electrochemical HOMO-LUMO gap is defined as $-(E_{HOMO}-E_{LUMO})$. [d]Optical HOMO-LUMO gaps were determined from the onset of the lowest-energy visible absorption band. [e]Calculations performed at the DFT level (B3LYP/TZV).

As can be seen in Table 3.1, optical data shows the reduction of the HOMO-LUMO gap by more than 1.0 eV upon metal coordination. E_g values show a good correlation between experimental methods and DFT calculations on the isolated molecules although this last is slightly above-estimated.

3.6.2 Electrical characterization

Conductance histograms of complexes [Cu(M2)(W)](PF$_6$) obtained by the MCBJ method

The trace histograms obtained for junctions exposed to copper complexes [Cu(**M2**)(**W1/W3/W5**)](PF$_6$) did not show horizontal regions of high counts at the same electrode displacement speed used in the backbones measurements (12 nm/s), see Figure 3.26.

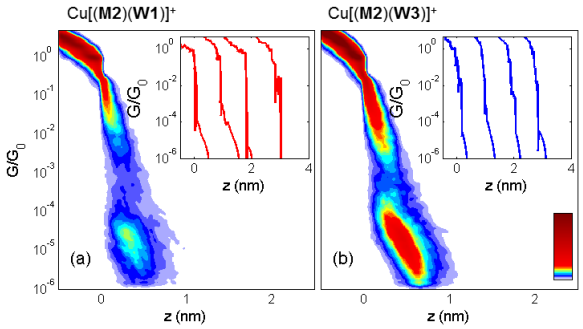

Figure 3.26 Trace histograms obtained from 1000 breaking traces as those shown in the insets for junctions exposed to 0.5 mM solutions of [Cu(**M2**)(**W1**)](PF$_6$) and [Cu(**M2**)(**W3**)](PF$_6$). The bias voltage was 0.1 V and the electrode displacement speed 12 nm/s.

This fact indicates a low probability of trapping a molecule between the electrodes. We have observed though, that the occurrence of conductance plateaus increased considerably by reducing the speed of the electrode displacement. However, this rendered the experiment extremely time consuming and lead us to discard this type of measurement for studying [Cu(**M2**)(**W1/W3/W5**)](PF$_6$). A possible explanation for the differences in behaviour between the backbone molecules and the copper complexes could rely on the fact that the central ring, being so bulky, prevents the formation of molecular junctions when the electrodes are moved apart with a high speed as illustrated in Figure 3.27.

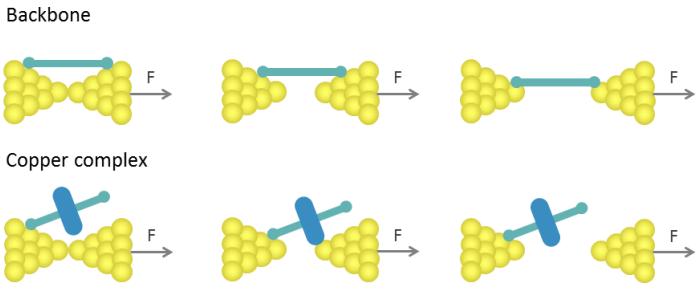

Figure 3.27 Sketch representing a possible explanation of the differences found between the backbones and the copper complexes.

As an alternative, a new junction-formation method, the so-called self-breaking (SB) technique, was tested.[139] This method turned out to be well-suited for the evaluation of the transport properties of bulky copper complexes, and thus, it was also employed for the characterization of backbones **W1**, **W3** and **W5**, in order to obtain comparable data for both, the coordinated and the uncoordinated wires.

Conductance histograms of backbone molecules W1, W3 and W5 obtained by the SB method

By using the self-breaking method, we have measured a total of 61, 336 and 139 self-breaking traces for **W1**, **W3** and **W5** respectively. In contrast to the traditional MCBJ method, the SB approach consists in following the conductance evolution of atomic-sized contacts, not as function of the electrode displacement, but as a function of time. Further details about this technique can be found in the Experimental section.

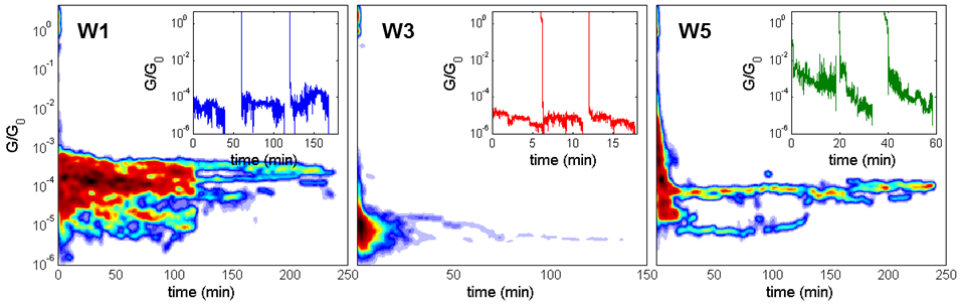

Figure 3.28 Self-breaking trace histograms obtained from 61, 336 and 139 breaking traces as those shown in the insets, for junctions exposed to 0.5 mM solutions of **W1**, **W3** and **W5**. The bias voltage was 0.1 V.

Figure 3.28 shows the histograms recorded by measuring consecutive SB traces in the presence of the wires without any data selection**.** To build these histograms, the individual SB traces have been shifted along the time-axis to fix the rupture of one-atom gold contact at zero. In the presence of pure solvent, the time that the junction has a conductance between 0.3 and 10^{-6} G_0 of is below 100 seconds (see Figure 3.52 in the experimental section). However, in the presence of the wires the lifetime of the junction increases significantly, which is a clear signature that a molecule has been trapped between the electrodes. The Junction Formation Probability (JFP), as defined in the experimental section, is different for each anchoring group and increases in the order: thiols (86%) > pyridines (59%) > acetylenes (39 %). Besides, the average lifetime for each molecule has been obtained from the Gaussian fit of the junction lifetime histograms (see Figure 3.29 B). Thiol and pyridine backbones display well-defined peaks at 97 and 3 min respectively. In the case of acetylenes, the trapping probability is significantly lower, thus, about a 61 % of the signal in the lifetime histogram comes from non-trapped molecules. Nevertheless, a peak at a lifetime above 10^4 seconds (167 minutes) can be distinguished, which corresponds to the lifetime of the plateau visible in the SB trace histogram.

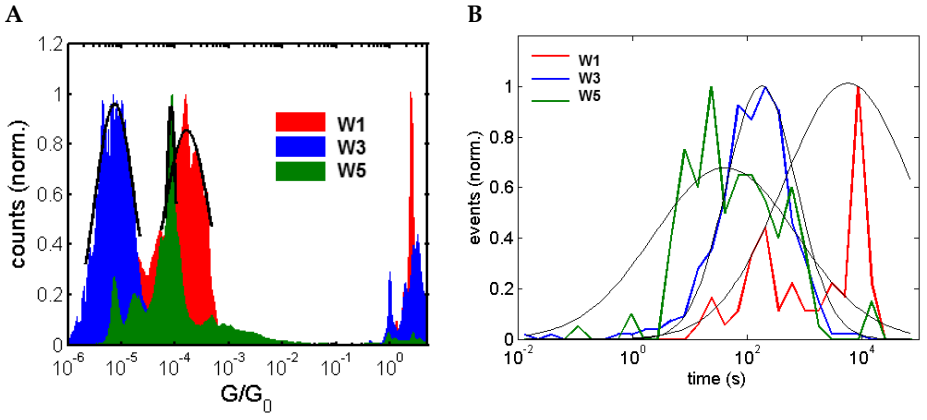

Figure 3.29 A) One dimensional conductance histogram obtained from the measured *trace histograms of molecular wires* **W1, W3** and **W5**. The most probable conductance values and their variance have been obtained from Gaussian fit of the conductance histogram. **B)** Lifetime histograms of the molecular wires.

One-dimensional conductance histograms constructed from the SB traces in Figure 3.28 reveal well-defined peaks for all three backbones (see Figure 3.29 A). The Gaussian fits to these peaks were used to identify the preferred conductance values of **W1** ($1.6 \cdot 10^{-4}\ G_0$), **W3** ($7.4 \cdot 10^{-6}\ G_0$) and **W5** ($8.3 \cdot 10^{-5}\ G_0$). Comparing these results with those obtained in the previous section using the traditional MCBJ method, we find that the SB method provides narrower single-conductance peaks, even for **W5**, for which a particularly well-defined peak is found. In the case of **W1** we pass from a broad peak centred around $2.1 \cdot 10^{-5}$ to a peak at $1.6 \cdot 10^{-4}\ G_0$ and with a variance comparable to that of **W3**. For molecule **W3**, the values obtained with the two methods compare quite well both in terms of conductance values and peak widths.

Conductance histograms of complexes [Cu(M2)(W)](PF6) obtained by the SB method

In contrast to MCBJ experiments, well-defined conductance plateaus could be obtained by the SB method for the Cu(I) complexes. Figure 3.30 shows the conductance histogram and lifetimes obtained from 35 and 77 and 52 self-breaking traces of [Cu(**M2**)(**W1/W3/W5**)](PF_6). In this case 88, 89 and 100 % of the curves displayed lifetimes larger than 100 seconds with average lifetimes of 31, 7 and 163 minutes (Figure 3.31).

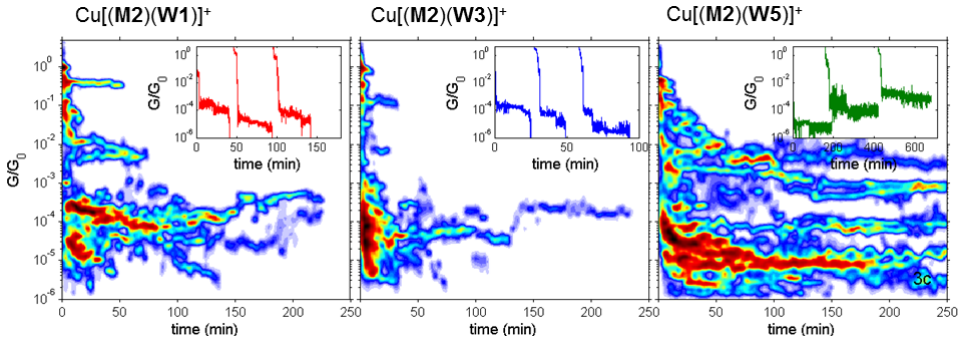

Figure 3.30 Self-breaking trace histograms obtained from 35, 77 and 52 breaking traces as those shown in the insets for junctions exposed to 0.5 mM solutions of [Cu(**M2**)(**W1**)](PF_6), [Cu(**M2**)(**W3**)](PF_6) and [Cu(**M2**)(**W5**)](PF_6). The bias voltage was 0.1V.

We found that the probability of junction formation obtained by the MCBJ method is below that found by the SB. We attribute this higher probability for the SB technique to a

difference in the trapping probability when the electrode displacement speed is varied.[140] In the particular case of the complexes, the presence of the ring makes the molecule bulkier, and this may hamper the junction formation when the electrodes are quickly displaced. However, in the SB method, the time of junction formation is higher, and thus, the chance of trapping the molecules in between increases. Furthermore, we found that once the complexes have been trapped they remain bonded to the leads for times similar to that of the wires. These facts suggest that a similar configuration is adopted in the junction and that the complexes are not attached by the ring component. Moreover, this junction average lifetime is in roughly agreement with the anchoring-Au bond strength according to the sequence: Au-C > Au-S >> Au-N.[141, 142]

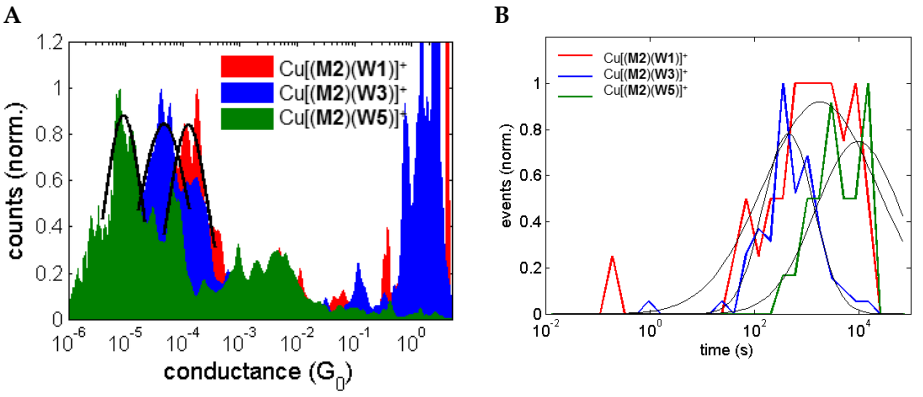

Figure 3.31 A) One dimensional conductance histograms obtained from the meauserd *trace histograms of complexes* [Cu(**M2**)(**W1**)](PF$_6$), [Cu(**M2**)(**W3**)](PF$_6$) and [Cu(**M2**)(**W5**)](PF$_6$). The most probable conductance values have been obtained from Gaussian fit of the conductance histogram. **B)** Lifetime histograms of the three complexes.

Most probable conductance values for the Cu(I) complexes were extracted from the Gaussian fit of the 1D-molecular histograms shown in Figure 3.31. Comparing with the conductance values obtained for the bare backbones, see Table 3.2, upon Cu(I) coordination, the conductance of [Cu(**M2**)(**W1**)](PF$_6$) experiences a subtle decrease with respect to **W1**, whereas [Cu(**M2**)(**W3**)](PF$_6$) displayed about one order of magnitude increase with respect to backbone **W3**, and [Cu(**M2**)(**W5**)](PF$_6$) displayed an about one order of magnitude decrease with respect to **W5**.

Table 3.2 Logarithms of the most probable conductance values found for the molecular backbones and their corresponding Cu(I) complexes by the SB method.

	log G/Go	JFP (%)[a]	J lifetime (min)[b]
W1	-3.80	86	97
[Cu(**M2**)(**W1**)]	-3.89	88	31
W3	-5.13	59	3
[Cu(**M2**)(**W3**)]	-4.33	89	7
W5	-4.08	39	167
[Cu(**M2**)(**W5**)]	-5.04	100	163

These different trends observed for the three terminations cannot be attributed to changes in the HOMO-LUMO gap since **W1, W3** and **W5** present a similar drop in the gap of about 1 eV upon Cu(I) coordination (see Table 3.1). Owing to that, we resort to theoretical calculations to get a closer look into the energy level alteration induced by copper coordination in the different molecules.

3.6.3 DFT calculations

As a first approximation, we performed DFT calculations for the isolated backbone molecules (**W1, W3** and **W5**) and those after the formation of the Cu(I) complexes ([Cu(**M2**)(**W1/W3/W5**)](PF_6)). The reduction of the gap in copper complexes respect to backbones is well reproduced in the calculations, with slightly higher calculated values, as shown in Table 3.1. Besides, the coordination of Cu(I) results in a general shift of the frontier orbitals of the three backbones to lower energies. This trend is consistent with the inclusion of a positively charged fragment that would withdraw some electron density from the backbone (Figure 3.32) and have been observed before upon metal coordination of the conjugated wires.[143]

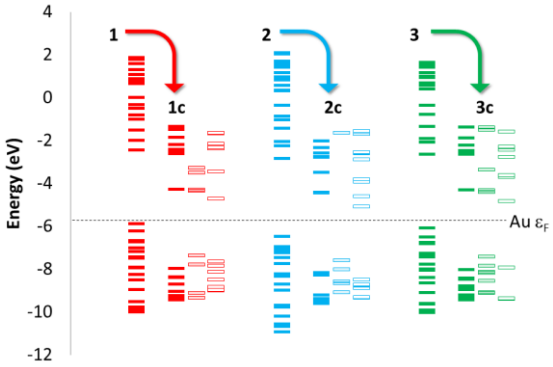

Figure 3.32 Orbital energy levels diagram showing the stabilization of the molecular wires upon Cu(I) coordination. Coloured rectangles correspond to backbone levels, empty rectangles to copper center and macrocycle orbitals and weakly coloured rectangles to mixed copper/macrocycle-backbone levels. Fermi level corresponding to the bulk gold phase (-5.53 eV) is presented as reference.

We also performed more realistic Non-equilibrium Green Functions together with DFT calculations (NEGF+DFT) for the molecular backbones and their corresponding Cu(I) complexes gold devices. As previously observed in the calculations of the isolated molecules, the coordination of Cu(I) results in a general shift of the density of states towards lower energies. Besides, the transmission spectra and molecule projected density of states of **W1, W3** and **W5** (Annex), are in concordance with previous studies,[144, 145] which indicate that transport in thiol and acetylene derivatives **W1** and **W5** is HOMO dominated, whereas in the pyridine-anchored system **W3** the LUMO is the closest orbital to the Fermi energy. The calculated zero-bias conductance showed that [Cu(**M2**)(**W3**)](PF_6) ($5.7{\cdot}10^{-4}$ G_0) is significantly more conductive than **W3** ($2.5{\cdot}10^{-6}$ G_0), whereas [Cu(**M2**)(**W1**)](PF_6) ($3.8{\cdot}10^{-3}$ G_0) and [Cu(**M2**)(**W5**)](PF_6) ($4.0{\cdot}10^{-4}$ G_0) are less conductive than their parent ligands **W1** ($1.4{\cdot}10^{-2}$ G_0) and **W5** ($1.0{\cdot}10^{-2}$ G_0). These trends are in qualitative good agreement with the experimental measured conductances, as illustrated in Figure 3.33, although a quantitative comparison fails for the well-known drawback of the GGA functionals in the estimation of the HOMO-LUMO gap due to the

presence of the self-interaction error that leads to an overestimation of the calculated conductance.[146, 147]

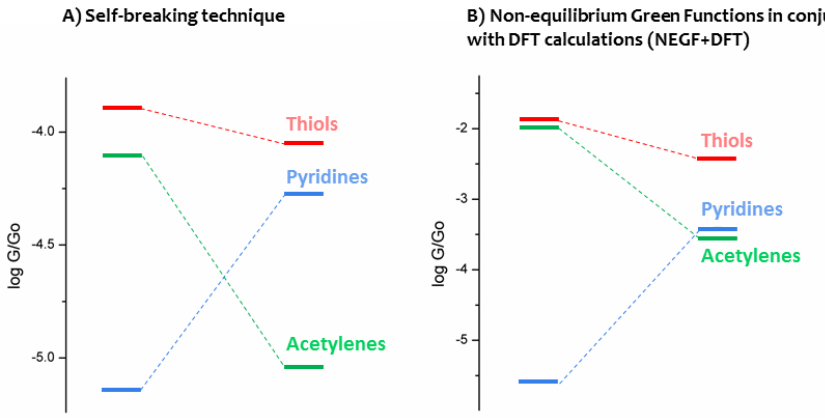

Figure 3.33 Comparison between molecular conductance values calculated and found experimentally**. A)** Representation of most probable conductance values found for the backbones (left) and those found for their corresponding Cu(I) complexes (right). **B)** Calculated zero bias conductance for the backbones (left) and those of their corresponding Cu(I) complexes (right).

In summary, experiment and theory agree that for pyridine-ended systems there is a considerable increase of the conductance upon coordination, whereas in the case of thiol and acetylene functionalized molecules molecular conductance decreases. This picture can be explained in terms of the alignment between the molecular orbitals and the gold Fermi level. Since the Fermi level of the gold electrodes lies in between the HOMO-LUMO gap, the orbital stabilization resulting from the coordination of Cu(I) should bring the LUMO level closer to it, enhancing its contribution to the current. That is the reason why the conductance in pyridines, where the transport is LUMO-mediated, increases upon coordination. By contrast, the shift of the HOMO towards lower energies moves this orbital away from the Fermi level decreasing the conductivity of the molecular systems in which the transport is HOMO-dominated, that is, thiol and acetylene derivatives upon coordination.

3.6.4 Conclusions

In contrast to the MCBJ, the SB method has afforded a high junction formation probability for our bulky Cu(I) complexes and turned out as a very suitable alternative independently of the anchoring group used. These differences between both techniques are probably related to the different time scales involved in the junction formation. The comparative study of the different backbones by both methods has afforded comparable low-bias conductance values for pyridine groups. However, in the case of thiols and acetylenes, the self-breaking method seems to favour the adoption of more conductive configurations in the junction and besides, more reproducible conductance values were obtained. In all cases, pyridine-ended derivatives afforded very stable and reproducible junctions, which confirm them as an excellent option for charge transport studies.

As far as the effect of metal coordination is concerned, the design of our molecular backbones enabled for the first time the evaluation, at the single-molecular level, of the effect of Cu(I) coordination, excluding any contribution from metal-induced conformational changes. As expected, the spectral and electrochemical features of the Cu(I) oligo(arylene-phenylene)phenanthroline complexes reflected significantly lower HOMO-LUMO energy gaps than their parent backbones. However, we have observed that, in contrast to that previously reported, [55-58] the metal coordination is not always followed by a molecular conductance enhancement. We have studied the energy density of states diagram, both in the case of the ligands and of the complex contacted molecules, by DFT-NEGF calculations. In accordance to previous works, in thiol- and acetylene-ended backbones (**W1** and **W5**) electronic transmission takes place through the HOMO level, whereas in the pyridine system **W3**, the orbital mainly involved in the conduction is the LUMO. The shift of the ligand levels to lower energies induced by the coordination of Cu(I), increases the energy difference between the HOMO and gold Fermi level, reducing the conductance in the case of [Cu(**M2**)(**W1**)](PF_6) and particularly in [Cu(**M2**)(**W5**)](PF_6). By contrast, in the case of [Cu(**M2**)(**W3**)](PF_6), the stabilization of the frontier orbitals reduces the energy difference between the LUMO and the Fermi level

and leads to a better level alignment that is reflected in a considerably conductance increase. Thereby, the observed differences in conductance after metal-coordination cannot be correlated with the reduction of the HOMO-LUMO gap, but with the particular displacement of the molecular levels involved in electronic transport with respect to the Fermi level of the electrodes. Qualitatively, this shift of the ligand energy levels towards lower energies is also expected to occur in the rest of transition metal ions.[143] Thus, similar trends on the molecular conductance of thiol, pyridine and acetylene ended OPE-like wires are expected for other metal ions.

3.7 Molecular conductance on a bistable copper rotaxane

Once we have investigated the electrical features in the Cu(I) non-bistable complexes, we proceed with the bistable Cu(I/II) system. Rotaxane **R3**$^{+}$ can exist in two topologically different redox states, Cu(I) and Cu(II), whose exchange can be controlled by an external redox potential that promotes the pirouetting motion of the ring component around the axle. The electrochemical characterization of the rotaxane molecule in solution has revealed a wide redox hysteresis, with both states separated by more than 1 V, and switching rates operating on the millisecond timescale (see section 1.5). These features made **R3**$^{+}$ a very promising candidate for the development of redox switching molecular devices.

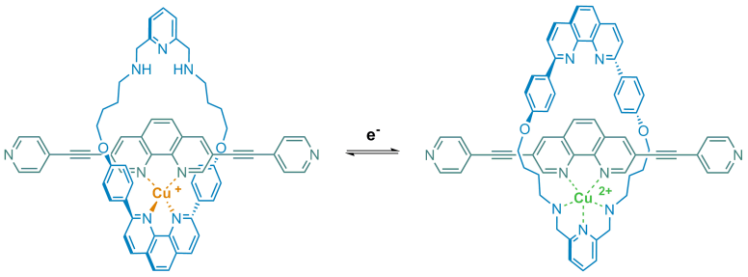

Figure 3.34 Redox switching in bistable system [Cu(**M3**)**W3**](PF_6).

In order to embed the bistable features of rotaxane **R3**$^+$ in between two gold electrodes, the system represented in Figure 3.34 was prepared by the copper-templated threading of the same macrocycle, **M3**, with bidentated wire **W3**. This reaction affords a pseudorotaxane complex that will be finally locked by the chemisorption of the anchoring groups onto the metal electrodes. Taking advantage of the previous work on the study of the metal coordination effect in Cu(I) complexes with different anchoring groups, we resolved to use pyridine-ended wire **W3** since it presented the best signal-noise ratio. The redox bistability of **R3**$^+$ over the electrochemical potential window ranging from -0.56 to 0.6V, implies that the system can be isolated in either the reduced or the oxidized form. This fact has a main importance since it enables to perform the preliminary electrical characterization of the two redox states separately.

3.7.1 Synthesis and chemical characterization

The threading of the reduced form of the pseudorotaxane was carried out by mixing equimolecular amounts of macrocycle **M3**, [Cu(CH_3CN)$_4$](PF_6) and molecular backbone **W3** under argon in a dichloromethane/acetonitrile mixture, as schematized in Figure 3.35. As in the case of complex [Cu(**M2**)**W3**](PF_6), the threading was evidenced by the appearance of a red-brown colour and was confirmed by HRMS and 1D and 2D ^{1}H NMR, elemental analysis and EDAX. Although the ^{1}H NMR signals in the aromatic region appeared poorly defined, the characteristic doublet of the ring phenoxy moieties

that indicates the coordination of the ring to the axle, see section 1.5.2, was clearly visible.

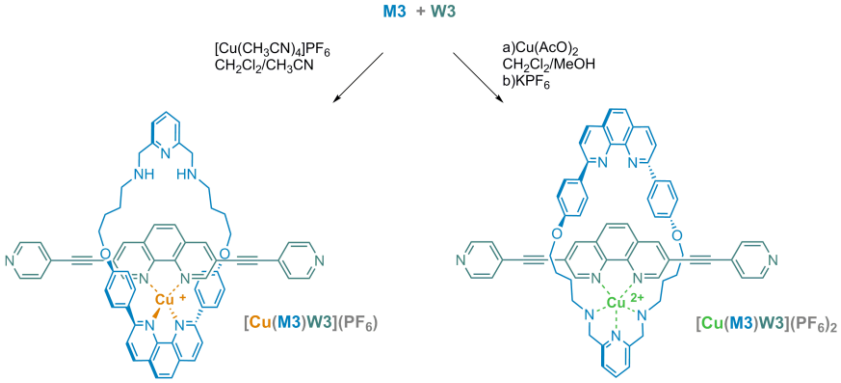

Figure 3.35 Synthesis of the oxidized and reduced forms of bistable system [Cu(**M3**)**W3**]$^{+/2+}$.

The oxidized form of the pseudorotaxane was isolated in quantitative yield by mixing macrocycle **M3**, $Cu(CH_3COO)_2$ and **W3** in 1:1:1 stoichiometry in a dichloromethane/methanol mixture, illustrated in Figure 3.35. As demonstrated by Ghosh et al. in a recent paper, not only Cu(I) but also Cu(II), can be used for the efficient templated synthesis of copper rotaxanes.

For comparison purposes, we also prepared [Cu(**M4**)**W3**]$(PF_6)_2$ by the copper-templated self-assembly of backbone **W3** with macrocycle **M4**, which have been already described in the first chapter. Along with [Cu(**M2**)**W3**](PF_6), which was already studied in section 3.6, these complexes represent the non-bistable analogues of system [Cu(**M3**)**W3**]$^{+/2+}$ in its oxidized and reduced forms.

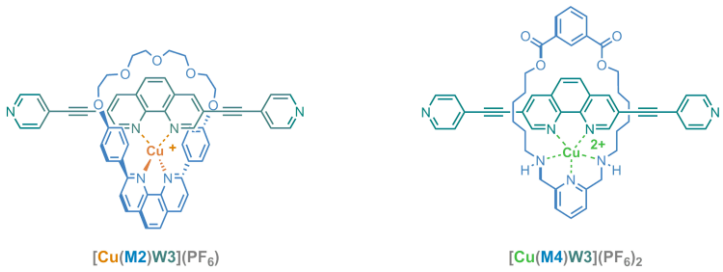

Figure 3.36 Chemical structure of non-bistable Cu(I) and Cu(II) control pseudorotaxanes.

Cu(II) complexes were characterized by HRMS, EPR, elemental analysis, IR and EDAX. Powder EPR spectra of [Cu(**M3**)**W3**](PF$_6$)$_2$, showed in Figure 3.37, presented the characteristic pattern of axially elongated mononuclear Cu(II) complexes, with $g_{\parallel} > g_{\perp} > 2.04$ and a hyperfine coupling of the parallel component with the 3/2 nuclear spin of the copper ion.[148, 149] This complex exhibits a pattern less resolved but very similar to that of rotaxane **R3**(PF$_6$)$_2$. The values of *g* and A parameters extracted for [Cu(**M3**)**W3**](PF$_6$)$_2$ lay closer to that of bistable rotaxane **R3**(PF$_6$)$_2$ rather than **R2**(PF$_6$)$_2$. This fact supports the idea that Cu(II) adopts a pentacoordinated environment in the bistable pseudorotaxane complex. In an analogous manner, control pseudorotaxane [Cu(**M4**)**W3**](PF$_6$)$_2$ exhibits close but even lower $g_{\parallel}$ and higher $A_{\parallel}$ values, which are characteristic of square pyramidal coordination geometries, as discussed in chapter 1.[149-151]

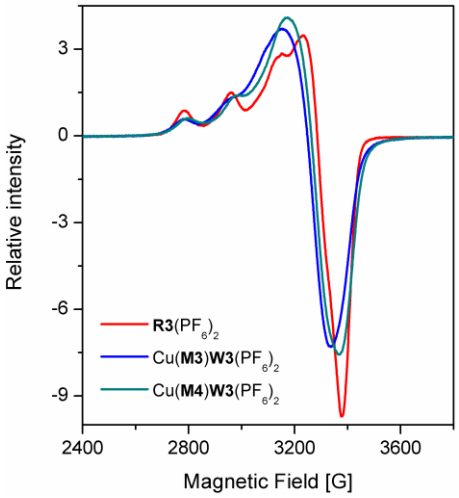

	$g_{\perp}$	$g_{\parallel}$	$A_{\parallel}$ (G)
R2(PF$_6$)$_2$	2.065	2.269	150
R3(PF$_6$)$_2$	2.063	2.225	172
[Cu(**M3**)(**W3**)](PF$_6$)$_2$	2.080	2.225	172
[Cu(**M4**)(**W3**)](PF$_6$)$_2$	2.070	2.208	176

Figure 3.37 X-band EPR spectra of **R3**(PF$_6$)$_2$, [Cu(**M3**)**W3**](PF$_6$)$_2$ and [Cu(**M4**)**W3**](PF$_6$)$_2$ recorded at 4 K in powder samples. Microwave frecuency used: 9.4723 GHz;

The two different redox states of the pseudorotaxane could be also distinguished by UV-Vis spectroscopy. Figure 3.38 shows the spectra of Cu(**M3**)**W3** and related threaded complexes in the region extending from 375 to 900 nm. Cu(I) complexes present the characteristic MLCT bands (ε < 3000 $M^{-1}cm^{-1}$) responsible of the red colour of

tetracoordinated $[Cu(phen)_2]^+$ complexes.[134] The visible spectra of [Cu(**M3**)**W3**](PF_6) matches very well with that of rotaxane **R3**(PF_6) but is less overlapped by the LC bands of the thread component due to the shorter extent of the conjugation. As in oxidized rotaxane **R3**$(PF_6)_2$, no maxima in the visible region associated to MLCT could be observed in the Cu(II) in complexes.

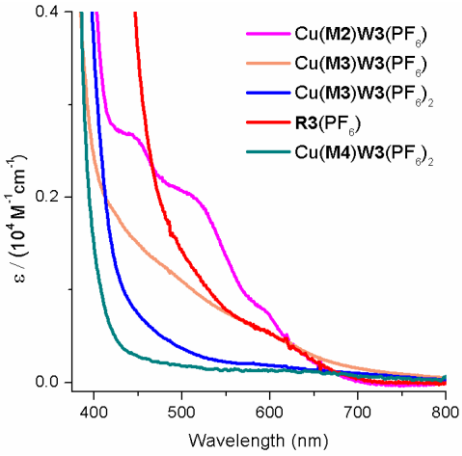

Figure 3.38 Absoption UV-Visible spectra of [Cu(**M3**)**W3**](PF_6), [Cu(**M3**)**W3**]$(PF_6)_2$ and [Cu(**M4**)**W3**]$(PF_6)_2$. The spectra of [Cu(**M2**)**W3**](PF_6) and **R3**(PF_6) were added for comparison. Data recorded in dichloromethane (Cu(I) complexes) and acetonitrile (Cu(II) complexes) C =$1 \cdot 10^{-5}$ M.

3.7.2 DFT calculations

The tetracoordinated Cu(I) and the pentacoordinated Cu(II) structures of the [Cu(**M3**)**W3**]$^{+/2+}$ complex were optimized by DFT. The obtained structures are shown in Figure 3.39. This calculations predict very close values for the HOMO-LUMO gap; 2.31 eV for [Cu(**M3**)**W3**]$^+$ and 2.36 eV for [Cu(**M3**)**W3**]$^{2+}$.

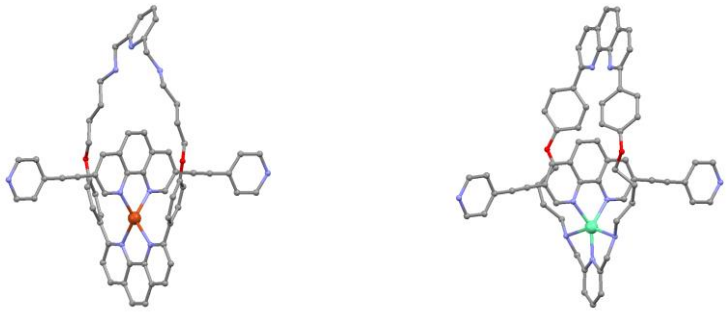

[Cu(**M3**)**W3**]$^{+}$ [Cu(**M3**)**W3**]$^{2+}$

Figure 3.39 DFT-optimized structures of the bistable system in the reduced and oxidized form.

Besides, NEGF-DFT calculations were carried out on the threaded systems gold devices in both oxidation states. The transmission spectrum of the pyridine-ended pseudorotaxanes in both redox states are shown in Figure 3.40.

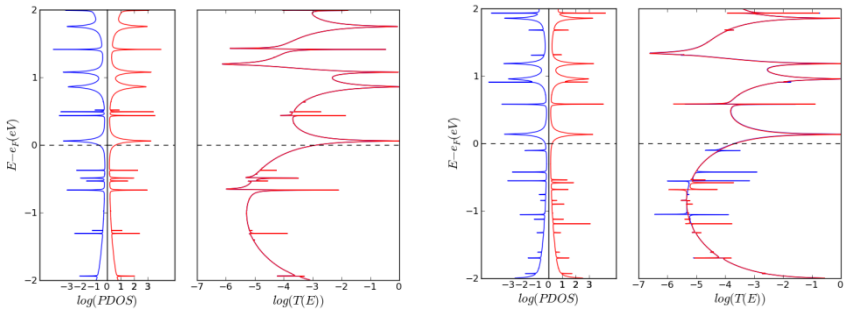

[Cu(**M3**)(**W3**)]$^{+}$ [Cu(**M3**)(**W3**)]$^{2+}$

Figure 3.40 Transmission spectrum and projected density of states calculated for the reduced and oxidized forms of the pyridine-ended rotaxanes.

In the previous section NEGT-DFT calculations revealed significant changes in the transmission spectra, and therefore on the conductance, upon Cu(I) coordination of the wires with the different terminations (see annex). By contrast, minor differences were found between the calculated transmission spectra of [Cu(**M3**)**W3**]$^{+}$ and [Cu(**M3**)**W3**]$^{2+}$ rotaxane systems with the pyridine anchoring group, illustrated in Figure 3.40. As in the previous studies for Cu(I) pyridine-ended complexes, in both cases the LUMO orbital localized in the wire, is the molecular level closer to the Fermi level, and thus the conduction is LUMO-mediated. Nevertheless, the calculated zero bias conductance

report one order of magnitude higher value for the Cu(II) system. Thereby, NEGF-DFT predicts that the high conductance state corresponds to the oxidized form, whereas the low conductance state corresponds to the reduced form.

The electrical characterization of the bistable threaded systems [Cu(**M3**)**W3**]$^{+/2+}$ as well as the control rotaxanes [Cu(**M4**)**W3**]$^{2+}$ is currently in progress using MCBJ setups in analogous conditions to those employed in the previous sections.

3.7.3 Conclusions

The coordination core of pirouetting rotaxane **R3**$^{+}$ have been transferred to a copper pseudorotaxane functionalized in its extremes with pyridine anchoring groups for its measurement in two-terminal MCBJ devices. Taking advantage of its redox bistability, the [Cu(**M3**)**W3**]$^{+/2+}$ system could be isolated and characterized separately in both oxidation states, Cu(I) and Cu(II). Besides, control non-bistable pseudorotaxanes for both oxidation states, Cu(I) and Cu(II), could be synthesized from macrocycles **M2** and **M4**. The chemical structure of all these complexes was confirmed by ^{1}H NMR, EPR, UV-vis spectroscopy, MS, elemental analysis, microanalysis (EDAX) and IR. Spectroscopic ^{1}H NMR and EPR techniques confirmed the bis-phen tetracoordinated nature of the copper environment in the reduced state and the pentacoordinated nature of the oxidized state in pseudorotaxane [Cu(**M3**)**W3**].

DFT-NEGF calculations suggest that the electrical discrimination between both conformers is possible and predict that the low conductance state may corresponds to the Cu(II). However, transport measurements need to be completed in order to confirm this hypothesis and to assess if the proposed [Cu(**M3**)**W3**]$^{+/2+}$ can give rise a voltage triggered switching behaviour in single-molecule junctions.

3.8 Photoluminescent iridium devices

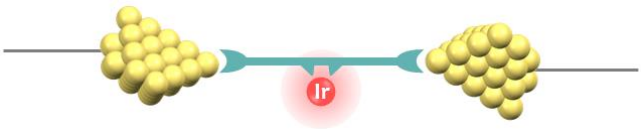

The field of molecular electronics has been recently enriched by the idea of incorporating electromagnetic radiation into molecular junctions.[11, 42, 152, 153] Theoretical studies have predicted a conductance response to light induced processes that alter the electronic structure of the junction.[153] On that basis, it has been proposed the use of light to the control and monitor electrical current passing through molecular junctions, in an analogous manner to the gate voltage in 3TD. As a control tool, electromagnetic irradiation supposes a great advantage in terms of efficiency, speed and selectivity.[153]

As mentioned in the discussion about conformational switches, light-triggered phoisomerization has demonstrated to be a feasible mechanism to switch electronic current.[67, 81-83, 85] Besides, some examples of light excitations that does not imply changes in the tridimensional structure of the molecules have also demonstrated its effect on the current flow.[154-157] In addition, the influence of molecular length[21, 158] and the electrical behaviour of molecules characterized by strong charge-transfer optical transitions[159] under illumination of molecular junctions have been studied from the theoretical point of view.

This section reports the preparation of photoactive iridium (III) cyclometallated compounds from wires **W1-W4** for their integration into electronic circuits. For that purpose, a bis-cyclometallated iridium complex of 2-phenylpyridine has been combined with diimine π-conjugated ligands **W1–W4** (see Figure 3.41) to afford a series of monocationic Ir(III) complexes with different lengths and terminations. This family of complexes combine the low resistance features of the molecular wires **W1-W4** with the rich photophysics of Ir(III) complexes. Despite molecular backbones **W2** and **W4** have demonstrated to present a higher resistance to the current flow, see section 3.7, they have

also been included in the series. First studies on diarylethenes-based switches reported a quenching of photoswitching processes on the contacted molecules, which could be overcome by decreasing the coupling between the molecule and the electrodes.[67, 85] Due to the possibility of finding analogous effects on the conductance features of the complexes with shorter ligands **W1** and **W3**, the iridium complexes of ligands **W2** and **W4** were also prepared and studied.

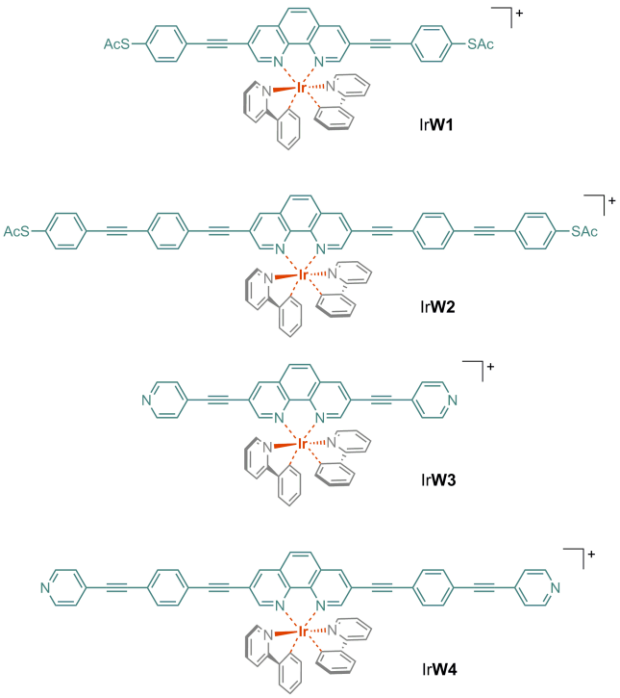

Figure 3.41 Chemical structure of iridium complexes $[Ir(ppy)_2(\mathbf{W1\text{-}W4})]^+$ (**IrW1-IrW4**).

Iridium (III) cyclometallated compounds constitute a focus of intense investigation due to its unique and tunable photphysical properties. These neutral octahedral complexes are formed by the spontaneous cyclometallation of Ir(III) salts with 2-phenylpyridines.[160] The high spin-orbit coupling of iridium, the largest among all the transition metals,[161] greatly enhances the occurrence of intersystem crossing processes that result in long-lived triplet excited states with intense photoluminescence and high quantum yields.[160] Thanks to all these features, this family of phosphorescent complexes have found wide

application on OLED emitters[162] and oxygen sensors[163] but, to the best of our knowledge, they have never been implemented into single-molecule junctions.

The substitution of one cyclometallated ligand (C^N) by a neutral diimine bischelate (N^N) gives rise to heteroleptic Ir(III) monocationic complexes of general formula $[Ir(C^N)_2(N^N)]^+$.[164-170] In the prototypical complex $[Ir(ppy)_2(bpy)]^+$, (bpy = 2,2'-bipyridine), the photoluminiscent emission takes place from a ^{3}MLCT state.[171] In these complexes the LUMO level is mostly located on the diimine ligand, whereas the HOMO is centred in the metal. Nevertheless, the high covalent character of the C-Ir bond implies that, in some $[Ir(C^N)_2(N^N)]^+$, the excited state is better described as mixed metal-to-ligand/ligand-to ligand charge-transfer (MLCT/LLCT).[165, 167] On the other hand, it has been observed that with increasing the conjugation extent on the bipy, ligand unoccupied energy levels are greatly stabilized. This leads to an increase of the ^{3}LC state contribution to the phospholuminescence.[164-170] Additionally, it has been evidenced that the nature of the substituents on the diimine ligand has also a marked influence on the luminescent properties of the complexes.[164, 168] The character of the exited state is expected to have a great influence on the photoconductance, but the interplay of these effects makes difficult to anticipate its nature. Therefore, the aim of this work is to draw the energy map of the photoexcited states and to study the influence of the conjugation length and the nature of the substituents on the photophysical and electrochemical properties of ligands **W1-W4** and complexes **IrW1-IrW4**. The characterization of the photoexcited state will very useful to understand the conductance response of these wires to light irradiation.

3.8.1 Synthesis of the iridium complexes

The preparation of mononuclear $[Ir(ppy)_2(N\wedge N)]^+$ adducts was carried out following a commonly used path that starts from the dichoro-bridged Ir(III) dimer $[Ir(ppy)_2Cl]_2$.[172] Treatment of this salt with one equivalent of the bis-pyridine ligand (N∧N) in a refluxing dichloromethane: methanol mixture under inert conditions and following treatment

with an excess of KPF_6 (Scheme 3.4), afforded monocationic complexes **Ir1-Ir4** in reasonable yields.[168]

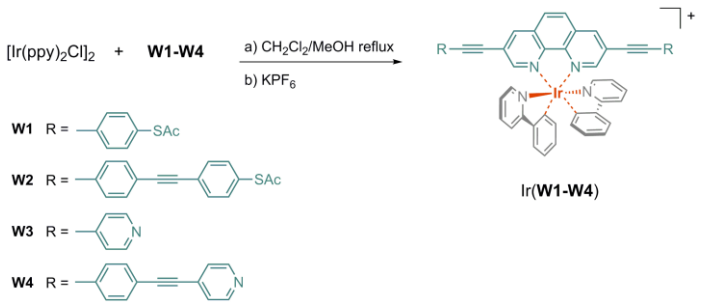

Scheme 3.4 Synthesis of iridium complexes **IrW1-IrW4**: a) dichloromethane/ methanol 2:1, reflux; b) KPF_6 escess.

The four complexes were characterized by ^1H NMR and HRMS. In the ^1H NMR spectra of all complexes, ppy ligands present one set of eight signals integrating to two protons. This equivalency is consistent with the selective formation of the isomer in which the Ir-C bonds remain in *trans* to the Ir-N bonds, according to the so-called '*trans* effect'.[160]

3.8.2 Electrochemical characterization

Cyclic voltammograms of **IrW1-IrW4** complexes are displayed in Figure 3.42 and their relevant electrochemical data is collected in Table 3.3. Electrochemical measurements reveal a great redox stability with oxidation and reduction half-wave potentials more than 1.8 V apart. All the complexes display oxidation processes centred at 1.38 V ($\Delta E < 90$ mV). This oxidation process has been previously observed in other bis-cyclometallated Ir(III) complexes as $[Ir(ppy)_2(phen)]^+$ (+ 1.36 V vs SCE)[168] and has been associated with the bis-cyclometallated Ir(III/IV) oxidation.[164-168, 173] This electrochemical potential presents minor variations along the **IrW1-IrW4** series, suggesting the lack of participation of the phen ligand in the process. Nevertheless, changes in the reversibility of these oxidation processes are appreciable. In the particular case of acetylthiol-ended

compounds **IrW1** and **IrW2,** the oxidation processes are almost completely irreversible. The irreversibility of this wave has been found to be proportional to the strength of the σ-(Ir-C) bond, and thus, it denotes a clear participation of the ppy moiety in the redox process.[174, 175]

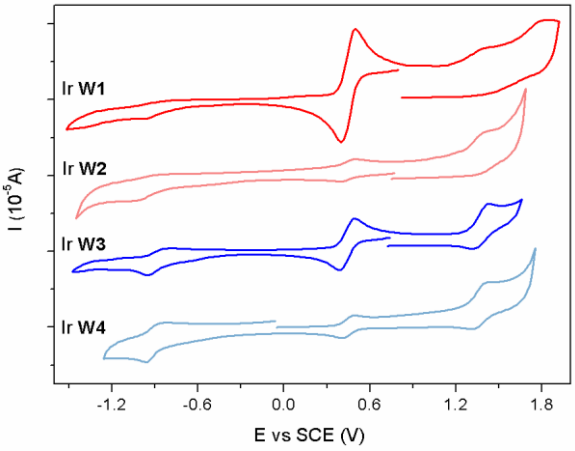

Figure 3.42 Cyclic voltamperograms of complexes **IrW1-IrW4** in 0.1 M $TBAPF_6$ acetonitrile (**IrW1** and **IrW2**) and a 1:1 acetonitrile:dichloromethane mixture (**IrW3** and **IrW4**) solutions. Ferrocene was added as internal reference, (E_{SCE} (Fc^+/Fc^0) = 0.45 V).[176]

Table 3.3 Oxidation and reduction potentials vs SCE for **IrW1-IrW4** complexes.

Compound	$E^{red}_{1/2}$ [V] ($\Delta E_{1/2}$)	$E^{ox}_{1/2}$ [V] ($\Delta E_{1/2}$)	$E_{g\text{-}elec}$ (eV)
IrW1	-0.96[a]	+1.39[a]	2.35
IrW2	-1.03[a]	+1.39[a]	2.40
IrW3	-0.88 (0.12)	+1.38 (0.08)	2.36
IrW4	-0.91 (0.08)	+1.37 (0.07)	2.36

[a]Irreversible peaks. [b]Electrochemical gaps were obtained from the difference between the anodic potential of the Ir(IV/III) couple and the catodic potential of the Ir(III/II) couple.

At negative potentials, a single reduction process was visible between -1.03 and -0.88 V. Again, the ratio between cathodic and anodic peaks was far from the unit. This fact was attributed to the high tendency of the ligands to get adsorbed onto the electrodes upon reduction, as observed in the CV of **W1** and **W3** (Figure 3.25), this effect being more pronounced in the case of acetylthiol derivatives than in pyridine-ending complexes.

The potential of the first reduction process does not vary considerably along the series, and, in all cases, the values were far below from those described for the parent complex $[Ir(ppy)_2(phen)](PF_6)$ (-1.28 vs SCE).[168] Both facts suggest that, as mentioned in previous reports,[164, 165, 167, 168] the reduction process is centred in the N^N ligand.

3.8.3 Photophysical characterization

Absorption spectroscopy

The absorption spectra in dichloromethane of ligands **W1-W4** along with their iridium complexes **IrW1-IrW4** are shown in Figure 3.43 A; the corresponding maxima positions and molar extinction coefficients are listed in Table 3.4. Short ligands **W1** and **W3** exhibit two strong absorption bands, the first peaking at 289 and 283 nm ($\varepsilon \approx 55\,000\ M^{-1}\,cm^{-1}$) and the second at 351 and 340 nm ($\varepsilon \approx 60\,000\ M^{-1}\,cm^{-1}$). These maxima are significantly shifted to lower energies on increasing conjugation (**W2** and **W4**), the bathochromic effect being more accused in the pyridine-ending molecular backbones. As reported in related ligands, the lower- and higher-energy bands are respectively assigned to long- and short-axis polarized π-π* transitions.[135, 177, 178]

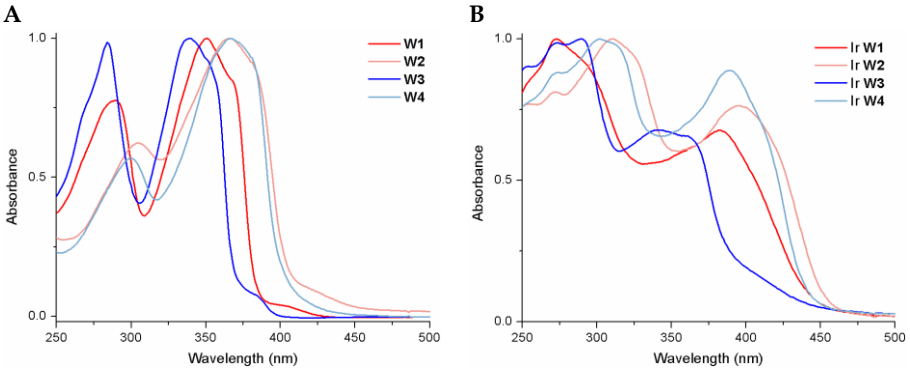

Figure 3.43 Normalized absorption spectra in dichloromethane of oligomers **W1-W4** (**A**) and complexes **IrW1-IrW4** (**B**).

The absorption bands of the Ir-complexes are broader than those of the bare oligomers (Figure 3.43 B). The spectra displays intense absorption bands below 350 nm ($\varepsilon > 50\,000$

$M^{-1}cm^{-1}$), less intense bands in the 350–450 nm range ($\varepsilon > 45\ 000\ M^{-1}cm^{-1}$), and moderately intense bands ($\varepsilon < 1\ 000\ M^{-1}cm^{-1}$) above 450 nm, which extend far within the visible region. Based on previous reports, [164, 165, 167, 168, 170, 178] from left to right, the former bands have been assigned to π–π*(ppy, phen) LC transitions and the latter ones are the result of the overlap of π–π* LC with spin allowed mixed MLCT transitions. In **Ir3**, this last band can be distinguished around 400 nm. Finally, weak absorption bands above 450 nm are the result of spin forbidden ^{3}MLCT transitions. The red-shift (up to 30 nm) experienced by the bands peaking in the 360-390 nm range compared to these of **W1-W4** is in part attributed to the stabilization of the π-electron system of the phen chromophore as a result of the coordination to the cationic Ir(III) center (see later).[143, 177]

Table 3.4 Absorbance maxima and molar extinction coefficients in dichloromethane of ligands **W1–W4** and complexes **IrW1-IrW4**.

Compound	λ_{max} [nm] (ε [$M^{-1}cm^{-1}$])
W1	289 (55000), 351 (62000)
W2	305 (45000), 367 (74000)
W3	283 (57000), 340 (60000)
W4	300 (39000), 367 (64000)
IrW1	272 (69000), 380 (46000)
IrW2	314 (66000), 395 (51000)
IrW3	290 (56000), 362 (38000)
IrW4	301 (53000), 389 (51000)

Photoluminescence

Luminescence spectra of ligands **W1-W4** in dichloromethane at 298 K (λ_{exc} = 340 nm) are shown in Figure 3.44 A. The emissions are centred in the 380-400 nm range and show relatively high quantum yields (ϕ), which are essentially not affected by the presence of oxygen (Table 3.5). The emission maxima of ligands **W1** and **W3** appear at shorter wavelengths than those of **W2** and **W4**. Besides, the fluorescence quantum yields of the former molecules are lower than those of the higher conjugated ligands. Thus, the

enhancement of the π-conjugation results in higher ϕ and in a stabilization of the lower energy transitions, in agreement with what is observed in the absorption spectra. The fluorescence lifetimes (τ) of **W1-W4** are below 1 ns and could not be resolved by our experimental setup.

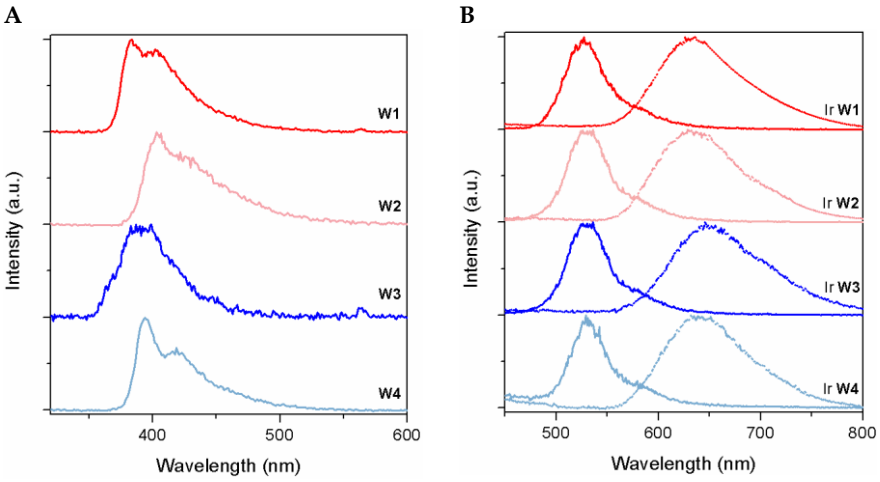

Figure 3.44 A) Normalized luminescence spectra of ligands **W1-W4** in dichloromethane at 298 K (λ_{exc} = 300 nm); **B)** Normalized luminescence spectra registered at λ_{exc} = 375 nm of complexes **IrW1-IrW4** in dichloromethane at 298 K (·····) and in ethanol glass at 77K (—) .

Table 3.5 Photophysical properties of ligands **W1-W4** and complexes **IrW1-IrW4** in dichloromethane (DCM) and ethanol solutions (C = 3 ×·10^{-6} M).

	λ_{em}[a] DCM 278 K	λ_{em}[a][nm] Ethanol 278 K	λ_{em}[a][nm] Ethanol 77 K	ϕ_{air}	ϕ_{Ar}	τ[b][ns] DCM 278 K	τ[c][μs] DCM 77K	k_r[d] /10^6[s^{-1}]	k_{nr}[d] /10^6[s^{-1}]
W1	384			0.76	0.79	< 1			
W2	403			0.83	0.84	< 1			
W3	384			0.12	0.15	< 1			
W4	394			0.90	0.93	< 1			
IrW1	638	644	527	0.097	0.151	502	9.50	0.30	1.7
IrW2	638	644	528	0.113	0.179	564	12.31	0.32	1.5
IrW3	648	658	504, 537	0.057	0.073	202	7.22	0.36	4.6
IrW4	640	646	531	0.049	0.073	460	8.50	0.16	2.0

[a]λ_{exc} (**W1-W4**) = 300 nm, λ_{exc} (**IrW1-IrW4**) = 375 nm. [b]Measurements in deaerated dicholoromethane solution at the emission maximum (λ_{exc} = 375 nm; lifetimes for **W1-W4** are shorter than 1 ns and cannot be resolved by our system). [c] Lifetimes in ethanol solid matrix at the maximum of the phosphorescence band (λ_{exc} = 355 nm). [d] k_r and k_{nr} in dichloromethane solution were calculated according to the equations: $k_r = \phi_{Ar}/\tau$ and $k_{nr} = (1-\phi_{Ar})/\tau$.

The luminescence of complexes **IrW1-IrW4** at room temperature and 77 K are shown in Figure 3.44 B. In contrast to what is observed for the oligomers, the shape of the emission in dichloromethane solution at 298 K is broad and unstructured, which is typical MLCT.[179] Quantum yields are higher for acetylthiols than for pyridine-ended derivatives, and all of them fall in the range reported for other ppy-cyclometallated Ir(III) complexes with CT emissive excited states.[165, 166, 170] The emission quantum yields are much lower in energy than those observed for the bare ligands and are affected by the presence of oxygen, ϕ in 10 min air-equilibrated solutions decreases ~30-40% compared to those of argon-saturated media. Besides, the emission lifetimes of **IrW1-IrW4** at room temperature range in the submicrosecond time scale and are two orders of magnitude longer than for **W1-W4** (τ < 1 ns). All these features are consistent with the triplet nature of the excited state for all Ir-complexes, according to the ability of Ir(III) to favour the intersystem crossing quantum yield from the singlet to the triplet excited state.

The emission maxima at room temperature are around 638-640 nm in **IrW1**, **IrW2** and **IrW4**, and lightly above in **IrW3** (648 nm). The HOMO-LUMO energy gap of **IrW3** is anomaly low and does not follow the expected tendency with the increasing conjugation that, by contrast, was observed in the photophysical properties of the bare diimine conjugated ligands (**W1-W4**). This is further supported by the values of the radiative and non-radiative decay rates k_r and k_{nr} obtained from ϕ and τ in deaerated dichloromethane solutions. In general, k_r are one order of magnitude lower than k_{nr}, with values of about $1.5\text{-}2\cdot10^6$ s^{-1}. However, **IrW3** displays the highest k_{nr} ($4.6\cdot10^6$ s^{-1}), in line with its lower energy gap and consequently with its lower emission lifetime.

The emission of **IrW1-IrW4** at 77K (Figure 3.44) is blue-shifted (3300 cm^{-1}) and narrower than the emission at room temperature. This rigidochromic effect is characteristic of CT exited states.[179] In the rigid ethanol matrix, CT states cannot be stabilized by the

reorganization of the solvent molecules before emission takes place, and thus, at low temperature a blue shift of the emission band is observed. Similarly, in the liquid phase polar solvents stabilize more efficiently the charge separation states giving rise to a solvatochromic effect. This behaviour has been also detected in the emission of **IrW1-IrW4** in ethanol (Table 3.5), where the emission maxima of the complexes are shifted around 6-10 nm towards longer wavelengths compared to what has been measured in dichloromethane. By contrast, ^{3}LC emissive states are characterized by structured bands whose position is not affected by the temperature.[164, 167] Although it has been reported that in cationic Ir(III) the ^{3}LC contribution to the emissive state increases with the larger extent of the conjugation,[135, 177, 178, 180] this effect is not observed in the **IrW1-IrW4** series. In all of our complexes the lack of structure in the emission bands and the occurrence of solvatochromic and rigidochromic effects points to a very low contribution of LC processes in the emissive triplet state of **IrW1-IrW4**, and fit better with CT nature transitions.

Besides, the extent of the blue shift in the rigid matrix is related to the degree of charge separation in the excited state.[165] In **IrW1-IrW4**, the magnitude of the rigidochromic effect is significantly higher than that expected for a typical ^{3}MLCT emitter. Pure ^{3}MLCT emitters such as Ru(bpy)$_3$ and other Ir(III) cyclometallated compounds,[165, 175, 181, 182] display blue-shifts at 77 K in the range of 1000-2000 cm^{-1}. However, we have obtained shifts above 3300 cm^{-1}for **IrW1**, **IrW2** and **IrW4,** and above 4600 cm^{-1} for **IrW3**. These large blue-shifts point to the existence of excited states with appreciable ^{3}MLCT/LLCT (ppy-Ir $\rightarrow$ phen) character.[165-167, 170] In this case, the transition involves the promotion of an electron from a metal-ligand σ-bonding orbital to a π*-acceptor orbital of the ligand, which implies a substantial charge separation in the excited state. This assignment is consistent with the low reversibility observed in the anodic wave of the complexes, which denotes a substantial participation of the ppy in the HOMO level.[174, 175]

Finally, the emission decay traces of **IrW1-IrW4** at 77 K were accurately fitted with a one-exponential function, giving rise to lifetimes between 7 and 12 μs. These values are

shorter than those expected for systems whose emission was dominated by pure ^{3}LC states.[160] Additionally, **IrW3** emission at low temperature showed vibronic structure (Figure 3.44). The resolution of the vibronic structure of the emission at 77K is very common in Ir(III)-cyclometallated emitters.[165-167, 170] Thus, taking together all the fluorescence results, we can conclude that the emission of **IrW1-IrW4** arises from a ^{3}MLCT/LLCT state.

Transient absorption

In order to further investigate the nature and photophysical behaviour of the excited states governing the bare ligands and Ir-complexes, transient absorption (TA) measurements were performed at λ_{exc} = 355 nm in deaerated dichloromethane. Laser flash photolysis of **W1-W4** at room temperature affords long-lived absorption species that are highly quenched by oxygen and low-energy triplet acceptors such as β-carotene. On the basis of these observations, the absorption transients are assigned to the triplet ($^3\pi\pi^*$) excited states of the oligomers. Figure 3.45 shows the TA spectra of **W1-W4** in deaerated dichloromethane solution. They are characterized by a broad absorption band throughout the visible region, which extends to the near infrared, with triplet lifetimes ranging from 9.3 to 16.5 μs (see Figure 3.45).

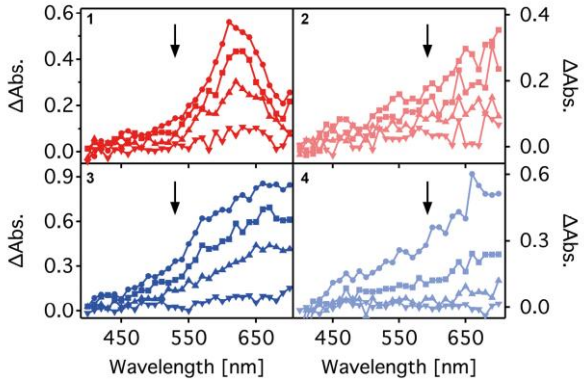

Figure 3.45 Transient absorption spectra of ligands **W1-W4** in deaerated dichloromethane solution at 298 K after laser flash photolysis at 355 nm. Spectra acquired at 0.4, 4, 10 and 30 μs after the laser pulse.

Table 3.6 Photophysical properties of oligomers **W1-W4** and complexes **IrW1-IrW4** in dichloromethane solution derived from the transient absorption measurements.

	E_T [eV][a]	λ_{max} [nm][b]	τ_T [μs][b]
W1	2.48	620	9.3
W2	2.37	700	15.8
W3	2.56	670	12.4
W4	2.35	660	16.5
IrW1	2.22	510	0.43
IrW2	2.21	500	0.54
IrW3	2.13	500	0.24
IrW4	2.19	540	0.27

[a]E_T determined from the 10% rise phosphorescence spectra in dichloromethane. [b]Measurements in deaerated dichloromethane solution; lifetimes from the signal monitored at the maximum absorption.

The TA spectra of **IrW1-IrW4** contrast with those obtained for the oligomers. In all cases, the transient absorption is characterized by a ground-state bleaching centred at *ca*. 400 nm, a broad absorption band with maxima at about 510 nm, and finally a bleaching at *ca.* 640 nm. As an example, the TA spectra and the decay traces monitored at the maximum absorption band of **IrW2** and **IrW4** in deaerated dichloromethane solution are shown in Figure 3.46 (**IrW1** and **IrW3** display similar behaviour).

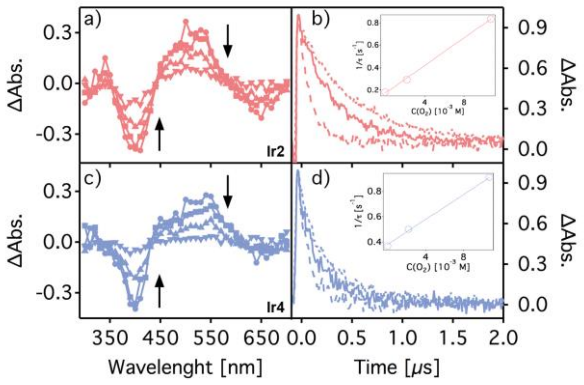

Figure 3.46 Transient absorption spectra of **IrW2** a) and **IrW4** c) recorded at 0.01, 0.1, 0.3 and 1 μs after the laser pulse. Decay traces of **IrW2** b) and **IrW4** d) monitored at 510 nm in N_2 (solid), air

(dash) and O_2 (dot). The insets show the Stern-Volmer plots of quenching by oxygen. The measurements were performed at 298 K in deaerated dichloromethane solution, λ_{exc} = 355 nm.

The absorption species with λ_{max} ~ 510 nm are highly quenched by oxygen, with rate constants of about 6×10^8 $M^{-1} s^{-1}$ (see Figure 3.46 b and d and insets). The decay traces of **IrW1-IrW4** at 510 nm are accurately fitted with a one-order exponential function. The lifetimes range from 0.24 to 0.54 μs and are higher for the acetylthiol-ended compounds than for the pyridine-ended derivatives, and are longer-lived for the more conjugated Ir-complexes. It is worth to note that the bleaching observed around 640 nm corresponds to the photoluminescence detected in deaerated dichloromethane solution. Besides, there is a strong correlation between the lifetime of the transients observed by the laser flash photolysis technique and the luminescence decay components detected by fluorescence spectroscopy. This correspondence suggests that the excited states of **IrW1-IrW4,** explored by the luminescence and transient absorption techniques at room temperature, are related to the same transitions. In other related Ir(III) complexes, similar transient absorption species (λ_{max} ~ 510 nm) have been detected and assigned to ^{3}MLCT excited states.[135, 178, 180] Thus, we assign these absorption species to ^{3}CT states.

3.8.4 DFT calculations

To gain further insight into the electrochemical and photophysical properties of cationic complexes **IrW1-IrW4**, density functional theory (DFT) and time-dependent (TD)-DFT calculations were performed at the B3LYP/(6-31G**+LANL2DZ) level in the presence of dichloromethane (see the computational details). Isolated phenantroline-based ligands **W1-W4** were also computed at the B3LYP/6-31G** level for comparison purposes.

Calculations on the electronic ground state (S_0) correctly predict a near-octahedral coordination for the Ir metal and provide geometrical parameters in good agreement with experimental data for similar Ir-based complexes. For instance, the values computed for the Ir-N1, Ir-C2 and Ir-N3 bonds are 2.085, 2.023 and 2.227 Å, in **IrW1** are in good agreement with the experimental bond lengths (2.04-2.06, 1.99-2.04, and 2.12-2.16

Å) found for a $[Ir(ppy)_2(3,8\text{-diphenyl-phen})]^+$ derivative[169] and with (2.05, 2.00, and 2.15 Å) reported for $[Ir(piq)_2(phen)]^+$ (piq = 1-phenyl-isoquinoline).[167]

Figure 3.47 displays the energies calculated for the HOMOs and LUMOs of phenantroline-based ligands **W1-W4** and complexes **IrW1-IrW4**, and Figure 3.48 shows the molecular orbital contours of **IrW1** and **IrW2** as representative examples. An identical topology of the frontier molecular orbital was found for the rest of complexes. Similar to other related ppy-based cyclometallated Ir complexes,[167, 169, 170] the HOMO is composed by a mixture of Ir(III) dπ orbitals (t_{2g}) and phenyl π orbitals with little contributions from the pyridine rings of the cyclometallated ligands. Since the family of complexes **IrW1-IrW4** only differs on the diimine ligand, the energy of the HOMO remains almost constant along the series (Figure 3.47 B). The similar energy computed for the HOMO in all complexes justifies the small variation of the oxidation potentials observed on going from **IrW1** (+1.39 V) and **IrW2** (+1.39 V) to **IrW3** (+1.38 V) and **IrW4** (+1.37 V) (Table 3.3). In contrast to the HOMO, the LUMO is completely spread out over the large diimine ligands. The comparison between complexes **IrW1-IrW4** and the parent complex $[Ir(ppy)_2(phen)]^+$,[168] evidences that the attachment of phenylethylene groups in 3- and 8-positions of the phen leads to an stabilization of the LUMO orbital and thus, to a reduction of HOMO-LUMO gap. In agreement with the electrochemical data, the level energy varies more in the LUMO orbital than in the HOMO. The comparison between terminal acethylthiol (**IrW1** and **IrW2**) and pyridine-ended (**IrW3** and **IrW4**) complexes reveals that the LUMO in the latter complexes lightly increases in energy with respect to the former ones, however, the energy of this orbital is little affected by the length of this ligand (Figure 3.47).

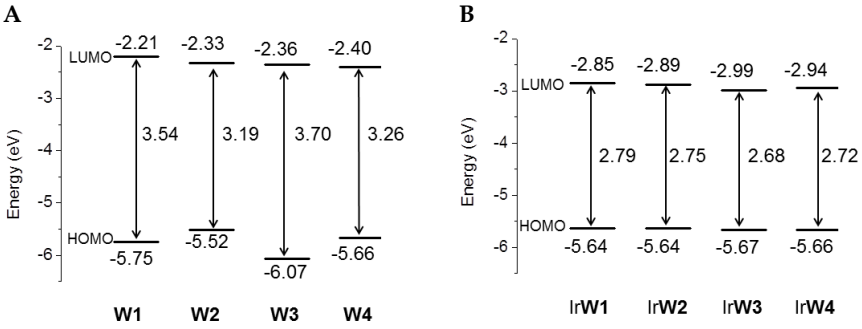

Figure 3.47 Energy diagram showing the energies calculated for the HOMOs and LUMOs of ligands **W1-W4** (**A**) and complexes **IrW1-IrW4** (**B**).

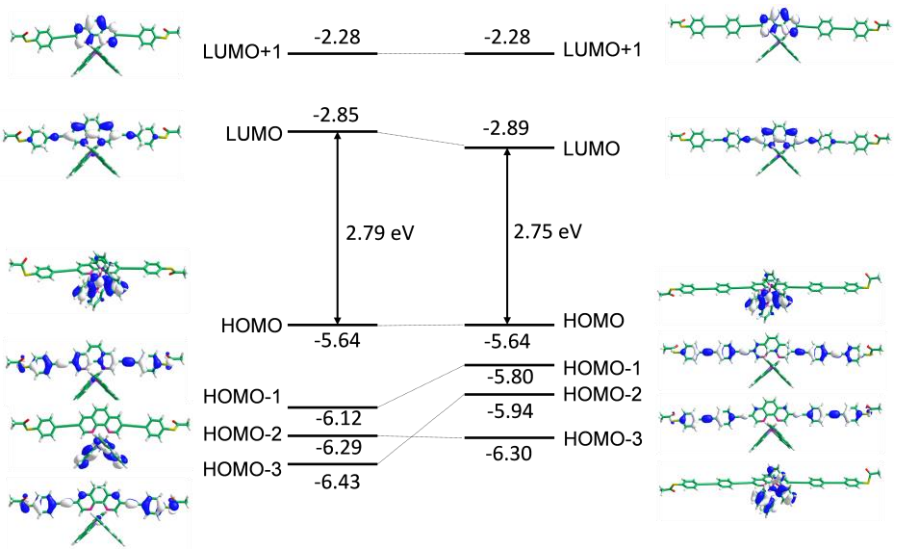

Figure 3.48 Schematic representation showing the electron-density contours (0.03 e bohr^{-3}) and the energy values (in [eV]) calculated for the highest occupied and lowest unoccupied molecular orbitals of **IrW1** and **IrW2**.

The atomic orbital composition calculated for the HOMO and LUMO supports the assignment of the lowest-energy triplet excited state to a mixed ^{3}MLCT/LLCT. To explore in more detail this hypothesis and characterize the nature of emitting excited state, the molecular structure of the lowest triplet excited state (T_1) was optimized using the spin-unrestricted UB3LYP approach. After full-geometry relaxation, the T_1 state is computed to lay in the range 1.89-2.05 eV above S_0 (adiabatic energy differences, ΔE in

Figure 3.49). These values are in good agreement with the energy of the emitting triplet extracted from the luminescence spectra. For complexes **IrW1-IrW4**, the T_1 states mainly results from the HOMO→LUMO monoexcitation and implies an electron transfer from the Ir-ppy environment to the conjugated diimine ligand. As illustrated in Figure 3.49 B and C, the unpaired-electron spin density distribution calculated for **IrW1** (Ir: 0.48, ppy: 0.50, **1**: 1.02 e) and **IrW2** (Ir: 0.48, ppy: 0.50, **2**: 1.02) perfectly matches the topology of the HOMO→LUMO excitation (see Figure 3.48). Similar spin density distributions are found for complexes **IrW3** and **IrW4**. Therefore, the calculations suggest that the emitting T_1 state for complexes **IrW1-IrW4** has a ^{3}MLCT/LLCT character, in good concordance with the broad and unstructured aspect of the experimental emission bands at room temperature, as well as the large rigidochromic effect observed upon temperature decreasing (Figure 3.44 B).

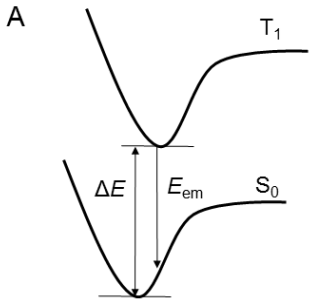

Complex	Δ*E* [eV]	E_{em} [eV/nm]
IrW1	2.05	1.85 / 671
IrW2	2.03	1.84 / 673
IrW3	1.89	1.76 / 706
IrW4	2.01	1.83 / 682

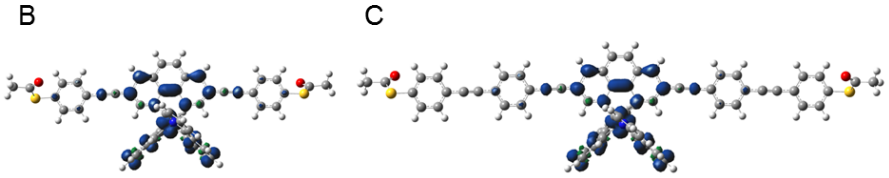

Figure 3.49 A) Schematic energy diagram showing the adiabatic energy difference (Δ*E*) between the S_0 and T_1 states and the emission energy (E_{em}) from T_1 calculated for complexes **IrW1-IrW4**. Unpaired-electron spin density contours (0.003 e bohr^{-3}) calculated for **B)** the fully relaxed T_1 state of **IrW1** and **C) IrW2**.

To estimate the phosphorescence emission energy, the vertical energy difference between T_1 and S_0 was computed by performing a single-point calculation of S_0 at the optimized minimum-energy geometry of T_1 (E_{em} in Figure 3.49 A). The calculations

predict vertical emission energies in the 1.82-1.85 eV range (671-682 nm, Figure 3.49A) for complex **IrW1**, **IrW2** and **IrW4**, and a slightly red-shift vertical emission energy computed at 1.76 eV (706 nm). The theoretical estimation of the phosphorescence emission maxima follows the same trend that the maxima of the emission bands at room temperature and DFT finely predicts the red-shift in the emission of **IrW3** in comparison with their counterparts (Table 3.5 and Figure 3.44).

3.8.5 Conclusions

The synthesis of a new family of highly conjugated diimine ligands and its corresponding cyclometallated monocationic Ir(III) complexes functionalized with suitable groups for their anchoring to metal electrodes[23, 31, 32] have been described. In these complexes, the energy of the LUMO orbital, centred on the diimine ligand, is greatly stabilized by the increased conjugation of ligands **W1-W4** with respect to bare phen ligand. Accordingly, the electrochemical and photophysical features of **IrW1-IrW4** show lower HOMO-LUMO gaps than in the case of $[Ir(ppy)_2(phen)](PF_6)$.[168] Nevertheless, the HOMO-LUMO gap is little affected by the increased conjugation in the diimine ligand. The emission wavelength remains almost constant along the series except for **IrW3**, whose emission is red-shifted with respect to the other complexes.

According to the emission data, transient absorption experiments and DFT calculations, the phosphorescent emission of the Ir complexes has been unambiguously assigned in all cases to ^{3}MLCT/LLCT excited states. In contrast to what has been observed in other monocationic Ir(III) complexes,[135, 177, 178, 180] the increase of the conjugation extent on the conjugated diimine ligand has no significant effect on the luminescent properties and did not lead to a higher contribution of triplet LC emissive states. Besides, the large blue-shift of the emission energy observed on passing to the glass phase denotes a very marked charge state separation in the triplet emissive state. Induced dipolar moments are a pursued feature in molecular electronics owing to their ability to generate current rectification effects on molecular conductance.[58, 75, 76] The deep charge transfer nature of

the excited along with the reported good conducting features of ligands **1** and **3**,[183] denote the promising features of these complexes for the observation of photoconducting phenomena in molecular junctions.

General conclusions

This chapter has begun with the systematically study of single–molecule conductance in a series of wires containing metal-binding sites with different lengths and anchors. The phen coordination unit included in the design of these molecular wires enabled the evaluation of electron transport in metal complexes avoiding metal-induced conformational changes. The electrical characterization of shorter wires in MCBJs has manifested good conducting features and a preferred value of conductance can be defined for the three of them by the self-breaking junction formation method. In agreement with the literature, thiols were found to be more conductive, but pyridines formed less noisy and more reproducible junctions, which point them as a very suitable option for charge transport studies.

The Cu(I) complexation effect studied in section 3.7 revealed a very nice correlation between the conductance and the molecular level alignment with the gold Fermi level. This work evidenced the crucial role of the anchoring group in the single-molecule conductance features of our metal-complexed wires, and confirmed pyridines as the most suitable termination for the observation of an electrically-triggered conductance switching in the pirouetting rotaxane system described in chapter 1. We expect that the relationships observed herein concerning the influence of metal ions in the conductance pathway could be corroborated by the measurement of charge transport in other chemical structures like Ir(III) complexes.

The measurement of bistable system [Cu(**M3**)**W3**]$^{+/2+}$ in MCBJ represents the first single-molecule approximation to switchable electronic devices based on interlocked molecules. The single-molecule MCBJ technique seems a very suitable option for the evaluation of the conductance differences between the two conformational and redox states of this system. The good correlation found between the chemical structure and the conducting properties for Cu(I) complexes in MCBJ make us to expect a good conductance response to the redox change from the diamagnetic [Cu(**M3**)**W3**]$^{+}$ to the

paramagnetic [Cu(**M3**)**W3**]$^{2+}$ species. Besides, this technique is expected to minimize the kinetic problems found in densely packed molecular arrays. Nevertheless, this approach constitutes a great challenge taking into account that the switching of copper-based interlocked molecules has never been achieved in the solid state. On the other hand, solution-based techniques, like electrochemical STM, seem to be more appropriated for the introduction of a permanent charge on the molecule and for the induction of the molecular motion that characterize these molecules.

Finally, the synthesis of a series of Ir(III) cyclometallated complexes with molecular wires **W1-W4** represents a first stage into the construction of nanoscale optoelectronic devices with metallic complexes. According to the effect observed in Cu(I) complexation, the great stabilization of the LUMO orbital evidenced in the electrochemical characterization of the Ir(III) complexes, is expected to largely increase the conductance of pyridine ended complexes (**W3**, **W4**), whereas the influence of Ir complexation on thiol backbones (**W1**, **W2**) should be lower.

As extracted from the photophysical study, the photoexcitation of **IrW1-IrW4** complexes involves the HOMO ground state, located on the metal center and ppy ligands to the LUMO, mostly located on the backbone. For that reason, light irradiation is expected to have a profound effect on the conduction of the pyridine-ended wires **IrW3** and **IrW4**, for which charge transport is LUMO dominated. By contrast, the lack of participation of the high electrically-coupled HOMO orbital of thiol-terminated wires **W1** and **W2** in the photoexcitation process of **IrW1** and **IrW2**, make us expect a low influence of light in the molecular conductance through these complexes. The investigation of electron transport in these molecules could contribute to confirm the correlations established in section 3.6. The measurement of the iridium wires is programed in the future.

Experimental

Spectrochemical measurements

For mass spectrometry, ^{1}H NMR, IR and UV-Vis spectroscopy and elemental analysis details see the experimental section of chapter 1.

Laser Flash Photolysis Measurements

A pulsed Nd:YAG SL404G-10 Spectron Laser Systems was used at the excitation wavelength of 355 nm. The single pulses were ~10 ns in duration and the energy was lower than 15 mJ/pulse. The detecting light source was a pulsed Lo255 Oriel xenon lamp. The laser flash photolysis system consisted of a pulsed laser, a Xe lamp, a 77200 Oriel monochromator, an Oriel photomultiplier tube (PMT) system made up of a 77348 side-on PMT tube, 70680 PMT housing, and a 70705 PMT power supply. The oscilloscope was a TDS-640A Tektronix. The output signal from the oscilloscope was transferred to a personal computer. All transient measurements were recorded in dichloromethane or ethanol employing 10 × 10 mm^2 quartz cells with 4 mL capacity and were purged with nitrogen or oxygen for at least 10 min before acquisition. All the experiments were carried out at room temperature.

Phosphorescence Measurements

Phosphorescence spectra were obtained from a Photon Technology International (PTI, TimeMaster TM-2/2003) spectrofluorometer equipped with a pulsed Xe lamp. The apparatus was operated in time-resolved mode, with a delay time of 0.5 ms. Compounds were dissolved in ethanol, placed in a quartz tube (5 mm of diameter), and cooled to 77 K. The absorbance of the samples was 0.3 at the excitation wavelength (355 nm).

Fluorescence Measurements

Fluorescence decay traces were recorded with an EasyLife X system from OBB with a PTI lifetime detector. The solutions were purged with N_2 at least during 10 min. The experiments were performed at room temperature (λ_{exc} = 375 nm).

Electrochemical measurements

Electrochemical measurements were performed in a nitrogen glove box using an Autolab PGSTAT 128N potentiostat using a three-electrode electrochemical cell consisting in a Glassy carbon working electrode, a platinum wire counter electrode and a silver wire quasi-reference electrode. Ferrocene (0.45 V vs SCE in acetonitrile) or $[Cu(dmp)_2](PF_6)$ (0.64 V vs SCE in dichloromethane)[184] were used as reference potentials. Supporting electrolyte solutions were prepared from anhydrous dichloromethane and $TBA(PF_6)$.

Computational calculations

The computational calculations presented in sections 3.6 and 3.7 were performed by Prof. Eliseo Ruiz and Daniel Aravena from the Electronic structure group in Universitat de Barcelona. DFT calculations of the isolated molecules were performed employing the B3LYP[185] functional and TZV basis set, as implemented in the Gaussian09[186] software package. NEGF+DFT calculations were carried out by means of the TranSIESTA[186] routine included in SIESTA 3.1,[187] using the PBE functional,[188] and a DZP basis for the molecule and a SZ basis for the gold atoms. Device models consisted in two five-layer Au(111) electrodes bridged with gas-phase optimized molecules. The adsorption site and distances of the anchoring groups to the gold surface were chosen according to previous studies,[189-191] to be: bridge site, 2.5 Å for **W1;** on top, 2.5 Å for **W3** and on top, 2.0 Å for **W5**. Copper coordinated models preserved the adsorption geometry of the corresponding backbones.

Electronic transport measurements

Single-molecule transport measurements were carried out by Dr. Carlos R. Arroyo and Riccardo Frisenda from Prof. Van der Zants group, in the Kavli Institute of Nanoscience, Deft University of Technology.

Deposition of the Conjugated Molecular Wires into the electrodes

In the experiments reported here, the molecules were deposited onto the MCBJ devices by pipetting 2 μl of a freshly prepared 0.5 mM solution. In the case of **W1** and **W3,** one equivalent of tetrabutylammonium hydroxide (TBAOH) or tetrabutylammonium fluoride (TBAF) was added to the solution just before the deposition to promote the deprotection of the AcS and TMS groups, respectively. The solvents used for the different backbones were dichlorobenzene for **W1**, dichloromethane for **W3** and a 1:4 mixture of tetrahydrofuran and octane in the case of **W5**. For the Cu(I) complexes [Cu(**M2**)(**W1/W3/W5)**](PF_6) dichloromethane was used as solvent. Moreover, in the case of the complexes [Cu(**M2**)(**W1/W3/W5)**](PF_6)**,** 10 equivalents of hydrazine in THF were added to the solution just before the deposition to prevent the oxidation to Cu(II). The rotaxane complexes treated in section 3.9, [Cu(**M3**)(**W3)**](PF_6) and [Cu(**M3**)(**W3)**]$(PF_6)_2$ were deposited in dichloromethane and acetonitrile solvents, respectively, without the addition of any deprotecting group. Finally, after the solvent had dried over the electrode a vacuum can was placed and the sample was pumped down to around 10^{-6} mbar for approximately one hour before starting the experiments.

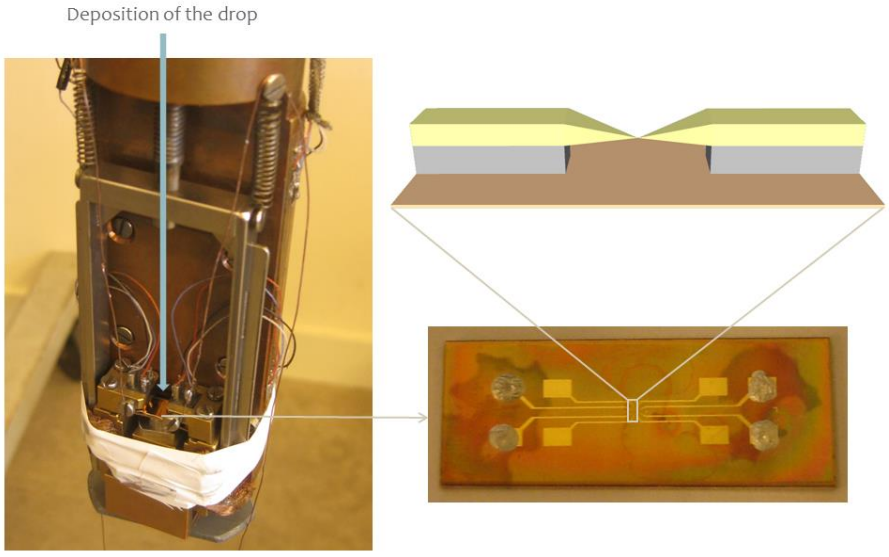

Figure 3.50 Pictures of the measurement instrumentation:

Conductance measurements

Single-molecule conductance measurements were carried out at room temperature using the MCBJ technique.[192] Briefly, the device consists of a narrow gold bridge suspended above a flexible substrate. This device is clamped in a three-point bending configuration, as schematically shown in Figure 3.10. After the deposition of the molecules from solution at ambient conditions, the suspended gold bridge is stretched by driving the pushing rod against the bottom part of the MCBJ device until it breaks, leaving a pair of atomically sharp electrodes. Once the bridge is broken for the first time, atomic-sized contacts can be repeatedly formed and broken by moving the electrodes towards and away from each other. During the whole process the conductance G=I/V is simultaneously measured by applying a bias voltage of 0.1 V across the electrodes. During the breaking process the conductance decreases in a stepwise fashion. Just before the complete rupture of the gold wire the conductance usually exhibits a plateau which is nearly flat and very close to the fundamental quantum conductance 1 G_0 (=$2e^2/h$). This plateau characterizes the formation of a contact consisting of a single gold atom bridging the gap between the electrodes (Figure 3.51 **i**). Upon further stretching, the contact breaks and the conductance drop abruptly to a value around 10^{-3} to 10^{-4} G_0. Beyond this point, electron tunneling between the electrodes leads to an exponential conductance decay as a function of the electrode displacement. The abrupt drop in conductance after the breaking of the one-atom contact is associated to mechanical relaxation and atomic rearrangements at the electrode apexes.[193] When a molecule is trapped between the electrodes, conductance plateaus can be observed for long electrodes displacements (Figure 3.51 A **ii**). After the contact-rupture, the electrodes are fused together to a value around 80 G_0 to ensure the formation of clean gold contacts.

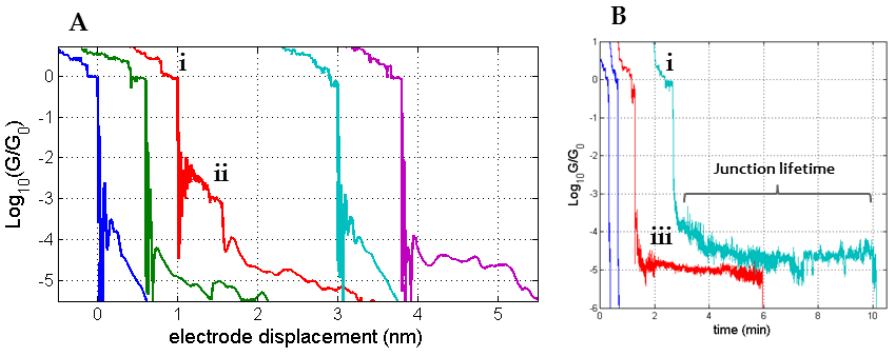

Figure 3.51 Typical MCBJ **(A)** and SB **(B)** traces for junctions exposed to molecular solutions.: i) one gold-atom plateau, ii) and iii) molecular plateaus.

Alternatively, a variation of the traditional MCBJ experiment, the self-breaking method, was used to form molecular junctions.[139] This method has been previously used to investigate the stability of atomic-gold contacts. In these experiments the junction is first stretched by bending the substrate with a bias voltage of 0.1 V applied across the electrodes. Once the conductance of the junction reaches a value below 10 G_0 (typically 6 G_0) the bending process is stopped and the conductance is continuously monitored as a function of time. Due to the high mobility of gold atoms at room temperature the junction breaks by itself. When the conductance drops below a minimum conductance value ($G < 10^{-7}$ G_0) the electrodes are fused together again to 80 G_0 and a new SB trace starts again. The key point of this technique is that, when no molecules are present, the time interval from 10^0 G_0 to 10^{-7} G_0 is short, see Figure 3.52 A. However, when sample molecules are present conductance plateaus can be observed for long periods of time, even several hours (Figure 3.51 B **iii**). These plateaus are indicative of the presence of the target molecules trapped in between the electrodes. We have defined the junction lifetime as the time that conductance takes to drop from $G = G_0$ to $G < 10^{-7}$. Considering that lifetimes measured for pure solvent molecules are typically below 100 seconds, see Figure 3.52 B, we can assume that molecular junctions are formed when junction lifetime exceeds 100 seconds, and hence, a trapping probability can be calculated.

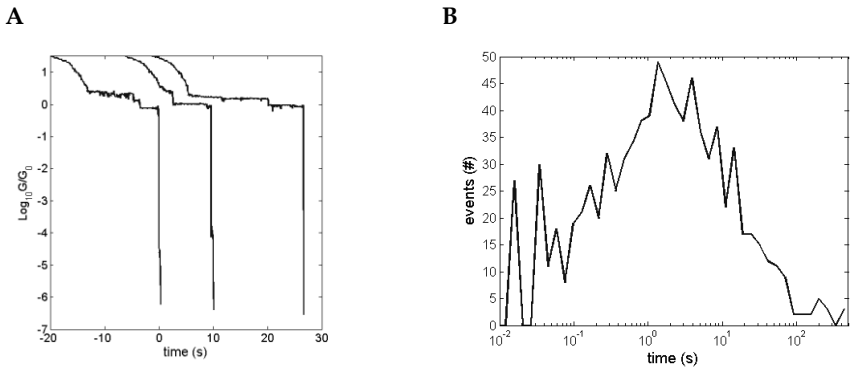

Figure 3.52 A) Example of self-breaking traces for junctions exposed to pure solvent. **B)** Histogram of the lifetime, in logarithmic scale, built from 900 self-breaking traces as that shown in **A**.

Materials and general procedures

All chemicals used were purchased from commercial sources and used without further purification. Anhydrous dichloromethane, acetonitrile and tetrahydrofuran solvents were freshly distilled under argon over the appropriate drying agent (calcium chloride, calcium hydroxide and sodium, respectively). Column chromatographies were carried out on silica or alumina gel (60 Å, 230-400 mesh).

The synthesis of 3,8-dibromo-1,10-phenanthroline (**11**), ((4-ethynylphenyl)ethynyl)trimethylsilane (**28**), 3,8-bis((trimethylsilyl)ethynyl)-1,10-phenanthroline (**35**), and 3,8-bis((4-ethynylphenyl)ethynyl)-1,10-phenanthroline (**30**) were previously described in chapter 1.

The starting iridium dichloro bridge dimer $[Ir(ppy)_2Cl]_2$ was prepared according to a literature procedure.[172]

3,8-diethynyl-1,10-phenanthroline *41*

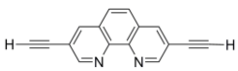

A suspension of the bis-silylated phenanthroline **35** (0.27g, 0.73 mmol) and K_2CO_3 (0.1 g, 0.73 mmol), in methanol (10 mL) was stirred at room temperature for 1 h. Evaporation of the solvent yielded a solid which was suspended in water, filtered and washed with plenty of water to afford the pure product as an off-white solid (0.16 g, 97%).

^{1}H NMR (300 MHz, $CDCl_3$) δ 9.26 (d, *J* = 2.1 Hz, 2H), 8.39 (d, *J* = 2.1 Hz, 2H), 7.81 (s, 2H), 3.40 (s, 2H).

MS (ES): *m*/*z* (%): calcd for $[C_{16}H_8N_2]^+$: 229.1; found: 229.2 $[MH]^+$.

1-(acetylthio)-4-iodobenzene **42**

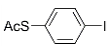

A mixture of 4-iodobenzenesulfonyl chloride (5.0 g, 16.5 mmol), Zn in powder (3.8 g, 58,0 mmol), dichloro(dimethyl)silane (7.0 mL, 58.0 mmol), DMA (4.6 mL) and dichloroethane (250 mL) was heated under argon at 75 ^{0}C for 3 h. After that time, the mixture was allowed to reach 50 ^{0}C and acetyl chloride was added (1.5 mL, 21.5 mmol) and heated at 50 ^{0}C overnight. The resulting mixture was filtered to remove the white solid and washed with water (4x30 mL). The resulting organic solution was dried over Na_2SO_4, concentrated under reduced pressure and keep under vacuum for one day to afford the pure product as a white solid (4.5 g, 98%).

^{1}H NMR (300 MHz, $CDCl_3$) δ 7.74 (d, *J* = 8.5 Hz, 2H), 7.13 (d, *J* = 8.5 Hz, 2H), 2.42 (s, 3H).

MS (ES): *m*/*z* (%): calcd. for C_8H_7IOS: 278.9; found: 278.8 (100) $[MH]^+$.

Molecular wire ***W1***

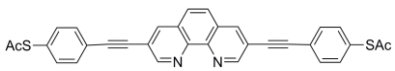

A mixture of **41** (0.11 g, 0.50 mmol), 1-(acetylthio)-4-iodobenzene (**42**) (0.35 g, 1.25 mmol), CuI (0.05 g, 0.25 mmol), $Pd(dba)_2$ (0.04 g, 0.06 mmol), PPh_3 (0.03 g, 0.13 mmol), *N*,*N*-

diisopropylethylamine (DIEA) (4 mL) and anhydrous THF (10 mL) was stirred under an argon atmosphere at 60 ^{0}C for 3 days. After that time, THF was evaporated; the solid was dissolved in dichloromethane (20 mL) and treated with an aqueous solution of KCN (6 mg/mL, 10 mL) for 2 h. Then, the two phases were separated and the aqueous phase was washed four times with dichloromethane (4x10 mL). The combined organic phases were washed with water (4x15 mL), dried over Na_2SO_4, filtered and concentrated under reduced pressure. The resulting solid was washed with plenty of ether to eliminate the remaining triphenylphosphines and then purified by column chromatography on silica gel using CH_2Cl_2/MeOH as eluent to afford **W1** as a pale yellow solid (0.11 g, 40%).

^{1}H NMR (300 MHz, $CDCl_3$) δ 9.27 (d, *J* = 2.1 Hz, 2H), 8.38 (d, *J* = 2.1 Hz, 2H), 7.80 (s, 2H), 7.65 (d, *J* = 8.6 Hz, 4H), 7.45 (d, *J* = 8.6 Hz, 4H), 2.45 (s, 6H).

MS (ES): *m*/*z* (%): calcd. for $C_{32}H_{20}N_2O_2S_2$: 529.1; found: 529.5 (100) $[MH]^+$.

Molecular wire **W2**

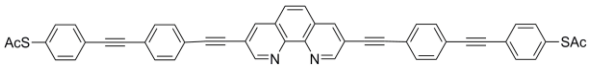

A mixture of **30** (0.21 g, 0.50 mmol), 1-(acetylthio)-4-iodobenzene (**42**) (0.33 g, 1.20 mmol), CuI (0.023 g, 0.12 mmol), $Pd(dba)_2$ (0.034 g, 0.06 mmol), PPh_3 (0.063 g, 0.24 mmol), DIEA (4 mL) and anhydrous THF (10 mL) was stirred at 60 ^{0}C for 3 days. After evaporation of the solvents, the crude was dissolved in 10 mL of dichloromethane and treated with an aqueous solution of KCN (6 mg/mL, 5 mL) for 2 h. The two phases were separated and the aqueous phase was washed with dichloromethane (4x20 mL). The collected organic phases were washed with water (4x20 mL), dried over Na_2SO_4, filtered and concentrated affording a yellow solid that was then suspended in diethyl ether, filtered and washed with plenty of ether to eliminate the remaining triphenylphosphines. The resulting solid was chromatographed over silica gel using CH_2Cl_2/MeOH as eluent to afford the pure product as a yellow solid (0.23 g, 63%).

^{1}H NMR (300 MHz, $CDCl_3$) δ 9.29 (d, *J* = 2.0 Hz, 2H), 8.40 (d, *J* = 2.0 Hz, 2H), 7.82 (s, 2H), 7.64 – 7.52 (m, 12H), 7.42 (d, *J* = 8.6 Hz, 4H), 2.45 (s, 6H).

HRMS (MALDI): *m*/*z* (%) calcd for $C_{48}H_{28}N_2O_2S_2$: 728.16; found: 727.08 (100) [M^+].

Molecular wire ***W3***

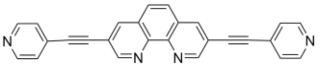

A mixture of **35** (0.16 g, 0.70 mmol), 4-iodopyridine (0.33 g, 1.61 mmol), CuI (0.01 mg, 0.06 mmol), $Pd(PPh_3)_4$ (0.08 g, 0.07 mmol), DIEA (3 mL) and anhydrous THF (6 mL) was stirred at 60 ^{0}C for 2 days. After evaporation of the solvents, the crude was dissolved in 10 mL of dichloromethane, treated with an aqueous solution of KCN (6 mg/mL, 5 mL) and stirred for 2 h. The two phases were separated and the aqueous phase was washed with dichloromethane (4x10 mL). The collected organic phases were washed with water (4x15 mL), dried over Na_2SO_4, filtered and concentrated affording a yellow solid which was chromatographed over silica gel using CH_2Cl_2/MeOH as eluent to yield the pure product as a white solid (0.13 g, 84%).

^{1}H NMR (300 MHz, $CDCl_3$) δ 9.29 (d, *J* = 2.1 Hz, 2H), 8.67 (d, *J* = 6.0 Hz, 4H), 8.43 (d, *J* = 2.1 Hz, 2H), 7.84 (s, 2H), 7.47 (dd, *J* = 4.4, 1.6 Hz, 4H).

MS (ES): *m*/*z* (%): calcd. for $C_{26}H_{14}N_4$: 383.1; found: 383.3 (100) [$MH]^+$.

IR: (KBr) = 3422 (br), 3169 (br), 2217 (w), 1592 (s), 1423 (m), 1405 (m), 1384 cm^{-1} (m).

Molecular wire ***W4***

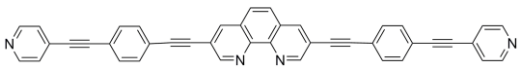

Method c

A mixture of **30** (0.15 g, 0.35 mmol), 4-iodopyridine (0.18 g, 0.88 mmol), CuI (0.017 g, 0.09 mmol), $Pd(dba)_2$ (0.025 g, 0.04 mmol), PPh_3 (0.046 g, 0.18 mmol), DIEA (4 mL) and

anhydrous THF (10 mL) was stirred at 60 ^{0}C for 7 days. After evaporation of the solvents, the crude was dissolved in 10 mL of dichloromethane and treated with an aqueous solution of KCN (6 mg/mL, 5 mL) for 2 h. The two phases were separated and the aqueous phase was washed with dichloromethane (4x20 mL). The collected organic phases were washed with water (4x20 mL), dried over Na_2SO_4, filtered and concentrated affording a yellow solid that was then suspended in diethyl ether, filtered and washed with plenty of ether to eliminate the remaining triphenylphosphines. The resulting solid was chromatographed over silica gel using CH_2Cl_2/MeOH as eluent to afford the pure product as a yellow solid (0.20 g, 96%).

Method e

4-((4-ethynylphenyl)ethynyl)pyridine (**46**) (0.20g, 0.98 mmol), 3,8-dibromo-1,10-phenanthroline (**11**) (0.11 g, 0.33 mmol), CuI (0.01 g, 0.052 mmol), $Pd(PPh_3)_4$ (0.038 g, 0.033 mmol) and anhydrous THF (15 mL) were heated under argon at 65 ^{0}C for 3 days. The resulting mixture was filtered and the solid washed with dichloromethane (40 mL). The combined organic phases were washed with water (4x15 mL), dried over Na_2SO_4 and concentrated under reduced pressure. The resulting solid was chromatographied over silica gel using CH_2Cl_2/MeOH as eluent (Yellow solid, 0.064 g, 33%).

^{1}H NMR ($CDCl_3$, 300 MHz): δ 9.30 (d, *J*=2.1 Hz, 2H), 8.64 (d, *J*=6 Hz, 4H), 8.41 (d, *J*=2.1 Hz, 2H), 7.83 (s, 2H), 7.62 (m, 8H), 7.41 (d, *J*=6 Hz, 4H).

MS (ES): *m*/*z* (%) calcd for $C_{42}H_{23}N_4$: 583.66; found: 583.35 (100) [MH^+].

Molecular wire **W5**

Previously described in chapter 1 (compound **29**).

S-(4-((4-((trimethylsilyl)ethynyl)phenyl)ethynyl)phenyl) ethanethioate **43**

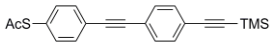

A mixture of 1-(acetylthio)-4-iodobenzene (**42**) (0.33 g, 1.20 mmol), CuI (0.023 g, 0.12 mmol) $PdCl_2(PPh_3)_2$ (0.042 g, 0.06 mmol), DIEA (3 mL) and THF (2 mL) was stirred under argon for 10 min. Addition of the mixture of mono and diprotected ((4-ethynylphenyl)ethynyl)trimethylsilane **28** (0.272g, ca. 1.0 mmol of **28**) turned the color of the mixture into dark. The reaction mixture was refluxed for 3 days. Dichloromethane (50 mL) was added, and the organic phase was washed with water (4x20 mL) and dried over Na_2SO_4. Organic solvents were removed under reduced pressure and the resulting brown solid was purified by silica column chromatography (hexane/CH_2Cl_2), affording the pure product as a yellow solid (0.15 g, 43%).

^{1}H NMR (300 MHz, $CDCl_3$) δ 7.54 (d, *J* = 8.6 Hz, 2H), 7.45 (s, 4H), 7.40 (d, *J* = 8.6 Hz, 2H), 2.44 (s, 3H), 0.26 (s, 9H).

4-((4-((trimethylsilyl)ethynyl)phenyl)ethynyl)pyridine ***44***

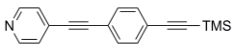

4-Bromopyridine hydrochloride (0.36 g, 1.86 mmol) was placed in a conical bottom flask under Ar and stirred under argon for 10 min with i-Pr_2NH (6 mL), CuI (0.01 g, 0.04 mmol) and $PdCl_2(PPh_3)_2$ (0.03 g, 0.04 mmol). The colour of the mixture changed from green to yellow. Addition of the mixture of ((4-ethynylphenyl)ethynyl)trimethylsilane **28** and the diprotected 1,4-bis((trimethylsilyl)ethynyl)benzene (0.33 g, ca.1.69 mmol of **6**), turned the color into dark. After 24 hours of stirring at 40 °C, 50 mL of dichloromethane were added to the reaction mixture. The organic phase was washed with water (4x20 mL), dried over Na_2SO_4 and concentrated under reduced pressure. The resulting brown solid was purified by silica column chromatography (hexane/ diethyl ether, 8:2), affording the pure product as a yellow crystalline solid (0.34g, 74%).

^{1}H NMR ($CDCl_3$, 300 MHz): δ 8.62 (d, *J* = 6 Hz, 2H), 7.45 (s, 4H), 7.42 (d, *J* = 6 Hz, 2H), 0.26 (s, 9H).

S-(4-((4-ethynylphenyl)ethynyl)phenyl) ethanethioate ***45***

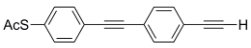

Compound **43** (0.65 g, 1.87 mmol), THF (10 mL), acetic anhydride (0.35 mL, 3.74 mmol), acetic acid (0.22 mL, 3.74 mmol), and tetrabutylammonium fluoride (2.1 mL of a 1.0 M solution in THF) were stirred together under argon overnight. Dichloromethane (40 mL) was added and the organic phase was washed with water (4x20 mL) and dried over Na_2SO_4. Organic solvents were removed under reduced pressure to afford the pure product as a yellow solid (0.50g, 93%).

^{1}H NMR (300 MHz, CDCl3) δ 7.56 (d, *J* = 8.1 Hz, 2H), 7.49 (s, 4H), 7.41 (d, *J* = 8.1 Hz, 2H), 3.19 (s, 1H), 2.44 (s, 3H).

4-((4-ethynylphenyl)ethynyl)pyridine ***44***

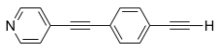

A solution of **44** (0.15 g, 0.54 mmol) in 25 mL of methanol was stirred for 1 h with 0.10 g (0.76 mmol) of K_2CO_3. Solvent was removed and the resulting solid was uptaken in diethyl ether (60 mL) and washed with brine (2x20 mL) and water (2x20 mL). The organic solvent was evaporated affording the pure product in quantitative yield (0.11 g, 100 %).

^{1}H NMR (CDCl3, 300 MHz): δ 8.62 (d, *J* = 6 Hz, 2H), 7.50 (s, 4H), 7.42 (d, *J* = 6 Hz, 2H), 3.21 (s, 1H).

MS (ES): *m*/*z* (%): calcd. for $C_{15}H_{10}N$: 204.08; found: 204.23 (100) $[MH]^+$.

General procedure for the threading of the copper complexes ***[Cu(M2)(W)](PF$_6$)***

A degassed solution of $[Cu(CH_3CN)_4]PF_6$ (19 mg, 0.05 mmol) in acetonitrile (4 mL) was added via cannula over a degassed mixture of macrocycle **M2** (26 mg, 0.05 mmol) in dichloromethane (4 mL). After 30 minutes of stirring under an inert atmosphere a

degassed solution of molecular backbones **W1/W3/W5** (0.05 mmol) in dichloromethane (10 mL) was added turning the colour into dark red. After 3 h of stirring, organic solvents were evaporated under reduced pressure and the residue was suspended in a 1:1 mixture of hexane and diethyl ether and filtered to yield the pure product as a red solid.

[Cu(M2)W1](PF$_6$)

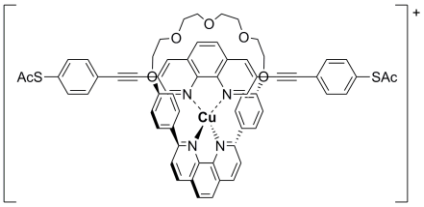

^{1}H NMR (300 MHz, CD_2Cl_2) δ 8.93 (s, 2H), 8.67 (s, 2H), 8.39 (s, 2H), 8.33 – 7.96 (m, 6H), 7.61 (d, *J* = 8.1 Hz, 4H), 7.46 (d, *J* = 8.1 Hz, 4H), 7.08 (s, 4H), 5.84 (s, 4H), 3.91 (d, *J* = 5.0 Hz, 4H), 3.81 (d, *J* = 5.0 Hz, 4H), 3.49-3.47 (m, 4H), 3.12-3.09 (m, 4H), 2.44 (s, 6H).

MS (ES): *m*/*z* (%): calcd. for $CuC_{64}H_{50}N_4O_7S_2$: 1113.2; found: 1113.7 (100) [Cu(**M2**)**W1**]$^+$.

[Cu(M2)W3](PF$_6$)

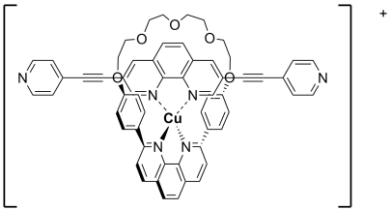

^{1}H NMR (500 MHz, CD_2Cl_2) δ 8.98 (s, 2H), 8.72 (d, *J* = 4.6 Hz, 2H), 8.42 (s, 2H), 8.30 (s, 2H), 8.18 (s, 4H), 8.10 (d, *J* = 4.6 Hz, 2H), 7.48 (s, 4H), 7.07 (d, *J* = 8.1 Hz, 4H), 5.81 (d, *J* = 8.1 Hz, 4H), 3.99 – 3.87 (m, 4H), 3.88 – 3.75 (m, 4H), 3.48 (t, *J* = 4.8 Hz, 4H), 3.08 (t, *J* = 4.8 Hz, 4H).

MS (ES): *m*/*z* (%): calcd. for $CuC_{58}H_{44}N_6O_5$: 967.3; found: 967.6 (100) [Cu(**M2**)**W3**]$^+$.

IR: (KBr) = 3471 (br), 3415 (br), 3232 (br), 2923 (m), 2838 (m), 2207 (w), 1637 (s), 1617 (s), 1489 (m), 1399 (s), 1247 (m), 1174 (m), 1115 (m), 839 (m), 618 cm^{-1} (m).

[Cu(M2)W5](PF$_6$)

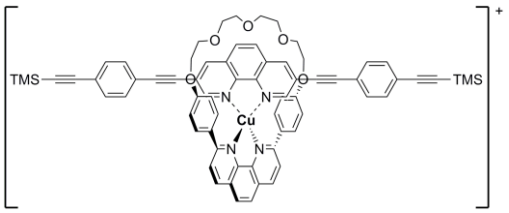

^{1}H NMR (300 MHz, CD_2Cl_2) δ 8.47 (m, 4H), 8.18 (s, 2H), 8.02 (s, 2H), 7.99 – 7.88 (m, 4H), 7.27 (dt, *J* = 19.9, 7.6 Hz, 12H), 5.80 (d, *J* = 7.4 Hz, 4H), 3.89 (d, *J* = 5.0 Hz, 4H), 3.76 (d, *J* = 5.0 Hz, 4H), 3.49-3.47 (m, 4H), 3.12-3.09 (m, 4H), 0.05 (s, 18H).

MS (ES): *m*/*z* (%): calcd. for $CuC_{70}H_{62}N_4O_5Si_2$: 1157.4; found: 1157.5 (100) [Cu(**M2**)**W5**]$^+$.

[Cu(M3)W3](PF$_6$)

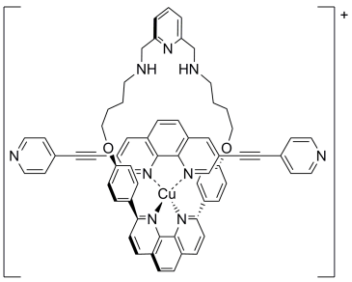

A degassed solution of $[Cu(CH_3CN)_4]PF_6$ (19 mg, 0.05 mmol) in acetonitrile (4 mL) was added via cannula over a degassed mixture of macrocycle **M3** (31 mg, 0.05 mmol) in dichloromethane (4 mL). After 30 minutes of stirring under an inert atmosphere a degassed solution of molecular backbones **W3** (19 mg, 0.05 mmol) in dichloromethane (10 mL) was added turning the colour into dark red. After 3 hours of stirring, organic

solvents were evaporated under reduced pressure to yield the pure product as a red solid (0.055 g, 82%).

^{1}H NMR (300 MHz, CD_2Cl_2) δ 8.81 (br, 2H), 8.60 (d, *J* = 8.4, 2H), 8.36 (m, 4H), 8.23 (br, 2H), 8.06 (s, 2H), 8.06 (d, *J* = 8.4 Hz, 2H), 7.88 (s, 2H), 7.74 (m, 4H), 7.70 (s, 1H), 7.37 (d, *J* = 8.6 Hz, 4H), 7.27 (br, 2H), 5.92 (d, *J* = 8.6 Hz, 4H), 3.98 (m, 4H), 2.65 (m, 4H), 1.57 (m, 8H).

HRMS (MALDI): *m*/*z* (%) calcd for $CuC_{65}H_{53}N_9O_2$: 1054.36; found: 1054.37 (80) [Cu(**M3**)**W3**]$^+$.

Elemental analysis (%) calcd. for $CuC_{65}F_6H_{53}N_9PO_2$: C, 65.02; H, 4.45; N, 10.50; Found: C, 64.07; H, 4.87; N, 8.42.

IR: (KBr) = 3439 (br), 3163 (br), 2952 (m), 2924 (m),2854 (m), 2217 (w), 1657 (m), 1589 (s), 1488 (m), 1401 (s), 1248 (m), 1174 (m), 842 (s), 558 cm^{-1} (m).

EDAX (calculated for [Cu(**M3**)**W3**](PF_6)): Found Cu = 48.90 % (50.00%); P = 51.10 % (50.00%).

[Cu(M3)W3](PF$_6$)$_2$

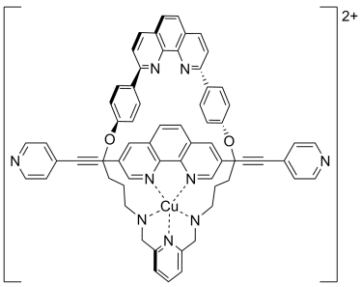

A solution of $Cu(CH_3COO)_2{\cdot}H_2O$ (10 mg, 0.05 mmol) in methanol (4 mL) was added over a solution of macrocycle **M3** (31 mg, 0.05 mmol) in dichloromethane (4 mL). After 30 minutes of stirring a degassed solution of **W3** (19 mg, 0.05 mmol) in dichloromethane (10 mL) was added changing the color from green into brown-green. After 3 hours of stirring, the dichloromethane was evaporated under reduced pressure and an excess of

aqueous KPF_6 (100 mg, 10 mL) was added. The resulting solid was filtered and washed with plenty of water to yield the pure product as a brown solid (45 mg, 66%).

HRMS (ES): *m/z* (%) calcd. for $CuC_{65}H_{53}N_9O_2$: 527.1809; found: 527.1805 (100) [Cu(**M3**)**W3**]$^{2+}$.

Elemental analysis (%) calcd. for $CuC_{65}F_{12}H_{53}N_9P_2O_2$: C, 58.10; H, 3.83; N, 9.38; Found: C, 52.89; H, 3.61; N, 8.00.

IR: (KBr) = 3405 (br), 3133 (br), 2926 (w), 2870 (w), 2217 (w), 1600 (s), 1490 (m), 1427 (m), 1406 (m), 1248 (m), 1175 (w), 842 (s), 557 cm^{-1} (m).

EDAX (calculated for [Cu(**M3**)**W3**]$(PF_6)_2$): Found Cu = 29.75 % (33.33 %); P = 70.25 % (66.66 %).

Cu(M4)W3(PF$_6$)$_2$

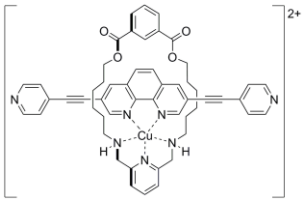

A solution of $Cu(CH_3COO)_2{\cdot}H_2O$ (8 mg, 0.04 mmol) in methanol (4 mL) was added over a solution of macrocycle **M4** (19 mg, 0.04 mmol) in dichloromethane (4 mL). After 30 minutes of stirring a degassed solution of **W3** (15 mg, 0.04 mmol) in dichloromethane (10 mL) was added changing the colour from blue into brown-green. After 3 hours of stirring, the dichloromethane was evaporated under reduced pressure and an excess of aqueous KPF_6 (100 mg, 10 mL) was added. The resulting solid was filtered and washed with plenty of water to yield the pure product as a brown solid (45 mg, 66%).

HRMS (ES): *m/z* (%) calcd. for $CuC_{53}H_{51}N_7O_4$: 456.1649; found: 456.1646 (100) [Cu(**M4**)**W3**]$^{2+}$.

Elemental analysis (%) calcd. for $CuC_{53}F_{12}H_{51}N_7P_2O_4$: C, 52.84; H, 4.27; N, 8.15; Found: C, 55.63; H, 3.98; N, 8.50.

IR: (KBr) = 3546 (m), 3470 (m), 3413 (m), 3139 (br), 2931 (m), 2856 (w), 2224 (w), 1714 (s), 1592 (s), 1427 (m), 1406 (m), 1307 (m), 1241 (m), 1173 (w), 842 (s), 558 cm^{-1} (m).

EDAX (calculated for [Cu(**M4**)**W3**]$(PF_6)_2$): Found Cu = 32.74 % (33.33 %); P = 67.26 % (66.66 %).

General procedure for the preparation of the Iridium complexes ***$[Ir(ppy)_2(W)](PF_6)$***

A mixture of $[Ir(ppy)_2Cl]_2$ (0.05 mmol) and **W1-W4** (0.1 mmol) was dissolved in a dichloromethane: methanol mixture (12 mL, 2:1 v/v) and heated under reflux for 24 h. Evaporation of the solvents afforded a red solid which was redissolved in dichloromethane. An excess of KPF_6 (1 mmol) was added, and the residue was filtered in order to eliminate the remaining inorganic salts. The resulting solution was evaporated under reduced pressure and the solid was purified by silica column chromatography (CH_2Cl_2/MeOH 1%) affording the pure products as a bright orange solids.

$[Ir(ppy)_2(W1)](PF_6)$

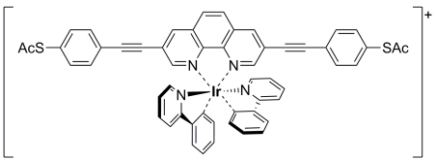

Yield = 54%.

^{1}H NMR (300 MHz, CD_2Cl_2) δ 8.72 (d, *J* = 1.8 Hz, 2H), 8.37 (d, *J* = 1.8 Hz, 2H), 8.21 (s, 2H), 8.00 (d, *J* = 8.0 Hz, 2H), 7.85 – 7.72 (m, 4H), 7.58 (d, *J* = 8.5 Hz, 4H), 7.47 (d, *J* = 8.5 Hz, 4H), 7.40 (d, *J* = 7.5 Hz, 2H),7.15 (td, *J* = 7.5, 1.2 Hz, 2H), 7.02 (td, *J* = 7.5, 1.2 Hz, 2H), 6.91 (td, *J* = 7.5, 1.2 Hz, 2H), 6.40 (dd, *J* = 7.5, 1.2 Hz, 2H), 2.44 (s, 6H).

HRMS (MALDI): *m*/*z* (%): calcd. for $C_{54}H_{36}N_4IrO_2S_2$: 1029.19; found: 1028.98 (100) [Ir(ppy)(**W1**)]$^+$.

[Ir(ppy)$_2$(W2)](PF$_6$)

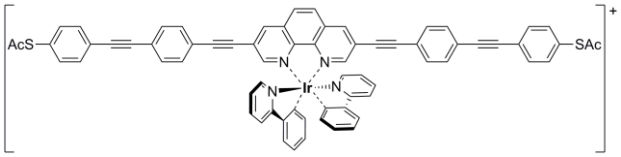

Yield = 35%.

^{1}H NMR (300 MHz, CD_2Cl_2) δ 8.71 (d, *J* = 1.8 Hz, 2H), 8.39 (d, *J* = 1.8 Hz, 2H), 8.20 (s, 2H), 8.01 (d, *J* = 8.0 Hz, 2H), 7.85-7.72 (m, 4H), 7.60-7.53 (m, 12H), 7.47 – 7.38 (m, 6H), 7.17 (td *J* = 7.5, 1.2 Hz, 2H), 7.04 (td *J* = 7.5, 1.2 Hz, 2H), 6.91 (td *J* = 7.5, 1.2 Hz, 2H), 6.41 (d, *J* = 7.5 Hz, 2H), 2.44 (s, 6H).

HRMS (MALDI): *m*/*z* (%): calcd. for $C_{70}H_{44}N_4IrO_2S_2$: 1229.25; found: 1228.95 (100) [Ir(ppy)(**W2**)]$^+$.

[Ir(ppy)$_2$(W3)](PF$_6$)

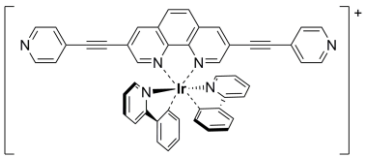

Yield = 40%.

^{1}H NMR (300 MHz, CD_2Cl_2) δ 8.79 (d, *J* = 1.8 Hz, 2H), 8.64 (d, *J* = 6.0 Hz, 4H), 8.39 (d, *J* = 1.8 Hz, 2H), 8.26 (s, 2H), 8.00 (d, *J* = 8.0 Hz, 2H), 7.85 – 7.72 (m, 4H), 7.40 (m, 6H), 7.15 (td, *J* = 7.5, 1.2 Hz, 2H), 7.02 (td, *J* = 7.5, 1.2 Hz, 2H), 6.92 (td, *J* = 7.5, 1.2 Hz, 2H), 6.39 (dd, *J* = 7.5, 1.2 Hz, 2H).

HRMS (MALDI): *m*/*z* (%): calcd. for $C_{48}H_{30}N_6Ir$: 883.22; found: 883.17 (100) [Ir(ppy)(**W3**)]$^+$.

[Ir(ppy)$_2$(W4)](PF$_6$)

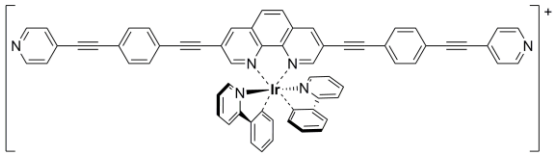

Yield= 41%.

^{1}H NMR (300 MHz, CD_2Cl_2) δ 8.73 (d, *J* = 1.8 Hz, 2H), 8.61 (d, *J* = 6.0 Hz, 4H), 8.38 (d, *J* = 1.8 Hz, 2H), 8.22 (s, 2H), 8.01 (d, *J* = 8.0 Hz, 2H), 7.82- 7.78 (m, 4H), 7.58 (m, 8H), 7.41-7.39 (m, 6H), 7.16 (td, J = 7.5, 1.2 Hz, 2H), 7.03 (td, J = 7.5, 1.2 Hz, 2H), 6.91 (td, J = 7.5, 1.2 Hz, 2H), 6.41 (dd, J = 7.5, 1.2 Hz, 2H).

HRMS (MALDI): *m*/*z* (%): calcd. for $C_{64}H_{38}N_6Ir$: 1083.28; found: 1038.31 (100) [Ir(ppy)(**W4**)]$^+$.

Annex

Calculated transmission spectra by NEGF+DFT

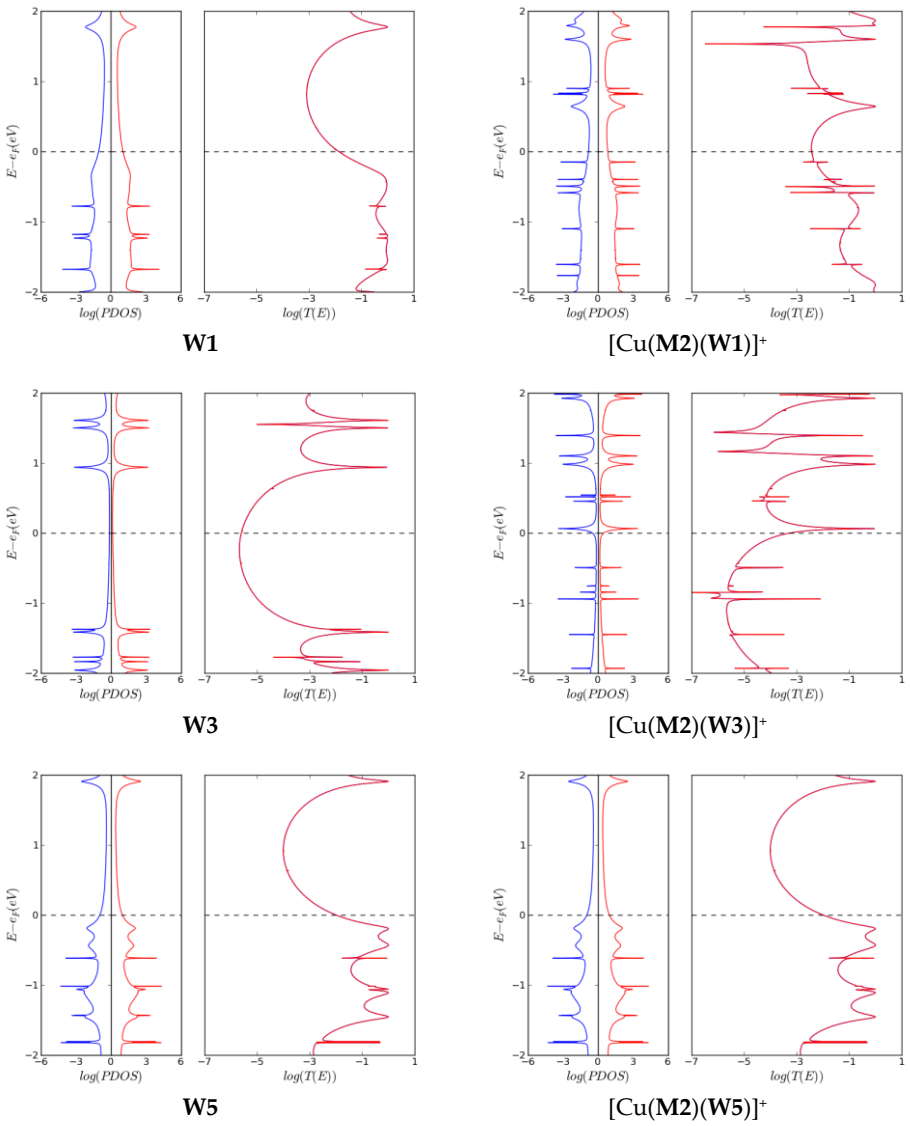

Figure 3.53 Transmission spectra and molecule projected density of states for the backbone-gold devices (**W1**, **W2** and **W3**) and its corresponding Cu(I) complexes.

References

References

(1) Cuevas, J. C.; Scheer, E.; ebrary, I. In *Molecular electronics;* World Scientific series in nanoscience and nanotechnology; World Scientific Pub. Co.: Singapore; Hackensack, N.J., 2010; Vol. 1, pp 703.

(2) Aviram, A.; Ratner, M. A. *Chem. Phys. Lett.* **1974**, *29*, 277-283.

(3) Mirkin, C. A.; Ratner, M. A. *Annu. Rev. Phys. Chem.* **1992**, *43*, 719-754.

(4) Joachim, C.; Gimzewski, J. K.; Aviram, A. *Nature* **2000**, *408*, 541-548.

(5) Tour, J. M. *Acc. Chem. Res.* **2000**, *33*, 791-804.

(6) http://spectrum.ieee.org The Status of Moore's Law: It's Complicated. 2013).

(7) Weibel, N.; Grunder, S.; Mayor, M. *Org. Biomol. Chem.* **2007**, *5*, 2343-2353.

(8) Song, H.; Reed, M. A.; Lee, T. *Adv. Mater.* **2011**, *23*, 1583-1608.

(9) Xiang, D.; Jeong, H.; Lee, T.; Mayer, D. *Adv. Mater.* **2013**.

(10) Ratner, M. *Nat. Nanotechnol.* **2013**, *8*, 378-381.

(11) Aradhya, S. V.; Venkataraman, L. *Nat. Nanotechnol.* **2013**, *8*, 399-410.

(12) Osorio, E. A.; Bjørnholm, T.; Lehn, J. M.; Ruben, M.; Van Der Zant, H. S. J. *J. Phys. : Condens. Matter* **2008**, *20*.

(13) Jia, C.; Guo, X. *Chem. Soc. Rev.* **2013**, *42*, 5642-5660.

(14) Salomon, A.; Cahen, D.; Lindsay, S.; Tomfohr, J.; Engelkes, V. B.; Frisbie, C. D. *Adv. Mater.* **2003**, *15*, 1881-1890.

(15) Liu, H.; Wang, N.; Zhao, J.; Guo, Y.; Yin, X.; Boey, F. Y. C.; Zhang, H. *ChemPhysChem* **2008**, *9*, 1416-1424.

(16) Vonlanthen, D.; Mishchenko, A.; Elbing, M.; Neuburger, M.; Wandlowski, T.; Mayor, M. *Angew. Chem. , Int. Ed.* **2009**, *48*, 8886-8890.

(17) Mishchenko, A.; Vonlanthen, D.; Meded, V.; Bürkle, M.; Li, C.; Pobelov, I. V.; Bagrets, A.; Viljas, J. K.; Pauly, F.; Evers, F.; Mayor, M.; Wandlowski, T. *Nano Lett.* **2010**, *10*, 156-163.

(18) Venkataraman, L.; Klare, J. E.; Nuckolls, C.; Hybertsen, M. S.; Steigerwald, M. L. *Nature* **2006**, *442*, 904-907.

(19) Ulrich, J.; Esrail, D.; Pontius, W.; Venkataraman, L.; Millar, D.; Doerrer, L. H. *J. Phys. Chem. B* **2006**, *110*, 2462-2466.

(20) Müller, K. -. *Phys. Rev. B: Condens. Matter Mater. Phys.* **2006**, *73*.

(21) Viljas, J. K.; Pauly, F.; Cuevas, J. C. *Phys. Rev. B: Condens. Matter Mater. Phys.* **2008**, *77*.

(22) Flatt, A. K.; Dirk, S. M.; Henderson, J. C.; Shen, D. E.; Su, J.; Reed, M. A.; Tour, J. M. *Tetrahedron* **2003**, *59*, 8555-8570.

(23) Huber, R.; González, M. T.; Wu, S.; Langer, M.; Grunder, S.; Horhoiu, V.; Mayor, M.; Bryce, M. R.; Wang, C.; Jitchati, R.; Schönenberger, C.; Calame, M. *J. Am. Chem. Soc.* **2008**, *130*, 1080-1084.

(24) Ruben, M.; Landa, A.; Lörtscher, E.; Riel, H.; Mayor, M.; Görls, H.; Weber, H. B.; Arnold, A.; Evers, F. *Small* **2008**, *4*, 2229-2235.

(25) Grunder, S.; Huber, R.; Wu, S.; Schönenberger, C.; Calame, M.; Mayor, M. *J. Org. Chem.* **2010**, 833-845.

(26) Meded, V.; Bagrets, A.; Arnold, A.; Evers, F. *Small* **2009**, *5*, 2218-2223.

(27) González, M. T.; Leary, E.; García, R.; Verma, P.; Herranz, M. A.; Rubio-Bollinger, G.; Martín, N.; Agraït, N. *J. Phys. Chem. C* **2011**, *115*, 17973-17978.

(28) Chen, F.; Li, X.; Hihath, J.; Huang, Z.; Tao, N. *J. Am. Chem. Soc.* **2006**, *128*, 15874-15881.

(29) Venkataraman, L.; Klare, J. E.; Tam, I. W.; Nuckolls, C.; Hybertsen, M. S.; Steigerwald, M. L. *Nano Lett.* **2006**, *6*, 458-462.

(30) Fatemi, V.; Kamenetska, M.; Neaton, J. B.; Venkataraman, L. *Nano Lett.* **2011**, *11*, 1988-1992.

(31) Quek, S. Y.; Kamenetska, M.; Steigerwald, M. L.; Choi, H. J.; Louie, S. G.; Hybertsen, M. S.; Neaton, J. B.; Venkataraman, L. *Nat. Nanotechnol.* **2009**, *4*, 230-234.

(32) Hong, W.; Manrique, D. Z.; Moreno-García, P.; Gulcur, M.; Mishchenko, A.; Lambert, C. J.; Bryce, M. R.; Wandlowski, T. *J. Am. Chem. Soc.* **2012**, *134*, 2292-2304.

(33) Tam, E. S.; Parks, J. J.; Shum, W. W.; Zhong, Y. W.; Santiago-Berríos, M. B.; Zheng, X.; Yang, W.; Chan, G. K. L.; Abruña, H. D.; Ralph, D. C. *ACS Nano* **2011**, *5*, 5115-5123.

(34) Li, Z.; Borguet, E. *J. Am. Chem. Soc.* **2012**, *134*, 63-66.

(35) Lörtscher, E.; Cho, C. J.; Mayor, M.; Tschudy, M.; Rettner, C.; Riel, H. *ChemPhysChem* **2011**, *12*, 1677-1682.

(36) Kim, B.; Beebe, J. M.; Jun, Y.; Zhu, X. Y.; Frisbie, G. D. *J. Am. Chem. Soc.* **2006**, *128*, 4970-4971.

(37) Martin, C. A.; Ding, D.; Sørensen, J. K.; Bjørnholm, T.; Van Ruitenbeek, J. M.; Van Der Zant, H. S. J. *J. Am. Chem. Soc.* **2008**, *130*, 13198-13199.

(38) Cheng, Z. L.; Skouta, R.; Vazquez, H.; Widawsky, J. R.; Schneebeli, S.; Chen, W.; Hybertsen, M. S.; Breslow, R.; Venkataraman, L. *Nat. Nanotechnol.* **2011**, *6*, 353-357.

(39) Chen, W.; Widawsky, J. R.; Vázquez, H.; Schneebeli, S. T.; Hybertsen, M. S.; Breslow, R.; Venkataraman, L. *J. Am. Chem. Soc.* **2011**, *133*, 17160-17163.

(40) Hong, W.; Li, H.; Liu, S. X.; Fu, Y.; Li, J.; Kaliginedi, V.; Decurtins, S.; Wandlowski, T. *J. Am. Chem. Soc.* **2012**, *134*, 19425-19431.

(41) Mayor, M.; Weber, H. B.; Reichert, J.; Elbing, M.; Von Hänisch, C.; Beckmann, D.; Fischer, M. *Angew. Chem. , Int. Ed.* **2003**, *42*, 5834-5838.

(42) Rigaut, S. *Dalton Trans.* **2013**, *42*, 15859-15863.

(43) Low, P. J. *Coord. Chem. Rev.* **2013**, *257*, 1507-1532.

(44) Xiao, X.; Brune, D.; He, J.; Lindsay, S.; Gorman, C. B.; Tao, N. *Chem. Phys.* **2006**, *326*, 138-143.

(45) Osorio, E. A.; Moth-Poulsen, K.; Van Der Zant, H. S. J.; Paaske, J.; Hedegård, P.; Flensberg, K.; Bendix, J.; Bjørnholm, T. *Nano Lett.* **2010**, *10*, 105-110.

(46) Mayor, M.; Von Hänisch, C.; Weber, H. B.; Reichert, J.; Beckmann, D. *Angew. Chem. , Int. Ed.* **2002**, *41*, 1183-1186.

(47) Park, J.; Pasupathy, A. N.; Goldsmith, J. I.; Chang, C.; Yalsh, Y.; Petta, J. R.; Rinkoski, M.; Sethna, J. P.; Abruña, H. D.; McEuen, P. L.; Ralph, D. C. *Nature* **2002**, *417*, 722-725.

(48) Getty, S. A.; Engtrakul, C.; Wang, L.; Liu, R.; Ke, S. H.; Baranger, H. U.; Yang, W.; Fuhrer, M. S.; Sita, L. R. *Phys. Rev. B* **2005**, *71*.

(49) Kim, B.; Beebe, J. M.; Olivier, C.; Rigaut, S.; Touchard, D.; Kushmerick, J. G.; Zhu, X. Y.; Frisbie, C. D. *J. Phys. Chem. C* **2007**, *111*, 7521-7526.

(50) Sedghi, G.; Sawada, K.; Esdaile, L. J.; Hoffmann, M.; Anderson, H. L.; Bethell, D.; Haiss, W.; Higgins, S. J.; Nichols, R. J. *J. Am. Chem. Soc.* **2008**, *130*, 8582-8583.

(51) Liu, K.; Wang, X.; Wang, F. *ACS Nano* **2008**, *2*, 2315-2323.

(52) Lu, Q.; Yao, C.; Wang, X.; Wang, F. *J. Phys. Chem. C* **2012**, *116*, 17853-17861.

(53) Chen, C. P.; Luo, W. R.; Chen, C. N.; Wu, S. M.; Hsieh, S.; Chiang, C. M.; Dong, T. Y. *Langmuir* **2013**, *29*, 3106-3115.

(54) Wen, H. M.; Yang, Y.; Zhou, X. S.; Liu, J. Y.; Zhang, D. B.; Chen, Z. B.; Wang, J. Y.; Chen, Z. N.; Tian, Z. Q. *Chem. Sci.* **2013**, *4*, 2471-2477.

(55) Xiao, X.; Xu, B.; Tao, N. *Angew. Chem. , Int. Ed.* **2004**, *43*, 6148-6152.

(56) Koyama, E.; Naitoh, Y.; Tokuhisa, H.; Nakamura, T.; Horikawa, M.; Ishida, T.; Fujiwara, K.; Mizutani, W.; Nagawa, Y.; Kanesato, M. *Jpn. J. Appl. Phys.* **2008**, *47*, 7369-7371.

(57) Lee, Y.; Yuan, S.; Sanchez, A.; Yu, L. *Chem. Commun.* **2008**, 247-249.

(58) Lee, Y.; Yuan, S.; Yu, L. *Sci. China: Chem.* **2011**, *54*, 410-414.

(59) Seo, K.; Konchenko, A. V.; Lee, J.; Gyeong, S. B.; Lee, H. *J. Am. Chem. Soc.* **2008**, *130*, 2553-2559.

(60) Seo, K.; Konchenko, A. V.; Lee, J.; Gyeong, S. B.; Lee, H. *J. Am. Chem. Soc.* **2008**, *130*, 2553-2559.

(61) Seo, K.; Konchenko, A. V.; Lee, J.; Bang, G. S.; Lee, H. *J. Mater. Chem.* **2009**, *19*, 7617-7624.

(62) Wagner, S.; Kisslinger, F.; Ballmann, S.; Schramm, F.; Chandrasekar, R.; Bodenstein, T.; Fuhr, O.; Secker, D.; Fink, K.; Ruben, M.; Weber, H. B. *Nat. Nanotechnol.* **2013**, *8*, 575-579.

(63) Li, T.; Hu, W.; Zhu, D. *Adv. Mater.* **2010**, *22*, 286-300.

(64) Feldman, A. K.; Steigerwald, M. L.; Guo, X.; Nuckolls, C. *Acc. Chem. Res.* **2008**, *41*, 1731-1741.

(65) Dadosh, T.; Gordin, Y.; Krahne, R.; Khivrich, I.; Mahalu, D.; Frydman, V.; Sperling, J.; Yacoby, A.; Bar-Joseph, I. *Nature* **2005**, *436*, 677-680.

(66) Liao, J.; Bernard, L.; Langer, M.; Schönenberger, C.; Calame, M. *Adv. Mater.* **2006**, *18*, 2444-2447.

(67) Van Der Molen, S. J.; Liao, J.; Kudernac, T.; Agustsson, J. S.; Bernard, L.; Calame, M.; Van Wees, B. J.; Feringa, B. L.; Schönenberger, C. *Nano Lett.* **2009**, *9*, 76-80.

(68) Matsuda, K.; Yamaguchi, H.; Sakano, T.; Ikeda, M.; Tanifuji, N.; Irie, M. *J. Phys. Chem. C* **2008**, *112*, 17005-17010.

(69) Akkerman, H. B.; De Boer, B. *J. Phys. : Condens. Matter* **2008**, *20*.

(70) Martin, C. A.; Van Ruitenbeek, J. M.; Van Der Zant, H. S. J. *Nanotechnology* **2010**, *21*.

(71) Xu, B.; Tao, N. J. *Science* **2003**, *301*, 1221-1223.

(72) Chen, W.; Widawsky, J. R.; Vazquez, H.; Schneebeli, S. T.; Hybertsen, M. S.; Breslow, R.; Venkataraman, L. *J. Am. Chem. Soc.* **2011**, *133*, 17160-17163.

(73) Li, C.; Mishchenko, A.; Wandlowski, T. *Top. Curr. Chem.* **2012**, *313*, 121-188.

(74) Osorio, E. A.; O'Neill, K.; Stuhr-Hansen, N.; Nielsen, O. F.; Bjømholm, T.; Van Der Zant, H. S. J. *Adv. Mater.* **2007**, *19*, 281-285.

(75) Elbing, M.; Ochs, R.; Koentopp, M.; Fischer, M.; Von Hänisch, C.; Weigend, F.; Evers, F.; Weber, H. B.; Mayor, M. *Proc. Natl. Acad. Sci. U. S. A.* **2005**, *102*, 8815-8820.

(76) Jiang, P.; Morales, G. M.; You, W.; Yu, L. *Angew. Chem. , Int. Ed.* **2004**, *43*, 4471-4475.

(77) Szacilowski, K. *Chem. Rev.* **2008**, *108*, 3481-3548.

(78) Jan Van Der Molen, S.; Liljeroth, P. *J. Phys. : Condens. Matter* **2010**, *22*, 1-30.

(79) Lörtscher, E.; Ciszek, J. W.; Tour, J.; Riel, H. *Small* **2006**, *2*, 973-977.

(80) Liljeroth, P.; Repp, J.; Meyer, G. *Science* **2007**, *317*, 1203-1206.

(81) Comstock, M. J.; Levy, N.; Kirakosian, A.; Cho, J.; Lauterwasser, F.; Harvey, J. H.; Strubbe, D. A.; Fréchet, J. M. J.; Trauner, D.; Louie, S. G.; Crommie, M. F. *Phys. Rev. Lett.* **2007**, *99*.

(82) Yasuda, S.; Nakamura, T.; Matsumoto, M.; Shigekawa, H. *J. Am. Chem. Soc.* **2003**, *125*, 16430-16433.

(83) Kumar, A. S.; Ye, T.; Takami, T.; Yu, B. C.; Flatt, A. K.; Tour, J. M.; Weiss, P. S. *Nano Lett.* **2008**, *8*, 1644-1648.

(84) Dulić, D.; Van Der Molen, S. J.; Kudernac, T.; Jonkman, H. T.; De Jong, J. J. D.; Bowden, T. N.; Van Esch, J.; Feringa, B. L.; Van Wees, B. J. *Phys. Rev. Lett.* **2003**, *91*, 207402/1-207402/4.

(85) Katsonis, N.; Kudernac, T.; Walko, M.; Van Der Molen, S. J.; Van Wees, B. J.; Feringa, B. L. *Adv. Mater.* **2006**, *18*, 1397-1400.

(86) Chen, F.; He, J.; Nuckolls, C.; Roberts, T.; Klare, J. E.; Lindsay, S. *Nano Lett.* **2005**, *5*, 503-506.

(87) Xiao, X.; Nagahara, L. A.; Rawlett, A. M.; Tao, N. *J. Am. Chem. Soc.* **2005**, *127*, 9235-9240.

(88) Wu, S. W.; Ogawa, N.; Nazin, G. V.; Ho, W. *J. Phys. Chem. C* **2008**, *112*, 5241-5244.

(89) Olsson, F. E.; Paavilainen, S.; Persson, M.; Repp, J.; Meyer, G. *Phys. Rev. Lett.* **2007**, *98*.

(90) Liang, W.; Shores, M. P.; Bockrath, M.; Long, J. R.; Park, H. *Nature* **2002**, *417*, 725-729.

(91) Xu, B.; Xiao, X.; Yang, X.; Zang, L.; Tao, N. *J. Am. Chem. Soc.* **2005**, *127*, 2386-2387.

(92) Gittins, D. I.; Bethell, D.; Schiffrin, D. J.; Nichols, R. J. *Nature* **2000**, *408*, 67-69.

(93) Albrecht, T.; Moth-Poulsen, K.; Christensen, J. B.; Hjelm, J.; Bjørnholm, T.; Ulstrup, J. *J. Am. Chem. Soc.* **2006**, *128*, 6574-6575.

(94) Haiss, W.; Van Zalinge, H.; Higgins, S. J.; Bethell, D.; Höbenreich, H.; Schiffrin, D. J.; Nichols, R. J. *J. Am. Chem. Soc.* **2003**, *125*, 15294-15295.

(95) Li, C.; Mishchenko, A.; Li, Z.; Pobelov, I.; Wandlowski, T.; Li, X. Q.; Würthner, F.; Bagrets, A.; Evers, F. *J. Phys. : Condens. Matter* **2008**, *20*.

(96) Collier, C. P.; Wong, E. W.; Belohradský, M.; Raymo, F. M.; Stoddart, J. F.; Kuekes, P. J.; Williams, R. S.; Heath, J. R. *Science* **1999**, *285*, 391-394.

(97) Collier, C. P.; Mattersteig, G.; Wong, E. W.; Luo, Y.; Beverly, K.; Sampaio, J.; Raymo, F. M.; Stoddart, J. F.; Heath, J. R. *Science* **2000**, *289*, 1172-1175.

(98) Diehl, M. R.; Steuerman, D. W.; Tseng, H. R.; Vignon, S. A.; Star, A.; Celestre, P. C.; Stoddart, J. F.; Heath, J. R. *ChemPhysChem* **2003**, *4*, 1335-1339.

(99) Yu, H.; Luo, Y.; Beverly, K.; Stoddart, J. F.; Tseng, H. R.; Heath, J. R. *Angew. Chem. , Int. Ed.* **2003**, *42*, 5706-5711.

(100) Stewart, D. R.; Ohlberg, D. A. A.; Beck, P. A.; Chen, Y.; Williams, R. S.; Jeppesen, J. O.; Nielsen, K. A.; Stoddart, J. F. *Nano Lett.* **2004**, *4*, 133-136.

(101) Green, J. E.; Wook Choi, J.; Boukai, A.; Bunimovich, Y.; Johnston-Halperin, E.; Deionno, E.; Luo, Y.; Sheriff, B. A.; Xu, K.; Shik Shin, Y.; Tseng, H. R.; Stoddart, J. F.; Heath, J. R. *Nature* **2007**, *445*, 414-417.

(102) Shimizu, K. T.; Fabbri, J. D.; Jelincic, J. J.; Melosh, N. A. *Adv. Mater.* **2006**, *18*, 1499-1504.

(103) Guo, X.; Zhou, Y.; Feng, M.; Xu, Y.; Zhang, D.; Gao, H.; Fan, Q.; Zhu, D. **2007**, *17*, 763-769.

(104) Zhang, W.; Deionno, E.; Dichtel, W. R.; Fang, L.; Trabolsi, A.; Olsen, J. -.; Benítez, D.; Heath, J. R.; Stoddart, J. F. *J. Mater. Chem.* **2011**, *21*, 1487-1495.

(105) Coskun, A.; Spruell, J. M.; Barin, G.; Dichtel, W. R.; Flood, A. H.; Botros, Y. Y.; Stoddart, J. F. *Chem. Soc. Rev.* **2012**, *41*, 4827-4859.

(106) Choi, J. W.; Flood, A. H.; Steuerman, D. W.; Nygaard, S.; Braunschweig, A. B.; Moonen, N. N. P.; Laursen, B. W.; Luo, Y.; Delonno, E.; Peters, A. J.; Jeppesen, J. O.; Xu, K.; Stoddart, J. F.; Heath, J. R. **2005**, *12*, 261-279.

(107) Collier, C. P.; Mattersteig, G.; Wong, E. W.; Luo, Y.; Beverly, K.; Sampaio, J.; Raymo, F. M.; Stoddart, J. F.; Heath, J. R. *Science* **2000**, *289*, 1172-1175.

(108) Hipps, K. W. *Science* **2001**, *294*, 536-537.

(109) Kushmerick, J. G.; Holt, D. B.; Pollack, S. K.; Ratner, M. A.; Yang, J. C.; Schull, T. L.; Naciri, J.; Moore, M. H.; Shashidhar, R. *J. Am. Chem. Soc.* **2002**, *124*, 10654-10655.

(110) Ciszek, J. W.; Tour, J. M. *Tetrahedron Lett.* **2004**, *45*, 2801-2803.

(111) Resendiz, M. J. E.; Noveron, J. C.; Disteldorf, H.; Fischer, S.; Stang, P. J. *Org. Lett.* **2004**, *6*, 651-653.

(112) Saitoh, Y.; Koizumi, T.; Osakada, K.; Yamamoto, T. *Can. J. Chem.* **1997**, *75*, 1336-1339.

(113) Ziessel, R.; Suffert, J.; Youinou, M. *J. Org. Chem.* **1996**, *61*, 6535-6546.

(114) Resendiz, M.; Noveron, J.; Disteldorf, H.; Fischer, S.; Stang, P. *Org. Lett.* **2004**, *6*, 651-653.

(115) Flatt, A. K.; Yao, Y.; Maya, F.; Tour, J. M. *J. Org. Chem.* **2004**, *69*, 1752-1755.

(116) Huang, S.; Tour, J. M. *J. Org. Chem.* **1999**, *64*, 8898-8906.

(117) Gryko, D. T.; Clausen, C.; Roth, K. M.; Dontha, N.; Bocian, D. F.; Kuhr, W. G.; Lindsey, J. S. *J. Org. Chem.* **2000**, *65*, 7345-7355.

(118) Pearson, D. L.; Tour, J. M. *J. Org. Chem.* **1997**, *62*, 1376-1387.

(119) Nielsen, M.; Gothelf, K. V. *J. Chem. Soc. , Perkin Trans. 1* **2001**, *19*, 2440-2444.

(120) Wu, I.; Lin, J. T.; Luo, J.; Sun, S.; Li, C.; Lin, K. J.; Tsai, C.; Hsu, C.; Lin, J. *Organometallics* **1997**, *16*, 2038-2048.

(121) Holmes, B. T.; Pennington, W. T.; Hanks, T. W. *Synth. Commun.* **2003**, *33*, 2447-2461.

(122) Kamenetska, M.; Koentopp, M.; Whalley, A. C.; Park, Y. S.; Steigerwald, M. L.; Nuckolls, C.; Hybertsen, M. S.; Venkataraman, L. *Phys. Rev. Lett.* **2009**, *102*, 126803.

(123) Dretschkow, T.; Lampner, D.; Wandlowski, T. *J Electroanal Chem* **1998**, *458*, 121-138.

(124) Pinheiro, L. S.; Temperini, M. L. A. *Appl. Surf. Sci.* **2001**, *171*, 89-100.

(125) Cafe, P. F.; Larsen, A. G.; Yang, W.; Bilic, A.; Blake, I. M.; Crossley, M. J.; Zhang, J.; Wackerbarth, H.; Ulstrup, J.; Reimers, J. R. *J. Phys. Chem. C* **2007**, *111*, 17285-17296.

(126) Lörtscher, E.; Ciszek, J. W.; Tour, J.; Riel, H. *Small* **2006**, *2*, 973-977.

(127) Wang, L. J.; Yong, A.; Zhou, K. G.; Tan, L.; Ye, J.; Wu, G.; Xu, Z.; Zhang, H. L. *Chem. Asian J.* **2013**, *8*, 1901-1909.

(128) Zhao, X.; Huang, C.; Gulcur, M.; Batsanov, A. S.; Baghernejad, M.; Hong, W.; Bryce, M. R.; Wandlowski, T. *Chem. Mater.* **2013**, *25*, 4340-4347.

(129) Valkenier, H.; Huisman, E. H.; Van Hal, P. A.; De Leeuw, D. M.; Chiechi, R. C.; Hummelen, J. C. *J. Am. Chem. Soc.* **2011**, *133*, 4930-4939.

(130) Dietrichbuchecker, C. O.; Sauvage, J. P.; Kintzinger, J. P. *Tetrahedron Lett.* **1983**, *24*, 46.

(131) Schmittel, M.; Michel, C.; Liu, S. X.; Schildbach, D.; Fenske, D. *Eur. J. Inorg. Chem.* **2001**, 1155-1166.

(132) Collin, J. P.; Gavinã, P.; Sauvage, J. P. *Chem. Commun.* **1996**, 2005-2006.

(133) Livoreil, A.; Sauvage, J. P.; Armaroli, N.; Balzani, V.; Flamigni, L.; Ventura, B. *J. Am. Chem. Soc.* **1997**, *119*, 12114-12124.

(134) Armaroli, N. *Chem. Soc. Rev.* **2001**, *30*, 113-124.

(135) Kim, K. Y.; Farley, R. T.; Schanze, K. S. *J. Phys. Chem. B* **2006**, *110*, 17302-17304.

(136) Armaroli, N.; Balzani, V.; Collin, J. P.; Gavina, P.; Sauvage, J. P.; Ventura, B. *J. Am. Chem. Soc.* **1999**, *121*, 4397-4408.

(137) D'Andrade, B. W.; Datta, S.; Forrest, S. R.; Djurovich, P.; Polikarpov, E.; Thompson, M. E. *Org. Electron.* **2005**, *6*, 11-20.

(138) Djurovich, P. I.; Mayo, E. I.; Forrest, S. R.; Thompson, M. E. *Org. Electron.* **2009**, *10*, 515-520.

(139) Tsutsui, M.; Shoji, K.; Taniguchi, M.; Kawai, T. *Nano Lett.* **2008**, *8*, 345-349.

(140) González, M. T.; Díaz, A.; Leary, E.; García, R.; Herranz, M. A.; Rubio-Bollinger, G.; Martín, N.; Agraït, N. *J. Am. Chem. Soc.* **2013**, *135*, 5420-5426.

(141) Ed:Haynes, W. M. In *Handbook of Chemistry & Physics, 94th edition*; CRC: 2013-2014; .

(142) Abdou, H. E.; Mohamed, A. A. and Fackler,J. P. Jr In *Gold(I) Nitrogen Chemistry;* Fabian Mohr, Ed.; Gold Chemistry: Applications and Future Directions in the Life Sciences; WILEY-VCH Verlag GmbH & Co.: 2009; pp 1-45.

(143) Manas, E. S.; Chen, L. X. *Chem. Phys. Lett.* **2000**, *331*, 299-307.

(144) Malen, J. A.; Doak, P.; Baheti, K.; Don Tilley, T.; Segalman, R. A.; Majumdar, A. *Nano Lett.* **2009**, *9*, 1164-1169.

(145) Widawsky, J. R.; Darancet, P.; Neaton, J. B.; Venkataraman, L. *Nano Lett.* **2012**, *12*, 354-358.

(146) Ke, S. H.; Baranger, H. U.; Yang, W. *J. Chem. Phys.* **2007**, *126*.

(147) Solomon, G. C.; Herrmann, C.; Ratner, M. A.; Metzger, R. M., Eds.; In *Unimolecular and Supramolecular Electronics II: Chemistry and Physics Meet at Metal-Molecule Interfaces;* 2012; Vol. 313, pp 1.

(148) Arena, G.; Bonomo, R. P.; Musumeci, S.; Purrello, R.; Rizzarelli, E.; Sammartano, S. *J. Chem. Soc. , Dalton Trans.* **1983**, 1279-1283.

(149) Fernandes, A. S.; Cabral, M. F.; Costa, J.; Castro, M.; Delgado, R.; Drew, M. G. B.; Félix, V. *J. Inorg. Biochem.* **2011**, *105*, 410-419.

(150) Saha, S.; Ravikumar, I.; Ghosh, P. *Chem. Commun.* **2011**, *47*, 6272-6274.

(151) Nunes, R. M.; Delgado, R.; Cabral, M. F.; Costa, J.; Brandão, P.; Félix, V.; Goodfellow, B. J. *Dalton Trans.* **2007**, 4536-4545.

(152) Shamai, T.; Selzer, Y. *Chem. Soc. Rev.* **2011**, *40*, 2293-2305.

(153) Galperin, M.; Nitzan, A. *Phys. Chem. Chem. Phys.* **2012**, *14*, 9421-9438.

(154) Mangold, M. A.; Calame, M.; Mayor, M.; Holleitner, A. W. *J. Am. Chem. Soc.* **2011**, *133*, 12185-12191.

(155) Battacharyya, S.; Kibel, A.; Kodis, G.; Liddell, P. A.; Gervaldo, M.; Gust, D.; Lindsay, S. *Nano Lett.* **2011**, *11*, 2709-2714.

(156) Vadai, M.; Nachman, N.; Ben-Zion, M.; Bürkle, M.; Pauly, F.; Cuevas, J. C.; Selzer, Y. *J. Phys. Chem. Lett.* **2013**, *4*, 2811-2816.

(157) Gerster, D.; Reichert, J.; Bi, H.; Barth, J. V.; Kaniber, S. M.; Holleitner, A. W.; Visoly-Fisher, I.; Sergani, S.; Carmeli, I. *Nat. Nanotechnol.* **2012**, *7*, 673-676.

(158) Viljas, J. K.; Pauly, F.; Cuevas, J. C. *Phys. Rev. B: Condens. Matter Mater. Phys.* **2007**, *76*.

(159) Galperin, M.; Nitzan, A. *J. Chem. Phys.* **2006**, *124*, 234709.

(160) Flamigni, L.; Barbieri, A.; Sabatini, C.; Ventura, B.; Barigelletti, F. *Top. Curr. Chem.* **2007**, *281*, 143-203.

(161) Cotton, F. A.; Wilkinson, G. In *Advanced inorganic chemistry: a comprehensive text;* Wyley: New York, 1980; .

(162) Evans, R. C.; Douglas, P.; Winscom, C. J. *Coord. Chem. Rev.* **2006**, *250*, 2093-2126.

(163) Ruggi, A.; van Leeuwen, F. W. B.; Velders, A. H. *Coord. Chem. Rev.* **2011**, *255*, 2542-2554.

(164) Lo, K. K. W.; Chung, C. K.; Lee, T. K. M.; Lui, L. H.; Tsang, K. H. K.; Zhu, N. *Inorg. Chem.* **2003**, *42*, 6886-6897.

(165) Neve, F.; La Deda, M.; Crispini, A.; Bellusci, A.; Puntoriero, F.; Campagna, S. *Organometallics* **2004**, *23*, 5856-5863.

(166) Lepeltier, M.; Lee, T. K. M.; Lo, K. K. W.; Toupet, L.; Le Bozec, H.; Guerchais, V. *Eur. J. Inorg. Chem.* **2005**, 110-117.

(167) Zhao, Q.; Liu, S.; Shi, M.; Wang, C.; Yu, M.; Li, L.; Li, F.; Yi, T.; Huang, C. *Inorg. Chem.* **2006**, *45*, 6152-6160.

(168) Dragonetti, C.; Falciola, L.; Mussini, P.; Righetto, S.; Roberto, D.; Ugo, R.; Valore, A.; De Angelis, F.; Fantacci, S.; Sgamellotti, A.; Ramon, M.; Muccini, M. *Inorg. Chem.* **2007**, *46*, 8533-8547.

(169) Zeng, X.; Tavasli, M.; Perepichka, I. F.; Batsanov, A. S.; Bryce, M. R.; Chiang, C. J.; Rothe, C.; Monkman, A. P. *Chem. -Eur. J.* **2008**, *14*, 933-943.

(170) Kiran, R. V.; Hogan, C. F.; James, B. D.; Wilson, D. J. D. *Eur. J. Inorg. Chem.* **2011**, 4816-4825.

(171) Ohsawa, Y.; Sprouse, S.; King, K. A.; DeArmond, M. K.; Hanck, K. W.; Watts, R. J. *J. Phys. Chem.* **1987**, *91*, 1047-1054.

(172) Sprouse, S.; King, K. A.; Spellane, P. J.; Watts, R. J. *J. Am. Chem. Soc.* **1984**, *106*, 6647-6653.

(173) Zhao, L.; Ghosh, K.; Zheng, Y.; Lyndon, M. M.; Williams, T. I.; Stang, P. J. *Inorg. Chem.* **2009**, *48*, 5590.

(174) Neve, F.; Crisping, A.; Campagna, S.; Serroni, S. *Inorg. Chem.* **1999**, *38*, 2250-2258.

(175) Didier, P.; Ortmans, I.; Mesmaeker, A. K. -.; Watts, R. J. *Inorg. Chem.* **1993**, *32*, 5239-5245.

(176) Bao, D.; Millare, B.; Xia, W.; Steyer, B. G.; Gerasimenko, A. A.; Ferreira, A.; Contreras, A.; Vullev, V. I. *J. Phys. Chem. A* **2009**, *113*, 1259-1267.

(177) Walters, K. A.; Ley, K. D.; Cavalaheiro, C. S. P.; Miller, S. E.; Gosztola, D.; Wasielewski, M. R.; Bussandri, A. P.; Van Willigen, H.; Schanze, K. S. *J. Am. Chem. Soc.* **2001**, *123*, 8329-8342.

(178) Glusac, K. D.; Jiang, S.; Schanze, K. S. *Chem. Commun.* **2002**, *8*, 2504-2505.

(179) Juris, A.; Balzani, V.; Barigelletti, F.; Campagna, S.; Belser, P.; von Zelewsky, A. *Coord. Chem. Rev.* **1988**, *84*, 85-277.

(180) Lafolet, F.; Welter, S.; Popovic, Z.; De Cola, L. *J. Mater. Chem.* **2005**, *15*, 2820-2828.

(181) Plummer, E. A.; Hofstraat, J. W.; De Cola, L. *Dalton Trans.* **2003**, 2080-2084.

(182) Colombo, M. G.; Hauser, A.; Güdel, H. U. *Inorg. Chem.* **1993**, *32*, 3088-3092.

(183) Ponce, J.; Arroyo, C. R.; Tatay, S.; Frisenda, R.; Gaviña, P.; Aravena, D.; Ruiz, E.; van der Zant, Herre S. J.; Coronado, E. *J. Am. Chem. Soc. submitted* .

(184) Ruthkosky, M.; Castellano, F. N.; Meyer, G. J. *Inorg. Chem.* **1996**, *35*, 6406-6412.

(185) Becke, A. D. *J. Chem. Phys.* **1993**, *98*, 5648-5652.

(186) Frisch, M. J.; Trucks, G. W.; Schlegel, H. B.; Scuseria, G. E.; Robb, M. A.; Cheeseman, J. R.; Scalmani, G.; Barone, V.; Mennucci, B.; Petersson, G. A.; Nakatsuji, H.; Caricato, M.; Li, X.; Hratchian, H. P.; Izmaylov, A. F.; Bloino, J.; Zheng, G.; Sonnenberg, J. L.; Hada, M.; Ehara, M.; Toyota, K.; Fukuda, R.; Hasegawa, J.; Ishida, M.; Nakajima, T.; Honda, Y.; Kitao, O.; Nakai, H.; Vreven, T.; Montgomery, J. A., Jr.; Peralta, J. E.; Ogliaro, F.; Bearpark, M.; Heyd, J. J.; Brothers, E.; Kudin, K. N.; Staroverov, V. N.; Kobayashi, R.; Normand, J.; Raghavachari, K.; Rendell, A.; Burant, J. C.; Iyengar, S. S.; Tomasi, J.; Cossi, M.; Rega, N.; Millam, N. J.; Klene, M.; Knox, J. E.; Cross, J. B.; Bakken, V.; Adamo, C.; Jaramillo, J.; Gomperts, R.; Stratmann, R. E.; Yazyev, O.; Austin, A. J.; Cammi, R.; Pomelli, C.; Ochterski, J. W.; Martin, R. L.; Morokuma, K.; Zakrzewski, V. G.; Voth, G. A.; Salvador, P.; Dannenberg, J. J.; Dapprich, S.; Daniels, A. D.; Farkas, Ö.; Foresman, J. B.; Ortiz, J. V.; Cioslowski, J.; Fox, D. J. In *Gaussian 09, Revision B.01;* Gaussian, Inc.: Wallingford CT, 2009; .

(187) Soler, J. M.; Artacho, E.; Gale, J. D.; García, A.; Junquera, J.; Ordejón, P.; Sánchez-Portal, D. *J. Phys. : Condens. Matter* **2002**, *14*, 2745-2779.

(188) Perdew, J. P.; Burke, K.; Ernzerhof, M. *Phys. Rev. Lett.* **1996**, *77*, 3865-3868.

(189) Ma, Z.; Rissner, F.; Wang, L.; Heimel, G.; Li, Q.; Shuai, Z.; Zojer, E. *Phys. Chem. Chem. Phys.* **2011**, *13*, 9747-9760.

(190) Vargas, M. C.; Giannozzi, P.; Selloni, A.; Scoles, G. *J. Phys. Chem. B* **2001**, *105*, 9509-9513.

(191) Hines, T.; Díez-Pérez, I.; Nakamura, H.; Shimazaki, T.; Asai, Y.; Tao, N. *J. Am. Chem. Soc.* **2013**, *135*, 3319-3322.

(192) Martin, C. A.; Ding, D.; Van Der Zant, H. S. J.; Van Ruitenbeek, J. M. *New J. Phys.* **2008**, *10*, 1-18.

(193) Rubio-Bollinger, G.; Bahn, S. R.; Agraït, N.; Jacobsen, K. W.; Vieira, S. *Phys. Rev. Lett.* **2001**, *87*, 026101/1-026101/4.

Resumen

Esta tesis se centra en el estudio de compuestos de coordinación de interés en el campo de la electrónica molecular. Este campo tiene como objetivo la utilización de unidades moleculares como componentes activos en circuitos electrónicos. Los dispositivos unimoleculares presentan cualidades únicas, inherentes a la nanoescala, que no poseen equivalencia en los componentes convencionales, actualmente basados en el silicio. Además, la síntesis de moléculas dispone de un altísimo grado de control sobre el tamaño y estructura final que permite la fabricación 'a medida' de estos componentes. Entre otros compuestos, los complejos metálicos despiertan un especial interés debido sus ricas propiedades ópticas, redox y magnéticas. Además, la combinación de los centros metálicos con ligandos de tipo orgánico permite un alto grado de funcionalización.

El primero de los capítulos de esta tesis ha sido dedicado a los rotaxanos de cobre. Los rotaxanos son moléculas entrelazadas compuestas por un anillo enhebrado por un fragmento de tipo lineal que ha sido taponado en ambos extremos para evitar la disociación de sus componentes. En este caso la interacción que ejerce de plantilla y que posteriormente va a determinar la posición relativa del anillo respecto al eje es la coordinación a un ión de cobre. Las diferentes preferencias de coordinación de Cu(I), tetra, y Cu(II), penta o hexacoordinado, hace que estos sistemas sean sensibles al estado de oxidación del metal. De este modo, la incoporación de chelatos bi y tridentados en la estructura da lugar al movimiento relativo de anillo y eje como respuesta a un impulso electroquímico en un proceso reversible.

El primero de los rotaxanos sintetizados, **R1**$^{+}$, fue de tipo lanzadera molecular en los que las diferentes posiciones de coordinación se distribuyen a lo largo del eje buscando el desplazamiento longitudinal del anillo a lo largo de este. La estructura de este rotaxano, mostrada en la Figura 1, engloba una unidad de 2,2':6',2''-terpiridina (terpy) directamente enlazada a una unidad de 1,10-fenantrolina (phen) en el eje. Esta

disposición ha sido elegida para facilitar el movimiento del anillo a lo largo del eje. Con el mismo propósito, el diseño del entorno tetracoordinado, incluye dos unidades de fenantrolina funcionalizadas en las posiciones 2,9 y 3,8. Se ha demostrado que los entornos de coordinación poco congestionados posibilitan la aproximación de una molécula auxiliar y de este modo aceleran la reorganización del ión de Cu(II) desde la posición tetra hasta la pentacoordinada, que es típicamente la etapa limitante del movimiento.

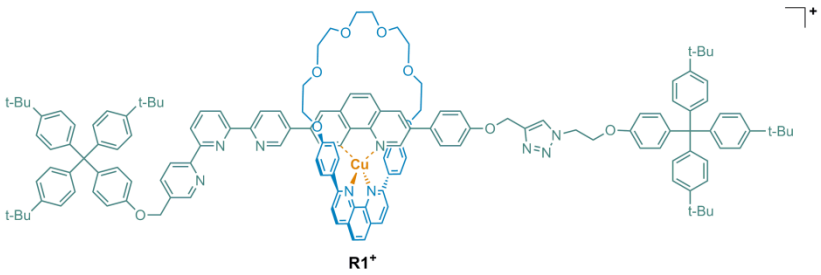

R1^{+}

Figura 1 Estructura del rotaxano **R1**$^{+}$.

El autoensamblado de este sistema fue llevado a cabo mediante el enhebrado del anillo por el eje mono-taponado asistido por el efecto platilla del Cu(I) y la posterior incorporación del segundo grupo taponador en el eje por 'click chemistry'. La obtención del rotaxano **R1**$^{+}$, en el que el anillo se sitúa sobre la phen fue verificada por resonancia magnética de protón (^{1}H RMN), espectrometría de masas de alta resolución y espectroscopía UV-vis. Por su parte, el movimiento cíclico y reversible del anillo desde la posición de tetra hasta la pentacoordinada fue evidenciado por voltamperometría cíclica. De acuerdo con lo observado en ejemplos anteriores, la reorganización de la especie inestable de Cu(II) tetracoordinado es el proceso limitante del ciclo. La constante del velocidad de este proceso fue calculada a partir de la evolución de la relación de intensidades de los picos anódico y catódico del proceso Cu(II/I) en la posición tetracoordinada con la velocidad de barrido. El valor obtenido, k = 0.3 s^{-1}, demuestra que tanto la proximidad de las dos posiciones de coordinación como la disminución de la congestión en torno a la esfera de coordinación teracoordinada contribuyen a acelerar el movimiento del anillo. Sin embargo, este valor es ligeramente inferior al descrito por

otros rotaxanos basados en unidades de bipiridina en lugar de fenantrolina. La flexibilidad del quelato bidentado es otro factor que favorece la labilidad del ión Cu(II).

El segundo de los rotaxanos sintetizados, **R3**$^{+}$, fue diseñado para realizar un movimiento radial del anillo en torno al eje. Con este fin, la estructura de **R3**$^{+}$, mostrada en la Figura 2, contiene una posición bidentada en el eje y dos posiciones, una bi y otra tridentada, en el anillo.

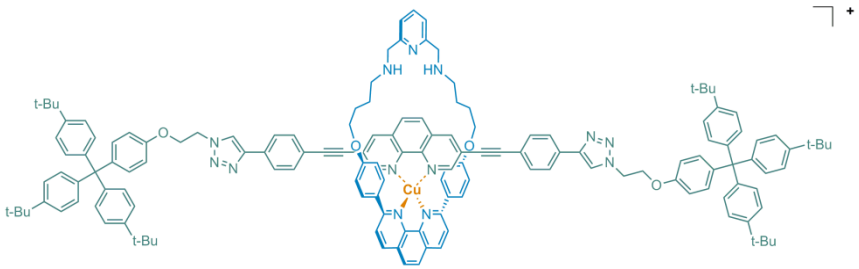

Figura 2 Estructura del rotaxano **R3**$^{+}$.

En este rotaxano hemos sustituido la unidad de terpy por una unidad de piridina bisamina. Estos últimos ligandos se forman fácilmente por la condensación de la piridina 2,6-dicarboxaldehído con dos aminas terciarias, y posterior reducción in situ que evita la apertura del enlace imina. De tal modo, su síntesis resulta mucho más sencilla que la síntesis de terpyridinas, basada en reacciones de acoplamiento cruzado. Además, este quelato es más flexible que la terpy y por tanto estabiliza mejor el estado de oxidación Cu(II), caracterizado por entornos de coordinación axialmente elongados. Por otra parte, el entorno de coordinación tetracoordinanado está formado por dos phens sustituidas en 2,9 y 3,8, al igual que en el rotaxano **R1**$^{+}$, con la única diferencia de que en esta ocasión la phen del eje ha sido funcionalizada con grupos acetileno, escogidos por motivos de tipo electrónico, como veremos posteriormente.

La compatibilidad de la reacción de formación de la piridina bisamina con los complejos de Cu(I) posibilitó que el ensamblado del rotaxano **R3**$^{+}$ se llevara a cabo por 'clipping'. Este procedimiento parte de un eje doblemente taponado sobre el cual se engarza el

precursor abierto del anillo, en este caso por el efecto plantilla del cobre, que finalmente se cierra en torno al eje. Este rotaxano fue caracterizado en sus dos estados Cu(I) y Cu(II) por ^{1}H RMN (Cu(I)), espectrometría de masas, EPR Cu(II) y espectroscopías IR y UV-vis; que confirmaron la coordinación del ión de Cu(II) a la unidad de piridina bisamina.

El estudio electroquímico reveló que la esfera pentacoordinada en **R3**$^{2+}$ estabiliza el estado de oxidación Cu(II) en mayor medida que los entornos basados en el quelato terpy. De este modo, los potenciales de oxidación en este rotaxano están separados por más de 1 V, que define el intervalo de potencial en el que el sistema es termodinámicamente estable en cualquiera de sus 2 estados de oxidación. En cuanto a la cinética del sistema, el movimiento del anillo demostró ser más rápido que la máxima velocidad de barrido alcanzable por el experimento. Sin embargo, la constante cinética del proceso pudo ser estimada en 620 s^{-1} a partir del desplazamiento anódico del pico de oxidación. Este valor hace de **R3**$^{+}$ el más rápido de los rotaxanos de cobre descritos hasta la fecha.

En conclusión, la respuesta electroquímica del rotaxano **R1**$^{+}$ muestra el efecto de la proximidad de las posiciones de coordinación sobre la cinética de los rotaxanos lanzadera basados en el sistema Cu(I/II) y refleja la importancia de la flexibilidad del quelato en el grado de labilidad del cobre. Por su parte, la introducción del ligando piridina bisamina en el rotaxano **R3**$^{+}$ ha supuesto una gran simplificación de los procedimientos sintéticos y apunta a la formación y posterior reducción de iminas como una alternativa a la 'click chemistry' muy conveniente para la preparación de sistemas entrelazados de cobre. Además este quelato contribuye en gran medida a la estabilización del estado oxidado del cobre en estos rotaxanos, lo cual da lugar a amplios rangos de biestabilidad redox y, adicionalmente, a muy elevadas constantes cinéticas.

En el segundo capítulo de esta tesis hemos querido investigar las posibilidades de dos ligandos basados en un conjugado de terpy/phen para la construcción de estructuras metálicas supramoleculares. Los ligandos **A** y **B**, mostrados en la Figura 3, han surgido de la síntesis de rotaxanos tratada en el capítulo anterior. Al poseer varias posiciones de

coordinación, estos ligandos pueden dar lugar a entidades discretas de coordinación de distinta dimensionalidad en su combinación con metales de transición.

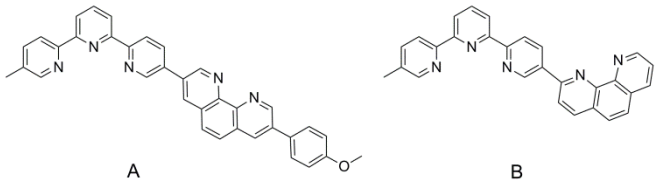

Figura 3 Estructura de los ligandos **A** y **B.**

Teniendo en cuenta las demandas de coordinación de metales y ligandos, el autoemsamblado de entidades de coordinación prediseñadas han podido ser obtenidas con un alto grado de selectividad. De acuerdo con el principio de máxima ocupación, metalociclos de distinta nuclearidad fueron obtenidos en nuestro grupo a partir de sales de Cu(II) en un trabajo anterior.

Siguiendo con esta investigación, el ligando **A** fue combinado con una sal de Fe(II) en estequiometría 5:6 Fe:**A** para dar lugar a una caja pentanuclear con geometría de bipirámide trigonal. En esta estructura, la coordinación de seis ligandos **A** completa las 5 esferas octaédricas del hierro en dos entornos distintos $[Fe(phen)_3]^{2+}$ (2+2+2) and $[Fe(terpy)_2]^{2+}$ (3+3), como se ilustra en la Figura 4. La geometría de esta caja fue propuesta de acuerdo con los ensayos de ^1H RMN y su espectro de masas y fue optimizada por DFT. A pesar de la elevada carga positiva de la caja, diferentes ensayos realizados con aniones no mostraron dar lugar a fenómenos de inclusión.

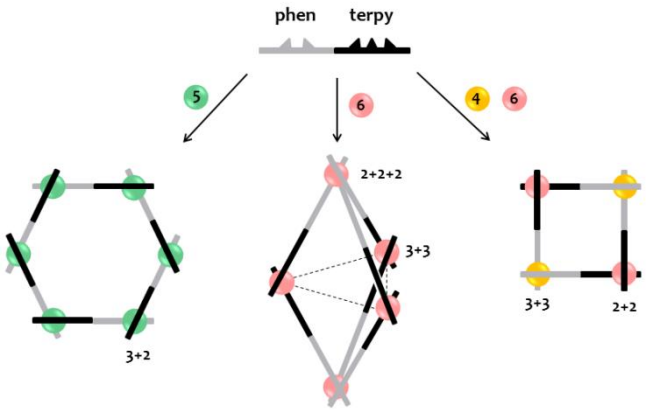

Figura 4 Superestructuras obtenidas mediante el autoensamblado de los ligandos **A** y **B**: un hexágono (3+2) (izq.), una caja (2+2+2)-(3+3) (centro) y un cuadrado (2+2)-(3+3) (dcha.). Los números entre paréntesis indican el índice de coordinación.

A continuación, con el propósito de obtener cuadrados heterometálicos, el ligando **A** fue hecho reaccionar con sales de metales divalentes hexacoordinados y monovalentes tetracoordinados en estequiometría 1:1:2 M(II):M(I):**A** (véase la Figura 4). Aunque el ligando **A** no dio los resultados esperados, el conjugado **B**, el cual posee la mismas unidades de coordinación enlazadas de diferente manera, sí que dio lugar a cuadrados heterometálicos con las combinaciones de metales: Fe(II)/Cu(I), Co(II)/Cu(I) y Fe(II)/Ag(I). Este autoemsamblado pudo realizarse de manera toposelectiva en un único paso aprovechando la diferente denticidad de las unidades de terpy y phen. La estructura de estos cuadrados fue resuelta por difracción de rayos X, y confirma la disposición de los iones metálicos en vértices opuestos de una estructura de tipo cuadrangular.

Resumiendo, un alto grado de control ha sido alcanzado en la formación de superestructuras de coordinación a partir de los ligandos **A** y **B**. La combinación en la estequiometría apropiada con metales de distinto índice de coordinación ha dado lugar a una caja de geometría bipirámide trigonal y a cuadrados heterometálicos, ambas arquitecturas poco comunes entre las superestructuras de coordinación. Desafortunadamente, la distancia entre ambas posiciones de coordinación no dio lugar a efectos cooperativos en las propiedades redox de estos compuestos.

En el tercer capítulo trata del desarrollo de dispositivos electrónicos unimoleculares a partir de compuestos de coordinación. La amplia histéresis redox presentada por el rotaxano **R3**$^{4+}$ y su rápida respuesta electroquímica hacen de este sistema biestable un óptimo candidato para el desarrollo de dispositivos de memoria de tamaño nanométrico. Este hecho motivó la adaptación química del sistema para ser estudiado en dispositivos de transporte unimoleculares de tipo MCBJ.

Con este objetivo en mente, el primer paso fue la sustitución de los grupos taponadores del eje del rotaxano por grupos de anclaje a electrodos de oro. El establecimiento de enlaces químicos con los electrodos metálicos es fundamental a la hora de conseguir un buen acoplamiento entre los electrodos y la molécula y de este modo conseguir disminuir la altura de la barrera túnel al paso de la corriente eléctrica. Además la naturaleza de este enlace juega un papel fundamental y va a determinar en gran medida las propiedades conductoras del sistema. Por este motivo tres grupos de anclaje distintos fueron probados: tioles, piridinas y acetilenos. El segundo factor determinante en las propiedades conductoras de un cable molecular es la estructura química de la cadena. La transmisión de corriente túnel disminuye de manera exponencial con la longitud del polímero orgánico de acuerdo con un factor que es característico de la naturaleza de la cadena. En moléculas conjugadas este factor es menor, y por lo tanto presentan una menor resistencia al paso de corriente. La elección de grupos de tipo oligophenylenethylene (OPE) para la construcción de la cadena se basó además en la inexistencia de isómeros y en su fácil acoplamiento a través de reacciones de Sonogashira. Adicionalmente, moleculas de distinta longitud fueron testados con el objetivo de modular el acoplamiento con los electrodos. Todo esto dio lugar a la preparación de la familia de cables moleculares que se muestra en la Figura 5.

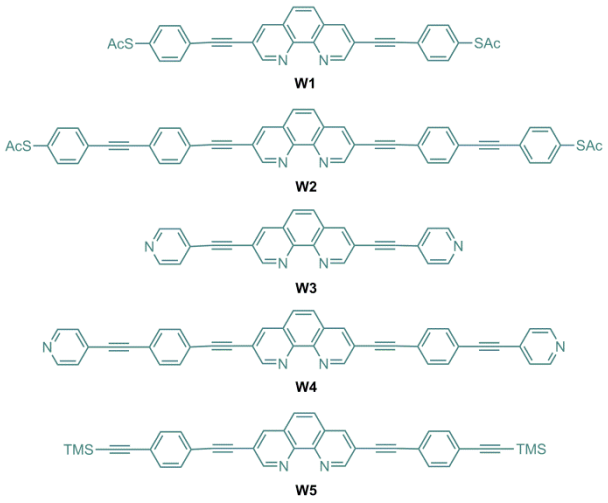

Figura 5 Estructura de los cables moleculares sintetizados.

La medida de las propiedades eléctricas de estos cables en evidenció que **W2** y **W4** conducían por debajo del límite de detección del aparato de medida y sólo pudo obtenerse un valor definido de conductancia para **W1** y **W3**.

A continuación, con vistas a la medida del complejo biestable de Cu(I/II) se llevó a cabo la caracterización eléctrica de complejos no biestables de Cu(I) con los cables **W1**, **W3** y **W5**. En oposición a los estudios realizados hasta la fecha, las medidas de transporte en estos complejos revelaron un efecto variable frente a la coordinación en función del grupo de anclaje: las moléculas funcionalizadas con grupos tiol y acetileno, aumentaban su resistencia al paso de corriente al formar el complejo, mientras que, en las funcionalizadas con piridinas esta resistencia disminuía. Los trabajos anteriores describen en todos los casos un aumento de la conductancia en el complejo debido a un cambio en la conformación. Sin embargo, en nuestro caso la unidad de phen no ve alterada su conformación con la complejación, y por tanto la conductancia es únicamente sensible a efectos electrónicos. Los estudios de DFT de nuestros sistemas desvelaron que este comportamiento es debido al distinto alineamiento de los orbitales moleculares con el nivel de Fermi de los electrodos. La complejación a un metal conlleva en todos los casos una disminución de la energía de los orbitales moleculares del ligando. Este efecto

hace que en los cables que conducen a través del HOMO (tioles y acetilenos) la diferencia de este nivel con el nivel de Fermi aumente, lo que conlleva una disminución de la conductancia. Sin embargo en las piridinas, al conducir a través del nivel LUMO, el efecto es el contrario. Esta correlación en principio es aplicable al resto de metales de transición.

La caracterización eléctrica de los compuestos anteriores mostró que los cables con grupos de anclaje piridina presentan la mejor relación señal/ruido y por tanto fueron escogidos para la construcción del complejo biestable funcionalizado para ser medido en uniones moleculares. La biestabilidad redox del rotaxano **R3**$^{+}$ hizo posible la preparación del sistema en sus dos estados a partir del enhebrado con sales de Cu(I) y Cu(II). Los dos complejos se muestran en la Figura 6. Ambos moléculas fueron caracterizados por ^{1}H RMN (Cu(I)), EPR (Cu(II)), espectrometría de masas de alta resolución y análisis elemental.

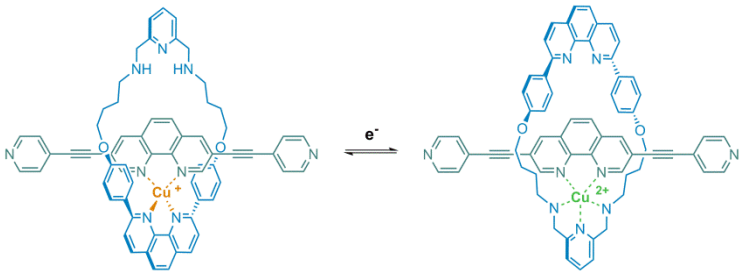

Figura 6 Movimiento radial inducido por la oxidación/reducción del ión cobre en el sistema biestable aplicado a uniones moleculares.

Los cálculos de DFT realizados sobre este sistema predicen que el estado de alta conductancia corresponde al complejo en su forma de Cu(II), mientras que el complejo en su forma de Cu(I) corresponde al estado de baja conductancia. La versión no-biestable de ambos complejos ha sido preparada con el objetivo de ejercer de experimento de control. La medida de las propiedades eléctricas del sistema en ambos estados de oxidación se realiza actualmente en dispositivos MCBJ de con dos terminales, de manera que, por el momento, no hemos podido corroborar si la discriminación eléctrica entre ambos estados es posible.

De manera adicional, esta familia de cables moleculares fue empleada para la construcción de complejos ciclometalados de Ir(III) que puedan ser integrados en uniones eléctricas moleculares. La irradiación con luz de estos complejos da lugar a estados fotoexcitados de larga vida caracterizados por una distribución electrónica muy diferente a la del estado fundamental. De acuerdo con este hecho, se espera que la conducción eléctrica de estos compuestos se vea considerablemente afectada por la luz. Este hecho podría dar lugar a dipositivos optoelectrónicos en los cuales la resistencia al paso de la corriente eléctrica pueda ser modulado por acción de la iluminación. La combinación de sales ciclometaladas de Ir(III) con los cables moleculares vistos anteriormente (Figura 5) dio lugar a una familia de complejos monocationicos de iridio, mostrados en la Figura 7, que combinan la baja resistencia de los cables con las propiedades luminiscentes de los compuestos de iridio. Se ha visto que las propiedades ópticas de los complejos de Ir(III) es muy sensible a la funcionalización de los ligandos. Un amplio estudio fotofísico y electroquímico fue llevado a cabo con el objetivo de caracterizar en profundidad la naturaleza electrónica del estado fotoexcitado en nuestros complejos, y así poder predecir su comportamiento eléctrico en presencia de luz. De los resultados de este estudio se extrajo que en los cuatro complejos el estado fundamental es un triplete caracterizado por una fuerte transferencia de carga desde el HOMO (localizado en el metal) hacia el LUMO (localizado sobre el cable molecular). De acuerdo con el efecto de la complejación visto anteriormente, se espera que el efecto de la luz provoque un aumento considerable de la conductancia en los cables de iridio funcionalizados con piridinas terminales.

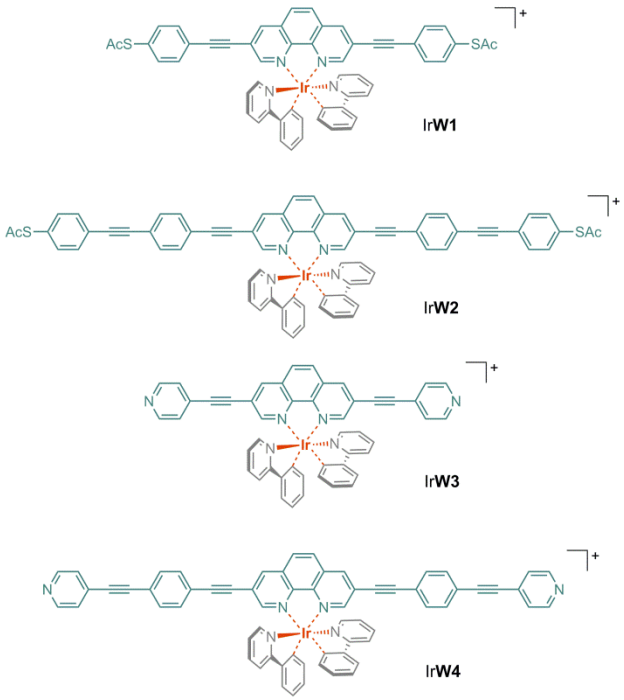

Figura 7 Estructura de los cables luminiscentes de Ir(III).

List of publications

- 'Self-assembly of an iron(II)-based M_5L_6 metallosupramolecular cage' Cardona Serra, S.; Coronado, E.; Gavina, P.; Ponce, J.; Tatay, S. *Chem. Commun.* **2011**, *47*, 8235-8237.
- 'Fast pirouetting motion in a pyridine bis-amine-containing copper-complexed rotaxane' Coronado, E.; Gaviña, P.; Ponce, J.; Tatay S. *Chem. Eur. J.* **2014**, *in press*. DOI: 10.1002/chem.201304434
- 'Effect of metal complexation on the conductance of single molecular wires measured at room temperature' Ponce, J.; Arroyo, C. R.; Tatay, S.; Frisenda, R.; Gaviña, P.; Aravena, D.; Ruiz, E.; van der Zant, Herre S. J.; Coronado, E.. *JACS submitted.*
- 'Fast redox-triggered shuttling motions in a copper rotaxane based on a directly bonded phenanthroline/terpyridine conjugate' Coronado, E.; Gaviña, P.; Ponce, J.; Tatay, S.. *Tetrahedron. submitted*.
- 'Photophysical properties of conjugated Iridium (III) complexes functionalized with metal anchoring groups' Ponce, J.; Tatay, S.; Aragó, J.; Vayà, I.; Ortí, E.; Coronado, E. *To be submitted*.

I want to clarify that in papers published by Prof. Eugenio Coronado's group, due to internal policy, authors of the group appear in alphabetic order. If the paper is fruit of collaboration with other groups, authors from the other groups appear afterwards in the order that they decide. Therefore I am the first researcher in all the works listed herein, although in most of them I do not appear as first author.